Czech Technical University in Prague

Faculty of Nuclear Sciences and Physical Engineering

DISSERTATION

Plasmonic structures for biosensing

Prague, 2021 Jiří Slabý

Bibliografický záznam

Autor	Ing. Jiří Slabý České vysoké učení technické v Praze Fakulta jaderná a fyzikálně inženýrská Katedra fyzikální elektroniky
Název práce	Plazmonické struktury pro biodetekci
Studijní program	Aplikace přírodních věd
Studijní obor	Fyzikální inženýrství
Školitel	prof. Ing. Jiří Homola, CSc., DSc. Ústav fotoniky a elektroniky AV ČR
Školitel specialista	doc. Ing. Ivan Richter, Dr. České vysoké učení technické v Praze Fakulta jaderná a fyzikálně inženýrská Katedra fyzikální elektroniky
Akademický rok	2021-2022
Počet stran	127
Klíčová slova	povrchový plazmon, optické biosenzory, nanostruktury

Bibliographic Entry

Author	Ing. Jiří Slabý
	Czech Technical University in Prague
	Faculty of Nuclear Sciences and Physical Engineering
	Department of Physical Electronics

Title of Dissertation	Plasmonic structures for biosensing
Degree Programme	Applications of Natural Sciences
Field of Study	Physical Engineering

Supervisor	prof. Ing. Jiří Homola, CSc., DSc.
	Institute of Photonics and Electronics
	The Czech Academy of Sciences
Supervisor specialist	doc. Ing. Ivan Richter, Dr.
	Czech Technical University in Prague
	Faculty of Nuclear Sciences and Physical Engineering
	Department of Physical Electronics

Academic Year	2021-2022
Number of Pages	127
Keywords	surface plasmon,
	optical biosensor,
	nanostructures

Abstrakt

Optické biosenzory založené na rezonanci povrchových plazmonů (SPR) představují nejrozvinutější přímou (bezznačkovou) biodetekční technologii. Použití plazmonických nanostruktur pro rozvoj těchto biosenzorů může vést k dosáhnutí nižších detekčních limitů či pro vytvoření nových funkčních vlastností. Tato dizertační práce se zabývá pokroky ve výzkumu a vývoji plasmonických nanostruktur pro biodetekci, konkrétně se pak zaměřuje na pochopení plasmonických jevů, návrh a výrobu plasmonických nanostuktur a jejich využití v nových optických biosenzorech a to jak založených na měření indexu lomu, tak na povrchově zesílené Ramanově spektroskopii (SERS). V této práci byla teoreticky i experimentálně studována široká škála nanostruktur. Potenciál biosenzorů při využití těchto nanostruktur byl kvantitativně vyjádřen jako nejmenší detekovatelná koncentrace analytu a to v závislosti na optoelektronických vlastnostech detekčního systému a vlastnostech ovlivňující transport analytu k povrchu senzoru a jeho následný záchyt. Pomocí tohoto přístupu byly navrženy dva nové biosenzory a na modelových experimentech bylo demonstrováno zlepšení limitu detekce při srovnání s konvenčními SPR biosenzory. V rámci dizertační práce byly studovány také přístupy pro překonání omezení biosenzorů založených na SERS plynoucího ze závislosti intenzity SERS signálu na vzdálenosti analytu a detekčního povrchu. První přístup využil nanostrukturu citlivou na teplo, která pomocí přechodu mezi nabobtnalým a smrštěným stavem umožňovala aktivně ovlivnit tok kapaliny obsahující analyt do oblastí s velkou intenzitou elektromagnetického pole. Druhý přístup využil speciální mnohovrstevnatou nanostrukturu založenou na poli nanoděr, která umožňovala vybudit elektromagnetický mód, jehož intenzita dosahuje dále od zlatého povrchu struktury.

Abstract

Optical biosensors based on surface plasmons (SPs) present the most advanced label-free biosensing technology. The introduction of plasmonic nanostructures into biosensing is envisioned to provide plasmonic biosensors with improved performance or new functionalities. This dissertation describes several advancements in the development of plasmonic structures for plasmonic biosensing with a focus on the understanding, design, and fabrication of these structures and their use for the construction of novel optical biosensors based on refractometry and surface-enhanced Raman spectroscopy (SERS). In this work, a broad range of nanostructures was studied both theoretically and experimentally. The biosensing potential of such structures was evaluated in terms of the minimal detectable concentration and related to propertied of optical read-out platform and mass-transport efficiency. Based on the theoretical investigation performed in this work, two novel sensors based on nanostructures have been designed and shown to exceed the performance of conventional SPR biosensors. In order to overcome the limitations related to the distance between the molecule and the substrate in SERS-based biosensors, two novel approaches were pursued. In the first approach, a thermoresponsive nanostructure was used to actively trigger fluid flow to the regions of high electromagnetic field by its swelling and collapsing. In the second approach, a special multilayer nanostructure based on a nanohole array was researched to extend the electromagnetic field associated with surface plasmons farther from the sensing structure.

ACKNOWLEDGMENT

Foremost, I would like to express my sincere gratitude to my supervisor prof. Jiří Homola for all the wonderful opportunities I have in the Optical Biosensor Research Team at the Institute of Photonics and Electronics.

Interdisciplinary science is a collaborative process of experts with diverse backgrounds. Completing this work thus would have been more difficult without the support and friendship provided by the other members of the team and our collaborators. All the shared experience helped me to understand many aspects of our fascinating field. I thank namely Barbora Špačková for all the discussions on simulations and effects in plasmonics, Milan Vala for discussions on nanofabrication processes, Nicolas Scott Lynn for all the expertise in the field of microfluidics and mass transport, and Markéta Bocková for responding to an innumerable number of questions related to biochemistry and applications of our biosensors. I am also grateful to nanofabrication heroes, Petra Lebrušková and Petr Dvořák, who support me with many gold structures. I thank Karel Chadt, who is prepared to be challenged with my optomechanical needs at any time.

I would like to thank my advisor doc. Ivan Richter for all the plasmonic discussions we underwent during my studies.

Special thanks to my friends. You pleasantly distracted me from work whenever it was needed.

And last but not least, I would like to thank my family for all the support and encouragement I got during my entire life.

TABLE OF CONTENTS

1 INTRODUCTION

Over the last three decades, optical biosensors offered a unique way for the detection of chemical and biological species [1]. Optical biosensors can provide important benefits, such as the real-time observation of molecular interactions and the label-free detection and quantification of chemical and biological species [2]. Various optical platforms for label-free biosensing have been developed, including interferometric sensors, spectroscopic sensors based on absorption and Raman scattering, and sensors based on spectroscopy of guided modes [3].

The biosensors based on the excitation of surface plasmons (SPs) present the most advanced technology in optical biosensors. The use of SPs enables squeezing the light tightly to the biosensor sensing surface thus boosting the sensitivity. Since their conception in the early 1990s, surface plasmon resonance (SPR) based sensors have become a key technology for the investigation of molecular interactions in molecular biology [4].

The introduction of plasmonic nanostructures into SPR-based biosensing at the beginning of the 21st century has opened a promising way to improve the optical biosensors' characteristics [5, 6]. The noble-metal nanostructures exhibit various plasmonic effects that offer unique properties. These effects include propagating SPs modes, localized SPs, the coupling of localized and propagating surface plasmons, lattice resonances, Fano resonances, etc. Each of the effects might provide different characteristics in terms of electromagnetic (EM) field distribution and spectral properties. Furthermore, a high intensity of electric field accompanying the excitation of SPs makes plasmonic nanostructures attractive for numerous other sensing approaches, including fluorescence and Raman scattering [7].

Despite all the advances, many of the characteristics of plasmonic biosensors still need to be improved to match the requirements in relevant applications in medical diagnostics, food safety, security, and others. The requirements include performance merits (the lowest concentrations of the analyte to be measured, precision and repeatability of the measurement), instrumental properties (number of simultaneous analyses, time required for analysis, size of the instrument, cost of the instrument, and

single analysis). Many of these issues can be uniquely addressed by using suitably designed plasmonic nanostructures.

This Dissertation is concerned with the theoretical and experimental research on nanostructures supporting surface plasmons and their application for biosensing carried out by the author in the Institute of Photonics and Electronics in Prague. Chapter 1 reviews the fundamental principles of surface plasmons supported by nanostructures and state-of-the-art in the biosensing using these SPs. Chapter 2 defines the objectives of this dissertation, Chapter 3 presents the published results of the author's research, and Chapter 4 summarizes the results of the research.

1.1 Surface plasmons

Surface plasmons are surface-bound collective oscillations of charge at the boundary between a medium with unbound electrons (e.g. noble metals at optical frequencies) and a dielectric [8]. There are two fundamental forms of surface plasmons: propagating surface plasmons (PSPs) at the planar metal-dielectric interface, and localized surface plasmons (LSPs) at the metal nanoparticle (Figure 1).

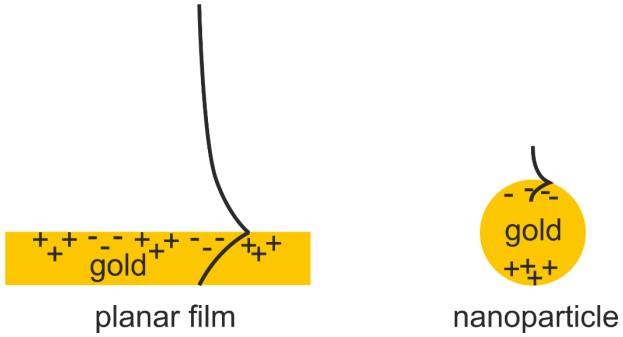

Figure 1: Illustration of charge distribution and the evanescent electromagnetic field of a propagating surface plasmon at planar gold film and localized surface plasmon at gold spherical nanoparticle.

Two important properties characterize surface plasmons:

1. **The surface plasmons are associated with high electromagnetic fields in the close vicinity of the metal-dielectric interface**. The amplitude of the electric field at the interface is increased up to a thousand times with respect to an incident field [9]. The field decays exponentially from the structure surface. The typical penetration depth is in order of hundreds (typical for PSPs) to tens (typical for LSPs) of nanometers. The areas with highly concentrated electromagnetic field are called “hot spots”. The extremely high field enhancement in hot spots arises from various mechanisms including constructive surface plasmons interference and enhancement due to specific morphology of the nanoparticle surface, such as enhancement at a sharp tip or in a narrow gap [10].

Figure 2: Illustration of electric field intensity in plasmonic hot spots: sharp tips and narrow gaps between the nanoparticles.

2. **Surface plasmons can be excited by light.** There are fundamental differences in conditions for excitation of different SPs. There are SPs that are accessible (bright modes) and inaccessible (dark modes) by an incident linearly-polarized plane wave. Some of the SPs require a special coupler, such as a prism or a grating. The interaction of the light with SPs is governed by both SP's properties (based on the nanostructure shape, size, and material) and incident light properties (angle of incidence, polarization, and wavelength). Importantly, the interaction of excitation light with the SPs results in strong wavelength-dependent characteristics (such as wavelength-dependent absorption or scattering).

1.2 Nanostructures supporting surface plasmons

Various types of surface plasmons can be supported by complex metallic nanostructures. There has been extensive theoretical and experimental research over the last decade covering different materials, shapes, and excitation schemes [5, 11, 12]. Many different materials are suitable for the excitation of SPs. Gold is undoubtedly the most used noble metal for many applications in visible and near-infrared; notably in biosensing, gold is used due to its convenient optical properties and its high chemical stability. In the following sections, the most prominent types of plasmonic nanostructures are discussed with respect to the modes they support: namely metal layers and waveguides, metal nanoparticles, and nanohole arrays in the metal layer.

1.2.1 Metal layers and waveguides

The structure that consists of a single interface between metal and dielectric can support (and guide) the propagating surface plasmon (PSP). The PSP mode is characterized by its electromagnetic field distribution and a propagation constant. The electromagnetic field of PSP is maximized at the interface and decays exponentially from the interface. The decay length from the interface is the penetration depth. The

electromagnetic field is also characterized by having only three non-zero components being transverse-magnetic. The propagation constant of PSP k_{PSP} can be expressed as

$$k_{PSP} = k_0 \sqrt{\frac{\varepsilon_m \varepsilon_d}{\varepsilon_m + \varepsilon_d}}, \tag{1}$$

where k_0, ε_m, ε_d are wavenumber in a vacuum, a dielectric constant of the metal, and a dielectric constant of the dielectric medium, respectively.

A metal layer sandwiched between two dielectrics supports also SPs. If the thickness of the metal layer is much larger than the penetration depth, the layer supports two independent SP modes. Once the thickness of the metal layer decreases, the SPs on the opposite boundaries of the layer couple and create mixed SP modes [13]. For a symmetric structure (both dielectric mediums are of the same dielectric constant), the two modes originate: symmetric (long-range) and antisymmetric (short-range) SPs. The former naming system refers to the symmetry in the distribution of a magnetic field and the latter refers to the level of attenuation in the direction of propagation as well as the penetration depth. For an asymmetric structure (the dielectric media are of different dielectric constant), the symmetric SPs ceases to exist as the thickness of the metal layer decreases (mode cut-off).

The 2D-infinite metal layer confines the EM field in a single dimension only. To confine the EM field even more closely in the plane perpendicular to the direction of propagation, a metal layer might be limited into a stripe of finite width (also called a wire or ribbon). A single metal stripe can support plasmonic modes as analyzed by Berini [14, 15]. Mode analysis of the stripes with a width of 0.5 um and 1 um was presented for various thicknesses of the gold stripe and various refractive indices of the surrounding medium. There are four fundamental modes related to symmetric and antisymmetric coupling between 4 different faces of a stripe. The full mode structure is rather complicated and depends strongly on the material and geometrical properties of the stripe. Contrary to the plasmonic modes supported by an infinite 2D layer, all the components of the EM field have non-zero values (no transverse-magnetic or transverse-electric modes), although some of the transversal components might dominate.

1.2.2 Metal nanoparticles

Small subwavelength metal nanoparticles (NPs) support localized surface plasmons (LSPs). The fundamental mode of the NP is a dipolar LSP. For a spherical particle, the electric field distribution is illustrated in Figure 3.

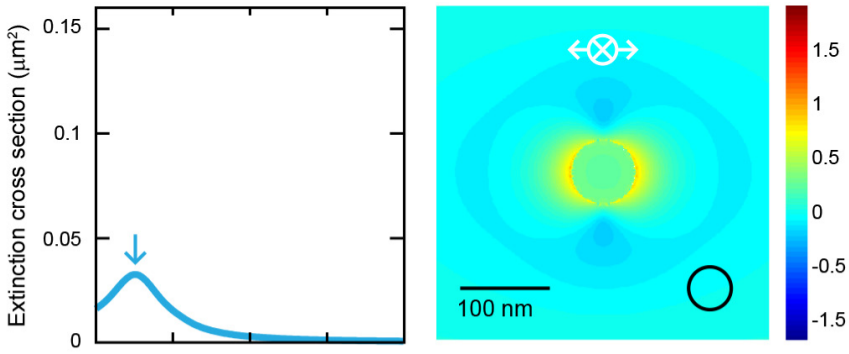

Figure 3: Extinction cross-section and electric field distribution E at the resonant wavelength of Au sphere with a diameter of 80 nm [5].

The frequency of dipolar mode depends on the NP material, size, shape, and permittivity of the surrounding medium. The effect of the NP shape on surface plasmon is illustrated in Figure 4. The dark field image shows directly that the color of the maximum scattered intensity (i.e. surface plasmon frequency) is changing with NP shape. The extinction cross-section for a spherical particle is shown in Figure 3.

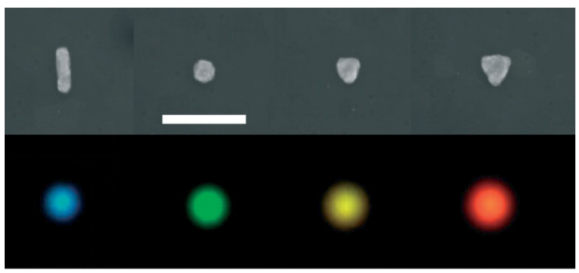

Figure 4: Scanning electron microscopy image (top) and dark field image (bottom) of various nanoparticles – nanorod, nanodisk, small and large triangle [16].

Unlike a spherical particle, a metallic nanorod supports two fundamental LSP modes – longitudinal and transversal. The longitudinal and transversal modes are excited when the incident light is polarized parallel to the long and short axis respectively (Figure 5, left). The electric field of longitudinal mode is strongly enhanced at the tips of nanorod (right) and the resonant frequency strongly depends on the rod aspect ratio

(length/width). The optimal ratio varies depending on application [17, 18]; in biosensing, nanorods with the aspect ratio between 3 and 4 provide the best performance [19, 20].

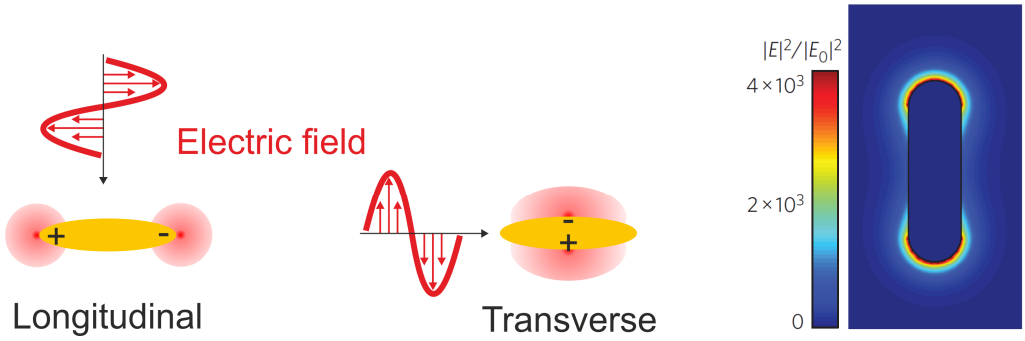

Figure 5: Longitudinal and transverse mode of gold nanorod (left) and enhancement of electric field at nanorod tips [21] (right).

1.2.3 Nanohole arrays

Various complex nanostructures support modes that arise from the mixing of localized and propagating surface plasmons. Among those, nanohole arrays exhibit a phenomenon called extraordinary optical transmission [22], which is a product of multiple effects [23, 24]. Most importantly for periodic arrays, the PSPs are excited by diffractive coupling and the EM field interacts with the plasmonic mode of the single nanohole. Also, propagating SPs may be excited in the form of an SP-Bloch wave. The electric field in the vicinity of the nanohole is illustrated in Figure 6.

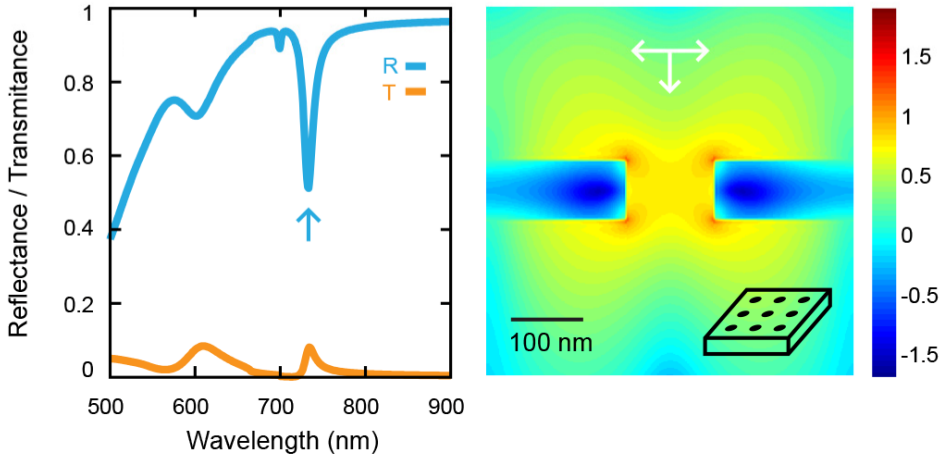

Figure 6: Reflectance/transmittance and electric field distributions E at the resonant wavelength for nanohole array with a diameter of 120 nm in Au film with a thickness of 80 nm [5].

A nanohole array may be combined with a dielectric spacer, and metal nanodiscs placed under the nanoholes. In addition to the previous case, the mode structure includes LSP modes of the discs and the mode (resonance) of the cavity originating as a Fabry-Pérot resonance between the top (nanoholes) and bottom (nanodiscs) layer [25, 26].

1.3 Biosensing using plasmonic nanostructures

Surface plasmons combine two interesting features: they are **sensitive to local refractive index changes** and also they create a **locally enhanced electromagnetic field**. They can thus be used for both affinity biosensing as well as for surface-enhanced spectroscopies such as Surface-Enhanced Raman Spectroscopy (SERS) [7].

1.3.1 Plasmonic affinity biosensors

Plasmonic affinity biosensors use the plasmonic modes for refractometry of biomolecules adsorbed on a surface of a plasmonic structure. The principle of plasmonic affinity biosensors is depicted in Figure 7. Light is coupled to SPs. A molecule of interest (an analyte) is bound to the biorecognition layer on the surface of the plasmonic structure increasing a local refractive index. This refractive-index change is then monitored via change of any of the characteristics of the light coupled to SPs (intensity, resonant wavelength, or phase).

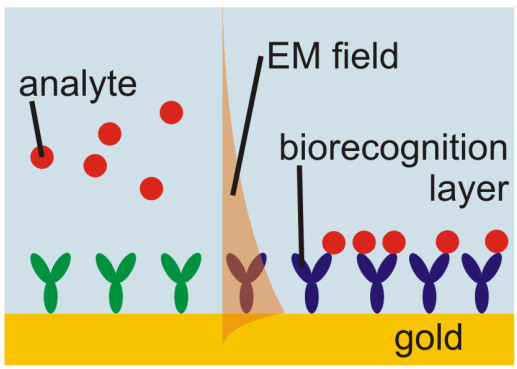

Figure 7: Affinity biosensing principle using plasmonic structure: an analyte is captured by a biorecognition layer.

The plasmonic biosensors use different mechanisms for the coupling of light into the surface plasmons. The most important geometries are illustrated in Figure 8. The excitation of propagating SPs supported by the metal layer requires a special coupling mechanism due to the momentum conservation, such as a prism coupler (A), a high-numerical-aperture microscope objective (B), or a grating coupler (D). In contrast, the excitation of localized SPs does not require any special coupling optics, but the

excitation of LSPs supported by metal NPs is often combined with bright-field or dark-field microscopy (C).

The optical nanostructure and its optical interrogation system are usually interfaced with a microfluidic cell. In this microfluidic cell, the liquid sample (containing an analyte) flows over the optical structure and the analyte might be captured by a biorecognition element. The analyte transport to the sensing surface is a process led by a complex interplay between convection, analyte diffusion, and an analyte-receptor reaction under the factors governed by a geometrical design of the microfluidic cell and optical nanostructure. All these aspects drive the rate of analyte collection on the surface which is then read by an optical system. The analyte transport is thus one of the main processes which influence the performance of the plasmonic biosensor.

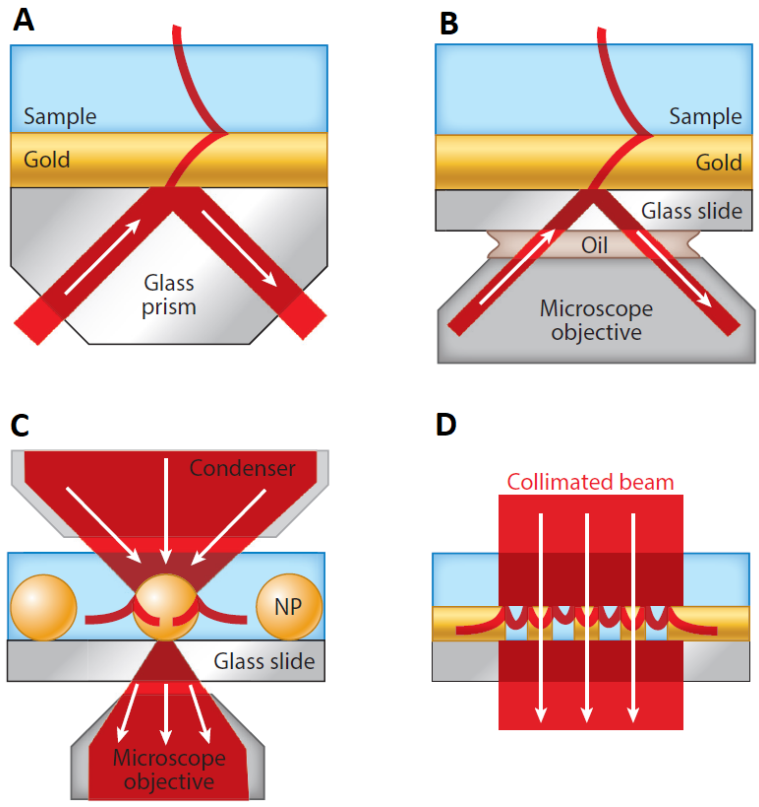

*Figure 8: Optical excitation of surface plasmons: A – a prism-based attenuated total reflection configuration for SPR imaging or spectroscopy, B – a high numerical aperture objective configuration for SPR microscopy, C – transmission arrangement for localized SPR microscopy, and D – a collinear transmission arrangement (Image taken from **Appendix I**)*

Performance characteristics

The ability to detect small changes in the refractive index is the main optical performance characteristic of a plasmonic biosensor. It is often quantified as the bulk sensitivity S, which is defined as the ratio between measured quantity Y and the bulk change of refractive index n

$$S = \frac{\partial Y}{\partial n}. \tag{2}$$

The measured quantity Y relates to the used interrogation method. Typically, Y is the wavelength of resonance in broad-band spectroscopy, the angle in angular spectroscopy, and the intensity/phase of light in imaging/microscopy of surface plasmons.

The bulk sensitivity is strongly affected by the level of localization of the electromagnetic field around the plasmonic structure. Higher bulk sensitivity does not necessarily result in a higher detection response to local (surface) refractive index change n_{surf}. For this reason, the surface sensitivity S_{surf} considers that the change occurs only in a thin layer at the vicinity of the structure surface

$$S_{\text{surf}} = \frac{\partial Y}{\partial n_{\text{surf}}} \ . \tag{3}$$

Both these sensitivities do not include the effect of the spatially inhomogeneous electromagnetic field around the structure. This is especially important for nanostructure-based sensors as the electromagnetic field is strongly confined to hot spots. It was demonstrated that the particle's "hot spot" is the volume with the highest refractive-index sensitivity [27]. The shift of SP resonance was reported to be spatially variable for the nanorods [28] and nanodisks [29]. Nanodisk local sensitivity is depicted in Figure 9.

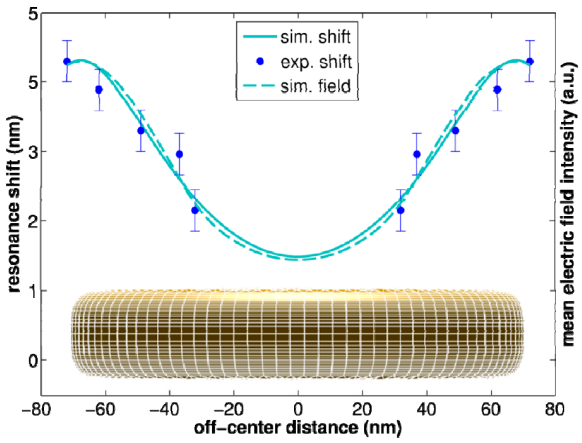

Figure 9: Shift of resonance (~sensitivity) for local change of refractive index at nanodisk surface and its corresponding electric field intensity [29].

The RI sensitivity describes the magnitude of the sensor output change with RI change; however, such RI sensitivity does not describe fully the ability to resolve these RI changes. To describe this ability, various figures of merit (FOMs) were introduced. The FOM for spectroscopy is defined as a ratio of sensitivity to the width of the resonance feature (full width in half maximum – FWHM) [4]

$$\mathrm{FOM} = \frac{S}{\mathrm{FWHM}}. \tag{4}$$

The FOM* for intensity-based sensors is defined as the relative change of intensity with respect to the change of refractive index

$$\mathrm{FOM}^* = \frac{\mathrm{d}I / \mathrm{d}n}{I}. \tag{5}$$

These FOMs are rather the result of empirical description of sensor performance. The RI sensor performance is directly quantified as a bulk RI resolution and expressed as

$$\sigma_{\mathrm{RI}} = \frac{\sigma_Y}{S}, \tag{6}$$

where σ_Y sigma is noise in sensor output. The typical RI resolution for plasmonic sensors is in the range of 10^{-6} to 10^{-7} [5]. It is possible to show that the value σ_{RI} is indirectly proportional to FOM [30].

The ability of a biosensor to detect a low number of molecules is usually described as the limit-of-detection and is expressed as

$$LOD = \frac{\sigma_{\text{blank}}}{S_{\Gamma}} \ , \tag{7}$$

where σ_{blank} is a standard deviation of sensor output to a blank sample and S_{Γ} is the sensitivity of the sensor output to the analyte concentration. The standard deviation of sensor output σ_{blank} is ultimately limited by instrumental noise.

The optimization of biosensing performance of plasmonic nanostructure is a complex task, where the application parameters (such as the size of analyte and the thickness of biorecognition layer) must be considered. In the recent review [5], the various modes on plasmonic structures were compared in terms of sensitivity and FOM. In general, the plasmonic structures with a rather short field penetration (localized surface plasmons) may be more efficient for smaller analytes.

1.3.2 Surface-enhanced Raman spectroscopy biosensors

Biosensors based on surface-enhanced Raman spectroscopy (SERS) use a metallic surface to enhance the inelastic Raman scattering of light on molecules. It provides the fingerprint of the molecular rotational-vibrational spectrum. SERS was the first vibrational spectroscopic technique claiming single-molecule sensitivity [31].

The enhancement factor (EF) is defined as the ratio between the SERS intensity of a given band and Raman intensity under the same but non-SERS conditions. Enhancement factors up to 10^{12} have been reported. The mechanism of enhancement is still not fully understood, but the enhancement is traditionally separated into two main parts [32]: chemical enhancement and electromagnetic enhancement. The electromagnetic enhancement is considered to be the largest contribution to the SERS signal. The enhancement arises from the large local electric fields. For plasmonic nanostructures, the electric field is increased by a factor of ten to thousands [33].

Considering approximation of only two fundamental mechanisms within classical theory – enhancement of local field (excitation) and radiation (re-emission), larger Stokes shifts and strong wavelength dependency of local field (what is the case of plasmonic nanostructures), and neglecting vector nature of the optical field, the SERS EF is

$$\mathrm{EF} \propto \frac{|E_{loc}(\omega_L)|^2 |E_{loc}(\omega_R)|^2}{|E_{inc}(\omega_L)|^2 |E_{inc}(\omega_R)|^2} \quad , \tag{8}$$

where ω_L is excitation wavelength, ω_R is Raman-shifted wavelength, E_{loc} is local field and E_{inc} is the incident field. The equation (8) shows that for a selected excitation and Raman band, the optimal condition for EF enhancement requires the surface plasmon frequency to be between excitation frequency and Raman-shifted frequency [7]. The formula also describes the enhancement at one place, often referred to as single-molecule enhancement. To achieve a full evaluation of the performance of a SERS substrate, the EF is spatially and spectrally averaged.

Assuming small Stokes shift and vector nature of the optical field, the SERS EM enhancement factor EF can be expressed in simple the "E^4 approximation"

$$\mathrm{EF} \propto \frac{|E_{loc}(\omega_L)|^4}{|E_{inc}(\omega_L)|^4} \quad . \tag{9}$$

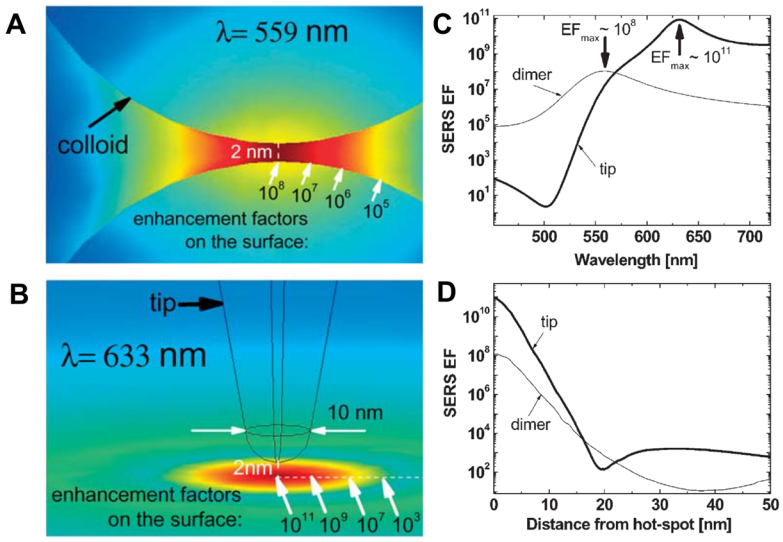

Figure 10: Electromagnetic field and the calculated SERS EF distribution A – in the nanogap (distance 2 nm) between two gold nanospheres (diameter 30 nm) with polarization along the vertical axis of the dimer and B – gold tip at two excitation wavelengths, 559 nm, and 633 nm. C and D shows SERS EFs distribution versus excitation wavelength in the region from 400 nm to 700 nm and the distance from the hot spot (in nm) [34, 35].

In Figure 10, the equation (9) was used to describe how enhanced electric field (for a tip and gap plasmonic hot-spots) influences the SERS EM enhancement factor. The SERS enhancement is spatially inhomogeneous, reaching several orders of magnitude higher EF in the very center of the hot spot than at the distance of 10 nm. The distance of the molecule from the surface is one of the factors limiting the magnitude of the SERS signal.

2 THE GOAL OF DISSERTATION

The main goal of this doctoral research is to expand the understanding of the plasmonic modes supported by nanostructures and exploit this knowledge for the development of novel biosensors.

In order to achieve this goal, the following objectives have been set:

- To analyze plasmonic modes of nanostructures suitable for biosensing.
- To analyze the performance merits of plasmonic biosensors with respect to the geometrical parameters of the nanostructures.
- To fabricate and characterize the selected nanostructures.
- To develop novel biosensors based on fabricated nanostructures for both plasmonic affinity biosensing and surface-enhanced Raman spectroscopy, which will provide a performance improvement or novel functionalities when compared with the current state-of-the-art biosensors.

3 RESULTS

This presented doctoral dissertation has resulted in 6 published papers authored or co-authored by the author of the thesis. The contribution of the author of the dissertation to each of these papers is provided in List of appendices. The results are organized into two subchapters, which focus on plasmonic nanostructures for affinity biosensors and plasmonic nanostructures combined with SERS.

3.1 Plasmonic nanostructures for affinity biosensors

The introduction of plasmonic nanostructures into biosensing has opened the door to novel sensing concepts offering potential benefits over continuous film SPR biosensors. One of the main benefits of nanostructure-based biosensors is a faster sensor response due to a lower sensing area and thus arguably a lower amount of captured molecules required to produce a sensor response. The faster sensor response might lead to an increased analytical biosensor performance in terms of the smallest resolvable amount of an analyte.

To analyze the performance of the plasmonic biosensor, a routine approach uses solely the optical characteristics of FOM. The role of analyte transport to nanostructures is an important but often overlooked theme despite its high contribution to the level of performance. For this reason, a multiphysical approach for the analysis of plasmonic biosensors is highly required. Moreover, such an approach can reveal the conditions and design parameters under which the performance of nanostructure-based plasmonic biosensors can surpass the performance of their continuous film-based counterparts.

In **Appendix II,** we addressed this issue by describing how the analyte capture depends on various parameters of the biosensor; in particular, we focused on design parameters of the micro- or nanostructures, characteristics of the interacting molecules, and the geometry of the microfluidic cell. We proposed an analytical model of the analyte transport in microfluidic systems interfaced with micro- and nanostructures. Each of these structures is characterized by its fill factor f (analyte capturing area over the whole surface area). The analytical model of mass transport to these structures is an empirical model based on the results of numerical simulations.

These were obtained by using the finite element method (COMSOL package). In the empirical model, the steady-state diffusion-limited mass-transfer coefficient (the rate of analyte transport to the surface of a nanostructure) is estimated by

$$k_m = k_p \frac{R_k - f}{R_k f - 2f + 1}, \tag{10}$$

where $R_k = k_{np} / k_p$ is a ratio of the mass transfer coefficient for an individual plasmonic element composing the array k_{np} existing outside the influence of any other functionalized elements, with respect to the mass transfer coefficient for a continuous surface k_p .

The theoretical model was verified by a series of experiments using a diverse group of micro- and nanostructures (microwires, nanodisks, and nanorods) and diverse analyte/receptor systems (DNA, RNA of different sequences). Firstly, these micro- and nanostructures were designed to allow a relatively wide range of possible fill factors by using computational electromagnetic methods (such as rigorous coupled-wave analysis for microwires and coupled dipole approximation for nanorods and nanodisks). Subsequently, the samples of micro and nanostructures were fabricated. The samples of microwires were fabricated by maskless UV lithography (widths of wire were 1.4, 10, and 100 μm, fill factors between 0.16 and 0.64), the samples of nanorods were fabricated by electron beam lithography (nanorod dimensions were: 110 nm × 30 nm × 30 nm, fill factors were between 0.01 and 0.05) and the samples of nanodisk were fabricated by the hole-mask colloidal lithography (nanodisk diameter was 110 nm, fill factor was 0.2). The samples were then interfaced with an optical prism (used for light coupling through an attenuated total reflection) and a microfluidic cell using various channel designs as illustrated in Figure 11.

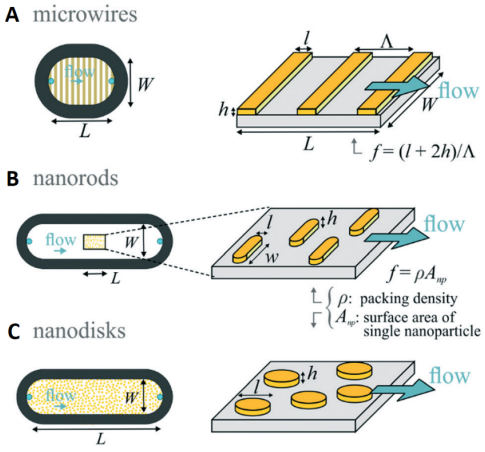

Figure 11: Illustration of the experimental arrangements for reported experiments – samples of microwires (A), nanorods (B), and nanodisks (C) with respective channel designs.

Plasmonic features were observed in normalized spectra and allowed recording sensor responses (shifts of resonance wavelength) to various analytes. We performed model oligonucleotide detection experiments. In particular, the kinetic analysis of the observed sensor response was used to extract the mass-transfer coefficients for the micro- and nanostructures and the mass-transfer coefficients are compared with those obtained with the SPR biosensor based on an unstructured gold film. To directly compare the analyte transport to nanostructure-based sensors with the analyte transport to a flat-film-based sensor, we calculated also mass transfer enhancement defined as

$$E = k_m / k_p \,. \tag{11}$$

The observed mass-transfer enhancements follow the trends theoretically predicted by the analytical model as depicted in Figure 12. For fill factors approaching 1, all the mass transfer enhancement for all the structures approaches the trend of 1/f. Generally, the structures with small feature sizes (nanodisks, nanorods) preserve 1/f trend also for lower fill factors whereas the structures with large feature sizes (microwires) do not provide further enhancement with lower fill factors. The analytical model correctly describes a deviation for these lower fill factors for all the structures.

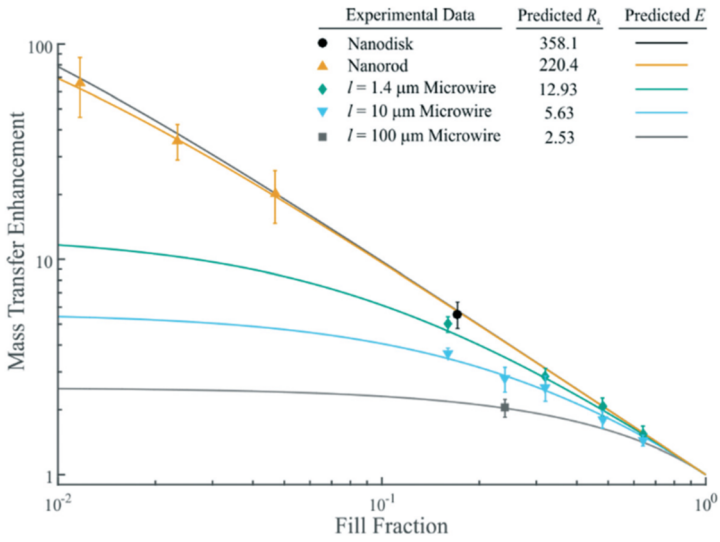

Figure 12: Mass transfer enhancement for different fill factors and different micro- and nanoplasmonic biosensors.

The results of the study **Appendix II** highlight that the analyte transport has to be considered during the design of nanostructure-based sensors and provide the analytical expression for accurate and simple calculation of the effect. Moreover, the study shows, that the analyte transport can be significantly enhanced (up to 100 times with a fill factor of 0.01) when using nanostructures resulting in the improved sensing performance of plasmonic nanobiosensors.

The performance of the nanoplasmonic biosensor is proportional to both the optical performance and the mass transport performance. These two properties are strongly affected by a variation in the fill factor of a nanostructure. Generally, the optical performance decreases, and mass transport performance increases with decreasing fill factor. The resulting trend of the biosensor performance is thus given by the interplay of these two competing effects.

To describe the full dependency of analytical performance on the fill factor, we proposed a novel universal model of the performance of nanoplasmonic biosensors in **Appendix III**. This universal model relates the performance characteristics of a biosensor with the design parameters of a plasmonic nanostructure, the microfluidic conditions, and the properties of the interacting molecules. Firstly, the minimal detectable concentration was expressed as

$$c_{\min} = \frac{3\sigma}{S_{\Gamma}\kappa}$$

where σ is the standard deviation of sensor response (noise), S_Γ is the sensitivity of sensor response to the changes of the surface density of the captured analyte, and κ is the efficiency of analyte transport from a bulk solution to the sensor surface and analyte capture by receptors. Secondly, all these three aspects were analytically estimated by appropriate theoretical models. Contributions of these aspects are also pronounced directly in the measured sensor responses. In an SPR biosensor based on a gold continuous film, the large read-out area and small mass transfer efficiency manifest as high signal-to-noise but slow sensor response. In contrast, in nanoplasmonic sensors, the small read-out area and high mass transfer efficiency result in low signal-to-noise but fast sensor response.

We applied the proposed theoretical model for the study of a nanoplasmonic biosensor based on an array of gold nanorods. We fabricated a series of samples with different packing densities of arrays (1-16 nanorods/μm^2) by electron beam lithography (Figure 13 A). We interfaced these samples with an attenuated-total-reflection-based read-out system and recorded spectra (B). As seen in Figure 13, these recorded spectra (C) corresponded well with the spectra obtained by a numerical simulation using the finite-difference time-domain method (Lumerical FDTD) combined with an analytical approximation based on island film theory (D).

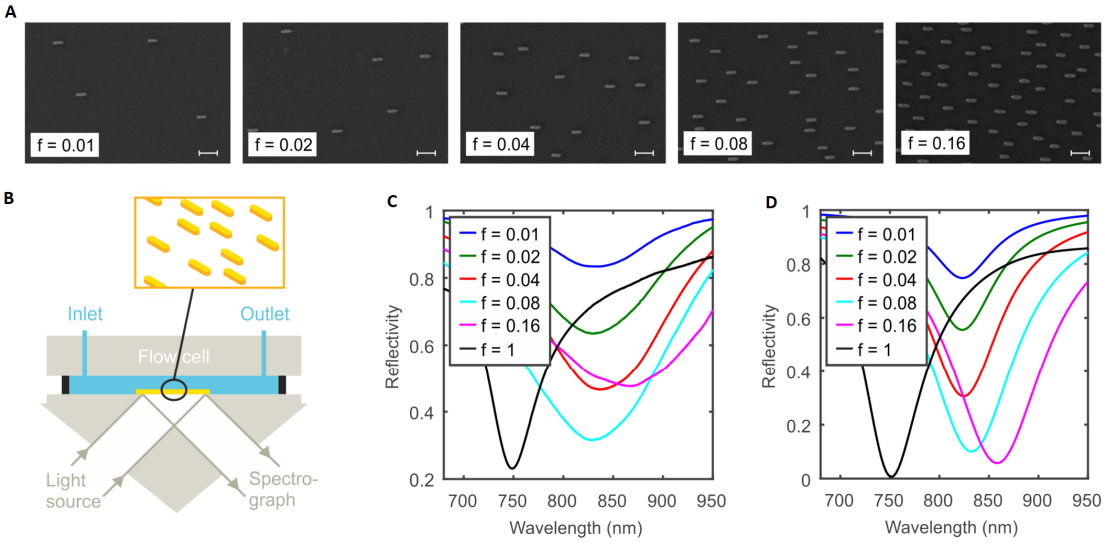

Figure 13: A – SEM images of sensing substrates with different fill fractions. B – Schematic of the biosensor. C – Experimental and D – theoretical reflectance spectra of the sensing substrates at optimal angles of incidence.

Subsequently, we used the nanorod arrays with different fill factors for the detection of single-stranded DNA (poly-A). We extracted the minimal detectable concentration for these biosensors based on different fill factors and showed this dependency in Figure 14. The minimal detectable concentration approaches a minimum for the fill factors of 0.04 and 0.08. Moreover, the nanorod-based biosensor offers a significant detection performance improvement over the standard SPR system (by a factor of 7) when the optimal packing density is selected. These trends were also confirmed by the results of theoretical model which predicts the performance increase by an order of magnitude.

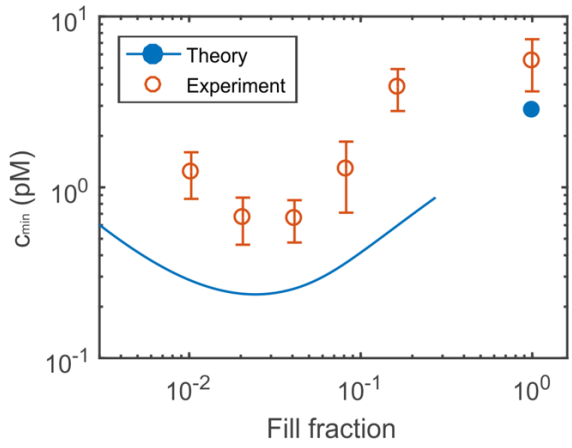

Figure 14: Comparison of the theoretical model with the experimental data showing the dependency of the smallest detectable concentration of the analyte that can be detected by a biosensor on the fill fraction of the sensing structures.

Importantly, the performance model of biosensors reported in **Appendix III** can be applied to a wide variety of optical platforms, nanoplasmonic sensing structures, and detection assays and used as an optimization tool to find the best biosensor design. It also emphasizes the role of the fill factor of the nanostructure, which has been shown to play an important role in both the noise of the optical measurement and in mass transfer.

The models developed within **Appendix II** and **III** also clarified the role of a size of a single plasmonic element which constitutes the array in the performance of the plasmonic biosensor. In general, the smaller elements provides higher mass transport enhancement and thus might lead to the higher performance of plasmonic biosensor.

In contrast, the small feature size of the plasmonic element requires more demanding fabrication techniques. To address both issues simultaneously, we used an array of gold nanostripes (**Appendix IV**). Gold nanostripes still require for its fabrication the use of nanopatterning techniques (such as electron beam lithography), but their dimensions result in a more stable fabrication process in comparison with previously reported gold nanorods.

The biosensor was designed in two consecutive steps. Firstly, the reflectivity of the nanostripe array was analyzed for various geometrical parameters of a single nanostripe (a width and a height) and a fixed period using rigorous coupled-wave analysis. Suitable geometrical parameters were selected in order to maximize the contrast of a resonance dip in the spectrum. For the wavelength corresponding to the minimum of the dip, the nanostripe array supports a plasmonic mode propagating along the nanostripes (Figure 15 A). The used fundamental plasmonic mode exhibits a maximum electric field on the top face of the nanostripe and thus is a mode with a potentially high sensitivity to RI (Figure 15 B). Secondly, the biosensing performance of a sensor using these nanostripe arrays was analyzed. In particular, the theoretical analysis encompassed the study of the effect of the nanostripe array period on the performance of a biosensor based on two different approaches: a complex performance model incorporating optical characteristics of the nanostructure as well as the actual noise characteristics of the optical readout system and a simple model based solely on the figure of merit of a plasmonic nanostructure.

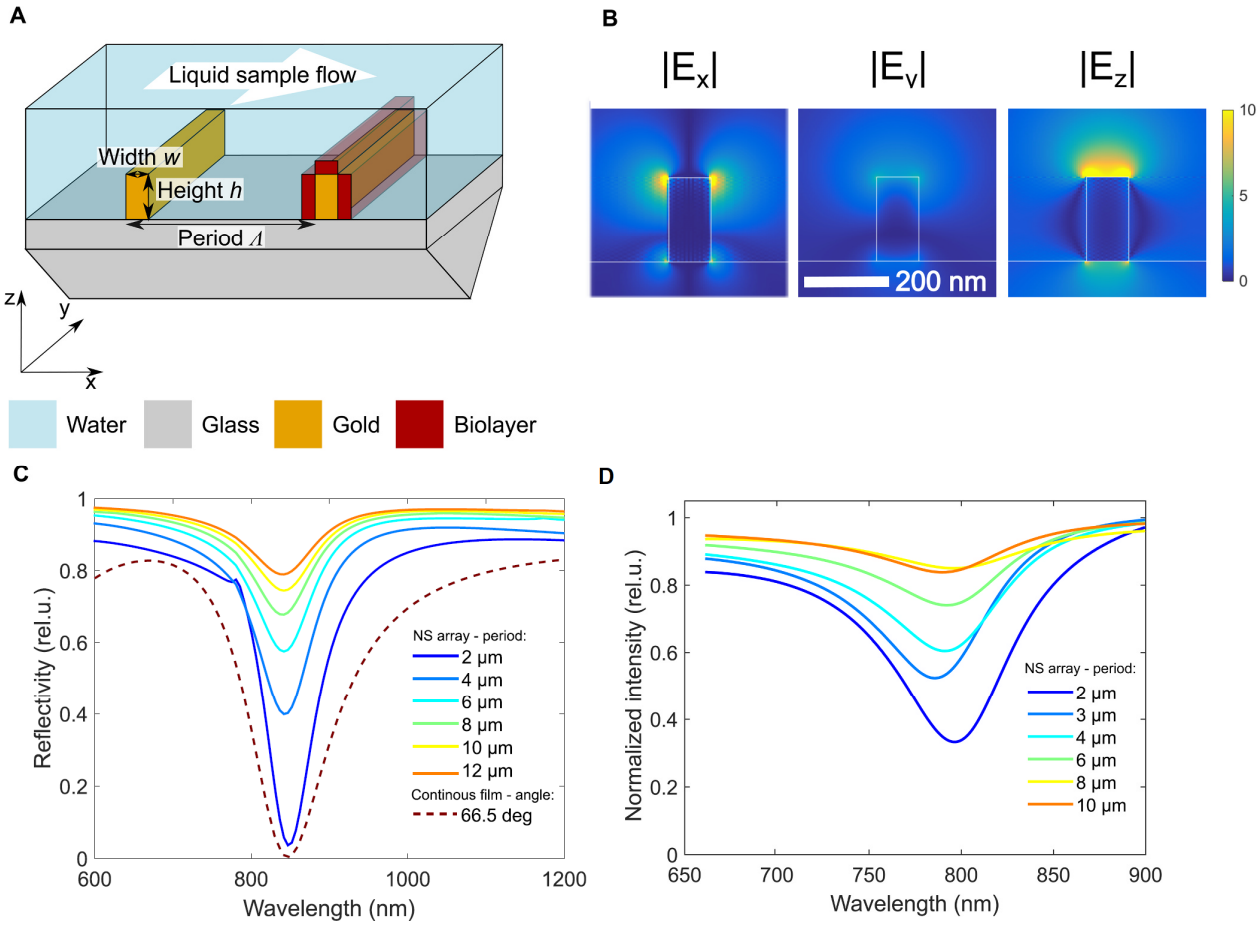

Figure 15: A – Scheme of the plasmonic nanostripe array, B – modulus of electric field for one period of a nanostripe array (height – 200 nm, width – 100 nm, period – 2 μm, wavelength – 850 nm), C – reflectivity spectra calculated for nanostripe arrays with 6 different periods by RCWA, D – normalized spectra measured for nanostripe arrays with 6 different periods (internal angle of incidence – 75 deg, sample – deionized water).

To experimentally verify the biosensor design, we have prepared gold nanostripe arrays of different parameters using electron-beam lithography. The samples were interfaced with a spectroscopy-based laboratory platform, which was modified to allow for conducting experiments under conditions suitable for excitation of surface plasmons on nanostripes (large angle of incidence, different beam sizes). The microfluidic system was modified to provide a sample flow that is orthogonal with respect to the direction of nanostripes as this is intrinsic. The comparison of theoretical and experimental spectra is shown in Figure 15 C and D. The contrasts of the dips

related to the excitation of surface plasmons are lower in the experiments than those provided by the theoretical calculations. Subsequently, the sensor was characterized in refractometric experiments in which refractive index sensitivity and the best refractive index resolution were shown to be 1989 nm/RIU and 3.6×10^{-7} RIU. The biosensing performance was characterized using a model detection of an MDS-related nucleic acid (miRNA-125b) in a buffer. The 4 different NW arrays (periods from 2 to 8 μm) provided different mass-transport properties as illustrated by different binding rates in the calibration curves in Figure 16 A. Minimal detectable concentration in Figure 16 B showed the best sensing performance for a 4 μm period. In particular, the biosensor can detect miRNA-125b at concentrations down to ~ 17 pM and provides a limit of detection better by a factor of ~ 2 than that of a conventional SPR biosensor. In comparison, the theoretical analysis suggested that the optimized biosensor is able to detect molecular analytes at concentrations lower by a factor of ~10 than the SPR biosensor using a continuous gold film.

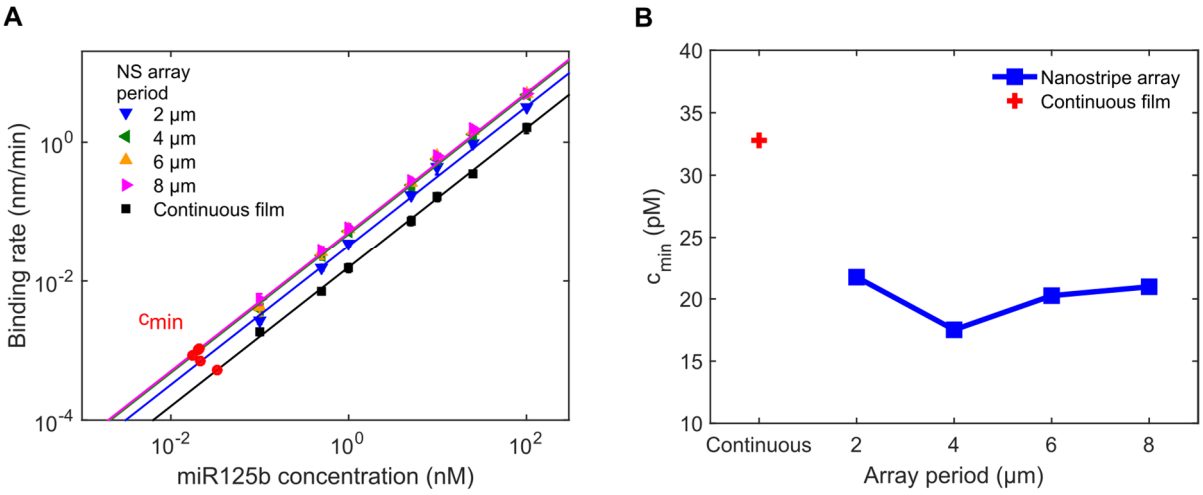

Figure 16: Detection of miR125b by the nanostripe-based plasmonic biosensor: A – Calibration curve and B – the minimum detectable concentration for 4 different periods of nanostripe array biosensor and SPR biosensor based on a continuous gold film.

The presented combined results in **Appendix IV** show how to improve the bioanalytical performance of the nanoplasmonic biosensor by selecting the appropriate packing density of plasmonic elements. The results also suggest an avenue for further improvement of the performance of this biosensor as the sidewalls of the nanostripes were not passivated against the binding of the analyte. The binding to the sidewalls

does not contribute significantly to the sensor response but removes the analyte from the liquid sample; thus the reduction of analyte binding to these areas should improve mass transfer and the performance of the biosensor even more.

3.2 Plasmonic nanostructures combined with SERS

Plasmonic sensing based on surface-enhanced Raman spectroscopy (SERS) is influenced by the distance of the molecule from the surface of the nanostructure and the magnitude of the electric field therein. The plasmonic nanostructures offer many different routes to redistribute the electromagnetic field. We present two types of nanostructures based on nanohole arrays (NHAs) to enhance the interaction of the plasmonic field with a Raman scattering molecule.

Nanohole arrays are frequently used substrates for both SERS and affinity biosensing due to easy fabrication and tunable operation. The NHAs provide the maximum intensity of electric field around the nanohole and inside the cavity. To deliver molecules of interest therein, two arrangements are considered. In a traditional arrangement, NHAs are employed as a sensor in a flow-over format; however, the performance is then strongly limited by mass transfer to the nanoholes and inside. In an unconventional format, the NHAs are employed as a sensor in a flow-through format; however, this approach requires fabricating NHA onto a nitride membrane and such nanostructure tends to be fragile.

To overcome these limitations, we firstly proposed an approach employing flow-through NHA without the need for a nitride membrane (**Appendix V)**. In this approach, the analyte flows through the porous hydrogel, which also constitutes a dielectric spacer between a nanohole array and a complimentary nanoparticle (Figure 17). The NHA-nanoparticle stack is then used to enhance the interaction of the electromagnetic field with the bound molecules. Moreover, the porous hydrogel can be actively driven to swell or collapse by a temperature. Below the critical temperature (32°C for the hydrogel used in the study – poly(N-isopropyl acrylamide)), the swelling of the hydrophilic hydrogel is accompanied by a liquid flow from the vicinity of the structure into the pores dragging the analyte inside. The hydrogel thus might serve as a quasi-3D matrix to capture the analyte. Above the critical temperature, the hydrogel's matrix collapses while expelling all the water.

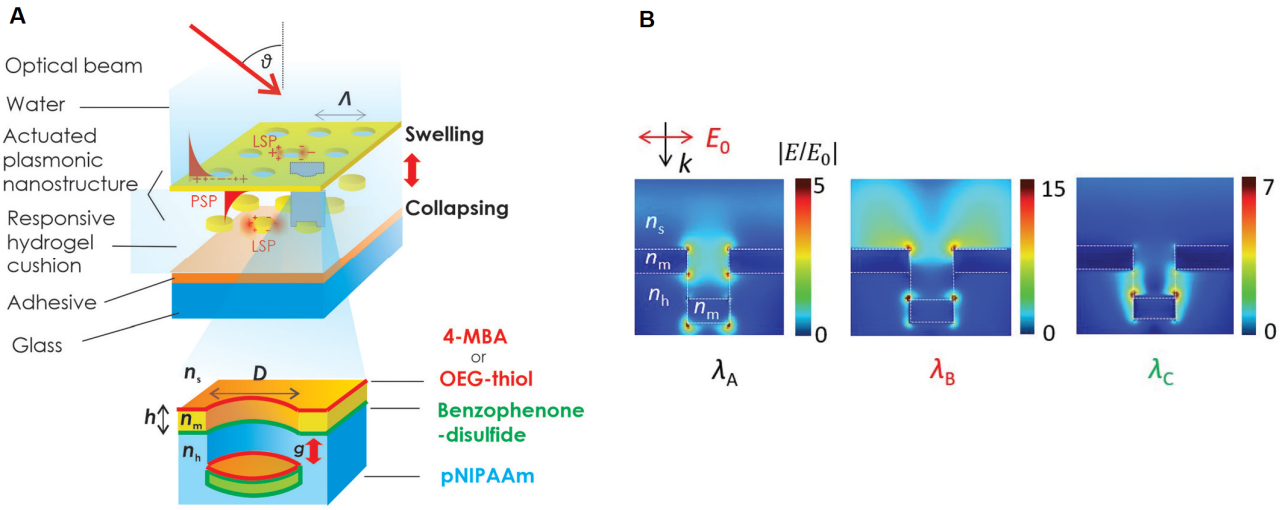

Figure 17: A – Schematics of plasmonic nanostructure composed of periodic nanohole arrays and B – the cross-section of the spatial distribution of the electric field amplitude for the plasmonic modes of the structure.

We analyzed the interaction of light with nanostructure by using Lumerical FDTD. The interplay between different modes (propagating mode on a perforated film, localized mode on a gold disk) was described with respect to the thickness and optical properties of the hydrogel layer. Subsequently, the samples of nanostructures with selected parameters were fabricated using UV nanoimprint technology combined with a template stripping method. The samples were characterized by recording normalized transmission spectra with varying angles of incidence and correspondence between the resonance peaks and dip in the theoretical simulations and experiments was identified.

To confirm the temperature-dependent behavior of the porous hydrogel, the samples were interfaced with an optical platform with a temperature-stabilized chamber. The temperature of the sample was swept between 22°C and 38°C with the increment of a single degree and the transmission spectra were recorded. Most importantly, the significant shifts of the peaks were observed above the critical temperature (Figure 18).

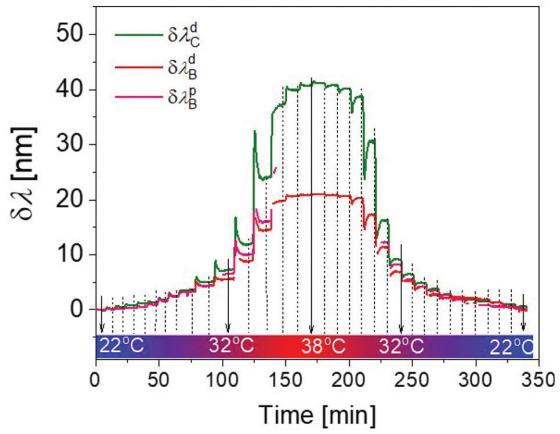

Figure 18: Dependence of spectral position of plasmonic features B and C plotted as a function of time for different temperatures in the range of T = 22 °C to T = 38°C.

To explore the potential of the developed hybrid nanostructure for biosensing, we carried out two experiments: affinity-based biosensing and SERS-based biosensing.

In the first experiment, we have directly monitored the covalent coupling of the mouse immunoglobulin G (mIgG) to a hydrogel layer while passivating the top surface of the nanostructure. By comparing sensor responses for two different resonances, we have shown that the mIgG molecules were able to penetrate through the pores into the swollen hydrogel while not biding directly to the gold surface of the nanostructure.

In the second experiment, we have tested the samples with hybrid nanostructures as a SERS substrate. The SERS spectrum of the pristine sample is rather complex due to the direct contact of a plasmonic structure and a hydrogel material (namely its benzophenone units) The observed peaks are close to previously reported values for this hydrogel. After the characterization, the samples of hybrid nanostructures were incubated overnight with a Raman label of 4-mercaptobenzoic acid (4-MBA) to form a monolayer. The main peaks connected with the label (1071 cm^{-1} and 1581 cm^{-1}) appeared in the measured spectra. Furthermore, we have compared the spectra before and after the hydrogel collapsing and the increase of the signal as high as 45 % was observed.

The work presented in **Appendix V** demonstrates how to overcome the common mass-transfer limitations of NHA-based sensors. Moreover, the approach shows the way how to enhance the performance of many different structures by incorporating an active hydrogel, which might increase the amount of captured molecules. An active

hydrogel also allows tuning the resonance wavelength of the plasmonic structure which might be useful in many wavelength-sensitive applications.

In our second approach, we suggested using the NHA with an extended electric field profile (**Appendix VI**) to probe Raman scattering molecules. The proposed nanostructure consists of a nanohole array placed on the refractive-index-matched dielectric spacer. This spacer allows excitation of plasmonic modes with a long-range characteristic not available from common SERS substrates.

To design these structures, we used Lumerical FDTD. The reflectivities and near-fields for resonant features were simulated for three different nanostructures: (a) NHA on a substrate (conventional), (b) NHA on a dielectric spacer (pseudo-long-range – PLR), and (c) NHA on a dielectric spacer combined with enhancing gold mirror (long-range – LR). The nanostructures are shown in Figure 19 A-D.

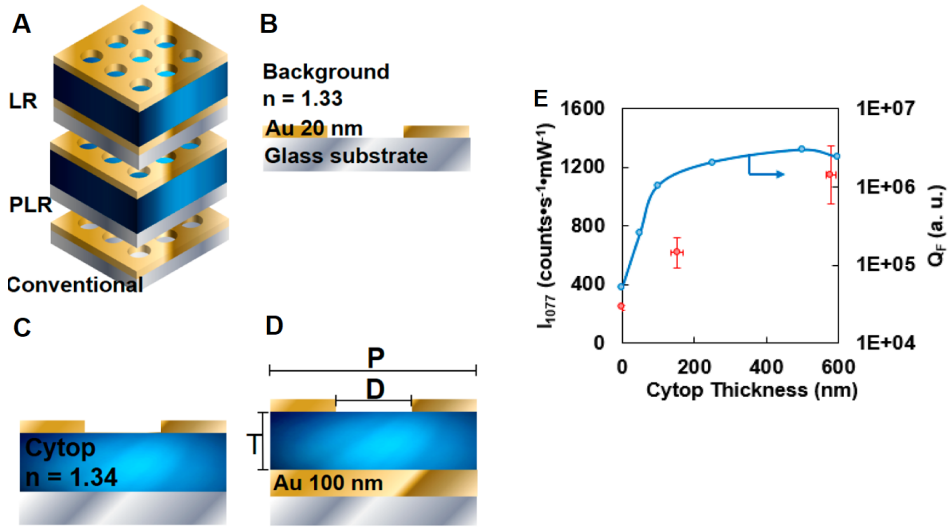

Figure 19: Three-dimensional and side-view schematic for the three types of SERS substrates investigated (A-D): long-range (LR), pseudo-long-range (PLR), and conventional.

E – The calculated Q_F and corresponding measured experimental SERS signal of a 4-MBA band at 1077 cm^{-1}.

To estimate the SERS performance for these nanostructures, we computed the quality factor Q_F in hot-spot using

$$Q_F = \frac{1}{\beta}\int_{\omega_{RS}^{\min}}^{\omega_{RS}^{\max}} \left|\frac{E(\omega_{Ex})}{E_0(\omega_{Ex})}\right|^2 \left|\frac{E(\omega_{RS})}{E_0(\omega_{RS})}\right|^2 \mathrm{d}\omega_{RS}\,, \tag{12}$$

where $\beta = \omega_{RS}^{\max} - \omega_{RS}^{\min}$ is the range of Raman shifted frequencies (300-1800 cm^{-1}) and E and E_0 are electric fields with and without the presence of nanostructure, respectively.

We have fabricated nanohole arrays using a process based on a solvent-assisted molding. For this technique, a master was fabricated using electron-beam lithography and reactive ion etching. This master comprises dielectric pillars on a silicon wafer. Then a PDMS stamp was cast from the silicon master. Solvent-assisted molding was used to replicate the pattern from the PDMS stamp to acetone-softened PMMA. Finally, gold was deposited and the sacrificial PMMA pillars were removed.

To experimentally investigate the dependence of the performance of the PLR substrates on the CYTOP thickness, we firstly incubated the samples of different CYTOP thicknesses with the 4-mercaptobenzoic acid (4-MBA) and then measured the intensity of the 1077 cm^{-1} band using a Raman microspectrometer. The results are shown in Figure 19E. The intensity of the band increases with the CYTOP thickness as the contrast of the plasmonic resonance increases. This trend corresponds with the results of the numerical simulation of Q_F. We also investigated the relationship between the SERS signal acquired using the long-range samples and the asymmetry of a refractive index around the nanostructure. The fabricated samples were incubated with 4-MBA to form a monolayer. To create RI symmetry, some of the samples were further coated with a CYTOP layer. The SERS spectra of 4-MBA were recorded and compared. The results confirm that the fabricated samples provide higher SERS signals when they are surrounded by a symmetrical environment (Figure 20).

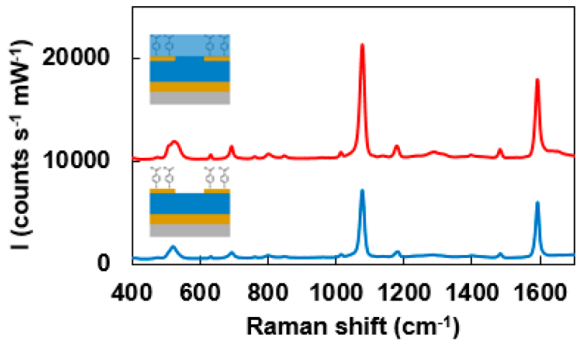

Figure 20: SERS spectra of 4-MBA collected in air (blue) and embedded in CYTOP layer (red) using LR-SERS substrates.

To confirm the extended profile of the field, a thin layer of CYTOP was used to create a dielectric spacer above the nanostructure, onto which a Raman label, rhodamine 6G (R6G), was deposited. To create RI symmetric environment, the sample was put in the contact with deionized water. The SERS spectrum was then measured by microspectrometry. The addition of the 10 nm thick CYTOP layer resulted in a signal intensity conservation of 4%, whereas none of the peaks were observed in the conventional substrate. It is important to highlight, that the decrease of the SERS signal could be due to multiple factors: the decay of the electric field (the electromagnetic enhancement mechanism), the absence of possible charge transfer between R6G and gold (the chemical enhancement mechanism), and the difference between R6G adsorption on CYTOP and gold surfaces. To partially clarify the role of electromagnetic field, we have simulated the quality factor dependence on the distance from the surface of the nanostructure. At the distance of 10 nm, the Q_F drops to 3 % of its initial surface value, which corresponds with our experimental data.

The study in **Appendix VI** shows how the specific design of SERS substrate can provide a high intensity of electromagnetic field further from the surface in order to obtain a measurable SERS signal. Although the SERS signal above the structure was substantially lower than the initial SERS signal, the presented approach shows a route towards more complex SERS assays than presented simple SAMs.

4 CONCLUSIONS

This dissertation presents the results of research into plasmonic nanostructures for biosensing. In particular, it focuses on advances in the understanding, design, and fabrication of plasmonic nanostructures as well as their use in affinity refractometric biosensors and biosensors based on surface-enhanced Raman spectroscopy.

A broad range of nanostructures was studied and various plasmonic modes were investigated, including localized plasmonic modes supported by arrays of gold nanorods and nanodisks, propagating modes of nanostripes and localized and propagating modes of nanohole arrays combined with gold nanoparticles or a gold layer. Based on the analysis of these nanostructures, new biosensors based on affinity refractometric biosensors and biosensors based on surface-enhanced Raman spectroscopy were proposed.

In addition, the performance of plasmonic affinity biosensors was investigated. In order to account for the effects of analyte transport to plasmonic nanostructures, a phenomenological model developed for the flow-over biosensors was used and validated using plasmonic nanostructures of different characteristics (ranging from random arrays of nanoparticles to periodic arrays of microstripes). Furthermore, the model was combined with the theoretical model of optical read-out platform yielding a universal model that allows predicting performance of plasmonic affinity biosensors and interrelates the minimum detectable concentration of analyte with design parameters of the sensing structure and flow cell design. By using the developed performance model, two novel sensors based on nanostructures have been designed and shown to exceed the performance of conventional SPR biosensors. First, a biosensor based on the random array of nanorods was developed and used for the detection of polyA oligonucleotide. Second, a biosensor based on the period array of nanostripes was developed and used for the detection of oncohematologically relevant miRNA-125b.

Furthermore, plasmonic nanostructures have been investigated to address the limitations of SERS-based biosensors related to the limited distance between the analyte and the sensing surface. In the first approach, a thermoresponsive nanostructure based on a nanohole array in a gold layer and nanodisks separated by

a hydrogel was used to actively trigger fluid flow to the regions of the high electromagnetic field. The functionality of the nanostructure was demonstrated by observing both affinity biosensing of mouse immunoglobulin and SERS experiments of Raman label under different temperatures. In the second approach, a sandwich nanostructure based on a nanohole array in a gold layer, low-refractive-index dielectric, and a continuous gold layer was designed to extend the electromagnetic field associated with surface plasmons farther from the sensing structure. The sensing performance of the nanostructure was investigated in a model SERS experiment in which Raman label (4-mercaptobenzoic acid) was detected.

The doctoral research has resulted in 6 publications in peer-reviewed scientific journals.

REFERENCES

1. Narayanaswamy, R. and Wolfbeis, O.S., *Optical Sensors: Industrial Environmental and Diagnostic Applications*. 2003: Springer Berlin Heidelberg.
2. Ligler, F.S. and Taitt, C.R., *Optical Biosensors: Today and Tomorrow*. 2011: Elsevier Science.
3. Fan, X., et al., *Sensitive optical biosensors for unlabeled targets: A review.* Analytica Chimica Acta, 2008. **620**(1–2): p. 8-26.
4. Homola, J., *Surface plasmon resonance sensors for detection of chemical and biological species.* Chemical Reviews, 2008. **108**(2): p. 462-493.
5. Špačková, B., et al., *Optical Biosensors Based on Plasmonic Nanostructures: A Review.* Proceedings of the IEEE, 2016. **104**(12): p. 2380-2408.
6. Estevez, M.-C., et al., *Trends and challenges of refractometric nanoplasmonic biosensors: A review.* Analytica chimica acta, 2014. **806**: p. 55-73.
7. Anker, J.N., et al., *Biosensing with plasmonic nanosensors.* Nat Mater, 2008. **7**(6): p. 442-453.
8. Ru, E.L. and Etchegoin, P., *Principles of Surface-Enhanced Raman Spectroscopy: and Related Plasmonic Effects*. 2008: Elsevier Science.
9. Stockman, M.I., *Nanofocusing of optical energy in tapered plasmonic waveguides.* Physical review letters, 2004. **93**(13): p. 137404.
10. Stockman, M.I., *Nanoplasmonics: The physics behind the applications.* Phys. Today, 2011. **64**(2): p. 39-44.
11. Li, J., et al., *Nanoplasmonic Sensors with Various Photonic Coupling Effects for Detecting Different Targets.* The Journal of Physical Chemistry C, 2015. **119**(52): p. 29116-29122.
12. Zayats, A.V. and Smolyaninov, I.I., *Near-field photonics: surface plasmon polaritons and localized surface plasmons.* Journal of Optics A: Pure and Applied Optics, 2003. **5**(4): p. S16.
13. Sarid, D., *Long-Range Surface-Plasma Waves on Very Thin Metal Films.* Physical Review Letters, 1981. **47**(26): p. 1927-1930.
14. Berini, P., *Plasmon-polariton waves guided by thin lossy metal films of finite width: Bound modes of symmetric structures.* Physical Review B, 2000. **61**(15): p. 10484.
15. Berini, P., *Plasmon-polariton waves guided by thin lossy metal films of finite width: Bound modes of asymmetric structures.* Physical Review B, 2001. **63**(12): p. 125417.

16. Murray, W.A. and Barnes, W.L., *Plasmonic materials.* Advanced materials, 2007. **19**(22): p. 3771-3782.
17. Mackey, M.A., et al., *The Most Effective Gold Nanorod Size for Plasmonic Photothermal Therapy: Theory and In Vitro Experiments.* The Journal of Physical Chemistry B, 2014. **118**(5): p. 1319-1326.
18. Lee, K.-S. and El-Sayed, M.A., *Dependence of the Enhanced Optical Scattering Efficiency Relative to That of Absorption for Gold Metal Nanorods on Aspect Ratio, Size, End-Cap Shape, and Medium Refractive Index.* The Journal of Physical Chemistry B, 2005. **109**(43): p. 20331-20338.
19. Becker, J., et al., *The Optimal Aspect Ratio of Gold Nanorods for Plasmonic Bio-sensing.* Plasmonics, 2010. **5**(2): p. 161-167.
20. Sekhon, J.S. and Verma, S.S., *Optimal Dimensions of Gold Nanorod for Plasmonic Nanosensors.* Plasmonics, 2011. **6**(1): p. 163-169.
21. Zijlstra, P., Paulo, P.M.R., and Orrit, M., *Optical detection of single non-absorbing molecules using the surface plasmon resonance of a gold nanorod.* Nature Nanotechnology, 2012. **7**(6): p. 379-382.
22. Ebbesen, T.W., et al., *Extraordinary optical transmission through sub-wavelength hole arrays.* nature, 1998. **391**(6668): p. 667-669.
23. Liu, H. and Lalanne, P., *Microscopic theory of the extraordinary optical transmission.* Nature, 2008. **452**(7188): p. 728-731.
24. Garcia-Vidal, F.J., et al., *Light passing through subwavelength apertures.* Reviews of Modern Physics, 2010. **82**(1): p. 729.
25. Xu, J., et al., *Light transmission and surface-enhanced Raman scattering of quasi-3D plasmonic nanostructure arrays with deep and shallow Fabry-Perot nanocavities.* The Journal of Physical Chemistry C, 2011. **115**(22): p. 10996-11002.
26. Xu, J., et al., *Understanding the effects of dielectric medium, substrate, and depth on electric fields and SERS of quasi-3D plasmonic nanostructures.* Optics express, 2011. **19**(21): p. 20493-20505.
27. Piliarik, M., et al., *Local refractive index sensitivity of plasmonic nanoparticles.* Optics Express, 2011. **19**(10): p. 9213-9220.
28. Leitgeb, V., et al., *Three dimensional sensitivity characterization of plasmonic nanorods for refractometric biosensors.* Nanoscale, 2016. **8**(5): p. 2974-2981.
29. Häfele, V., et al., *Local refractive index sensitivity of gold nanodisks.* Optics express, 2015. **23**(8): p. 10293-10300.

30. Nenninger, G.G., Piliarik, M., and Homola, J., *Data analysis for optical sensors based on spectroscopy of surface plasmons.* Measurement Science and Technology, 2002. **13**(12): p. 2038.
31. Nie, S. and Emory, S.R., *Probing single molecules and single nanoparticles by surface-enhanced Raman scattering.* science, 1997. **275**(5303): p. 1102-1106.
32. Kerker, M., *Electromagnetic model for surface-enhanced Raman scattering (SERS) on metal colloids.* Accounts of Chemical Research, 1984. **17**(8): p. 271-277.
33. Le Ru, E.C. and Etchegoin, P.G., *Quantifying SERS enhancements.* MRS bulletin, 2013. **38**(08): p. 631-640.
34. Radziuk, D. and Moehwald, H., *Prospects for plasmonic hot spots in single molecule SERS towards the chemical imaging of live cells.* Physical Chemistry Chemical Physics, 2015. **17**(33): p. 21072-21093.
35. Etchegoin, P.G. and Le Ru, E., *A perspective on single molecule SERS: current status and future challenges.* Physical Chemistry Chemical Physics, 2008. **10**(40): p. 6079-6089.

APPENDICES

List of appendices

Appendix I

Bocková, M., Slabý, J., Špringer, T., and Homola, J.: *Advances in Surface Plasmon Resonance Imaging and Microscopy and Their Biological Applications*. Annual Review of Analytical Chemistry, 2019. **12:** 151–176

Contribution: Review of the literature for the sections “Principles of SPR imaging and microscopy” and “Advances in Optical Platforms” and the writing of these sections of the manuscript.

Appendix II

Lynn, N. S., Špringer, T., Slabý, J., Špačková, B., Gráfová, M., Ermini, M. L., and Homola, J., *Analyte transport to micro-and nano-plasmonic structures*. Lab on a Chip, 2019. **19**(24), 4117-4127.

Contribution: Designing and fabricating of the nanostructures, interpretation of the spectroscopic data, editing of the manuscript.

Appendix III

Špačková, B., Lynn Jr., N. S., Slabý, J., Šípová, H., and Homola, J. *A route to superior performance of a nanoplasmonic biosensor: consideration of both photonic and mass transport aspects.* ACS Photonics, 2018. **5**, 1019-1025.

Contribution: Developing and fabricating of the nanostructures, participation in the experiments.

Appendix IV

Slabý, J., Bocková, M., and Homola, J.: *Plasmonic Biosensor Based On A Gold Nanostripe Array For Detection Of MicroRNA Related To Myelodysplastic Syndromes,* Sensors and Actuators B: Chemical, 2021. **347**,130629.

Contribution: Theoretical analysis of the biosensor performance, Designing and fabricating of the nanostructures, designing and modifications of the optical setup and microfluidics, writing of the manuscript.

Appendix V

Kotlarek, D., Fossati, S., Venugopalan, P., Quilis, N. G., Slabý, J., Homola, J., Lequeux, M., Amiard, F., de la Chapelle, M.L., Jonas, U., and Dostálek, J. *Actuated plasmonic nanohole arrays for sensing and optical spectroscopy applications*. Nanoscale, 2020. **12**, 9756-9768

Contribution: Designing and building of the optical setup with the temperature-stabilized chamber, performing the affinity biosensing experiments, editing the manuscript.

Appendix VI

Galvan, D., Špačková, B., Slabý, J., Sun, F., Ho, Y-H. Homola, J. and Yu, Q. *Surface-Enhanced Raman Scattering (SERS) on Gold Nanohole Arrays in Symmetrical Dielectric Environments Exhibiting Electric Field Extension*, Journal of Physical Chemistry C, 2016. **120**, 25519–25529.

Contribution: Fabrication of the nanostructures, performing part of the experiments (together with D. Galvan), editing the manuscript.

Appendix I

Advances in Surface Plasmon Resonance Imaging and Microscopy and Their Biological Applications.

Bocková, M., Slabý, J., Špringer, T., and Homola, J.

Annual Review of Analytical Chemistry, 2019. **12**: 151–176

ANNUAL REVIEWS

Annual Review of Analytical Chemistry

Advances in Surface Plasmon Resonance Imaging and Microscopy and Their Biological Applications

Markéta Bocková, Jiří Slabý, Tomáš Špringer, and Jiří Homola

Institute of Photonics and Electronics, Czech Academy of Sciences, 18251 Prague, Czech Republic; email: homola@ufe.cz

Annu. Rev. Anal. Chem. 2019. 12:151–76

First published as a Review in Advance on March 1, 2019

The *Annual Review of Analytical Chemistry* is online at anchem.annualreviews.org

https://doi.org/10.1146/annurev-anchem-061318-115106

Keywords

surface plasmon, surface plasmon resonance, imaging, microscopy, optical biosensor, detection of biomolecules, biomolecular interaction analysis

Abstract

Surface plasmon resonance microscopy and imaging are optical methods that enable observation and quantification of interactions of nano- and microscale objects near a metal surface in a temporally and spatially resolved manner. This review describes the principles of surface plasmon resonance microscopy and imaging and discusses recent advances in these methods, in particular, in optical platforms and functional coatings. In addition, the biological applications of these methods are reviewed. These include the detection of a broad variety of analytes (nucleic acids, proteins, bacteria), the investigation of biological systems (bacteria and cells), and biomolecular interactions (drug–receptor, protein–protein, protein–DNA, protein–cell).

INTRODUCTION

Understanding how life works on the molecular and cellular levels is an important challenge for modern science. Addressing this challenge requires the development of sensitive and robust tools for the investigation of biomolecules, cells, and their interactions. Label-free affinity biosensors present an emerging technology that holds vast potential for these applications (1). Affinity biosensors based on optically excited surface plasmons represent the most advanced label-free optical affinity biosensor method. The first reports on the use of surface plasmons for probing processes on the surfaces of metal layers (2) and sensing (3) date back to the 1980s. In the early 1990s, the first surface plasmon–based biosensors [referred to as surface plasmon resonance (SPR) biosensors] were demonstrated and applied to the investigation of biomolecular interactions (4). In the following years, SPR biosensors have become an important tool with a significant impact on biophysics, molecular biology, and pharmaceutical research. Conventional SPR biosensors enable real-time observation and quantification of interactions between biological objects in a liquid sample and their counterparts immobilized on the surface of a metal supporting surface plasmons. In contrast to such biosensors that create the sensor output by integrating signals from the interactions occurring within macroscopic areas of the surface, SPR imaging and microscopy are methods that aim to allow localization of these interactions through the imaging of the metal surface by means of surface plasmons. The origins of SPR microscopy and imaging date back to the 1980s, when Yeatman & Ash (5) and Rothenhäusler & Knoll (6) reported the first spatially resolved plasmonic measurements. These pioneering studies have inspired a great deal of research, and numerous SPR imaging and microscopy platforms have been developed and applied to a multitude of biological problems. SPR imaging and microscopy have been subject to numerous publications, including several comprehensive reviews (7–13).

In this review, we explain the fundamentals of surface plasmon imaging and microscopy and discuss selected advances in the development and applications of these methods over the past five years. These include the detection of biomolecules and the investigation of biological systems and biomolecular interactions.

PRINCIPLES OF SURFACE PLASMON RESONANCE IMAGING AND MICROSCOPY

Surface plasmon is a mode of electromagnetic field that is associated with collective oscillations of free conductive electrons in the metal near metal-dielectric interface. The electromagnetic field of the surface plasmon is localized to the interface and decays into both the metal and the dielectric. This characteristic makes surface plasmons an effective tool for probing processes on metal surfaces (14, 15). A wide variety of surface plasmon modes exist on different metal-dielectric (nano)structures (16).

Propagating surface plasmon (PSP) supported by a continuous metallic film is the surface plasmon mode most commonly used in SPR imaging and microscopy. The electromagnetism of PSP may be characterized by its penetration depth to the dielectric ($\sim 10^2$ nm) and its propagation length ($\sim 10^1$ μm). Metal-dielectric multilayers may alter these characteristics, as demonstrated by the long-range and short-range surface plasmons propagating along a thin metal film embedded between two dielectrics (17). Localized surface plasmon (LSP) is supported by an individual metal nanoparticle. The electric field of a fundamental LSP mode oscillates as an electric dipole and exhibits a penetration depth on the order of tens to hundreds of nanometers. Other surface plasmons are supported by periodic arrays of metal nanoparticles. These modes originate from the coupling of light diffracted parallel to the surface (surface lattice resonances) with single-particle LSPs. These modes exhibit rather delocalized electromagnetic field (in comparison with

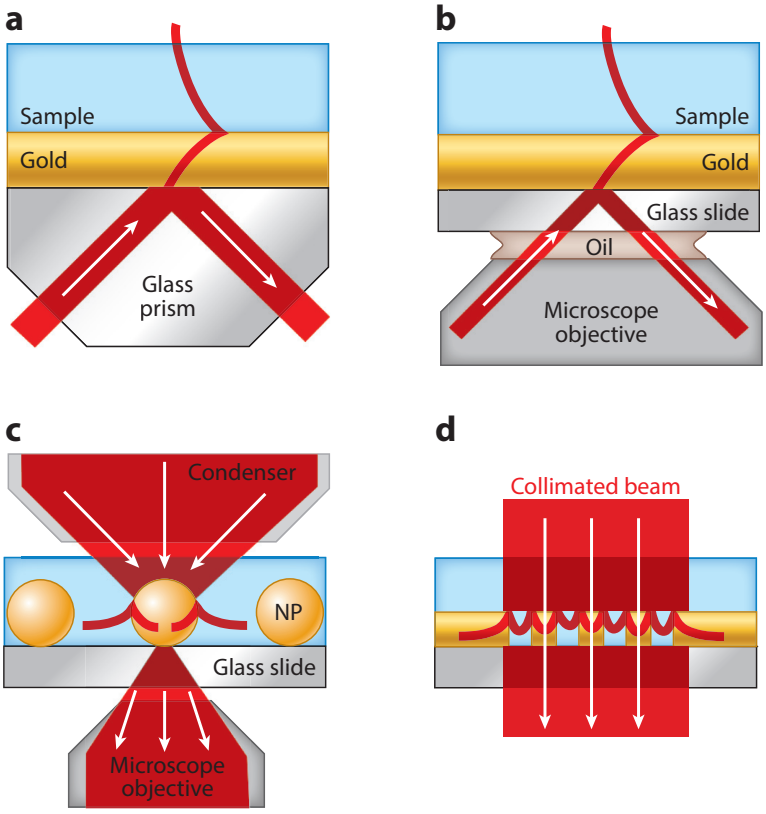

Figure 1

Optical excitation of surface plasmons: (*a*) a prism-based attenuated total reflection configuration for SPR imaging, (*b*) a high numerical aperture objective configuration for SPR microscopy, (*c*) transmission arrangement for localized SPR microscopy, and (*d*) a collinear transmission arrangement for SPR imaging. Abbreviations: NP, nanoparticle; SPR, surface plasmon resonance.

LSPs) and have a penetration depth on the order of hundreds of nanometers (18). Furthermore, surface plasmons originating from the interplay between various surface plasmons such as diffractively coupled PSPs and localized cavity modes may exist on a periodic array of nanoapertures in a metal film (19–22).

The main approaches to the optical excitation of surface plasmons are shown in **Figure 1**. The most widely used geometry is based on the attenuated total reflection (ATR) method and prism coupling (**Figure 1*a***). The ATR configuration is typically used to excite surface plasmons such as PSPs on unstructured metal films. Incident light passes through a prism and is made incident on the base interfaced with a plasmonic structure under an angle of incidence larger than the critical angle, generating an evanescent wave. When the propagation constant of the wave is equal to that of surface plasmons on the plasmonic structure, the light excites the surface plasmons, which results in a decreased intensity of the reflected light. PSPs on an unstructured metal film can also be excited by light focused to the side of the back focal plane of a high numerical aperture oil immersion objective to illuminate a metal film with the use of collimated beam at the desired angle of incidence (**Figure 1*b***). The reflected light from the metal film is collected by the same objective. Alternatively, surface plasmons on nanostructures (e.g., LSPs) can be excited and observed in a reflection or transmission microscope (**Figure 1*c***). The illumination is adjusted to be either collimated or convergent, depending on the characteristics of the surface plasmon; furthermore, dark-field illumination through a dark-field condenser can be employed, and the scattered light can

be collected and analyzed. Other optical platforms are based on collinear geometry (**Figure 1*d***). In this geometry, collimated light is made incident onto a plasmonic structure (periodic arrays of nanoparticles, nanoholes, nanoslits, randomly distributed nanoparticles) and excites surface plasmons while generating changes in the intensity of the reflected or transmitted light. Although the approach depicted in **Figure 1*a*** is often referred to as SPR imaging, and the approach depicted in **Figure 1*b*** is often referred to as SPR microscopy, this terminology is not used consistently in the literature. In this review, we use the term SPR imaging for all of the platforms in which the sensing surface (structured or unstructured) is illuminated by a rather large (and often collimated) beam of light and surface plasmons are excited by means of an ATR prism or diffraction couplers. Furthermore, we use the term SPR microscopy for all of the platforms in which a beam of light is focused onto a small area of the sensing surface (structured or unstructured) and surface plasmons are excited via a microscope objective.

ADVANCES IN OPTICAL PLATFORMS

Surface Plasmon Resonance Imaging and Prism-Based Platforms

The ATR method has been used in SPR imaging for over three decades, and numerous platforms based on this approach have been developed and even commercialized (23). Therefore, in recent years, attention has mainly focused on aspects affecting the performance of prism-based SPR imaging platforms.

Corso et al. (24) combined angle-resolved SPR and SPR imaging in one instrument, which allowed them to set the measurement conditions for SPR imaging that provide the best sensitivity. In addition, SPR imaging platforms were proposed that allow for the acquisition of the entire spectrum of light coupled to surface plasmons from each spot (spectral imaging). Shao et al. (25) developed a prism-based SPR two-dimensional (2D) spectral imaging sensor with phase interrogation. They used a liquid crystal tunable filter to vary the input wavelength and a liquid crystal modulator to introduce phase retardation between the s- and p-polarizations to create a platform enabling the measurement of phase retardation at multiple wavelengths. The sensor was demonstrated to attain a refractive index (RI) resolution as low as 2.7×10^{-7}. Subsequently, the same group developed an SPR imaging platform employing an acousto-optic tunable filter with an RI resolution of 1×10^{-6} (26). The factors limiting spatial resolution in prism-based SPR imaging were studied by Laplatine et al. (27), who showed that these platforms suffer from geometrical aberrations that can be even more limiting than the propagation length of surface plasmons. By optimizing the prism coupler and introducing the line-scan imaging mode, they demonstrated that lateral resolution can be improved down to 2.8 μm.

Surface Plasmon Resonance Imaging and Collinear Optics Platforms

Botazzi et al. (28) developed a compact optical platform using pillars buried in a gold film with an RI resolution of 4×10^{-6}. The same plasmonic structures were used in an even more compact platform ($10 \times 15 \times 6$ cm^3) with an RI resolution of 6×10^{-5} (22). Gomez-Cruz et al. (29) developed a fully integrated platform based on a nanohole array and achieved an RI resolution of 10^{-6}. Guner et al. (30) reported an SPR imaging platform based on a smartphone and a disposable grating coupler that achieved an RI resolution of 4×10^{-5}. Lee et al. (31) developed an SPR imaging platform based on a smartphone LED and camera and capped nanoslit arrays. Each chip contained several arrays with different periods. The transmitted light was recorded, and the period producing the strongest coupling was determined and used as a sensor output.

Cappi et al. (32) developed an SPR imaging platform employing gold nanoislands. They used a white LED and a color CMOS detector to enable spectral measurement. By analyzing images from pixels with red, green, and blue filters of the detector, the spectral position of the LSPR peak was determined. A spectral SPR imaging platform based on a hybrid surface plasmon mode of a periodic array of nanoholes was developed by Guo & Guo (20). They detected the first diffraction order with a camera enabling the acquisition of the spectrum of light coupled to surface plasmons without the use of an additional dispersive element. Van Duyne's group (33) developed a spectral SPR imaging sensor utilizing a liquid crystal tunable filter. Light transmitted through an array of metal nanodiscs was passed through a liquid crystal-tunable filter and received by a detector to yield images at multiple wavelengths. An alternative spectral SPR imaging approach was developed by Lee et al. (34), who used a broadband light source and a tunable monochromator attached to a microscope. They measured the intensity of light transmitted through a nanoslit array and achieved an RI resolution of 1×10^{-5}.

Surface Plasmon Resonance Microscopy

SPR microscopy platforms tend to exhibit better spatial resolution than their SPR imaging counterparts and are therefore the platform of choice when high spatial resolution is required. Spatial resolution for SPR microscopy platforms based on unstructured metal films is limited mainly by the propagating nature of surface plasmons, as their propagation length is usually much larger than diffraction-limited resolutions provided by high numerical aperture objectives (0.2 μm for an objective with a numerical aperture of 1.4 and a wavelength of 550 nm). Therefore, numerous studies were concerned with reducing the propagation length of surface plasmons. Banville et al. (35) demonstrated that the propagation length of surface plasmons can be reduced by the use of plasmonic nanostructures. They investigated the trade-off between the spatial resolution and image contrast and found that nanostructuring enables submicrometer spatial resolution. Banville et al. (36) also demonstrated a method to improve lateral resolution in SPR microscopy by combining images acquired with surface plasmons propagating in opposite directions. Kim's group (37) developed a similar approach by using a linear motor stage for spatially switching the direction of surface plasmon momentum. The resolution of the reported platform was almost 15 times better than that of conventional SPR microscopy. Another approach for improving the spatial resolution was developed by Somekh's group (38). They constructed a wide-field SPR microscope with angular scanning that employed an amplitude spatial light modulator placed in a conjugated back focal plane to allow for dynamic control of the illumination angle and collection of SPR images at different angles of incidence. The spatial resolution can also be improved by using a scanning approach proposed by Watanabe et al. (39), who used different SPR images generated while changing the position of the SPR chip. Argoul's group (40) has improved the scanning SPR microscope by reducing the readout area corresponding to a single detector pixel with radially polarized illumination and a fiber-based interferometer. They showed that the resolution of such a microscope reaches the theoretical diffraction limit.

Whereas most SPR microscopes gather only information about changes in the amplitude or phase of light coupled to surface plasmons, holographic approaches measure both of these quantities (41). Zhang et al. (42, 43) developed a compact SPR holographic microscope employing a Wollaston prism in which the p-polarized light (both amplitude and phase) that carried the information of interest was combined with reference s-polarized light; the resulting interferogram was used for SPR image reconstruction. Gao et al. (44) developed a platform based on an on-chip interferometer consisting of a slit and groove in a metallic film for monitoring the phase difference of surface plasmons propagating in between them. In addition, a design based on two

coupled interferometers was explored, and the resolution of the single-interferometer and double-interferometer sensors was 3×10^{-4} and 5×10^{-5}, respectively.

Another SPR microscopy platform was described by Chen et al. (45), who used dark-field illumination and an array of gold nanorods. The LSPs were excited by a light-passing condenser, and the scattered light was collected by a 10× magnification objective. The authors compared their proposed approach with a similar spectrometry-based LSPR sensor and estimated that it provides a tenfold improvement in sensing performance.

Altug's group (19, 46) developed a 1D spectral SPR microscopy platform using three nanohole arrays in a row. Light from a broadband source was transmitted through the nanohole substrate mounted in an inverted microscope and analyzed by an imaging spectrometer. The optical spectrum for each array was acquired, and the spectral position of the LSPR peak was determined.

Liu et al. (47) developed a platform for the interrogation of individual nanoparticles in a dark-field SPR microscope. The light transmitted through a sparse array of nanospheres was made incident on a grating and diffracted onto a camera. The recorded image contained mutually shifted zero and first diffraction order images, and the first diffraction order was used to obtain the spectral position of the LSPR.

ADVANCES IN FUNCTIONALIZATION METHODS

To fully exploit the potential of spatially resolved SPR imaging and microscopy methods, functionalization approaches are desired that can deliver biological functionality to plasmonic structures in a spatially resolved manner. The scale and spatial resolution vary broadly depending on the application, from immobilizing a multitude of different biomolecules into a large array (>100) of macroscopic (0.01 mm^2) spots, to delivering a single-type biomolecule to individual nanoscopic plasmonic features. A detailed description of common immobilization methods can be found in books (15, 48) and reviews (49, 50). In this section, we focus on advances in the functionalization of arrays on macroscopic areas. For advances in spatially resolved functionalization of nanostructures, we refer the reader to our recent review (16). The primary focus is on methods for the preparation of protein and nucleic acid arrays; immobilization of bacteria is typically accomplished via specific receptors (antibodies or carbohydrates) covalently attached to surface carboxy-terminated self-assembled monolayers (51) or via receptor-pyrrole conjugates that are prepared by electrochemical polymerization (52).

Most functionalization methods used to produce bimolecular arrays are typically based on microspotting techniques (contact or noncontact printing, or microfluidics-, microstamping- or lithography-based approaches) (49). A method for the preparation of arrays of peptide nucleic acid (PNA) probes was proposed by Simon et al. (53). The method is based on direct microspotting of thiol-terminated PNA probes prehybridized with a short complementary DNA strand [instead of using single-stranded PNA (ssPNA) probes] that are subsequently removed by NaOH. This ensures optimal surface density and orientation of the PNA probes. The resulting PNA arrays were demonstrated to be superior (or equal) in terms of binding capacity to those obtained by standard ssPNA microspotting. Nand et al. (54) proposed an in situ protein synthesis method to generate protein arrays directly from prearrayed plasmid DNA probes, exploiting the high-affinity interaction between the protein TUS tag and the TER DNA sequence. A mixture of plasmid DNA and amine-terminated TER DNA was microspotted on a sensor surface functionalized with polyethyleneimine; in vitro transcription and translation (IVTT) mix was added, and fusion proteins were synthetized. The feasibility of the method was demonstrated in experiments with the binding of protein-specific antibodies. A two-step templated, ribosomal biosynthesis-based printing method for the fabrication of protein microarrays was reported by Manuel et al. (55). In

the first step, a microarray of proteins was created in microwells by cell-free protein synthesis; each microwell contained both an IVTT mix and a specific DNA template sequence that were used together to create specific hexahistidine-tagged proteins. In the second step, the protein microwell array was used to contact print the protein microarray onto a nitrilotriacetic acid–functionalized SPR imaging chip. Another method for the preparation of proteins arrays was proposed by Kruis et al. (56), who utilized leucine zipper heterodimerization. The sensor surface was functionalized with thiol-terminated zwitterionic peptides, a small percentage of which carried leucine zipper moiety. Using a continuous flow microspotter, proteins with the complementary leucine zipper fusion tag were immobilized to create a protein array.

Wood et al. (57) used a polydopamine (PDA) multilayer for the fabrication of DNA microarrays. Dopamine monomers self-polymerize to create a PDA layer on gold that enables the covalent attachment of biomolecules via amine coupling. In this work, PDA multilayers were formed on gold spots through repeated injections of dopamine, after which amine-terminated DNA probes were attached.

BIOANALYTICAL APPLICATIONS

In this section, we review bioanalytical applications of SPR imaging and microscopy. The main characteristics of these applications are presented in **Table 1**.

Detection of Protein Biomarkers

C-reactive protein (CRP), a clinical biomarker of acute inflammatory diseases, was targeted by Altug's group (58). The authors used a brightfield SPR imaging sensor based on an array of gold nanoholes (see **Figure 2**) that allowed for the visualization of individual gold nanoparticles (AuNPs) captured on the surface of the array. The surface of the chip was functionalized with anti-CRP antibodies, and a sandwich assay with antibody-coated 100-nm AuNPs was used to detect CRP. The authors detected CRP down to 27 and 100 pg/mL in buffer and cell culture media with 10% horse serum, respectively.

An ovarian cancer marker, protein r-PAX8, was detected by Escobedo et al. (59) using a nanohole array–based platform. The sensor surface was functionalized with anti-r-PAX8 antibody via amino coupling, and protein r-PAX8 was detected in buffer at concentrations down to 0.25 μg/mL.

Hu et al. (60) used SPR imaging to detect the tumor marker α-fetoprotein. The sensing surface was functionalized with the poly[oligo(ethylene glycol) methacrylate-co-glycidyl methacrylate] (POEGMA-co-GMA) brush and an anti-α-fetoprotein antibody. A two-step sandwich assay with functionalized AuNPs was employed, and α-fetoprotein was detected in 10% human serum with a limit of detection (LOD) of 1 ng/mL.

Moreover, Hu et al. (61) detected a colorectal cancer biomarker, carcinoembryonic antigen (CEA), using SPR imaging, POEGMA-co-GMA functional coating, and a two-step sandwich assay where the sensor response was enhanced by an antibody-modified PDA reduced graphene oxide (PDA-rGO) followed by a PDA-induced spontaneous reductive deposition of gold on PDA-rGO. CEA was detected in 10% human serum with an LOD of 500 pg/mL. CEA was also targeted by Liu et al. (62). The surface of an SPR imaging sensor was microspotted with thiol-terminated aptamers against CEA, which was detected using a multistep sandwich assay in which the capture of CEA by aptamer was followed with repeated injections of concanavalin A and dextran to enhance the sensor response. CEA concentrations as low as 50 pg/mL were detected in both buffer and 10% human serum sample.

Table 1 Selected examples of applications of plasmonic biosensors for the detection of chemical and biological species

Target	Detection format (detection time)	Performance[a]	Optical platform	Reference
Protein biomarkers				
CRP	SA: Ab–AuNP (2 h)	LOC: 27 pg/mL LOC: 100 pg/mL, 10% horse serum	Collinear using gold nanohole array	58
r-PAX8	Direct detection (15 min)	LOC: 0.25 μg/mL	Collinear using gold nanohole array	59
AFP	2-Step SA: Ab–AuNP + polymerization (2.5 h)	LOD: 1 ng/mL, 10% human serum	Prism-based using gold film	60
CEA	2-Step SA: Ab–PDA-rGO + gold deposition (2.5 h)	LOD: 0.5 ng/mL, 10% human serum	Prism-based using gold film	61
CEA	Multistep SA: concavalin A + dextran (>1 h)	LOC: 50 pg/mL, 10% human serum	Prism-based using gold film	62
HER2	Direct detection (1 h)	LOC: 3 ng/mL	Collinear using nanoholes	63
PTX3	Direct detection (1 min)	LOC: 100 ng/mL	Collinear using buried nanoholes	28
CatG	Direct detection (10 min)	LOD: 0.23 ng/mL	Prism-based using gold film	64
CatG	Direct detection (10 min)	LOC: 0.9 pmol/mL, 2% endometrial tissue	Prism-based using gold film	65
Laminin-5	Direct detection (10 min)	LOD: 4 pg/mL LOC: 37 ng/mL, 0.1% human plasma	Prism-based using gold film	66
Collagen IV	Direct detection (10 min)	LOD: 2,400 pg/mL LOC: 50 ng/mL, 10% human plasma	Prism-based using gold film	67
Metalloproteinase-1	Direct detection (10 min)	LOD: 9 pg/mL LOD: 3 ng/mL, human plasma	Prism-based using gold film	68
IL-1 β, IL-6, IFN-γ, and TNF-α	SA: biotin–AuNP (3 h)	LOD: 1.2, 0.05, 22, and 15 pg/mL	Prism-based using gold film	69
IL-2, IL-4, IL-6, IL-10, IFN-γ, TNF-α	Direct detection (40 min)	LOD: 5–20 pg/mL LOC: 32 pg/mL, human serum	Dark-field microscopy of nanorods	45
IL-2, IFN-γ, TNF-α, IL-10	Direct detection (30 min)	LOD: 21–35 pg/mL	Dark-field microscopy of nanorods	70
Other proteins				
Thrombin, IgE, streptavidin, fibronectin	Direct detection (45 min)	LOD: 1 nM (60 ng/mL) for streptavidin	Dark-field microscope using nanorods, spectral imaging	71
Nucleic acids with medical relevance				
miR-15a	SA: ON + polymerization (2.5 h)	LOD: 0.5 fM (~2.5 fg/mL) LOC: 3.5 fM (~17.5 fg/mL), 40% human serum	Prism-based using gold film	72

(*Continued*)

Table 1 *(Continued)*

Target	Detection format (detection time)	Performance[a]	Optical platform	Reference
miR-16, miR-181, miR-34a, miR-125b	SA: strep–AuNP (35 min)	LOD: 0.35, 0.39, 0.5, 0.95 pM (~2, 2, 3, 5 pg/mL), 90% erythrocyte lysate samples	Prism-based using gold film	73
ON *ABCB1* gene	Direct detection (6 min)	LOD: 0.5 nM (~2.5 ng/mL)	Prism-based using gold film	74
BCR/ABL fusion gene	Direct detection (20 min)	LOD: 10 nM (~100 ng/mL)	Prism-based using gold film	75
Bacterial nucleic acids				
16S RNA (*Legionella pneumophila)*	SA: strep–quantum dots (3 h)	LOD: 1 pM (~10 pg/mL)	Prism-based using gold film	76
16S RNA: *L. pneumophila*	SA: ON–AuNP (1 h)	LOD: 1 pM (~10 pg/mL)	Prism-based using gold film	77
16S RNA: *L. pneumophila*, *Pseudomonas aeruginosa*, *Salmonella typhimurium*	SA: ON–AuNP (0.5 h)	LOC: 10 pg/mL (all three strains)	Prism-based using gold film	78
Genomic DNA (*Staphylococcus aureus*)	SA: ON–AuNP (T > 30 min)	LOC: 1 fM (~10 fg/mL)	Prism-based using gold film	79
Bacteria				
Salmonella enteritidis, *S. pneumoniae*, *Escherichia coli* O157:H7	Direct detection (<7 h), CCM	LOC: 3 CFU/mL, culture medium LOC: 60 CFU/mL, 10% milk, mineral water, ground bee	Prism-based using gold film	80
E. coli O157:H7	Direct detection (<10 h), CCM	LOC: 100 CFU/mL, culture medium	Prism-based using gold film	52
E. coli O157:H7	Direct detection (<10 h), CCM	LOC: 10 CFU/mL, culture medium	Prism-based using gold film	81
Cronobacter spp., *Salmonella* spp.	Direct detection (<24 h), CCM	LOC: 30 CFU/25 g, powdered infant formula	Prism-based using gold film	82
Chlamydia trachomatis, *Neisseria gonorrheae*	Direct detection (10 min)	LOD: 300 CFU/mL LOD: 1,500 CFU/mL	Collinear system using nanoholes, spectral imaging	46
Candida albicans	SA: Ab (1 h)	LOD: 10^6 cells/mL	Prism-based using gold film	83
Bioparticles				
IAV, HIV-VLP	Direct detection (~seconds)	LOC: 10^9/mL	Prism-based using gold film	84
Exosomes	Direct detection (10 min)	LOC: 5 μg/mL	Prism-based using gold film	85

[a]Determined in buffer unless otherwise stated.

Abbreviations: Ab, antibody; AFP, α-fetoprotein; AuNP, gold nanoparticle; CatG, cathepsin G; CCM, culture/capture/measure approach; CEA, carcinoembryonic antigen; CRP, C-reactive protein; HER2, human epidermal growth factor receptor type 2; HIV-VLP, human immunodeficiency virus-based virus-like particles; IAV, inactivated influenza A virus; IFN-γ, interferon-gamma; IgE, immunoglobulin E; IL, interleukin; LOC, lowest observed concentration; LOD, limit of detection; ON, oligonucleotide; PDA, polydopamine; PTX3, pentraxin 3; rGO, reduced graphene oxide; SA, sandwich assay; Strep, streptavidin; TNF-α, tumor necrosis factor-alpha.

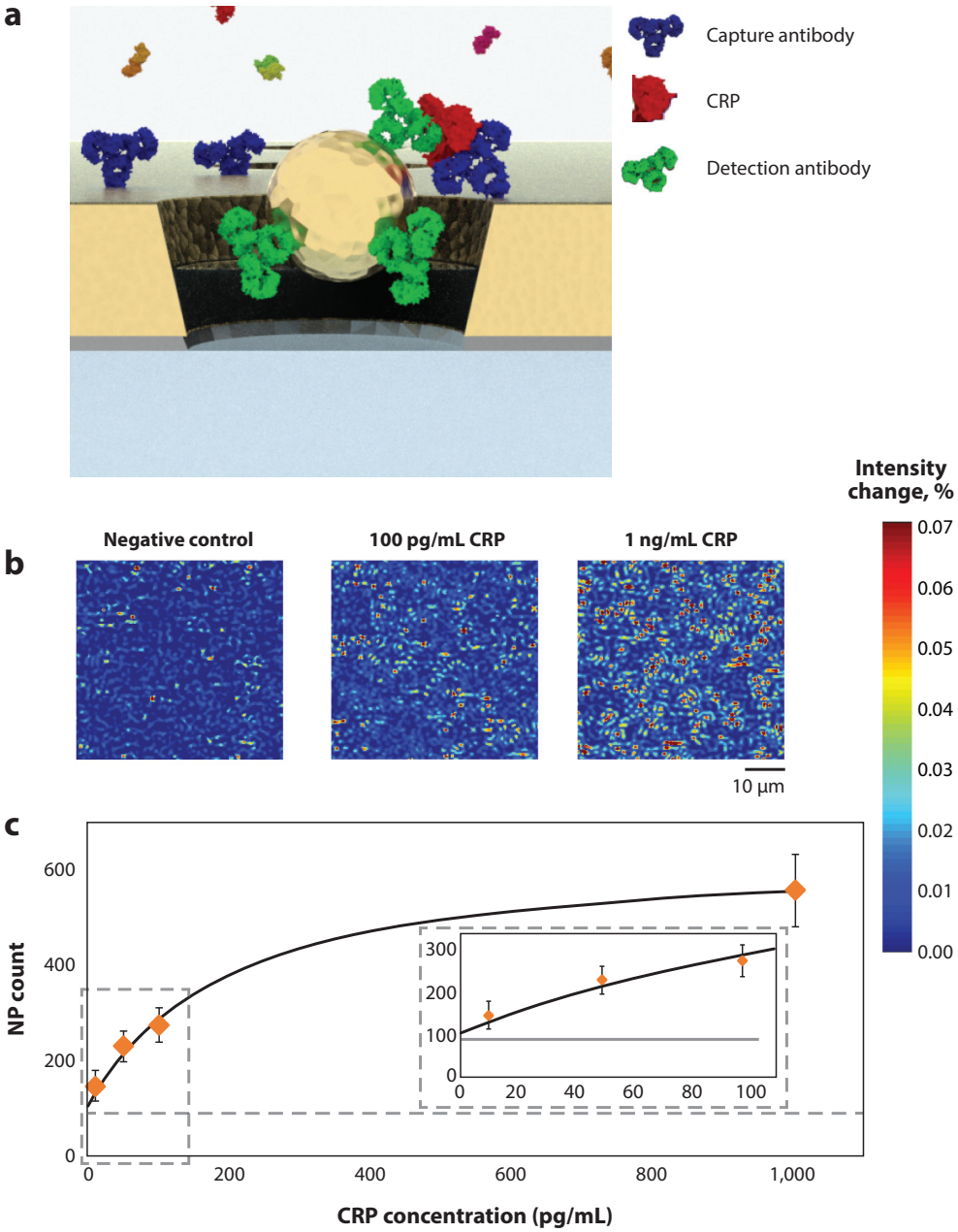

Figure 2

AuNP-enhanced detection of CRP using a surface with nanoholes. (*a*) CRP sandwich assay. (*b*) Different concentrations of CRP visually distinguished on surface plasmon resonance imaging. (*c*) Calibration curve for CRP. All panels adapted with permission from Reference 58. Copyright 2018 American Chemical Society. Abbreviations: AuNP, gold nanoparticle; CRP, C-reactive protein.

A breast cancer biomarker, human epidermal growth factor receptor 2 (HER2) antigen, was detected by Monteiro et al. (63). They used an SPR imaging platform based on an array of nanoholes functionalized with biotinylated anti-HER2 antibody attached via the immobilized streptavidin. The platform was demonstrated to directly detect HER2 in buffer at a concentration of 3 ng/mL.

Bottazzi et al. (28) developed an SPR imaging platform for the detection of pentraxin 3 (PTX3), a prospective biomarker of cardiovascular diseases and kidney pathologies. The platform was based

on a hexagonal lattice of polymeric pillars embedded in gold film to which anti-PTX3 was attached via amino coupling. Direct detection of PTX3 at concentrations of 100 ng/mL in buffer was achieved.

Cathepsin G (CatG), a molecule associated with an early immune response, was also targeted by the SPR imaging method (64, 65). The sensing spots were functionalized with MARS-115, a synthetic CatG inhibitor. Gorodkiewicz et al. (64) demonstrated the direct detection of CatG in buffer with an LOD of 0.23 ng/mL. In a subsequent study, the platform was applied to study endometriosis (65), and it was found that the CatG levels of patients suffering from this condition were twice as high as the control group. The same group also targeted other prospective cancer biomarkers, such as laminin-5, collagen IV, and metalloproteinase-1 (66–68), using the above-described methodology. In their study, laminin-5, collagen IV, and metalloproteinase-1 were directly detected in buffer with LODs of 4 (66), 2,400 (67), and 9 pg/mL (68), respectively. An analysis of clinical blood samples using SPR imaging revealed that patients with bladder and breast cancer exhibited higher concentrations of laminin-5 (66) and collagen IV (67), respectively.

Detection of cytokines using prism-based SPR imaging and specific antibodies was carried out by Kaiperien's group (69). Detection of selected cytokines, e.g., interleukin (IL)-1β, IL-6, interferon-gamma (IFN-γ), and tumor-necrosis-factor alpha (TNF-α), was performed in a three-step sandwich assay with a biotinylated antibody, neutravidin, and biotinylated AuNPs. LODs of 1.2, 0.05, 22, and 15 pg/mL were claimed for IL-1β, IL-6, IFN-γ, and TNF-α, respectively. Detection of 6 cytokines (IL-2, IL-4, IL-6, IL-10, IFN-γ, and TNF-α), was performed by Kurabayashi's group (45). They used dark-field LSPR imaging on a sparse array of antibody-coated nanorods. Cytokines were detected in buffer (LODs from 5 to 20 pg/mL) and then in undiluted human serum. In addition, the same group investigated the immunosuppressive drug-altered secretion of cytokines (IL-2, IFN-γ, TNF-α, and IL-10) by T cells (70). Initially, Jurkat T cells were activated with a mixture of ionomycine and phorbol 12-myristate 13-acetate, and then the tacrolinum immunosuppressant was added. Using the assay described elsewhere (45), the secretion of all cytokines was measured in buffer with LODs of 21–35 pg/mL.

Detection of Other Proteins

Multiplexed detection of four protein targets (thrombin, immunoglobulin E, streptavidin, and fibronectin) by dark-field SPR imaging was performed by Rosman et al. (71). The authors used four batches of nanorods, one for each protein, functionalized with their respective aptamers. Nanorods were sequentially injected over the sensor surface, and the position of each adsorbed nanorod was recorded. During the direct detection of proteins, the spatially resolved signal was matched with the map of aptamer-functionalized nanorods to determine the type of protein captured. LOD (1 nM) was only reported in the case of streptavidin.

Detection of Nucleic Acids with Medical Relevance

MicroRNA miR-15a, a colon cancer biomarker, was detected by Hu et al. (72). They used gold islands functionalized with hairpin-structured thiolated DNA probes and a two-step enhancement strategy based on a sandwich assay combining (*a*) multiple binding of secondary oligonucleotides to the hairpin-structured probes that were previously opened by single miR-15a and (*b*) prolongation of a secondary oligonucleotide by in situ DNA-initiated polymerization. This approach achieved an LOD for miR-15a as low as 0.5 fM. Detection of miR-15a in 40% serum

obtained from healthy controls and patients with colon cancer was also performed, and concentrations of 10.5 and 3.5 fM were detected, respectively. Four microRNAs (miR-16, miR-181, miR-34a, and miR-125b), potential biomarkers of myelodysplastic syndrome, were targeted by Homola's group (73). A prism-based SPR imaging sensor was functionalized with ultralow fouling poly(carboxybetaine acrylamide) brushes to which DNA probes were covalently attached. Detection of microRNA was performed by means of a sandwich assay with streptavidin-coated AuNPs. The LODs ranging from 0.35 pM to 0.95 pM were established for microRNAs spiked in 90% erythrocyte lysate. Mariani et al. (74) used SPR imaging to detect an oligonucleotide sequence related to the single nucleotide polymorphism of the human *ABCB1* gene. They used SPR chips with different nanostructures that were functionalized with thiolated oligonucleotide probes. A nanostructure based on silver nanoprisms was found to be most sensitive, and the target oligonucleotide was detected directly with an LOD of 0.5 nM. The sequence of the *BCR/ABL* fusion gene, which plays a crucial role in the evolution of chronic myelogenous leukemia, was detected using prism-based SPR imaging by Wu et al. (75). The total RNA was extracted from K562 cells, and cDNA was obtained by applying a reverse transcription. The target DNA sequence was detected using an SPR chip functionalized with thiolated DNA probes, and an LOD of 10 nM was attained.

Detection of Bacterial Nucleic Acids

Tabrizian's group (76, 77) reported on the use of SPR imaging for the detection of 16S rRNA from *Legionella pneumophila*. In the first report, they used an SPR chip functionalized with thiolated DNA probes and a sandwich assay with biotinylated secondary DNA probes and streptavidin-coated quantum dots (76) or a sandwich assay with oligonucleotide modified AuNPs (77). RNA from *L. pneumophila* was extracted and fragmented to obtain 16S rRNA. The same LOD of 1 pM was reported for both assays. The same group also demonstrated the simultaneous detection of 16S rRNA of three pathogenic bacterial strains: *L. pneumophila*, *Pseudomonas aeruginosa*, and *Salmonella typhimurium* using a sandwich assay with oligonucleotide-AuNPs (78). 16S rRNA at concentrations as low as 10 pg/mL was measured for all three strains. The detection of genomic DNA from *Staphylococcus aureus* was reported by Spoto's group (79) using an SPR chip functionalized with peptide nucleic acid probes and a sandwich assay with oligonucleotide-AuNPs. Genomic DNA concentrations down to 1 fM were detected.

Detection of Bacteria

Pathogenic bacteria, such as *Salmonella enterica*, *Streptococcus pneumoniae*, *Escherichia coli* and *Cronobacter* spp., have been targeted by the research groups of Livache and Roupioz (52, 80–82). To detect extremely low levels of bacteria, they incorporated bacteria cultivation on an SPR chip, allowing for the detection of a greater population of cells [this is referred to as the culture/capture/measure (CCM) approach]. They used a prism-based SPR imaging platform functionalized with specific receptors (antibodies or carbohydrates). Using this approach, Bouguelia et al. (80) detected *Salmonella enteritidis*, *S. pneumoniae*, and *E. coli* O157:H7 in the buffer at concentrations as low as 3 CFU/mL. Mondani et al. (81) reported detection of *E. coli* O157:H7 at levels below 10 CFU/mL in 10% milk, mineral water, and ground beef samples cultivated on an SPR chip. Moreover, detection of *E. coli* O157:H7 in spring water and tap water, apple peel, and green salad was demonstrated with a similar detection performance (81). Proof-of-concept detection of *Cronobacter* spp. and *Salmonella* spp. was reported by Morlay et al. (82). They used an array of antibodies and demonstrated detection of both at levels down to 30 CFU in 25 g of powdered infant formula. Bulard et al. (52) used the CCM approach and

an array of carbohydrates immobilized on an SPR imaging chip to monitor their interaction with five different *E. coli* strains. They showed that the bacterial strains interacted differently with immobilized carbohydrates, providing a "carbohydrate binding fingerprint." Using this platform, they detected and discriminated *E. coli* strains initially occurring at 10^2 CFU/mL levels.

Chlamydia trachomatis and *Neisseria gonorrhoeae*, which cause sexually transmitted infections, were detected using spectral SPR imaging with an array of nanoholes (46). The antibodies were captured on the surface of nanoholes via protein A/G. Bacteria were directly detected in buffer with LODs of 300 and 1,500 CFU/mL for *C. trachomatis* and *N. gonorrhoeae*, respectively.

Detection of *Candida albicans*, an opportunistic pathogenic yeast present in oral cavities, was detected using prism-based SPR imaging (83). The gold surface was functionalized with primary antibodies against *C. albicans* via amino coupling. The sandwich assay with antibodies was able to detect *C. albicans* in buffer with an LOD of 10^6 cells/mL.

Detection of Bioparticles

Individual biological submicrometer-size objects such as spherically shaped viruses [inactivated influenza A virus (IAV)] and virus-like particles [human immunodeficiency virus-based virus-like particles (HIV-VLP)] were detected by Shpacovitch and coworkers (84). They used a prism-based SPR imaging platform functionalized with mucins (via thiol groups of cysteine-rich regions on mucin) or biotinylated antibodies (via biotin to the immobilized streptavidin) to capture IAV and HIV-VLP, respectively. The binding of individual IAV and HIV-VLP was observed in buffer; the binding of HIV-VLP was also observed in serum.

Tumor-derived exosomes were detected by Zhu et al. (85). They used prism-based SPR imaging and antibodies against transmembrane proteins CD9, CD63, CD82, CD41b, EpCAM, and E-cadherin that were spotted on the surface of an SPR chip. Exosomes isolated from human hepatocellular carcinoma cell lines (MHCC97L, MHCC97H) and mouse melanoma cell lines (B16-F1, B16-F10) were detected directly, and the method was able to detect exosome from the MHCC97H cell line at a concentration of 5 μg/mL. It was also shown that highly metastatic cell lines (MHCC97H, B16-F10) secreted more exosomes than those with low metastatic effect (MHCC97L, B16-F1).

INVESTIGATION OF BIOLOGICAL SYSTEMS

Investigation of Bacteria

Tao's group (86) used SPR microscopy to monitor interactions of antibodies with individual bacteria. *E. coli* O157:H7 bacteria were attached to the sensor via covalently immobilized antibodies, and the interaction between the bacteria and the same antibodies contained in buffer was measured. The work demonstrates the feasibility of SPR microscopy-based analysis of biomolecular interactions involving single live bacteria and the effect of heterogeneity in a microbial population on these interactions. Tao's group also utilized SPR microscopy to quantify the motion of single bacteria and explored the correlation between this motion (resulting in changes in the image contrast) and antibiotic action on the bacterial metabolism (51). In this work, they studied *E. coli* O157:H7 interacting with a bactericidal antibiotic polymyxin B. The experiments revealed that antibiotic action significantly slows down bacterial motion.

Goluch's group (87) exploited SPR imaging to study bacterial films. In their earlier work they employed prism-based SPR imaging to monitor *E. coli* and *P. aeruginosa* that moved and attached across the sensor surface. Bacteria were placed in a growth medium on an SPR chip,

and the bacterial growth and biofilm formation were monitored in real time. Subsequently, they evaluated the efficacy of bovine serum albumin (BSA), casein, and penicillin/streptomycin surface coatings to prevent adhesion of *P. aeruginosa* and *S. aureus* (88). Prior to each experiment, protein and antibiotic solutions were pipetted to the SPR surface and left to dry. It was observed that bacterial attachment was most effectively inhibited by casein for both *P. aeruginosa* and *S. aureus*.

Mallevre et al. (89) used a prism-based SPR imaging sensor with the CCM approach to evaluate the toxicity of silver nanoparticles (AgNPs) and $AgNO_3$ on *S. enteritidis*. The dose-dependent changes in multiplication of the bacteria were consistent with those obtained by using a standard plating method. It was also shown that the toxic effect already occurs at mg/L levels.

Investigation of Cells

Investigation of living adherent cells using a high-resolution scanning SPR microscope was reported by Argoul's group (90). They studied C2C12 mouse myoblast cells cultured on an SPR chip with respect to their adherence and motility. The evolution in shape of the adherent cells was tracked, and local dynamics of filopodia and lamellipodia protrusions was observed. Subsequently, they also observed the cellular migration, adhesion, detachment, and attachment of C2C12 mouse myoblast cells on the gold substrate (40). The process of the attachment of individual cells was studied by Tu et al. (91). They used SPR microscopy on a nanohole array interfaced with microfluidics incorporating single-cell trapping units. Mouse embryonic stem cells (C3H10) and human tumor cells (HeLa) were monitored during culturing, and it was demonstrated that the single-cell attachment process follows the logistic retarded growth model (with different parameters for the different cells).

A study of the transport of mitochondria along primary rat hippocampus neurons was carried out by Tao's group (92). They used an SPR microscope with advanced image postprocessing to track moving objects (localization precision ~5 nm). Spatiotemporal measurements of neural cells seeded on a poly-L-lysine-coated SPR chip allowed for the tracking of mitochondria and determining the structure of microtubule bundles in neural cells.

As many intracellular signal transduction processes involve the remodeling of cytoskeleton or the translocation of signaling molecules, several attempts have been made to monitor cell response to various stimulations or to the spatial distribution of specific subcellular structures. Shinohara et al. (93) used prism-based SPR imaging to monitor intracellular signal transduction by translocation of protein kinase C (PKC). PC12 cells were cultured on an SPR chip and stimulated with K^+ or PKC activator phorbol-12-myristate-13-acetate (PMA) to induce PKC translocation that generated a sensor response. It was shown that cellular response to both K^+ and PMA increased with the concentration. The translocation of PKC was employed by Mir & Shinohara (94) who used prism-based SPR imaging to examine differentiation of PC12 cells on a poly-L-lysine-coated SPR chip. They demonstrated that their method can distinguish differentiated cells from nondifferentiated cells by comparing the sensor response to acetylcholine receptor agonists.

Zhang et al. (95, 96) used a prism-based SPR imaging method to investigate the response of living cells to various stimuli. Initially, they studied human type II alveolar epithelial cell line A549 cells cultured on an SPR chip that were stimulated by K^+ and epidermal growth factor (EGF). They demonstrated that the two different stimulants generated different sensor responses (95). Subsequently, they applied the same approach to analyze the response of a human hepatocellular carcinoma cell (HCC-LM3) to stimulation by K^+, EGF, and vascular EGF (VEGF) (96). The

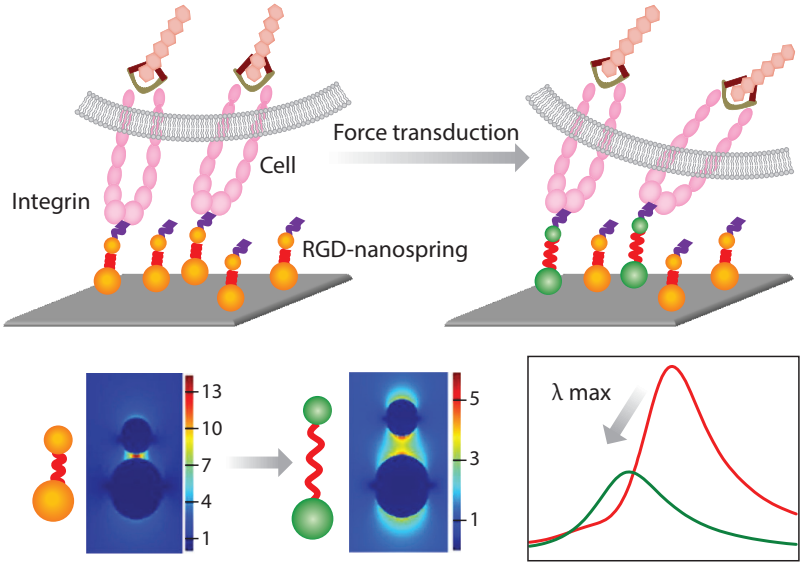

Figure 3

Schematic illustration for imaging mechanical force transduction with plasmonic nanosprings. Adapted with permission from Reference 98. Copyright 2017, American Chemical Society. Abbreviation: RGD, arginine–glycine–aspartic acid.

higher the concentration of K^+, the larger was the change in the sensor response. In contrast to EGF, VEGF did not produce any sensor response.

Tao's group (97) investigated the expression of EGF receptor (EGFR) and measured the kinetics of the binding of the antibody to EGFR on the cell surface with single-cell resolution. In this study, EGFR-overexpressed cells were grown on a collagen-coated SPR chip, and a monoclonal antibody (anti-EGFR) was used as a model to study the binding kinetics and affinity. The equilibrium dissociation constant was determined and shown to vary substantially from cell to cell. Experiments with cell lines having different EGFR-expression levels (A431, HeLa, and A549) showed that the steric hindrance effects of other membrane proteins may influence the drug-receptor interactions.

Xiong et al. (98) proposed an approach for the investigation of mechanical signals associated with mechanical forces propagating in cells. This approach is based on the combination of single-particle dark-field spectral microscopy and plasmonic nanosprings [two AuNPs connected by a polyethylene glycol (PEG) chain] that act as a mechanical sensor transferring force-induced molecular extension/compression to the optical response. The nanosprings used in this work consisted of AuNPs attached to the thiol-modified surface via Au–S chemistry and one smaller AuNP bound to the cell surface via RGD tripeptide–integrin interaction. Initially, the authors determined the relationship between the position of the spectral peak of one nanospring and the coupling distance, which was then correlated with the mechanical force exerted (**Figure 3**). This approach allowed for the visualization of the activation of localized mechanical force transduction in single live cells triggered by reactive oxygen species.

Berthuy et al. (99) tackled the problem of cell secretion by using prism-based SPR imaging. They employed human prostatic carcinoma cells (LNCaP) that were attached to an array of antibodies (anti-PSA, anti-B2M) microspotted on the sensor surface and monitored the secretion of PSA and B2M triggered by dihydrotestosterone by capturing the secreted PSA and B2M by the respective antibodies. Detection of antic-myc antibody secreted by an individual cell (9E10 hybridoma) attached to an array of nanodiscs was demonstrated by Raphael's group (100).

INVESTIGATION OF MOLECULAR INTERACTIONS

Drug–Protein Receptor Interactions

Li et al. (101) used prism-based SPR imaging to investigate the interaction between an immunosuppressive drug (FK506) and its target protein (FKBP12). The calibration curve for the binding of FK506 to the immobilized FKBP12 protein was established and used to determine the equilibrium rate constant of the interaction. Subsequently, Zhou et al. (102) further studied FK506. This involved a drug-target recognition study on a protein mutation microarray (the interaction of FK506 with FKBP12 WT and six mutants arrayed on the surface), a drug-mediated protein–protein interaction study (the formation of conditioned FKBP12-FK506-calcineurin complex), and a multiplexed drug binding specificity study on a protein microarray (FK506, SB203580, and biotin-specific binding to FKBP12, p38-a, and streptavidin).

Protein–DNA Interactions

Pillet et al. (103) used prism-based SPR imaging and dendrimeric functional coating to investigate the DNA–protein interaction model involved in *E. coli* plasmid segregation. They used five different amine-terminated DNA probes with different affinities to the SopB protein and determined the kinetic constants of their interactions with SopB. O'Sullivan's group (104) used prism-based SPR imaging to monitor the interaction between protein and different thiol-modified aptamers chemisorbed on sensor surface. They determined the equilibrium dissociation constants of the interactions among these β-conglutin binding aptamers to be 20 nM, 13 nM, and 1 nM for β-CBA I, β-CBA II, and 11-mer, respectively.

Protein–Protein Interactions

Miyachi et al. (105) used SPR imaging to investigate the binding of basic fibroblast growth factor 2 (FGF-2) to chondroitin sulfate (CS) tetrasaccharide conjugates. They found that the binding affinity of the CS tetrasaccharide structures to FGF-2 differed significantly, depending on whether they had a CS-E unit or a CS-D unit at the saccharide nonreducing end.

A nanoparticle-based SPR spectral imaging system was used for the analysis of carbohydrate-protein interactions (47). Bare AuNPs were attached to the glass substrate, functionalized with proteins (antitransferrin, antithrombin, BSA), and incubated with solutions containing carbohydrates (transferrin, heparin). Equilibrium binding constants of the interactions were extracted from the obtained calibration curves.

Zhao et al. (106) used prism-based SPR imaging for qualitative high-throughput profiling of epigenetic interactions between histone peptides and histone reader proteins. Selected 125 histone peptides were immobilized on the sensor surface, and their interactions with eight different proteins were analyzed in a single experiment to obtain respective binding affinities (**Figure 4**). Moreover, based on the kinetic analysis, the molecular basis of the structural recognition of two histone–protein pairs and a mechanism of histone-mediated DNA damage repair were proposed.

Protein–Cell Interactions

Tao's group (107) investigated interaction of herceptin (an antibody used as an antitumor drug) and the membrane HER2. In their study, the binding kinetics of herceptin with HER2 were measured in single intact cultured cells and primary cells extracted from breast tumor tissues.

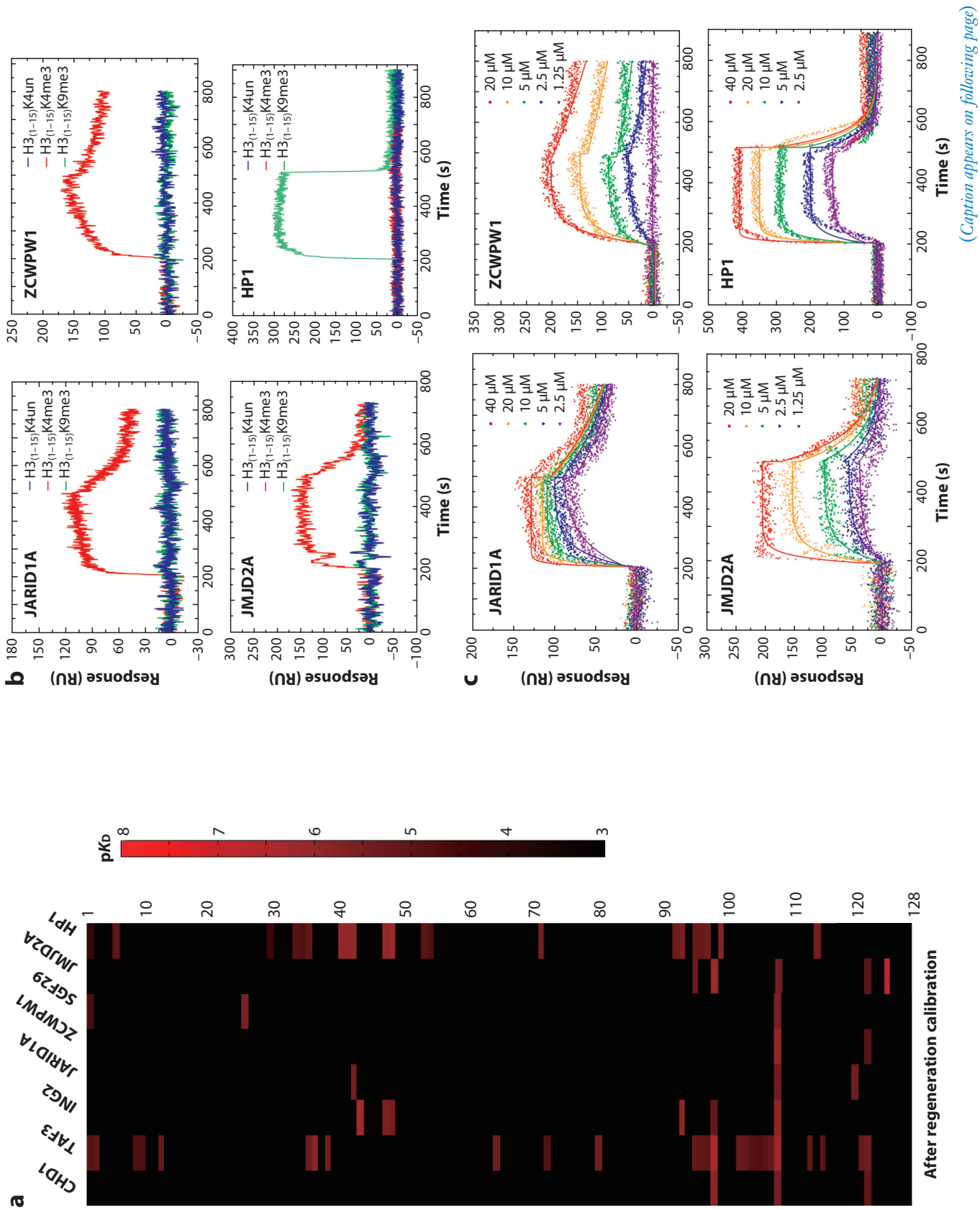

(Caption appears on following page)

Figure 4 (*Figure appears on preceding page*)

(*a*) Heatmap of binding affinities between histone peptides and histone reader proteins. (*b*) The binding curves of proteins to respective histones (*c*). Figure adapted with permission from Reference 106. Abbreviation: RU, refractive unit.

The equilibrium dissociation constant was determined and shown to vary among different cell lines. Significantly weaker herceptin–HER2 interaction was observed when using herceptin-resistant cells compared to those obtained using herceptin-sensitive cells. Furthermore, it was demonstrated that the steric hindrance of membrane protein mucin-4 can alter drug-receptor binding. Subsequently, they studied the same interaction except for the conjugation of herceptin with AuNPs (108). It was found that conjugation significantly affects the binding kinetic and that the mechanism of herceptin-AuNP binding depends on the conjugation density of herceptin on AuNPs and the expression level of HER2 on the cell membrane.

OTHER APPLICATIONS

Cheng et al. (109) used a prism-based SPR imaging platform to monitor the effect of chemical agents on amyloid-β (Aβ) fibril elongation. Aβ monomers were incubated with Fe^{3+}, Cu^{2+}, and Zn^{2+} (known to promote Aβ fibril growth). In addition, (−)-epigallocatechin gallate (EGCG) (known to inhibit Aβ fibril growth) and the fibrils were covalently attached to the sensor surface. Aβ monomers were then introduced, and the process of fibril elongation was monitored. It was demonstrated that the elongation process was modulated by the presence of metals and EGCG.

The process of toehold-mediated DNA strand displacement was studied using dark-field SPR microscopy and a plasmon ruler (110). The plasmon ruler used was a core-satellite AuNP assembly composed of several satellite nanoparticles bound to a core nanoparticle via DNA hybridization. DNA-strand displacement was triggered by an invader sequence (miRNA-21 oncogen) that released the satellite from the core. The kinetics of strand displacement was investigated for different toehold sequence lengths and homo-/hetero–DNA/RNA duplexes. Apparent rate constants were calculated from the probability of strand displacement. A plasmon ruler was also used for monitoring the extension process of DNA (telomerase primer) activated by a telomerase by Qian et al. (111). AgNPs dimers used as plasmon rulers were created via hybridization of AgNPs functionalized with complementary thiol-terminated DNA. AgNPs dimers were adsorbed on a glass substrate and cell extract, and deoxyribonucleotide triphosphates (dNTPs) were added to allow cellular telomerase to incorporate dNTPs to the end of the telomerase primer. The extended telomerase primer hybridizes with a DNA and forms a rigid structure that results in increasing the distance between AgNPs. Interparticle distance was determined from TEM images. Based on both spectral analysis and dark-field microscopy images, it was demonstrated that telomerases extracted from different cell lines exhibit different activity (i.e., DNA extension rate) and that the telomerase inhibitor EGCG indeed reduces the telomerase activity.

Jia et al. (112) used prism-based SPR imaging for DNA aptamer screening and real-time monitoring of the SELEX process. A target protein, lactoferrin, and a mixture of control proteins were covalently attached to the SPR chip via amine coupling. A DNA library was designed, and the respective DNA sequences were coupled with complementary DNA on AgNPs to create a DNA–AgNP library. In the reported experiments, DNA–AgNPs were flowed along the surface with immobilized lactoferrin and control proteins. Subsequently, the channel with target protein was disconnected and eluted, and the respective DNA was amplified by PCR and used in the following cycle. Finally, specific DNA was sequenced, and aptamer candidates were identified.

The SPR imaging based on a nanohole array was used for nucleic acid sequencing by Cetin et al. (113). They used a nanohole array to which primed-template DNA was attached. This methodology exploits the specificity with which a complex is formed between a primed-template DNA, a dNTP, and a polymerase. A model DNA (4 bp) was sequenced in this work.

SPR microscopy was also used to image and measure the length of a single DNA (114). Yu et al. functionalized a gold surface with amine-terminated thiols over which λ-DNA molecules were stretched by the capillary force. The SPR images were used to determine the average length of the whole λ-DNA and it was found to agree well with theoretical simulations and fluorescence images.

Corn's group (115, 116) investigated the uptake of small molecules (melitin) and large molecules (concanavalin) by hydrogel NPs for the controlled uptake and release of bioactive molecules in drug delivery. They loaded hydrogel NPs with different concentrations of molecules and adsorbed them on the surface of an SPR chip modified with hydrophobic alkanethiols. The difference in the sensor response to loaded and unloaded nanoparticles was found to correlate with the amount of loaded molecules.

DISCUSSION

The development of optical platforms for SPR imaging and microscopy has been driven by different needs and applications. Whereas in SPR microscopy, research into optical platforms has been concentrated mainly on achieving the best spatial resolution, research in SPR imaging has encompassed activities toward improving performance (both spatial resolution and RI resolution) as well as reducing the size and complexity of SPR imaging devices. RI resolution is one of the main characteristics that describes sensing performance of SPR imaging platforms. However, one should keep in mind that RI resolution (*a*) depends on multiple factors (e.g., spatial and temporal averaging of sensor response) that are often different (or not stated) in different reports and (*b*) is not the best characteristic when comparing platforms employing different surface plasmon modes (i.e., different surface plasmon modes may exhibit rather different electromagnetic field profiles). RI resolutions reported in the literature span a broad range of values (10^{-3} to 10^{-7}). The best laboratory SPR imaging platforms achieve an RI resolution of around 10^{-7} while being able to simultaneously measure ∼100 sensing spots with a temporal resolution of ∼1 s. In contrast, the performance of compact SPR imaging systems (often based on collinear optics and plasmonic nanostructures) is inferior, typically achieving RI resolutions on the order of 10^{-3}–10^{-6}. When assessing the potential of such devices for bioanalytical applications, it also remains to be seen to what extent miniaturization can be achieved while providing robust and stable optical systems insensitive to environmental factors (e.g., temperature variations), which are often sources of sensor response drifts. Although improving spatial resolution in SPR microscopy has clearly been the main motivation for a large number of research studies, it should be noted that the spatial resolutions reported by different groups were often determined under specific (and different) conditions, making direct comparison difficult. However, it should be noted that several approaches have been developed that allow SPR microscopy platforms to achieve a diffraction-limited resolution (∼200 nm). Moreover, SPR microscopy employing advanced image processing methods has been shown to be capable of visualizing the transport of biological objects (organelles) moving inside a cell with high precision (5 nm).

Biosensors based on SPR imaging have been applied in the detection of a broad variety of biologically relevant analytes, ranging from proteins and nucleic acids to viruses and bacteria. Detection performance is typically expressed in terms of the LOD. However, the reported LODs are often determined by different methods that make direct comparison difficult even when the

same analyte is to be detected. Comparison of the detection capabilities of different biosensors for different applications is even more elusive, as the ultimate detection performance of an SPR biosensor depends on multiple factors. These include the performance of the SPR instrument (optical platform, microfluidic system, and functional coating), the detection format, and composition of the sample (although most reports are concerned with the detection in buffer, the number of applications in real-world biological media is growing). Proteins represent the group of analytes targeted most frequently. The LODs achieved in buffer are typically in the pg/mL to ng/mL range; the LODs in complex samples (e.g., blood serum and plasma) are typically higher by an order of magnitude or more. Functional metal NPs are often employed to improve the specificity and LOD of the assay, which is more efficient in combination with the platforms that used surface plasmons with higher penetration depths (e.g., PSPs). Detection of nucleic acids has also been pursued, and the reported LODs are typically in the nM range or in the fM to pM range for direct and particle-enhanced sandwich assays, respectively. The SPR imaging technique has also been shown capable of detecting individual bioparticles. Moreover, SPR imaging platforms have been applied to high-throughput analyses of a multitude of biomolecular interactions, such as small drug–protein receptor, protein–nucleic acid, and protein–protein interactions. SPR imaging and microscopy methods have also been introduced in cell research to provide a platform for the study of individual cells as well as their groups and assemblies. This included investigation of the properties of intact living cells, such as their adhesion, response to external stimuli, signaling, and secretion as well as the interaction of ligands with membrane receptors embedded in the native environment of the cell. The concept of monitoring the interactions involving individual cells has been demonstrated, and SPR microscopy has been shown to provide resolution that allows tracking the individual subcellular structures (organelles, cytoskeleton).

OUTLOOK

Since their conception, SPR imaging and microscopy have made great advances in terms of both technology and applications. However, they have not yet reached the level of maturity and use of conventional SPR biosensors. Only a few SPR imaging and microscopy commercial platforms are available, which limits the development of new applications and the impact of this technology. This also contributes to a lack of standardization of instrumentation and measurement methodologies that need to be improved in the future. Although the LODs achieved by SPR imaging platforms meet the requirements of numerous relevant bioanalytical applications, analysis of complex samples (e.g., bodily fluids) with minimum or no sample preparation remains a challenge. In the future, this issue is expected to be alleviated by advances in the development of functional coatings and detection methodologies. The need for more sensitive and accurate SPR imaging and microscopy platforms may be addressed by new developments in plasmonics and optical measurement methods. Plasmonic nanostructures may play an important role in some future applications, but their routine use will require the development of cost-effective methods for their fabrication. Given the growing number of applications and complexity of problems addressed by SPR imaging and microscopy, these methods will undoubtedly continue to evolve and have an increasing impact on the fields of biology, medicine, food safety, and security.

DISCLOSURE STATEMENT

The authors are not aware of any affiliations, memberships, funding, or financial holdings that might be perceived as affecting the objectivity of this review.

ACKNOWLEDGMENT

This work was supported by the Czech Science Foundation under contract #P205/12/G118.

LITERATURE CITED

1. Nirschl M, Reuter F, Voros J. 2011. Review of transducer principles for label-free biomolecular interaction analysis. *Biosensors* 1:70–92
2. Gordon JG, Ernst S. 1980. Surface-plasmons as a probe of the electrochemical interface. *Surf. Sci.* 101:499–506
3. Nylander C, Liedberg B, Lind T. 1982. Gas-detection by means of surface-plasmon resonance. *Sens. Actuators* 3:79–88
4. Löfås S, Malmqvist M, Rönnberg I, Stenberg E, Liedberg B, Lundstrom I. 1991. Bioanalysis with surface-plasmon resonance. *Sens. Actuators B* 5:79–84
5. Yeatman E, Ash EA. 1987. Surface-plasmon microscopy. *Electron. Lett.* 23:1091–92
6. Rothenhäusler B, Knoll W. 1988. Surface-plasmon microscopy. *Nature* 332:615–17
7. Zeng YJ, Hu R, Wang L, Gu DY, He JN, et al. 2017. Recent advances in surface plasmon resonance imaging: detection speed, sensitivity, and portability. *Nanophotonics* 6:1017–30
8. Wong CL, Olivo M. 2014. Surface plasmon resonance imaging sensors: a review. *Plasmonics* 9:809–24
9. Abbas A, Linman MJ, Cheng Q. 2011. New trends in instrumental design for surface plasmon resonance-based biosensors. *Biosens. Bioelectron.* 26:1815–24
10. D'Agata R, Spoto G. 2013. Surface plasmon resonance imaging for nucleic acid detection. *Anal. Bioanal. Chem.* 405:573–84
11. Liu CJ, Hu FC, Yang W, Xu JY, Chen Y. 2017. A critical review of advances in surface plasmon resonance imaging sensitivity. *Trends Anal. Chem.* 97:354–62
12. Puiu M, Bala C. 2016. SPR and SPR imaging: recent trends in developing nanodevices for detection and real-time monitoring of biomolecular events. *Sensors* 16:870
13. Scarano S, Mascini M, Turner APF, Minunni M. 2010. Surface plasmon resonance imaging for affinity-based biosensors. *Biosens. Bioelectron.* 25:957–66
14. Maier SA. 2007. *Plasmonics: Fundamentals and Applications*. Berlin/Heidelberg: Springer Sci. & Bus. Media
15. Homola J. 2006. *Surface Plasmon Resonance Based Sensors*. Berlin/Heidelberg: Springer
16. Špačková B, Wróbel P, Bocková M, Homola J. 2016. Optical biosensors based on plasmonic nanostructures: a review. *Proc. IEEE* 104:2380–408
17. Berini P. 2009. Long-range surface plasmon polaritons. *Adv. Opt. Photon.* 1:484–588
18. Vecchi G, Giannini V, Rivas JG. 2009. Surface modes in plasmonic crystals induced by diffractive coupling of nanoantennas. *Phys. Rev. B* 80:201401
19. Li XK, Soler M, Ozdemir CI, Belushkin A, Yesilkoy F, Altug H. 2017. Plasmonic nanohole array biosensor for label-free and real-time analysis of live cell secretion. *Lab Chip* 17:2208–17
20. Guo H, Guo JP. 2015. Hybrid plasmon photonic crystal resonance grating for integrated spectrometer biosensor. *Opt. Lett.* 40:249–52
21. Seiler ST, Rich IS, Lindquist NC. 2016. Direct spectral imaging of plasmonic nanohole arrays for real-time sensing. *Nanotechnology* 27:184001
22. Rampazzi S, Danese G, Leporati F, Marabelli F. 2016. A localized surface plasmon resonance-based portable instrument for quick on-site biomolecular detection. *IEEE Trans. Instrum. Meas.* 65:317–27
23. Schasfoort RBM. 2017. Examples of SPR imaging instruments. In *Handbook of Surface Plasmon Resonance*, ed. RBM Schasfoort, pp. 89–97. Cambridge, UK: R. Soc. Chem. 2nd ed.
24. Corso AJ, Zuccon S, Zuppella P, Pelizzo MG. 2015. Flexible SPR system able to switch between Kretschmann and SPRi. *Proc. SPIE 9506*, Opt. Sens., 95061D. **https://doi.org/10.1117/12.2181223**
25. Shao YH, Li Y, Gu DY, Zhang K, Qu JL, et al. 2013. Wavelength-multiplexing phase-sensitive surface plasmon imaging sensor. *Opt. Lett.* 38:1370–72
26. Zeng YJ, Wang L, Wu SY, He JA, Qu JL, et al. 2017. Wavelength-scanning SPR imaging sensors based on an acousto-optic tunable filter and a white light laser. *Sensors* 17:90

27. Laplatine L, Leroy L, Calemczuk R, Baganizi D, Marche PN, et al. 2014. Spatial resolution in prism-based surface plasmon resonance microscopy. *Opt. Expr.* 22:22771–85
28. Bottazzi B, Fornasari L, Frangolho A, Giudicatti S, Mantovani A, et al. 2014. Multiplexed label-free optical biosensor for medical diagnostics. *J. Biomed. Opt.* 19:017006
29. Gomez-Cruz J, Nair S, Manjarrez-Hernandez A, Gavilanes-Parra S, Ascanio G, Escobedo C. 2018. Cost-effective flow-through nanohole array-based biosensing platform for the label-free detection of uropathogenic *E. coli* in real time. *Biosens. Bioelectron.* 106:105–10
30. Guner H, Ozgur E, Kokturk G, Celik M, Esen E, et al. 2017. A smartphone based surface plasmon resonance imaging (SPRi) platform for on-site biodetection. *Sens. Actuators B* 239:571–77
31. Lee KL, You ML, Tsai CH, Lin EH, Hsieh SY, et al. 2016. Nanoplasmonic biochips for rapid label-free detection of imidacloprid pesticides with a smartphone. *Biosens. Bioelectron.* 75:88–95
32. Cappi G, Spiga FM, Moncada Y, Ferretti A, Beyeler M, et al. 2015. Label-free detection of tobramycin in serum by transmission-localized surface plasmon resonance. *Anal. Chem.* 87:5278–85
33. Ruemmele JA, Hall WP, Ruvuna LK, Van Duyne RP. 2013. A localized surface plasmon resonance imaging instrument for multiplexed biosensing. *Anal. Chem.* 85:4560–66
34. Lee KL, Tsai JT, Chih MJ, Yao YD, Wei PK. 2013. High-throughput label-free detection using a gold nanoslit array with 2-D spectral images and spectral integration methods. *IEEE J. Sel. Top. Quantum Electron.* 19. **https://doi.org/10.1109/JSTQE.2012.2234444**
35. Banville FA, Moreau J, Sarkar M, Besbes M, Canva M, Charette PG. 2018. Spatial resolution versus contrast trade-off enhancement in high-resolution surface plasmon resonance imaging (SPRI) by metal surface nanostructure design. *Opt. Expr.* 26:10616–30
36. Banville FA, Söllradl T, Zermatten PJ, Grandbois M, Charette PG. 2015. Improved resolution in SPR and MCWG microscopy by combining images acquired with distinct mode propagation directions. *Opt. Lett.* 40:1165–68
37. Son T, Lee C, Seo J, Choi IH, Kim D. 2018. Surface plasmon microscopy by spatial light switching for label-free imaging with enhanced resolution. *Opt. Lett.* 43:959–62
38. Tan HM, Pechprasarn S, Zhang J, Pitter MC, Somekh MG. 2016. High resolution quantitative angle-scanning widefield surface plasmon microscopy. *Sci. Rep.* 6:20195
39. Watanabe K, Matsuura K, Kawata F, Nagata K, Ning J, Kano H. 2012. Scanning and non-scanning surface plasmon microscopy to observe cell adhesion sites. *Biomed. Opt. Expr.* 3:354–59
40. Berguiga L, Streppa L, Boyer-Provera E, Martinez-Torres C, Schaeffer L, et al. 2016. Time-lapse scanning surface plasmon microscopy of living adherent cells with a radially polarized beam. *Appl. Opt.* 55:1216–27
41. Mandracchia B, Pagliarulo V, Paturzo M, Ferraro P. 2016. Through-the-objective holographic surface plasmon resonance imaging for quantitative measurement of thin film thickness. *Proc. SPIE* 9718, Quant. Phase Imaging 2, 97182W. **https://doi.org/10.1117/12.2218419**
42. Zhang J, Dai S, Ma C, Di J, Zhao J. 2017. Common-path digital holographic microscopy for near-field phase imaging based on surface plasmon resonance. *Appl. Opt.* 56:3223–28
43. Zhang J, Dai S, Ma C, Di J, Zhao J. 2017. Compact surface plasmon holographic microscopy for near-field film mapping. *Opt. Lett.* 42:3462–65
44. Gao YK, Xin ZM, Gan QQ, Cheng XH, Bartoli FJ. 2013. Plasmonic interferometers for label-free multiplexed sensing. *Opt. Expr.* 21:5859–71
45. Chen PY, Chung MT, McHugh W, Nidetz R, Li YW, et al. 2015. Multiplex serum cytokine immunoassay using nanoplasmonic biosensor microarrays. *ACS Nano* 9:4173–81
46. Soler M, Belushkin A, Cavallini A, Kebbi-Beghdadi C, Greub G, Altug H. 2017. Multiplexed nanoplasmonic biosensor for one-step simultaneous detection of *Chlamydia trachomatis* and *Neisseria gonorrhoeae* in urine. *Biosens. Bioelectron.* 94:560–67
47. Liu XJ, Zhang QQ, Tu Y, Zhao WF, Gai HW. 2013. Single gold nanoparticle localized surface plasmon resonance spectral imaging for quantifying binding constant of carbohydrate-protein interaction. *Anal. Chem.* 85:11851–57
48. Schasfoort RBM. 2017. *Handbook of Surface Plasmon Resonance*. Cambridge, UK: R. Soc. Chem. 2nd ed.

49. Romanov V, Davidoff SN, Miles AR, Grainger DW, Gale BK, Brooks BD. 2014. A critical comparison of protein microarray fabrication technologies. *Analyst* 139:1303–26
50. Vaisocherova H, Brynda E, Homola J. 2015. Functionalizable low-fouling coatings for label-free biosensing in complex biological media: advances and applications. *Anal. Bioanal. Chem.* 407:3927–53
51. Syal K, Iriya R, Yang YZ, Yu H, Wang SP, et al. 2016. Antimicrobial susceptibility test with plasmonic imaging and tracking of single bacterial motions on nanometer scale. *ACS Nano* 10:845–52
52. Bulard E, Bouchet-Spinelli A, Chaud P, Roget A, Calemczuk R, et al. 2015. Carbohydrates as new probes for the identification of closely related *Escherichia coli* strains using surface plasmon resonance imaging. *Anal. Chem.* 87:1804–11
53. Simon L, Lautner G, Gyurcsanyi RE. 2015. Reliable microspotting methodology for peptide-nucleic acid layers with high hybridization efficiency on gold SPR imaging chips. *Anal. Methods* 7:6077–82
54. Nand A, Singh V, Perez JB, Tyagi D, Cheng ZQ, Zhu JS. 2014. *In situ* protein microarrays capable of real-time kinetics analysis based on surface plasmon resonance imaging. *Anal. Biochem.* 464:30–35
55. Manuel G, Lupták A, Corn RM. 2016. A microwell-printing fabrication strategy for the on-chip templated biosynthesis of protein microarrays for surface plasmon resonance imaging. *J. Phys. Chem. C* 120:20984–90
56. Kruis IC, Lowik D, Boelens WC, van Hest JCM, Pruijn GJM. 2016. An integrated, peptide-based approach to site-specific protein immobilization for detection of biomolecular interactions. *Analyst* 141:5321–28
57. Wood JB, Szyndler MW, Halpern AR, Cho K, Corn RM. 2013. Fabrication of DNA microarrays on polydopamine-modified gold thin films for SPR imaging measurements. *Langmuir* 29:10868–73
58. Belushkin A, Yesilkoy F, Altug H. 2018. Nanoparticle-enhanced plasmonic biosensor for digital biomarker detection in a microarray. *ACS Nano* 12:4453–61
59. Escobedo C, Chou YW, Rahman M, Duan XB, Gordon R, et al. 2013. Quantification of ovarian cancer markers with integrated microfluidic concentration gradient and imaging nanohole surface plasmon resonance. *Analyst* 138:1450–58
60. Hu WH, Chen HM, Shi ZZ, Yu L. 2014. Dual signal amplification of surface plasmon resonance imaging for sensitive immunoassay of tumor marker. *Anal. Biochem.* 453:16–21
61. Hu WH, He GL, Zhang HH, Wu XS, Li JL, et al. 2014. Polydopamine-functionalization of graphene oxide to enable dual signal amplification for sensitive surface plasmon resonance imaging detection of biomarker. *Anal. Chem.* 86:4488–93
62. Liu CJ, Wang X, Xu JY, Chen Y. 2016. Chemical strategy to stepwise amplification of signals in surface plasmon resonance imaging detection of saccharides and glycoconjugates. *Anal. Chem.* 88:10011–18
63. Monteiro JP, Predabon SM, Bonafé EG, Martins AF, Brolo AG, et al. 2017. SPR platform based on image acquisition for HER2 antigen detection. *Nanotechnology* 28. **https://doi.org/10.1088/1361-6528/28/4/045206**
64. Gorodkiewicz E, Sienczyk M, Regulska E, Grzywa R, Pietrusewicz E, et al. 2012. Surface plasmon resonance imaging biosensor for cathepsin G based on a potent inhibitor: Development and applications. *Anal. Biochem.* 423:218–23
65. Grzywa R, Gorodkiewicz E, Burchacka E, Lesner A, Laudanski P, et al. 2014. Determination of cathepsin G in endometrial tissue using a surface plasmon resonance imaging biosensor with tailored phosphonic inhibitor. *Eur. J. Obstet. Gynecol. Reprod. Biol.* 182:38–42
66. Sankiewicz A, Romanowicz L, Laudanski P, Zelazowska-Rutkowska B, Puzan B, et al. 2016. SPR imaging biosensor for determination of laminin-5 as a potential cancer marker in biological material. *Anal. Bioanal. Chem.* 408:5269–76
67. Sankiewicz A, Lukaszewski Z, Trojanowska K, Gorodkiewicz E. 2016. Determination of collagen type IV by Surface Plasmon Resonance Imaging using a specific biosensor. *Anal. Biochem.* 515:40–46
68. Tokarzewicz A, Romanowicz L, Sveklo I, Gorodkiewicz E. 2016. The development of a matrix metalloproteinase-1 biosensor based on the surface plasmon resonance imaging technique. *Anal. Methods* 8:6428–35

69. Hendriks J, Stojanovic I, Schasfoort RBM, Saris DBF, Kaiperien M. 2018. Nanoparticle enhancement cascade for sensitive multiplex measurements of biomarkers in complex fluids with surface plasmon resonance imaging. *Anal. Chem.* 90:6563–71
70. Oh BR, Chen P, Nidetz R, McHugh W, Fu J, et al. 2016. Multiplexed nanoplasmonic temporal profiling of T-cell response under immunomodulatory agent exposure. *ACS Sens.* 1:941–48
71. Rosman C, Prasad J, Neiser A, Henkel A, Edgar J, Sonnichsen C. 2013. Multiplexed plasmon sensor for rapid label-free analyte detection. *Nano Lett.* 13:3243–47
72. Hu FC, Xu JY, Chen Y. 2017. Surface plasmon resonance imaging detection of sub-femtomolar microRNA. *Anal. Chem.* 89:10071–77
73. Vaisocherová H, Šipová H, Visová I, Bocková M, Springer T, et al. 2015. Rapid and sensitive detection of multiple microRNAs in cell lysate by low-fouling surface plasmon resonance biosensor. *Biosens. Bioelectron.* 70:226–31
74. Mariani S, Ermini ML, Scarano S, Bellissima F, Bonini M, et al. 2013. Improving surface plasmon resonance imaging of DNA by creating new gold and silver based surface nanostructures. *Microchim. Acta* 180:1093–99
75. Wu JL, Huang Y, Bian XT, Li DD, Cheng Q, Ding SJ. 2016. Biosensing of BCR/ABL fusion gene using an intensity-interrogation surface plasmon resonance imaging system. *Opt. Commun.* 377:24–32
76. Foudeh AM, Daoud JT, Faucher SP, Veres T, Tabrizian M. 2014. Sub-femtomole detection of 16s rRNA from *Legionella pneumophila* using surface plasmon resonance imaging. *Biosens. Bioelectron.* 52:129–35
77. Melaine F, Tabrizian M. 2016. Functionalized gold nanoparticles for surface plasmon resonance detection of *Legionella pneumophila* 16s rRNA. *IEEE Sens.* **https://doi.org/10.1109/ICSENS.2016.7808696**
78. Melaine F, Saad M, Faucher S, Tabrizian M. 2017. Selective and high dynamic range assay format for multiplex detection of pathogenic *Pseudomonas aeruginosa*, *Salmonella typhimurium*, and *Legionella pneumophila* RNAs using surface plasmon resonance imaging. *Anal. Chem.* 89:7802–7
79. Aura AM, D'Agata R, Spoto G. 2017. Ultrasensitive detection of *Staphylococcus aureus* and Listeria monocytogenes genomic DNA by nanoparticle-enhanced surface plasmon resonance imaging. *Chem. Select* 2:7024–30
80. Bouguelia S, Roupioz Y, Slimani S, Mondani L, Casabona MG, et al. 2013. On-chip microbial culture for the specific detection of very low levels of bacteria. *Lab Chip* 13:4024–32
81. Mondani L, Roupioz Y, Delannoy S, Fach P, Livache T. 2014. Simultaneous enrichment and optical detection of low levels of stressed *Escherichia coli* O157:H7 in food matrices. *J. Appl. Microbiol.* 117:537–46
82. Morlay A, Piat F, Mercey T, Roupioz Y. 2016. Immunological detection of *Cronobacter* and *Salmonella* in powdered infant formula by plasmonic label-free assay. *Lett. Appl. Microbiol.* 62:459–65
83. Yodmongkol S, Thaweboon S, Thaweboon B, Puttharugsa C, Sutapun B, et al. 2016. Application of surface plasmon resonance biosensor for the detection of *Candida albicans*. *Jpn. J. Appl. Phys.* 55:02BE03
84. Shpacovitch V, Temchura V, Matrosovich M, Hamacher J, Skolnik J, et al. 2015. Application of surface plasmon resonance imaging technique for the detection of single spherical biological submicrometer particles. *Anal. Biochem.* 486:62–69
85. Zhu L, Wang K, Cui J, Liu H, Bu XL, et al. 2014. Label-free quantitative detection of tumor-derived exosomes through surface plasmon resonance imaging. *Anal. Chem.* 86:8857–64
86. Syal K, Wang W, Shan XN, Wang SP, Chen HY, Tao NJ. 2015. Plasmonic imaging of protein interactions with single bacterial cells. *Biosens. Bioelectron.* 63:131–37
87. Abadian PN, Tandogan N, Jamieson JJ, Goluch ED. 2014. Using surface plasmon resonance imaging to study bacterial biofilms. *Biomicrofluidics* 8:021804
88. Abadian PN, Goluch ED. 2015. Surface plasmon resonance imaging (SPRi) for multiplexed evaluation of bacterial adhesion onto surface coatings. *Anal. Methods* 7:115–22
89. Mallevre F, Templier V, Mathey R, Leroy L, Roupioz Y, et al. 2016. Real-time toxicity testing of silver nanoparticles to *Salmonella* Enteritidis using surface plasmon resonance imaging: a proof of concept. *NanoImpact* 1:55–59

90. Streppa L, Berguiga L, Provera EB, Ratti F, Goillot E, et al. 2016. Tracking in real time the crawling dynamics of adherent living cells with a high resolution surface plasmon microscope. *Proc. SPIE* 9724, Plasm. Biol. Med. 13, 97240G. **https://doi.org/10.1117/12.2211331**
91. Tu L, Li XZ, Bian ST, Yu YT, Li JX, et al. 2017. Label-free and real-time monitoring of single cell attachment on template-stripped plasmonic nano-holes. *Sci. Rep.* 7:11020
92. Yang YZ, Yu H, Shan XN, Wang W, Liu XW, et al. 2015. Label-free tracking of single organelle transportation in cells with nanometer precision using a plasmonic imaging technique. *Small* 11:2878–84
93. Shinohara H, Sakai Y, Mir TA. 2013. Real-time monitoring of intracellular signal transduction in PC12 cells by two-dimensional surface plasmon resonance imager. *Anal. Biochem.* 441:185–89
94. Mir TA, Shinohara H. 2013. Two-dimensional surface plasmon resonance imager: an approach to study neuronal differentiation. *Anal. Biochem.* 443:46–51
95. Zhang LL, Chen X, Wei HT, Li H, Sun JH, et al. 2014. Development of dual-channel surface plasmon resonance imaging system applied to living tumour cell analyses. *IET Micro Nano Lett.* 9:382–85
96. Zhang LL, Chen X, Du Y, Zhang Q, Li H, et al. 2015. A surface plasmon resonance imaging system for the stimulated living cell analysis. *Optoelectron. Lett.* 11:77–80
97. Zhang FN, Wang SP, Yin LL, Yang YZ, Guan Y, et al. 2015. Quantification of epidermal growth factor receptor expression level and binding kinetics on cell surfaces by surface plasmon resonance imaging. *Anal. Chem.* 87:9960–65
98. Xiong B, Huang ZR, Zou HY, Qiao CY, He Y, Yeung ES. 2017. Single plasmonic nanosprings for visualizing reactive-oxygen-species-activated localized mechanical force transduction in live cells. *ACS Nano* 11:541–48
99. Berthuy OI, Blum LJ, Marquette CA. 2016. Cancer-cells on chip for label-free detection of secreted molecules. *Biosensors* 6:2
100. Raghu D, Christodoulides JA, Delehanty JB, Byers JM, Raphael MP. 2015. A label-free technique for the spatio-temporal imaging of single cell secretions. *J. Vis. Exp.* 105:53120
101. Li SP, Yang M, Zhou WF, Johnston TG, Wang R, Zhu JS. 2015. Dextran hydrogel coated surface plasmon resonance imaging (SPRi) sensor for sensitive and label-free detection of small molecule drugs. *Appl. Surf. Sci.* 355:570–76
102. Zhou WF, Yang M, Li SP, Zhu JS. 2018. Surface plasmon resonance imaging validation of small molecule drugs binding on target protein microarrays. *Appl. Surf. Sci.* 450:328–35
103. Pillet F, Sanchez A, Formosa C, Séverac M, Trévisiol E, et al. 2013. Dendrimer functionalization of gold surface improves the measurement of protein-DNA interactions by surface plasmon resonance imaging. *Biosens. Bioelectron.* 43:148–54
104. Rubio MJ, Svobodová M, Mairal T, O'Sullivan CK. 2016. Surface plasmon resonance imaging (SPRi) for analysis of DNA aptamer: β-conglutin interactions. *Methods* 97:20–26
105. Miyachi K, Wakao M, Suda Y. 2015. Syntheses of chondroitin sulfate tetrasaccharide structures containing 4,6-disulfate patterns and analysis of their interaction with glycosaminoglycan-binding protein. *Bioorg. Med. Chem. Lett.* 25:1552–55
106. Zhao S, Yang M, Zhou WF, Zhang BC, Cheng ZQ, et al. 2017. Kinetic and high-throughput profiling of epigenetic interactions by 3D-carbene chip-based surface plasmon resonance imaging technology. *PNAS* 114:E7245–54
107. Wang W, Yin LL, Gonzalez-Malerva L, Wang SP, Yu XB, et al. 2014. *In situ* drug-receptor binding kinetics in single cells: a quantitative label-free study of anti-tumor drug resistance. *Sci. Rep.* 4:6609
108. Yin LL, Yang YZ, Wang SP, Wang W, Zhang ST, Tao NJ. 2015. Measuring binding kinetics of antibody-conjugated gold nanoparticles with intact cells. *Small* 11:3782–88
109. Cheng XR, Hau BYH, Veloso AJ, Martic S, Kraatz HB, Kerman K. 2013. Surface plasmon resonance imaging of amyloid-β aggregation kinetics in the presence of epigallocatechin gallate and metals. *Anal. Chem.* 85:2049–55
110. Li MX, Xu CH, Zhang N, Qian GS, Zhao W, et al. 2018. Exploration of the kinetics of toehold mediated strand displacement via plasmon rulers. *ACS Nano* 12:3341–50
111. Qian GS, Zhang TT, Zhao W, Xu JJ, Chen HY. 2017. Single-molecule imaging of telomerase activity via linear plasmon rulers. *Chem. Commun.* 53:4710–13

112. Jia WC, Li H, Wilkop T, Liu XH, Yu XD, et al. 2018. Silver decahedral nanoparticles empowered SPR imaging-SELEX for high throughput screening of aptamers with real-time assessment. *Biosens. Bioelectron.* 109:206–13
113. Cetin AE, Iyidogan P, Hayashi Y, Wallen M, Vijayan K, et al. 2018. Plasmonic sensor could enable label-free DNA sequencing. *ACS Sens.* 3:561–68
114. Yu H, Shan XN, Wang SP, Chen HY, Tao NJ. 2014. Plasmonic imaging and detection of single DNA molecules. *ACS Nano* 8:3427–33
115. Cho K, Fasoli JB, Yoshimatsu K, Shea KJ, Corn RM. 2015. Measuring melittin uptake into hydrogel nanoparticles with near-infrared single nanoparticle surface plasmon resonance microscopy. *Anal. Chem.* 87:4973–79
116. Maley AM, Terada Y, Onogi S, Shea KJ, Miura Y, Corn RM. 2016. Measuring protein binding to individual hydrogel nanoparticles with single-nanoparticle surface plasmon resonance imaging microscopy. *J. Phys. Chem. C* 120:16843–49

Appendix II

Analyte transport to micro-and nano-plasmonic structures

Lynn, N. S., Špringer, T., Slabý, J., Špačková, B., Gráfová, M., Ermini, M. L., and Homola, J.,

Lab on a Chip, 2019. **19**(24), 4117-4127.

Lab on a Chip

PAPER

Cite this: *Lab Chip*, 2019, **19**, 4117

Analyte transport to micro- and nano-plasmonic structures†

N. Scott Lynn Jr., Tomáš Špringer, Jiří Slabý, Barbora Špačková,‡ Michaela Gráfová, Maria Laura Ermini§ and Jiří Homola *

The study of optical affinity biosensors based on plasmonic nanostructures has received significant attention in recent years. The sensing surfaces of these biosensors have complex architectures, often composed of localized regions of high sensitivity (electromagnetic hot spots) dispersed along a dielectric substrate having little to no sensitivity. Under conditions such that the sensitive regions are selectively functionalized and the remaining regions passivated, the rate of analyte capture (and thus the sensing performance) will have a strong dependence on the nanoplasmonic architecture. Outside of a few recent studies, there has been little discussion on how changes to a nanoplasmonic architecture will affect the rate of analyte transport. We recently proposed an analytical model to predict transport to such complex architectures; however, those results were based on numerical simulation and to date, have only been partially verified. In this study we measure the characteristics of analyte transport across a wide range of plasmonic structures, varying both in the composition of their base plasmonic element (microwires, nanodisks, and nanorods) and the packing density of such elements. We functionalized each structure with nucleic acid-based bioreceptors, where for each structure we used analyte/receptor sequences as to maintain a Damköhler number close to unity. This method allows to extract both kinetic (in the form of association and dissociation constants) and analyte transport parameters (in the form of a mass transfer coefficient) from sensorgrams taken from each substrate. We show that, despite having large differences in optical characteristics, measured rates of analyte transport for all plasmonic structures match very well to predictions using our previously proposed model. These results highlight that, along with optical characteristics, analyte transport plays a large role in the overall sensing performance of a nanoplasmonic biosensor.

Received 19th July 2019,
Accepted 12th November 2019

DOI: 10.1039/c9lc00699k

rsc.li/loc

Introduction

In the past decade there has been an extraordinary growth of research into optical affinity biosensors based on plasmonic nanostructures (*i.e.*, nanoplasmonic biosensors).[1–4] In contrast to their surface plasmon resonance (SPR) predecessors based on a continuous metal film,[5] nanoplasmonic substrates are often composed of (metal) plasmonic features dispersed along a dielectric substrate. The architecture of these substrates can take many configurations, ranging from sensors based on positive relief nanodisks,[6] nanorods,[7] nanoprisms,[8] and nanowires,[9] to sensors based on negative relief nanoholes,[10] as well as *N*-particle clusters of both types (*e.g.*, nanorod dimers,[11] nanohole heptamers[12]). Although measurements on these substrates can proceed *via* several modes (*e.g.*, localized surface plasmons, collective resonances, and Fano resonances), they all follow a similar principle when used as a biosensor, whereby the selective capture of analyte by immobilized receptors causes a change in the sensor response.

The orthogonal functionalization of nanoplasmonic substrates – the immobilization of bioreceptors to sensitive regions (*i.e.*, plasmonic hot spots) and passivation of the remaining non-sensitive regions – has been demonstrated to significantly increase biosensing performance when compared to similar substrates with uniform functionalization.[13,14] This performance increase is due to increases in analyte transport: illustrated in Fig. 1 for a SPR and nanoplasmonic biosensor. SPR biosensors are often

Institute of Photonics and Electronics of the Czech Academy of Sciences, Chaberská 1014/57, 182 51 Prague, Czech Republic. E-mail: homola@ufe.cz; Fax: +420 284 681 534; Tel: +420 266 773 404

† Electronic supplementary information (ESI) available: The ESI includes details related to the prediction of mass transfer coefficients (and selected fitted sensorgrams) for all three substrate configurations and flow cells. See DOI: 10.1039/c9lc00699k

‡ Present address: Department of Physics, Chalmers University of Technology, 412 96 Göteborg, Sweden.

§ Present address: Center for Nanotechnology Innovation, Istituto Italiano di Tecnologia, 561 27 Pisa, Italy.

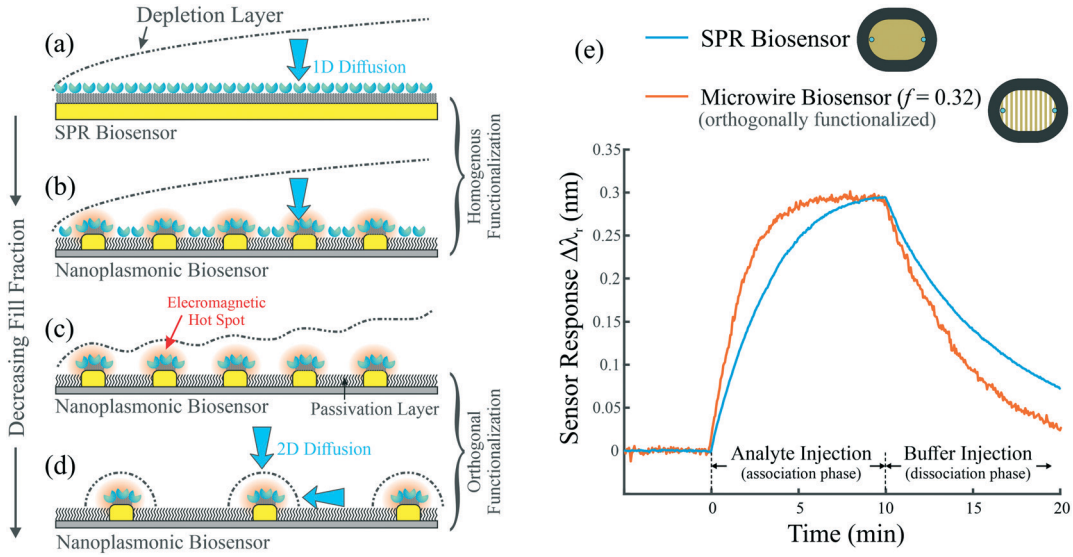

Fig. 1 The shape of the analyte depletion layer (dotted-dashed lines), and thus the rate of analyte transport, is dependent on the nanoplasmonic architecture. (a) A SPR biosensor will have similar analyte transport characteristics as (b) a uniformly functionalized nanoplasmonic biosensor, both having depletion layers of similar size. (c) When orthogonally functionalized, the same nanoplasmonic biosensor will exhibit a thinner analyte depletion layer (more complex in shape), along with increased rates of transport. (d) When the fill fraction of a nanoplasmonic biosensor is sufficiently low, the depletion layer will be hemispherical and much smaller in size than in case (a), where analyte transport, proceeding solely *via* diffusion, is two-dimensional, allowing for further increases in analyte transport. (e) Sensorgrams taken from both a SPR- and microwire-based biosensor using the same flow cell (details below, l = 10 μm, c = 10 nM); the increased sensor response for the microwire biosensor (in both the association and dissociation phases) is directly attributed to increased analyte transport.

subject to severe diffusion limitations, where a lack of fluid movement adjacent to the sensing surface results in a zone of depleted analyte (depletion layer) that grows in size along the flow direction (Fig. 1a).[15] When uniformly functionalized, a nanoplasmonic biosensor of similar size will exhibit a similar depletion layer (Fig. 1b). Conversely, analyte transport to an orthogonally functionalized nanoplasmonic biosensor will exhibit more complex depletion layers (Fig. 1c), where the passivated regions between plasmonic elements allow for depletion layer recovery and furthermore, enhanced rates of transport. When plasmonic elements become sufficiently far apart from one another, the depletion layers (with a size of the same magnitude as a single plasmonic element) become hemispherical in shape and smaller in size, leading to even higher rates of transport (Fig. 1d). Fig. 1e demonstrates how this phenomenon is manifested experimentally, where we compare the sensor response of a SPR biosensor with that of a microwire-based biosensor. The two sensors exhibit similar optical sensitivity (seen in the similar responses at equilibrium), however, the time to reach equilibrium for the microwire biosensor is much shorter: an effect solely attributed to an increase in analyte transport.

Hence, when orthogonally functionalized, the rate of analyte transport, and thus the sensor response, will be strongly influenced by the nanoplasmonic architecture – both in the size and shape of each plasmonic element as well as their spacing with respect to each other. Prediction of such transport rates to complex substrates (useful for sensor optimization) was unavailable until recently, when using the results of several numerical methods we proposed a simple analytical approach to estimate transport to array-based sensors.[16] We later demonstrated this effect experimentally, showing that the sensing performance for a nanoplasmonic biosensor is dependent on the product of optical performance with the rate of analyte transport.[17]

In this study we examine the analyte transport characteristics to a wide range of micro- and nanoplasmonic biosensors, all of which are practically relevant within the current literature. We examine the biosensing characteristics of plasmonic substrates having three configurations – based on microwires, nanorods, and nanodisks – with the former two having variable coverage of plasmonic elements. These substrates are functionalized using multiple analyte/receptor systems based on both DNA and RNA oligonucleotides. Sensorgrams created from individual channels on each substrate are used to extract both kinetic data (association and dissociation rate constants) as well as the rate of analyte transport (mass transfer coefficient). We show that, across all substrates, experimental measurements of analyte transport match very well to our previously developed analytical model.

This study serves as an experimental verification of our previously developed analytical model,[16] which had only been partially verified through experiments limited to only nanorod based substrates used for the detection of a single analyte.[17] Altogether, rather than focusing on optical characteristics, this study highlights the characteristics of analyte transport across many types of heterogeneous sensing surfaces. In addition to being relevant to the nanoplasmonic configurations shown herein (*i.e.*, sensors based on microwires, nanodisks, and nanorods), these results are

applicable to a majority of current nanoplasmonic biosensor designs used in a flow-over format. The results shown herein can be used to design optimal architectures for nanoplasmonic biosensing.

Background and methodology

Fig. 2 shows the three nanoplasmonic configurations and associated microfluidic channels considered in this study. Plasmonic substrates exhibited a unique reflectance spectra having a plasmonic feature (minimum or maximum) at a wavelength λ_r. The sensor response was calculated as the shift of this position ($\Delta\lambda_r$) as a result of changes in the surface density of captured analyte ($\Delta\Gamma$), where the proportionality between these changes defines the sensitivity $S_\Gamma = \Delta\lambda_r/\Delta\Gamma$, determined by the optical characteristics of each sensor.

We consider the microfluidic-based delivery of analyte to the sensing surface, where each microchannel has height H, width W, and the sensing region has length L. Nanoplasmonic sensors consist of individual gold plasmonic elements with characteristic length l (in the direction of flow), width w (orthogonal to flow), and height h. Each sensing substrate had a fill fraction f, defined as the ratio of the overall surface area of the plasmonic elements with respect to the projected surface area of the sensing surface (Fig. 2); by this definition, SPR-based sensors (having a continuous gold film) have a fill fraction of $f = 1$.

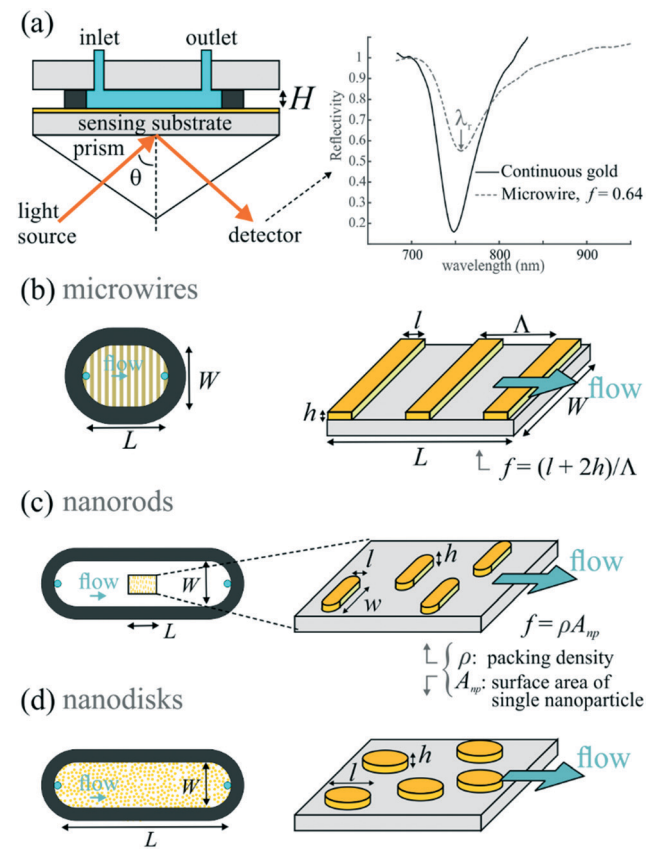

Fig. 2 (a) Schematic of the microfluidic flow cells and reflectance spectra for the substrates used in this study, specifically, configurations based on (b) microwires, (c) nanorods, and (d) nanodisks.

A liquid solution having an analyte concentration c is flowing through the sensing chamber. After transport to the sensing surface, analyte is captured in a 1:1 manner by functionalized bioreceptors having a surface density Γ_o (on each gold plasmonic element). Such capture can be described by both the association rate constant k_1 and the dissociation rate constant k_2. Using a quasi-steady approximation, time-rate changes in the sensor response can be described analytically as[18]

$$\frac{d\lambda_r}{dt} = S_\Gamma\left(\frac{k_1 c(\Gamma_o - \Gamma) - k_2\Gamma}{1 + k_1(\Gamma_o - \Gamma)/k_m}\right) \quad (1)$$

The value k_m represents the steady-state, diffusion-limited mass transfer coefficient, and is a measure of the efficiency of analyte transport; k_m is related to the analyte flux to the sensor surface J (averaged over the entire active surface) *via* $k_m = J/c$.

Analyte transport to a uniformly functionalized SPR biosensor is a relatively well studied topic. The mass transfer coefficient for a continuous gold film (here noted as k_p) situated in a rectangular geometry is dependent on the geometry of the microchannel (H, W, L), the diffusivity of the analyte D, and the volumetric flow rate Q. For flow in rectangular flow cells (with a single capture surface), k_p can be accurately predicted using a truncated solution proposed by Newman[19] as

$$k_p = 1.47\left(\frac{QD^2}{LH^2W}\right)^{\frac{1}{3}}. \quad (2)$$

Conversely, analyte transport to a nanoplasmonic biosensor is a much more complex problem. The study of transport to a heterogeneous reactive/passivated surface has only been recently examined, where several authors examined the problem theoretically from a microscopic perspective,[20,21] and we examined the problem from a macroscopic perspective.[16] In our model, the mass transfer coefficient to a nanoplasmonic sensor is predicted to follow

$$k_m = k_p\frac{R_k - f}{R_k f - 2f + 1}, \quad (3)$$

where $R_k = k_{np}/k_p$ is a ratio of the mass transfer coefficient for an individual plasmonic element composing the array (k_{np}), existing outside the influence of any other functionalized elements, with respect to the mass transfer coefficient for a continuous surface (k_p). In this study k_{np} would be representative of experiments consisting of a single microwire, nanodisk, or nanorod (we have also proposed a model to predict k_{np} to single nanodisks and nanorods[22]). From eqn (3) (when $R_k \gg 1$) it can be seen that as the fill fraction approaches unity ($f \rightarrow 1$), the mass transfer coefficient to an array approaches that to a continuous film

($k_m \rightarrow k_p$) and furthermore, scales inversely to the fill fraction ($k_m \sim k_p f^{-1}$) in the region of $f \approx 1$.

Eqn (1) is routinely used to extract kinetic parameters (k_1, k_2) from sensorgrams taken *via* the SPR method, specifically through fitting of eqn (1) to experimental data obtained at various analyte concentrations.[18] This equation also provides insight into the nature of affinity capture during a biosensing assay. The term $Da = k_1\Gamma_o/k_m$ represents the Damköhler number: a dimensionless parameter that represents the ratio between the rate of (reactive) affinity analyte capture with respect to the rate of analyte transport to the sensor surface.[15] The form of this term corresponds to the beginning of a detection experiment, where the surface density of captured analyte is very small ($\Gamma \approx 0$). Affinity capture is considered to be diffusion-limited when $Da \gg 1$, and reaction-limited when $Da \ll 1$.

When the Damköhler number is on the order of unity ($Da \approx 1$), contributions of both reactive and transport effects to the sensor signal are of similar magnitude. Therefore, in this regime one can use eqn (1) to extract both kinetic and mass transport parameters from sensorgram data. For the experiments shown herein, we thus used different analyte/receptor pairs for each substrate as to maintain $Da \approx 1$. Sensorgrams taken from each substrate, consisting of multiple injections with variable c, were used to obtain information on k_1, k_2 and k_m. This method provides an internal standard, as experiments using substrates having different fill fractions (similar configuration, analyte/receptor pairs, and detection conditions) will only lead to changes in measured mass transport behavior (k_m), where measurements of kinetic behavior are not expected to change (k_1, k_2).

The results herein are applicable to sensors operated in a flow over format, which are representative of the vast majority of previous work on nanoplasmonic biosensors. These results cannot be directly applied to flow through nanoplasmonic biosensors, which in a limited number of works, have been shown to overcome diffusion limitations (*via* flow directly adjacent to, and through, the sensing surface).[23–25] In a similar fashion, these results do not apply to sensors where analyte transport occurs through active means (*e.g.*, (di)electrophoresis).

Results

Plasmonic elements on each sensing substrate were functionalized with thiol-derivatized DNA or RNA sequences that were complementary to a target analyte, whereas the glass surfaces were untreated. We assumed no interaction between analyte and the glass surface, as both the analyte (ssDNA/ssRNA) and glass surface have a slight negative charge under the conditions of the assay.[26] The fill fraction was calculated for each substrate according to the equations shown in Fig. 2. For all flow cells and analyte/receptor pairs we also performed experiments using a continuous gold layer (*i.e.*, SPR biosensor, $f = 1$).

There were 2–5 individual measurement channels on each sensing substrate, from which we recorded the sensor response during the injection of analyte (association phase), followed by an injection of buffer without analyte (dissociation phase). The sensor surface was regenerated after each cycle. Sensorgrams taken from individual channels consisting of 3–6 injections (association and/or dissociation phases measured with variable analyte concentration) were used to extract characteristic interaction parameters, specifically k_1, k_2, Γ_o, and k_m (or k_p for SPR-based measurements). Unless noted, all experiments were conducted under conditions such that $0.1 < Da < 12$.

For both the continuous gold surfaces and large microwire substrates we assumed a sensitivity of $S_{\Gamma,SPR} = 5.56$ nm mm^2 ng^{-1}, which corresponds to the sensitivity of a propagating surface plasmon with a resonant wavelength of 750 nm to the addition of a 5 nm thick dielectric adlayer (RI = 1.43).[17] This value was used to estimate the probe density (Γ_o) for each analyte/receptor pair in each flow cell (*via* data taken from continuous gold films). The sensitivities of other substrates were estimated *via* the ratio between the average fitted value of Γ_o between a micro- or nano-structured substrate and that for a continuous gold surface, multiplied by $S_{\Gamma,SPR}$. The data shown in Fig. S1, S3, and S5 (ESI†) give representative values of the sensitivities across all of the substrates and fill fractions that we utilized in experiment.

Microwire experiments

We fabricated 21 substrates based on microwires of both varying wire size ($l = 1.4$, 10, 100 μm) and fill fraction ($0.16 < f < 0.64$), where each substrate had 2 measurement channels and 2 reference channels. The microwires were aligned with their long axis parallel with the plane of incidence (TM polarization). We performed experiments using two different target DNA oligomers complementary to a single probe sequence (Fig. 3a). Example sensorgrams for both a microwire substrate and a continuous gold surface are shown in Fig. 3d and e.

The normalized reflectance spectra taken from substrates based on larger microwires ($l = 10$, 100 μm, Fig. 3b) exhibited spectral dips which correspond to the excitation of propagating surface plasmons, where the contrast of the spectral dips decreased with decreasing fill fraction. We observed no significant difference in the high concentration equilibrium sensor response between the larger microwire substrates ($\Delta\lambda_r = 0.47 \pm 0.08$ nm, 26 sensorgrams) and continuous gold films ($\Delta\lambda_{r,SPR} = 0.45 \pm 0.08$ nm, 4 sensorgrams). This similarity suggests that the larger microwire substrates have a sensitivity equivalent to the continuous gold surface, which is consistent with the work by Sarkar *et al.*[9] concerning wires with dimension $l \gg \lambda_r$. These data lead to a density of immobilized probes of $\Gamma_o = 2.6 \pm 0.5 \times 10^{-14}$ mol mm^{-2}.

Conversely, the normalized reflectance spectra taken from the smaller microwire substrates ($l = 1.4$ μm, Fig. 3c) show a

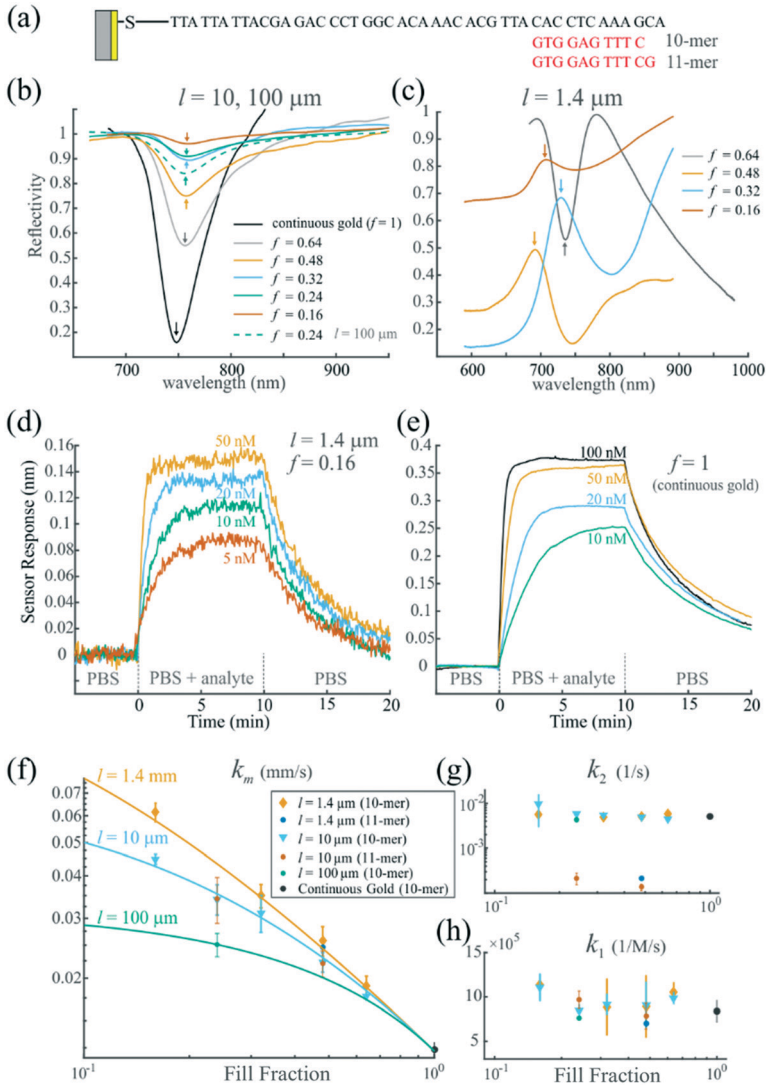

Fig. 3 Microwire experiments. (a) Schematic for the DNA receptor/analyte system. Reflectivity spectra for microwire sensing substrates for (b) larger (l = 10, 100 μm) and (c) smaller (l = 1.4 μm) microwires at varying fill fraction. Arrows indicate the plasmonic feature tracked during experiment. Selected sensorgrams (10-mer analyte) for both (d) a microwire substrate (f = 0.16, l = 1.4 μm) and (e) a continuous gold surface; fitted sensorgrams are shown in Fig. S1.† (f) Extracted values of k_m across all microwire substrates. Symbols represent experimental data; solid lines represent the predicted response for each microwire size (*via* eqn (3)). Extracted values of both (g) k_2 and (h) k_1 across all microwire substrates.

more complex spectra, a result of the coupling of propagating surface plasmons with lattice resonances.[27] These sensors were observed to exhibit a lower sensitivity, where the high concentration equilibrium sensor responses for smaller microwires were lower than that for a continuous gold surface (Fig. 3d and S1†).

Extracted values of k_m, k_2, and k_1 across all microwire substrates for both analytes are shown in Fig. 3f–h. A selection of fitted sensorgrams along with their extracted parameters are shown in Fig. S1.† It can be seen that extracted association rate constants are similar for both target sequences; however, dissociation rate constants for the 11-mer sequence are lower by over an order of magnitude with respect to those for the 10-mer sequence. We observed a large increase in the mass transfer coefficient with decreasing fill fraction, with larger increases observed for microwires having smaller dimension. No differences were seen in k_m between experiments using the two target analytes for a given substrate. Predictions for k_m as a function of the fill fraction match well with experimental data (Fig. 3f); the ESI† gives details on these predictions, along with information on both experimental and predicted parameters (Table S1).

Nanodisk experiments

We fabricated a single substrate with nanodisks arranged in a random packing order covering the entire floor of the sensing microchannel. The RNA analyte/receptor scheme is shown in Fig. 4a. In hybridized form this pair exhibits a stem-loop structure with an adenine bulge,[28] but otherwise demonstrated typical 1 : 1 binding kinetics. Fig. 4b shows the

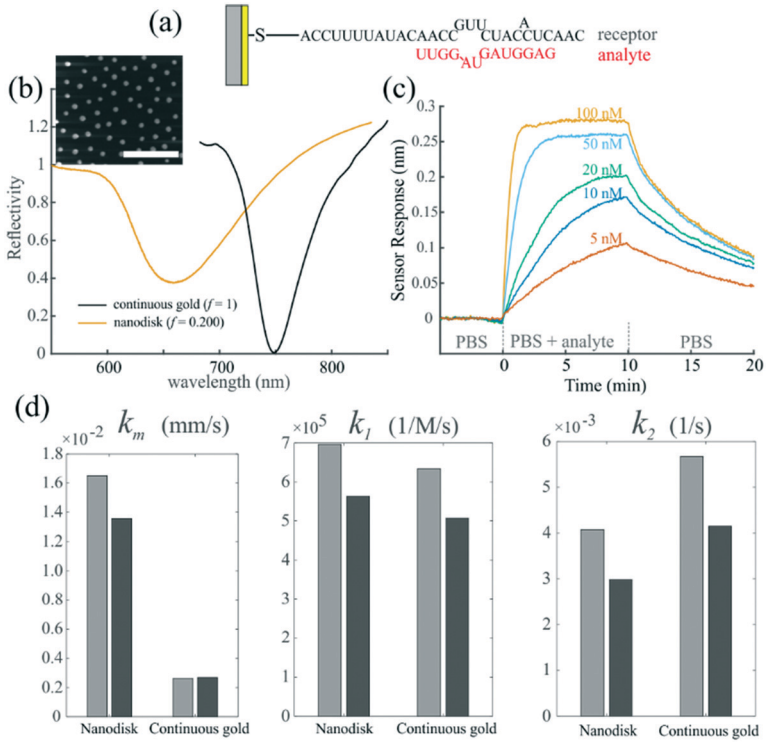

Fig. 4 Nanodisk experiments. (a) Schematic for the RNA receptor/analyte system. (b) Normalized reflectivity spectra for both a nanodisk substrate and a continuous gold film. The inset shows a SEM image of the nanodisk sensing substrate (scale bar 1 μm), where the disks had a mean diameter of l = 88 ± 8 nm. (c) Representative sensorgram for the nanodisk substrate. (d) Extracted values of k_m, k_1, and k_2 for both nanodisk and continuous gold substrates (using the same flow cell). Each bar represents data taken from a single sensorgram.

reflectance spectra of the substrate, where the dips in the reflectance spectra correspond to the excitation of longitudinal localized surface plasmons (TE polarization). From a SEM image we calculated a mean diameter of l = 88 ± 8 nm (h = 30 nm) and packing density of ρ = 13.9 μm^{-2}. The fill fraction was thus estimated as $f = \rho A_{np} = 0.200$.

We obtained two sensorgrams from both the nanodisk substrate (a single sensorgram is shown in Fig. 4c) and a continuous gold surface. The high concentration equilibrium sensor response for the continuous gold film ($\Delta\lambda_{r,SPR}$ = 1.42 ± 0.07 nm) led to a density of immobilized probes of Γ_o = 6.2 ± 0.3 × 10^{-14} mol mm^{-2}; data for the nanodisk substrates was lower ($\Delta\lambda_r$ = 0.281 ± 0.005 nm), indicating these substrates had a lower sensitivity; these values, along with fitted sensorgrams and other associated data, are shown in Fig. S3.†

Extracted values of k_m, k_2, and k_1 taken from nanodisk substrates are shown in Fig. 4d. We observed little difference between extracted values of k_1 and k_2 taken from nanodisk and continuous gold experiments, and a large difference in extracted values of k_m. Predicted values for the mass transfer coefficient for the nanodisk array (k_m = 0.0258 mm s^{-1}) and continuous gold film (k_m = 0.0052 mm s^{-1}) differed from average experimental values by a factor of 1.72 and 1.92, respectively (Table S2†). The differences between prediction and experiment are likely attributed to both the more complex flow cell design and the presence of nanodisks across the entire floor of the sensing chamber (outside of the interrogated region, Fig. S4†).

Nanorod experiments

We fabricated 6 substrates with nanorods arranged in a random packing order, having their long axis arranged parallel with the polarization of incident light (TE polarization). Substrates were fabricated with varying fill fraction, determined as $f = \rho A_{np}$, where A_{np} was calculated as the surface area of a rectangular block (l = 30 nm, w = 110 nm, h = 30 nm). An SEM image of one substrate can be seen in Fig. 5b, and details on the flow cell are shown in Fig. S6.† The dips in the reflectance spectra (Fig. 5b) correspond to the excitation of longitudinal localized surface plasmons. An example sensorgram taken from a nanorod substrate is shown in Fig. 5c (association phase only); we tested two chips per fill fraction, where each chip had 3 measurement channels. We observed a slight difference between the equilibrium response (high concentration) observed using a continuous gold film ($\Delta\lambda_{r,SPR}$ = 1.01 ± 0.12 nm, 6 sensorgrams, leading to Γ_o = 2.89 ± 0.34 × 10^{-14} mol mm^{-2}) and that using the nanorod substrates ($\Delta\lambda_r$ = 1.24 ± 0.21 nm, 18 sensorgrams), with no significant differences across different nanorod fill fractions, which we also observed in our previous study.[17]

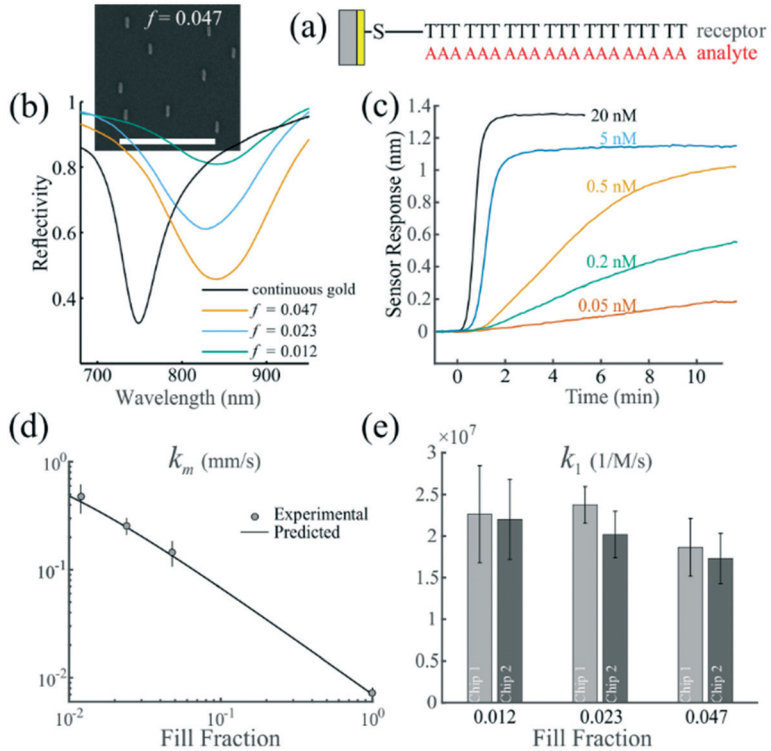

Fig. 5 Nanorod experiments. (a) Schematic for the DNA receptor/analyte system. (b) Reflectivity spectra for the nanorod substrates along with the continuous gold surface. (inset) SEM images of a nanorod substrate (scale bar 1 μm); individual nanorods had dimensions of l = 30 nm, w = 110 nm, and h = 30 nm. (c) Sensorgram for a nanorod substrate (f = 0.023). (d) Extracted values of k_m across all substrates. The solid line represents the predicted response. (e) Extracted values of k_1 for the nanorod substrates (3 sensorgrams per chip).

Extracted values of k_m for the nanorod substrates are plotted as a function of the fill fraction in Fig. 5d; experimental data match well with analytical predictions (Table S3†). There was little difference in the extracted values of k_1 across all nanorod substrates (Fig. 5e). Due to severe diffusion limitations (Da > 50), we did not obtain data for k_1 from continuous gold experiments; however, in that regime, extracted measurements of k_p can be considered to be accurate. The good match between predicted and experimental values of k_p and k_m suggests that there was little to no interaction between the ssDNA analytes and the non-functionalized glass surfaces.

Discussion

The experimental design used herein, *i.e.*, the use of different analyte/receptors for each substrate (each having a different association rate constant), ensured that all measurements were taken in the range of Da ≈ 1. These conditions allowed us to extract both kinetic and mass transfer parameters from sensorgrams using methods that are commonly used in biomolecular interaction analysis. When considering a single analyte/receptor system, the kinetic data (k_1, k_2) collected in this study show little dependence on the fill fraction across each substrate configuration, whereas as expected, extracted values of k_m vary significantly with changes in the fill fraction. Therefore, it is likely that the extracted values of k_m are void of artifact. The strong match between observed and predicted values of k_m across all substrates also suggests that other transport effects (*e.g.*, thermophoresis) are very limited under the conditions used here.

To directly compare the analyte transport behavior across the three experimental substrate configurations (and three different flow cells), we calculated the mass transfer enhancement $E = k_m/k_p$ for all of the experimental data shown above. These data are plotted in Fig. 6. In addition, using existing analytical solutions for analyte transport, we predicted R_k (*via* predictions of k_{np} and k_p) for all of the substrate configurations used herein; these predictions are detailed in the ESI† (Tables S1–S3). From the data shown in Fig. 6, it can be seen that the values predicted by eqn (3) match well to all of the experimental data taken across all fill fractions.

Design guidelines

The results shown herein have fairly strong implications for the design of a nanoplasmonic sensor: the rate of mass transport to a nanoplasmonic structure is strongly dependent on both the sensor fill fraction as well as the specific plasmonic architecture (where the difference in size between individual plasmonic elements and the overall sensing region will determine R_k). Thus, two different plasmonic nanostructures having similar R_k and f will have similar mass

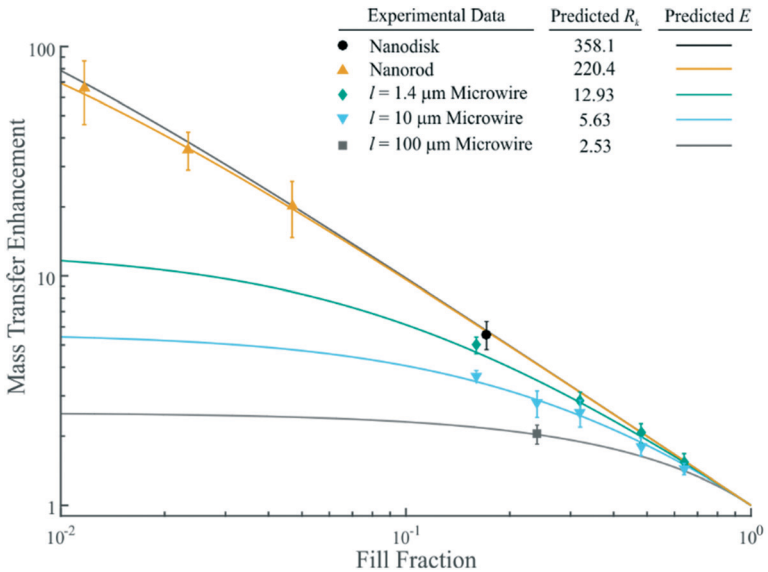

Fig. 6 Mass transfer enhancement ($E = k_m/k_p$) plotted *vs.* the fill fraction for all of the experimental substrates (symbols). All experimental data scale according to eqn (3), data from which are shown as the solid lines using respective values of R_k for each substrate.

transport characteristics, regardless of the substrate configuration or packing order. The value R_k is strongly dependent on the size and shape of an individual plasmonic element. Plasmonic structures having individual elements with smaller characteristic sizes will have higher R_k (and have a stronger dependence on the fill fraction), seen explicitly in the data herein taken from microwire substrates. A same argument holds related to how much an individual plasmonic element protrudes into the sensing medium: positive relief elements will have higher R_k with respect to negative relief elements (*e.g.*, nanohole) having similar characteristic sizes. Eqn (3) also sets the upper limit for mass transport, where the mass transfer enhancement for any nanostructure cannot exceed $E = 1/f$ (seen from eqn (3) as $R_k \rightarrow \infty$).

These results also suggest interesting behavior for plasmonic sensors based on *N*-particle clusters, for which an individual plasmonic element is represented by an individual cluster composing the array (larger size, smaller R_k), and not a single element (smaller size, larger R_k). Thus, at equal fill fraction, analyte transport to an array of clustered plasmonic elements (*e.g.*, nanodisk heptamers) is expected to be lower than that to an array of non-clustered elements. The difference in transport rates to *N*-particle clusters (*vs.* that to a non-clustered array) will increase as the overall size of the cluster increases.

For nanostructures with fill fraction such that $f > 1$, such as an array of high aspect ratio nanoparticles, mass transport should continue to scale as $E = 1/f$, with lower rates of transport compared to a continuous gold surface. As follows, nanoplasmonic structures that are not functionalized in a orthogonal manner (having immobilized receptors along the entire sensing surface) will have a fill fraction of $f \geq 1$, and will exhibit mass transport properties that are equal to (or less than) a sensor based on a continuous gold film. This property highlights the importance of the use of orthogonal functionalization methods for nanoplasmonic biosensors.

Conclusions

In summary, we have investigated the analyte transport characteristics for a wide range of micro- and nanoplasmonic substrates, with variations of both the substrate configuration (individual elements based on microwires, nanodisks, and nanorods) as well as the substrate fill fraction. Rates of analyte transport, quantified here as the mass transport coefficient, were obtained *via* the kinetic analysis of sensorgrams taken from individual channels on each substrate. We utilized multiple analyte/receptor pairs within (and across) different substrate configurations to ensure accurate measurements of both kinetic and mass transport data. In addition to their dissimilar sensing architectures, the substrates tested herein have vastly different spectral profiles and sensitivities. However, we show that the analyte transport characteristics across all substrates follow similar characteristics, which are dependent both on the sensor fill fraction f as well as the nature of the individual plasmonic elements composing the substrate (defining R_k), and invariant to the substrate configuration or packing order (random or periodic). Rates of transport across all substrates match well to those predicted by eqn (3), proposed in a previous study,[16] of which the results herein serve as an experimental verification.

The results of this study confirm that analyte transport to nanoplasmonic biosensors can be accurately predicted using a simple analytical model. This model, given by eqn (3) in the form of a mass transfer coefficient (k_m), can be applied to nearly all affinity-based nanoplasmonic biosensors in the

current literature. Along with knowledge of the kinetic parameters related to an affinity-interaction, these predictions can be used to predict the rate of analyte capture across both diffusion- and reaction-limited conditions (*via* eqn (1)). In terms of design optimization, these predictions are especially valuable when used with other methods to predict the optical characteristics of these sensors.

Material and methods

Fabrication of sensing substrates

All plasmonic substrates consisted of gold structures on a glass chip, fabricated *via* lift-off.

Microwire. Microwire lift-off templates were fabricated *via* UV lithography, where clean glass substrates were spin-coated (Laurell WS650, 4500 rpm, 60 s) with Microposit S1805 (Dow Chemical) and soft baked on a hot plate (120 °C, 120 s). Patterns corresponding to a microwire array (6 × 11 mm^2 overall size) were written by direct write laser lithography (MicroWriter ML2, Durham Magneto Optics) using a 1 μm, 405 nm laser. The samples were then post baked on a hot plate (120 °C, 120 s) and developed (75 s, Microposit MF-319, Dow Chemical) using mild agitation.

Nanodisk. Nanodisk lift-off templates were fabricated *via* hole-mask colloidal lithography, where clean glass substrates were spin-coated (3000 rpm, 60 s) with poly-(methylmethacrylate) (PMMA, 2% solution in anisole, 950 kDa, MicroChem) and soft baked on a hot plate (120 °C, 10 min). This layer was immersed into a 0.2% solution of polydiallyldimethyl ammonium (PDDA) for 30 s, rinsed with Milli-Q water (Q-water), and gently dried with nitrogen. The substrate was then immersed in a solution of sulphonated polystyrene particles (PPs, 110 nm mean diameter, 0.2% weight, Life Technologies, Czech Republic) for a short period, rinsed with Q-water, and gently dried with nitrogen, after which a 25 nm thick gold film was deposited *via* e-beam evaporation (UHV 350, Balzers). The PPs were removed *via* stripping with tape, after which the PMMA on the bottom of each nanohole was removed with oxygen plasma (10 min).

Nanorod. Nanorod lift-off templates were fabricated *via* e-beam lithography, where clean glass substrates were subsequently spin-coated (Laurell WS650, 3000 rpm, 30 s) with two layers of PMMA having different molecular weights (495 and 950 kDa, 2% solution in anisole, MicroChem Corp.), and soft-baked on a hot plate (120 °C, 120 s), after which a conductive polymer layer (AquaSAVE, Mitsubishi Rayon) was spin-coated (2500 rpm) and soft-baked (100 °C, 120 s). Patterns corresponding to a nanorod array (randomly distributed, overall size of 2 × 1 mm^2 for each sensing channel) were exposed *via* an electron beam (Raith eLINE Plus, 20 kV), after which the AquaSAVE layer was washed off by purified water. Samples were developed for 30 s in a 3 : 1 mixture of isopropyl alcohol (IPA) : methyl isobutyl ketone (MIBK), followed by immersion in IPA for 30 s.

Metal layers were deposited on all substrates using e-beam evaporation (microwires: 1.5 nm Ti, 50 nm Au; nanodisks: 1.5 nm Ti, 30 nm Au; nanorods: 1.5 nm Cr, 30 nm Au). Lift-off was carried out *via* sonication (Elmasonic P30H) in either acetone (nanorod, nanodisk substrates) or Mr-Rem700 (microwire substrates, Dow Chemical). Sensing substrates consisting of a continuous gold film (1.5 nm Ti, 50 nm Au) were produced by evaporation of metal layers onto either the entire glass substrate (microwires, nanodisks) or onto an array of 2 × 1 mm^2 rectangles (nanorods).

Optical and microfluidic setup

We used a multi-channel laboratory SPR platform with wavelength interrogation developed at the Institute of Photonics and Electronics (Prague). Optically, the sensor is based on the Kretschmann geometry using the attenuated total reflection method, where light from a halogen lamp (Ocean Optics, HL-2000-HP-B) is sent through a collimator, dichroic polarizer, and an optical prism (BK7 glass) interfaced to the sensing substrate *via* an index matching fluid. Reflected light was collected by a custom-built spectrograph (based on a gold diffraction grating) using a CMOS camera (Basler, acA1920-155um). Normalized reflectivity spectra were obtained *via* the ratio of the dark-noise corrected reflectance intensity with either (a) the dark-noise corrected reflectance from a plain glass slide (nanorods, nanodisks), or (b) the dark-noise corrected reflectance from a sensing substrate exposed to air (microwires). The sensor output (λ_r) was taken as the position of either the reflectance dip (nanodisks, nanorods, l = 10, 100 μm microwires) or the reflectance maximum (l = 1.4 μm microwires), where λ_r corresponded to the geometrical center of the spectral feature having intensities lower than 40% of its depth. Fluidic channels are formed by sealing a series of four open faced microchannels of similar design (consisting of vinyl gaskets glued to an acrylic flow cell with machined input/output ports) to a sensing substrate. The vinyl gaskets had a thickness of H = 50 μm, where the horizontal microchannel design was slightly different across experiments (shown in detail in Fig. S2, S4 and S6†). A multichannel peristaltic pump (Ismatec, ISM931C) was used to deliver samples to each channel on the flow cell, which for microwire and nanodisk experiments used passive fluidic switching described previously (with further descriptions of the flow cells used herein).[29] The flow cell and sensing substrate were maintained at a temperature of 25 °C during all experiments.

Biosensing experiments

All biosensing experiments were conducted in a similar fashion, with only slight changes in reagents and functionalization protocols between each substrate configuration.

Reagents. We used buffers of PBS (10 mM phosphate, 2.9 mM KCL, 137 mM NaCl, pH 7.4), PBS_{NaCl} (PBS + 500 mM NaCl, pH 7.4), and $Tris_{Mg}$ (10 mM Tris-HCl, 30 mM $MgCl_2$, pH 7.4). Mercaptohexanol ($HS–(CH_2)_6–OH$) was purchased

from Sigma-Aldrich. A thiolated carboxy-terminated polyethylene glycol (ctPEG, HS–$(CH_2)_{11}$–$(EG)_6$–OCH_2–COOH) was purchased from Prochimia (Poland). The DNA and RNA oligonucleotides DNA probes PR_{wire} (DNA, 5′-5ThioMC6D-iSp18-TTA TTA TTA CGA GAC CCT GGC ACA AAC ACG TTA CAC CTC AAA GCA-3′), PR_{disk} (RNA, 5′-5ThioMC6D-iSp18-ACC UUU UAU ACA ACC GUU CUA CAC UCA AC-3′), PR_{ref} (DNA, 5′-5ThioMC6D-TTA TTA TTA TTA TGC TTT GAG GTG-3′), PR_{rod} (DNA, 5′-HS-T_{20}-3′), and the oligonucleotide targets TAR_{wire1} (DNA, 3′-GTG GAG TTT C-5′), TAR_{wire2} (DNA, 3′-GTG GAG TTT CG-5′), TAR_{disk} (RNA, 5′-5Phos-GAG GUA GUA GGU U-3′), and TAR_{rod} (DNA, 5′-A_{20}-3′) were purchased from Integrated DNA Technologies (USA). All other chemicals were of analytical grade.

Microwire and nanodisk functionalization. Before functionalization, substrates were rinsed with ethanol and Q-water, cleaned with ozone for 10 min, rinsed with ethanol and Q-water, and dried with nitrogen. Substrates were then mounted into the SPR setup. A short injection of PBS buffer (<5 min) was then followed by a 25 minute injection of 200 nM probes in PBS (measurement channels for microwire and nanodisk substrates had PR_{wire} and PR_{disk}, respectively, and reference channels for both had PR_{ref}), followed by a 5 minute injection of PBS, a 15 minute injection of ctPEG (microwires) or mercaptanol (nanodisks), a 3 minute injection of PBS_{NaCl}, and finally a sustained injection of PBS (running buffer).

Nanorod functionalization. Before functionalization, substrates were rinsed with ethanol and Q-water, dried with nitrogen, and immersed in a solution of 4 : 3 : 28 NH_3 : H_2O_2 : Q-water for 30 minutes (40 °C). Substrates were then rinsed with Q-water, dried with nitrogen, and cleaned with ozone for 10 min. Substrates were then immersed overnight in a refrigerated solution of probes (2 μM PR_{rod}) in $Tris_{Mg}$. Substrates were then rinsed with Q-water, dried with nitrogen, mounted to the SPR prism using an index matching fluid, and sealed to a flow cell. An injection of mercaptohexanol (1 M, 20 min) was followed by a 5 minute injection of PBS, a 5 minute injection of 2 mM NaOH, a 5 minute injection of PBS, and a sustained injection of $Tris_{Mg}$ (running buffer).

Experimental protocol. Before analyte injection, running buffer was pumped for a minimum of 10 minutes to obtain a stable baseline, after which target analytes at variable concentration (microwires: TAR_{wire1} and TAR_{wire2}; nanodisks: TAR_{disk}, nanorods: TAR_{rod}) were injected for a period of 10–15 minutes (association phase), followed by an injection of running buffer for at least 20 minutes (dissociation phase). After each association/dissociation cycle, substrates were regenerated with 5 mM NaOH for 2 minutes. Sensor responses were corrected for long term drift, and for microwire and nanodisk experiments, the reference channel response was subtracted from the measurement channel. All injections for each sensorgram were obtained from the same detection channel. Aside from variable flow cells and receptor/analyte pairs, other assay conditions (flow rate, microchannel height, and temperature) were constant across all experiments.

Analysis of sensorgrams

All sensorgrams were analyzed to extract bioanalytical information as follows. We assumed that analyte was captured in a 1 : 1 manner by immobilized bioreceptors, which has been successfully used in a number of studies relevant to the kinetic analysis of solid phase DNA hybridization.[30–32] Under such capture mechanism, when mass transport effects are included (*i.e.*, using a two compartment model), the time-rate sensor response can be described according to eqn (1).[18]

We used non-linear least squares optimization to extract the parameters k_1, k_2, Γ_o, and k_m from experimental sensorgrams (3–6 injections at variable c) taken from individual channels. Specifically, after providing initial estimates of $k_1 = 1 \times 10^6$ 1/M s^{-1}, $k_2 = 4 \times 10^{-4}$ 1/s, $S_\Gamma\Gamma_o = 0.45$ nm, and $k_m = 0.035$ mm s^{-1}, we searched for a minimum in the vector difference between the time-series experimental data and the solution to eqn (1). At each iteration the solution to eqn (1) was obtained *via* ode23 with relative and absolute tolerances of 10^{-6}, Jacobian values were calculated using finite differences, and the best-fit values of k_1, k_2, Γ_o, and k_m were updated. Iterations were terminated when the squared 2-norm of the residual was below 10^{-6} (<2000 iterations). The nanorod experiments did not use passive fluidic valving, thus for those sensorgrams we modified c as a function of time to account for axial dispersion *via* the results of Taylor.[33]

For each fit we allowed k_1, k_2, and k_m to be global parameters. The probe density Γ_o was set to be a local parameter for each injection, as there was a small deviation in the probe density for each injection due to the sequential nature of obtaining each sensorgram from a single channel (incomplete regeneration after each injection cycle). We observed only a small deviation in fitted values of Γ_o across all injections for each channel on each substrate (Fig. S1, S3 and S5†). In addition, we observed only a small difference in extracted values of k_1, k_2, Γ_o, and k_m when allowing Γ_o to be a global parameter across all injections for each sensorgram. Extracted parameters had little sensitivity to initial estimates, which is highlighted in Fig. S7,† where changes in the initial estimates for k_m by over 3 orders of magnitude had little to no influence on the resulting fits for k_1, k_2, Γ_o, and k_m. Similar results were obtained *via* variation of initial estimates of k_1, k_2, and Γ_o. Results from a selected set of sensorgrams matched well with results obtained *via* commercial software (BIAevaluation 4.1).

Author contributions

N. S. L., J. S., B. Š., and J. H. conceived the concept of the study. N. S. L, J. S., B. Š., and T. Š. designed the experiments. M. G., M. L. E., B. Š., and T. Š. performed the experiments. N.

S. L. analyzed the results and wrote the manuscript. J. S., B. Š., and J. H. edited the manuscript.

Conflicts of interest

There are no conflicts of interest.

Acknowledgements

The authors wish to acknowledge Petra Lebrušková for fabrication of the nanodisk substrates, and Jan Bukáček for fabrication of the smaller microwire substrates used herein. This work was supported by the Czech Science Foundation (contract #P205/12/G118, #19-02739S), and the European Union's Horizon 2020 research and innovation program (project ULTRAPLACAD, contract #633937).

References

1 A. B. Dahlin, N. J. Wittenberg, F. Höök and S.-H. Oh, *Nanophotonics*, 2013, **2**, 83–101.
2 A. R. Ferhan, J. A. Jackman, J. H. Park, N.-J. Cho and D.-H. Kim, *Adv. Drug Delivery Rev.*, 2018, **125**, 48–77.
3 G. A. Lopez, M.-C. Estevez, M. Soler and L. M. Lechuga, *Nanophotonics*, 2017, **6**, 123.
4 B. Špačková, P. Wrobel, M. Bocková and J. Homola, *Proc. IEEE*, 2016, **104**, 2380–2408.
5 J. Homola, *Chem. Rev.*, 2008, **108**, 462–493.
6 S.-W. Lee, K.-S. Lee, J. Ahn, J.-J. Lee, M.-G. Kim and Y.-B. Shin, *ACS Nano*, 2011, **5**, 897–904.
7 J. Cao, T. Sun and K. T. Grattan, *Sens. Actuators, B*, 2014, **195**, 332–351.
8 G. K. Joshi, S. Deitz-McElyea, M. Johnson, S. Mali, M. Korc and R. Sardar, *Nano Lett.*, 2014, **14**, 6955–6963.
9 M. Sarkar, M. Chamtouri, J. Moreau, M. Besbes and M. Canva, *Sens. Actuators, B*, 2014, **191**, 115–121.
10 A. B. Dahlin, *Analyst*, 2015, **140**, 4748–4759.
11 A. M. Funston, C. Novo, T. J. Davis and P. Mulvaney, *Nano Lett.*, 2009, **9**, 1651–1658.
12 A. Hajebifard and P. Berini, *Opt. Express*, 2017, **25**, 18566–18580.
13 L. Feuz, M. P. Jonsson and F. Höök, *Nano Lett.*, 2012, **12**, 873–879.
14 L. Feuz, P. Jonsson, M. P. Jonsson and F. Hook, *ACS Nano*, 2010, **4**, 2167–2177.
15 T. M. Squires, R. J. Messinger and S. R. Manalis, *Nat. Biotechnol.*, 2008, **26**, 417.
16 N. S. Lynn Jr and J. Homola, *Anal. Chem.*, 2016, **88**, 12145–12151.
17 B. Špačková, N. S. Lynn Jr, J. Slabý, H. Šípová and J. Homola, *ACS Photonics*, 2018, **5**, 1019–1025.
18 D. G. Myszka, X. He, M. Dembo, T. A. Morton and B. Goldstein, *Biophys. J.*, 1998, **75**, 583–594.
19 J. Newman, *Electroanal. Chem.*, 1973, **6**, 279–297.
20 A. S. Sangani, *J. Fluid Mech.*, 2017, **830**, 350–368.
21 P. N. Shah and E. S. Shaqfeh, *J. Fluid Mech.*, 2015, **782**, 260–299.
22 N. S. Lynn Jr and J. Homola, *Chem. – Eur. J.*, 2018, **24**, 12031–12036.
23 F. Eftekhari, C. Escobedo, J. Ferreira, X. Duan, E. M. Girotto, A. G. Brolo, R. Gordon and D. Sinton, *Anal. Chem.*, 2009, **81**, 4308–4311.
24 S. Kumar, S. Cherukulappurath, T. W. Johnson and S.-H. Oh, *Chem. Mater.*, 2014, **26**, 6523–6530.
25 A. A. Yanik, M. Huang, A. Artar, T.-Y. Chang and H. Altug, *Appl. Phys. Lett.*, 2010, **96**, 021101.
26 S. P. Han, S. Yoda, K. J. Kwak, K. Suga and M. Fujihira, *Ultramicroscopy*, 2005, **105**, 148–154.
27 F. G. De Abajo, *Rev. Mod. Phys.*, 2007, **79**, 1267.
28 M. Cevec, C. Thibaudeau and J. Plavec, *Nucleic Acids Res.*, 2010, **38**, 7814–7821.
29 T. Špringer, M. Piliarik and J. Homola, *Sens. Actuators, B*, 2010, **145**, 588–591.
30 H. Šípová and J. Homola, *Anal. Chim. Acta*, 2013, **773**, 9–23.
31 K. Tawa and W. Knoll, *Nucleic Acids Res.*, 2004, **32**, 2372–2377.
32 F. Yu, D. Yao and W. Knoll, *Nucleic Acids Res.*, 2004, **32**, e75.
33 G. I. Taylor, *Proc. R. Soc. London, Ser. A*, 1953, **219**, 186–203.

Appendix III

A route to superior performance of a nanoplasmonic biosensor: consideration of both photonic and mass transport aspects

Špačková, B., Lynn Jr., N. S., Slabý, J., Šípová, H., and Homola, J.

ACS Photonics, 2018. **5**, 1019-1025.

ACS Photonics

Article

Cite This: ACS Photonics 2018, 5, 1019−1025

A Route to Superior Performance of a Nanoplasmonic Biosensor: Consideration of Both Photonic and Mass Transport Aspects

Barbora Špačková,[†] N. Scott Lynn, Jr., Jiří Slabý, Hana Šípová, and Jiří Homola*

Institute of Photonics and Electronics of the Czech Academy of Sciences, Chaberská 57, Prague, 18251, Czech Republic

Supporting Information

ABSTRACT: Optical biosensors based on plasmonic nanostructures present a promising alternative to conventional biosensing methods and provide unmatched possibilities for miniaturization and high-throughput analysis. Previous works on the topic, however, have been overwhelmingly directed toward elucidating the optical performance of such sensors, with little emphasis on the topic of mass transport. To date, there exists no examination, experimental nor theoretical, of the bioanalytical performance of such sensors (in terms of detection limits) that simultaneously addresses both optical and mass transport aspects in a quantitative manner. In this work we present a universal model that describes the smallest concentration that can be detected by a nanoplasmonic biosensor. Accounting for both optical and mass transport aspects, this model establishes a relationship between bioanalytical performance and the biosensor's design parameters. We employ the model to optimize the performance of a nanoplasmonic DNA biosensor consisting of randomly distributed gold nanorods on a glass substrate. Through both experimental and theoretical results, we show that the proper design of a nanostructured sensing substrate is one that maximizes mass transport efficiency while preserving the quality of the optical readout. All results are compared with those obtained using a conventional SPR biosensor. We show that an optimized nanoplasmonic substrate allows for the detection of DNA at concentrations of an order of magnitude lower with respect to an SPR biosensor.

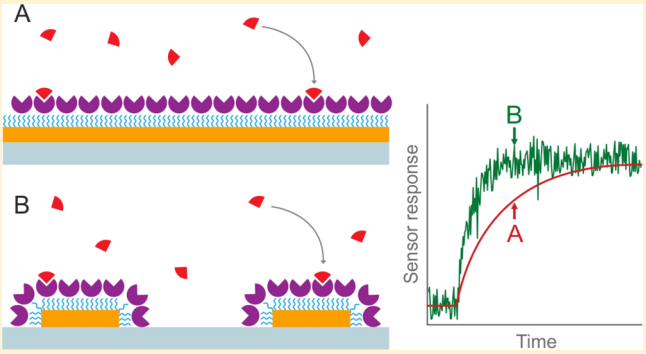

KEYWORDS: *affinity biosensing, nanoplasmonics, analyte transport, limit of detection, nanoparticle arrays, DNA detection*

Since their first applied use in the 1980s,[1,2] refractometric biosensors based on surface plasmon resonance (SPR) have undergone significant technological advances.[3] Owing to their real-time, sensitive, and label-free operation, SPR biosensors have become the gold-standard to measure the kinetic parameters of a biomolecular interaction and, thus, have been widely used in molecular biology and drug discovery.[4] In addition, these biosensors are increasingly being used for the detection of (bio)chemical species within a variety of fields, including medical diagnostics,[5,6] environmental monitoring,[7] and food safety and security.[8]

In the past two decades, however, progress in nanofabrication and characterization techniques[9,10] has led to rapid advancements in the field of nanoplasmonics: the study of nanoscale optical phenomena occurring on nanostructured surfaces.[11] These advancements have spawned an extensive amount of research into the development of nanoplasmonic biosensors.[12−16] Although nanoplasmonic biosensors offer a multitude of benefits, including sensor miniaturization and multiplexing opportunities, there has been a lack of evidence that they can exceed their conventional SPR counterparts in terms of detection performance.[17]

A significant amount of previous work has focused on the characterization and optimization of different types of nanoplasmonic sensing structures. The sensing potential of these structures is often reported strictly in terms of optical performance, for example, in terms of the so-called figure of merit: a characteristic related to the resolution of refractive index (RI) within the bulk sample solution. High values of such a figure of merit have been reported for periodic plasmonic structures supporting diffractive coupling to surface plasmons,[18−21] complex geometries supporting Fano resonances,[22−27] and plasmonic metamaterials supporting a waveguide mode.[28] However, in plasmonic affinity biosensors, the capture of analyte induces RI changes only within a confined region close to the sensing surface. Therefore, to fully evaluate the potential of a sensing structure, a performance characteristic describing the resolution of surface RI changes must be considered.[29] Several authors have presented comparative studies of the characteristics describing the response of a nanoplasmonic and conventional plasmonic sensors to surface RI changes, showing rather comparable performances.[20,30−32]

It is important to point out that the bioanalytical power of a sensor is best described by the minimum amount of analyte in a sample that can be detected. Hence, to sufficiently evaluate a

Received: November 3, 2017
Published: January 8, 2018

DOI: 10.1021/acsphotonics.7b01319
ACS Photonics 2018, 5, 1019−1025

sensor's performance, one must also consider the rate of analyte transport from the bulk volume to the sensor surface. For nanoplasmonic sensors, this topic has been subject to relatively little discussion. The selective immobilization of receptors to high-sensitivity regions (i.e., electromagnetic hot-spots on individual nanoparticles) serves to reduce the effective area where analyte capture takes place, which under diffusion-limited conditions will result in faster analyte transport.[33] This effect has been demonstrated experimentally, where passivation of nonsensitive regions both in between[34] and within[35] each hot-spot has been shown to lead to improvements in performance. Despite these early works, a quantitative elucidation of this effect has remained unknown until recently, where several groups have since examined the problem (via numerical simulation) from both a microscopic[36] and macroscopic[37] perspective.

It follows that changes to the architecture of the sensing substrate will affect both the optical and the mass transport properties of the sensor, both of which have direct influence on performance. These two properties often compete with one another in a complex manner: for example (as shown herein), decreasing the packing density of active sensing elements can lead to increased analyte transport, albeit at the expense of increased sensor noise. Hence, simple and accurate methods to optimize such sensing architectures (without the need for intensive computation) remain desirable.

In this study we propose a universal model to predict the performance of an optical affinity biosensor, which accounts for both optical and mass transport aspects. The model interrelates the design parameters of a biosensor with its detection performance and thus provides a tool for improving biosensor design with respect to the lowest detectable analyte concentration. We apply this model to a case study regarding the optimization of the performance of a DNA biosensor based on the spectroscopy of localized surface plasmons excited on gold nanoparticles (NPs). We demonstrate, both by theory and experiment, that this model allows the identification of a plasmonic nanostructure that yields a nanoplasmonic biosensor with the best performance. Furthermore, we show that the optimized nanostructure enables the detection of analyte at a concentration that is an order of magnitude lower with respect to that detectable by a conventional SPR biosensor.

UNIVERSAL MODEL FOR THE PERFORMANCE OF AN OPTICAL AFFINITY BIOSENSOR

Although there are multiple characteristics that can be used to describe the performance of a biosensor, perhaps the most analytically relevant is the smallest concentration of target molecules (analyte) that can be detected (c_{min}). Assuming that the uncertainty of the sensor response is limited only by the noise in the sensor output, c_{min} can be defined as the concentration of analyte that produces a sensor response (Y) equal to three standard deviations of the noise (σ) (Figure 1),

$$c_{min} = \frac{3\sigma}{S_c(c = c_{min})} \tag{1}$$

where $S_c = dY/dc$ is the sensitivity of the sensor response (Y) to the concentration of the analyte (c). For affinity biosensors, in which target molecules bind to receptors immobilized on the active surface, S_c can be further decomposed into $S_c = S_\Gamma\, d\Gamma/dc$, where the first term, $S_\Gamma = dY/d\Gamma$, is the sensitivity of the sensor response to the changes in the surface density of the captured analyte (Γ). The second term, $d\Gamma/dc$, represents the efficiency of analyte transport from the bulk solution to the sensor surface. Defining $\kappa = (d\Gamma/dc)_{c=cmin}$, c_{min} can be expressed as

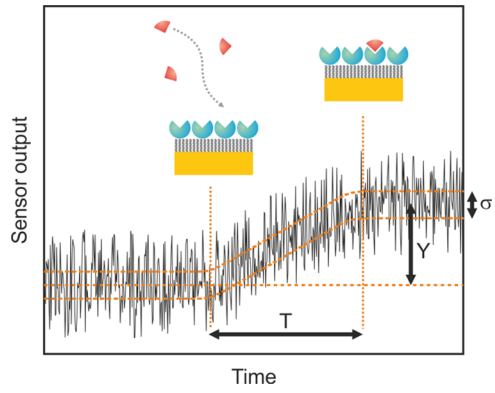

Figure 1. Schematic of the response of an affinity biosensor to the smallest concentration of target molecules that can be detected (c_{min}).

$$c_{min} = \frac{3\sigma}{S_\Gamma \kappa} \tag{2}$$

As shown here, all three terms can be theoretically predicted from parameters related to different components of the sensor. The rate of analyte transport, and thus the term κ, is described by a complex interplay of convection, diffusion, and the (reactive) capture of analyte. This process can be described in terms of the rate of analyte capture as[38]

$$\frac{d\Gamma}{dt} = \frac{k_1 c(\Gamma_o - \Gamma) - k_2\Gamma}{1 + \frac{k_1(\Gamma_0 - \Gamma)}{k_m}} \tag{3}$$

where k_1 and k_2 are the association and dissociation rate constant, respectively, Γ_0 and Γ are the surface density of the receptors and captured analyte, respectively, and k_m is the diffusion-limited mass transport coefficient, which can be calculated analytically via parameters related to both the microfluidic conditions and the architecture of the sensing substrate.[37] For low analyte concentrations ($c \to c_{min}$, $c_{min} \ll \Gamma_0/\kappa T$) the surface density of captured analyte will be negligible ($\Gamma \ll \Gamma_0$); thus κ can be expressed as

$$\kappa = \left(\frac{1}{k_1\Gamma_0 T} + \frac{1}{k_m T}\right)^{-1} \tag{4}$$

where T is the total detection time. The terms in eq 4 can be used to calculate the Damköhler number $Da = k_1\Gamma_0/k_m$, a term that relates the relative rate of analyte capture with respect to the rate of analyte transport. When $Da \gg 1$ (i.e., $k_1\Gamma_0 \gg k_m$), the capture of analyte will be *diffusion-limited*. Conversely, when $Da \ll 1$, the capture of analyte will be *reaction-limited*.[33]

In optical plasmonic biosensors, the amount of captured target molecules is determined by measuring changes in several characteristics of light (the resonant wavelength, intensity, or phase). Thus, S_Γ can be defined as $S_\Gamma = S_n M(dn/dc)h$, where M denotes the molecular weight of the analyte, (dn/dc) denotes the RI increment,[39] and S_n denotes the sensitivity to surface RI changes, defined as $S_n = d\lambda_r/n_S$, where n_S corresponds to RI within a distance from the sensor surface h.

The noise is subject to both short- and long-term variation as well as long-term drift, which originate from inherent random variation in the measured light intensity as well as general

DOI: 10.1021/acsphotonics.7b01319
ACS Photonics 2018, 5, 1019−1025

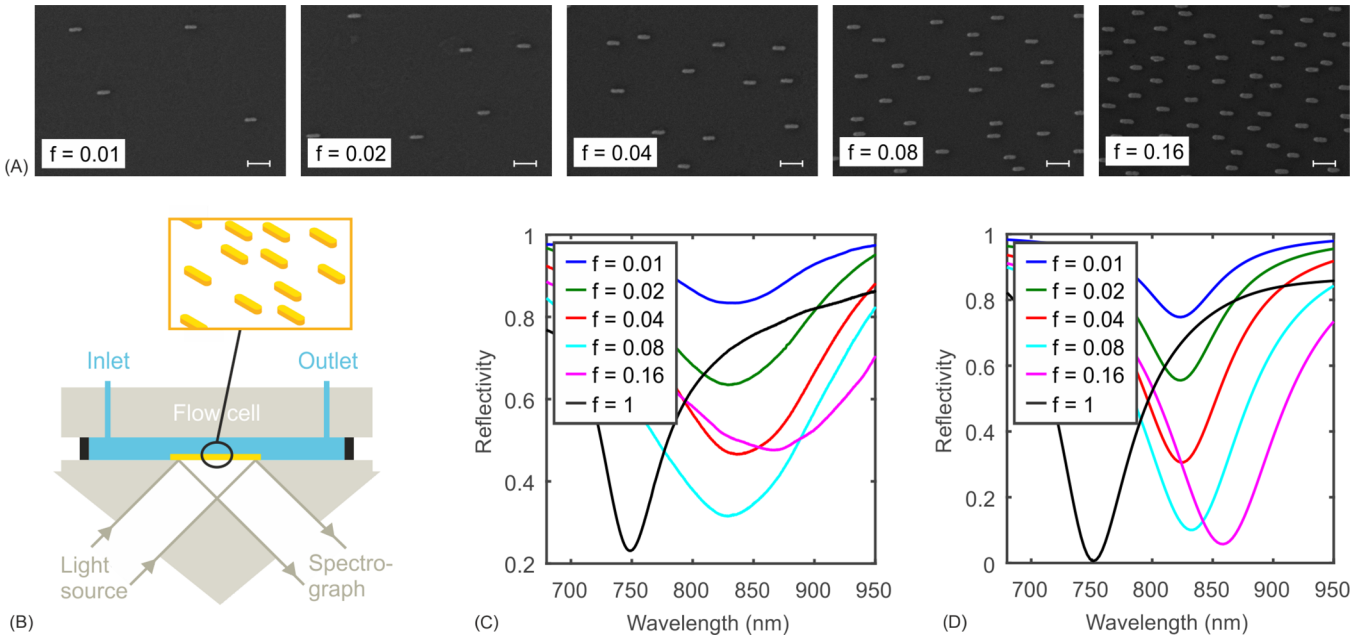

Figure 2. (A) SEM images of sensing substrates with different fill fractions. (B) Schematic of the biosensor. (C) Experimental and (D) theoretical reflectance spectra of the sensing substrates at optimal angles of incidence.

instabilities in the system. For a sensing scenario such that uncertainty of the sensor response is limited only by the noise originating in the optical system and readout electronics, σ depends on the shape of the resonant feature in the spectra as well as the properties of the light source and the detector and can be calculated via the theory proposed by Piliarik et al. (see SI for details).[40]

Both the term S_n and the shape of the resonant feature in the spectrum are highly dependent on the characteristics and spatial distribution of the plasmonic nanoparticles and can be calculated by electromagnetic simulations.[14]

PERFORMANCE OF A DNA BIOSENSOR BASED ON SPECTROSCOPY OF LOCALIZED SURFACE PLASMONS

We have applied the aforementioned model to a case study regarding the direct detection of short DNAs using a biosensor based on the spectroscopy of localized surface plasmons. The sensing substrates consisted of randomly distributed nanorods on a glass substrate having optimized dimensions (30 × 30 × 105 nm, details of optimization in the SI) and variable packing density (ρ = 1−16 NPs/μm^2) (Figure 2A). For purposes of comparison, we performed similar experiments using a continuous gold layer, the results of which pertain to a conventional SPR biosensor. The gold surfaces were functionalized by DNA probes with a complementary sequence to the target molecule. We classified each nanostructure according to its fill fraction $f = \rho A$, where ρ is the packing density and A is the surface area of a single NP exposed to the medium onto which bioreceptors are immobilized: f thus represents the ratio of the active sensing area (where collection takes place) to the entire area of the sensing region. As per this definition, $f = 1$ for a continuous gold layer. The nonspecific adsorption of a target molecule to the inter-NP area was assumed to be negligible due to a slight DNA/glass repulsive force.[41] For other analyte molecules, such as proteins, a selective functionalization to passivate the glass surface would have to be utilized.[34] The sensing substrates were mounted to the flow-cell and illuminated through the prism in the ATR configuration (Figure 2B) at an optimized angle of incidence. For sensing substrates consisting of nanorods the light was polarized parallel to the incident plane (TE polarization); for sensing substrates consisting of a continuous gold layer the light was polarized perpendicular to the incident plane (TM polarization).

Figure 2C shows collected experimental reflectance spectra along with those obtained from theory (details in the SI). It can be seen that the experimental positions of the minima correspond very well with theory; however, they are shallower and wider due to the nonuniform distribution of NP sizes used in experiment.

A sample containing target DNA was injected into the flow cell for 10 min, during which the sensor output (position of the spectral minimum λ_r) was recorded over time. A total of 220 injections were performed across all sensing substrates. Figure 3 shows selected sensorgrams related to the injection of target DNA at variable concentration (20 pM to 20 nM). It can be seen that whereas the sensor response ($\Delta\lambda_r$) to the highest concentration (20 nM) is comparable across all of the sensing substrates, the sensor response to lower concentrations increases with decreasing f. On the other hand, the sensor output from sensing substrates with lower f suffers from higher noise. Figure 4 plots the average binding rate ($d\lambda_r/dt$, measured just after injection) across all substrates as a function of concentration (2−8 injections per substrate per concentration). The solid lines were obtained via linear regression (fit to $d\lambda_r/dt = cS_c(c \to 0)/T$). The extracted values of $S_c(c \to 0)$ are shown in the inset of Figure 4. The two contributions to sensitivity, S_Γ and κ, were determined via $S_\Gamma = \Delta\lambda_r^{eq}/\Gamma^{eq}$, and $\kappa = S_c(c \to 0)/S_\Gamma$, where $\Delta\lambda_r^{eq}$ and Γ^{eq} are the resonant wavelength shift and the surface density of the formed complexes after reaching an equilibrium state (Figure 3A, 20 nM). The receptor density $\Gamma^{eq} \approx \Gamma_0 = 3.9 \times 10^{-14}$ mol·mm^{-2} was determined from SPR measurements (details in the SI). Values of c_{min} were then determined using eq 1, where σ was measured as the standard

DOI: 10.1021/acsphotonics.7b01319
ACS Photonics 2018, 5, 1019−1025

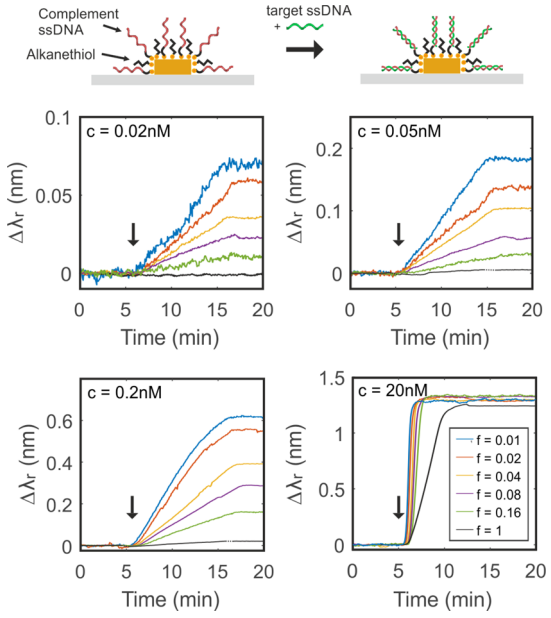

Figure 3. Experimental binding curves corresponding to different concentrations of DNA in solution for sensing substrates with varying fill fraction.

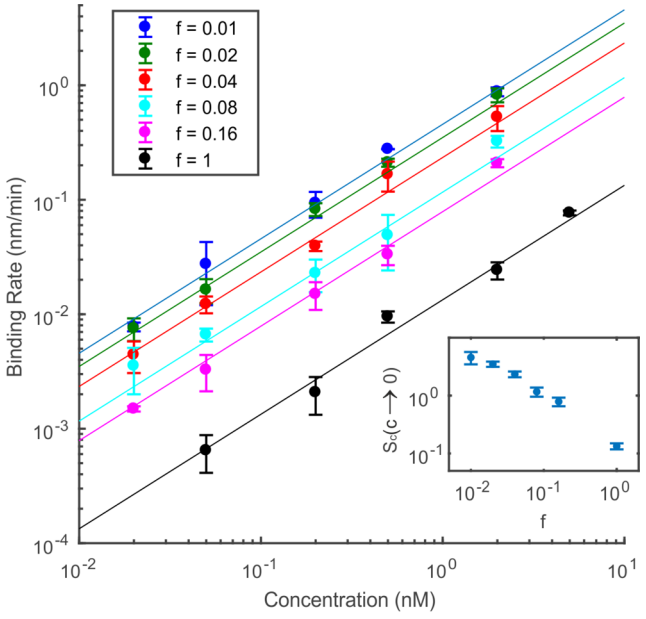

Figure 4. Calibration curves corresponding to the different fill fraction of the sensing structure. (Inset) Dependency of $S_c(c \to 0)$ on the fill fraction.

deviation of the sensor output over a time period of 10 min prior to detection (in the running buffer, three independent measurements for each sensing substrate).

Figure 5 summarizes all the relevant performance characteristics determined from experiment; these data are compared to those taken from theory (see SI for calculation details). According to theoretical calculation of the noise, σ scales as $\sigma \propto \sqrt{w/d}$ where w is the full-width-at-half-maximum and d is the contrast (depth) of the resonance dip. According to the theory pertinent to calculation of the reflectance from random arrays of NPs, w is only marginally dependent on the fill fraction, whereas at low fill fraction d scales as $d \propto f$, and at high fill fraction d asymptotically approaches a maximum. Therefore, at low fill fraction σ scales as $\sigma \propto f^{-1}$, and at high fill fraction σ asymptotically approaches a minimum (Figure 5A). On the contrary, S_Γ is only marginally dependent on fill fraction (Figure 5B).

According to the theoretical calculation pertinent to the analyte transport, κ scales as $\kappa \propto f^{-1}$ (indicative of diffusion-limited conditions) at high fill fraction, whereby at low fill fraction κ asymptotically approaches a constant value of $\kappa = k_1\Gamma_0$ (indicative of reaction-limited conditions) (Figure 5C).

According to eq 2, the dependency of c_{min} on fill fraction stems from the interplay between σ, S_Γ, and κ. For our sensing scenario, the best value of c_{min} = 0.7 pM corresponds to the sensing substrate with optimal fill fraction f = 0.04 (corresponding to packing density ρ = 4 NP/μm^2) (Figure 5D). The performance of the more sparse arrays suffers due to increases in noise; the performance of the more dense arrays suffers due to decreases of analyte transport efficiency (the system is diffusion-limited).

It is important to note that the most favorable values of S_Γ and σ taken from arrays of NPs are comparable to those taken from a continuous gold layer, which corresponds with conclusions reported by other authors.[30−32] Conversely, favorable values of c_{min} are about an order of magnitude lower, which for these data is a direct result of significantly improved analyte transport.

All of the experimental data in Figure 5 are in excellent agreement with theory. The differences in predictions of c_{min} with respect to experimental values can be attributed mainly to the differences in the prediction of σ; however, data from both theory and experiment can be seen to scale similarly. The roots of this difference can be attributed to the following: (I) for theoretical calculations we considered only high-frequency noise originating in both the optical system and readout electronics, whereas experimental values of σ also included long-term noises and drifts, both originating in general instabilities of the system; and (II) the high-frequency noise is dependent on the shape of the reflectance dip, which was wider and shallower compared to theory (Figure 2C,D) as a result of nonuniform distribution of NP sizes used in experiment. In addition, the extreme broadening seen in the most dense arrays (f = 0.16) can be attributed to near-field interactions between neighboring NPs.

CONCLUDING REMARKS

We have presented a universal model to predict the smallest concentration of target molecules that can be detected by an optical affinity biosensor. The model combines all the relevant performance characteristics of a biosensor (the sensitivity to the changes in the surface density of the captured analyte, baseline noise, and mass transport efficiency), it provides a straightforward method to quantify them, and it shows that the ultimate performance of a biosensors is determined by the interplay between them. Due to the general definition of the relevant aspects, the model can be applied to a wide variety of optical platforms, nanoplasmonic sensing structures, and biodetection assays as an optimization tool to find the best biosensor design.

We have employed this model to determine the optimal performance of a DNA biosensor based on spectroscopy of localized surface plasmons excited on random arrays of gold NPs. We have shown, in both theory and experiment, that a properly designed sensing substrate can offer significant increases in detection performance when compared to a

DOI: 10.1021/acsphotonics.7b01319
ACS Photonics 2018, 5, 1019−1025

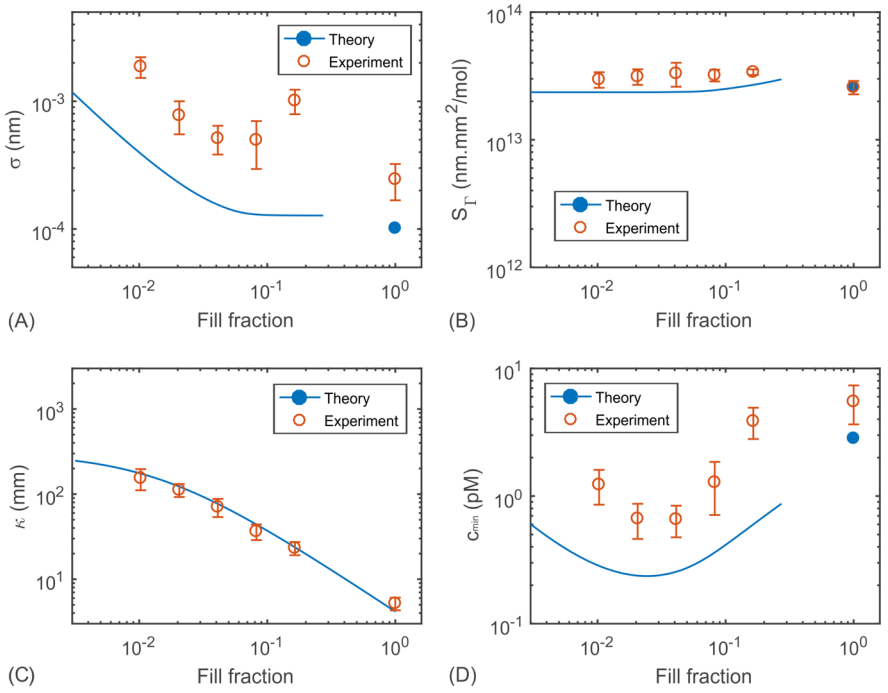

Figure 5. Comparison of the theoretical model with the experiment, showing the dependency on fill fraction of the sensing structures of (A) noise, σ, (B) sensitivity to the changes in the surface density of the captured analyte, S_Γ, (C) mass transport efficiency, κ, and (D) the smallest concentration of target molecules that can be detected by a biosensor, c_{min}.

conventional SPR biosensor (here shown as a decrease in the detection limit of about an order of magnitute). To the best of our knowledge, such an improvement in the performance of a nanoplasmonic biosensor—stemming from a model that considers both photonic and transport aspects—is the first of its kind. The improvement shown herein is primarily attributed to a reduction of the active sensing area (by decreasing the surface density of the plasmonic NPs) while preserving the quality of the optical readout (by the excitation of the localized resonance in ATR configuration[42]). Such reduction of the sensitive area (i.e., the fill fraction) helps to reduce effects stemming from diffusion-limited conditions and leads to increases in mass transport. On the contrary, a reduction of the sensitive area also leads to increases in the sensor output noise, a result of the decrease of the contrast of the characteristic spectral dip.

It should be noted, however, that these results (i.e., the specific level of sensing improvement, along with the responsible mechanism) are pertinent to the experimental conditions used herein and might not be applicable to other experimental systems. We remind the reader that this topic is inherently complex, where an optimal nanoplasmonic architecture will depend on many factors that remained constant within this study, including (i) the overall size of the readout area, (ii) the microfluidic conditions (e.g., size of flow cell, flow rate), (iii) the properties of the analyte and receptor (e.g., sizes, kinetic parameters, surface density of receptors), (iv) the arrangement of the optical platform, and finally (v) properties of the light source and readout electronics. A full examination of these effects remains outside the scope of what can be discussed here. Nevertheless, the results shown herein demonstrate that both optical *and* mass transport aspects have to be considered for the proper design/analysis of a nanoplasmonic sensor.

MATERIALS AND METHODS

Fabrication of the Sensing Substrates. Arrays of gold nanorods were fabricated using electron beam lithography as follows. Glass substrates were cleaned with acetone, dried, subjected to ozone for 10 min (UVO-Cleaner 42-220, Jelight Company Inc.), rinsed subsequently with ethanol and purified water (Milli-Q, EMD Millipore), and dried. Two layers of poly(methyl methacrylate) (PMMA) with different molecular weights (495 and 950 kDa, 2% solution in anisole, MicroChem Corp.) were spin-coated (Laurell WS650, 3000 rpm for 30 s for both layers) and soft-baked on a hot plate (120 °C for 120 s for both layers). A conductive polymer layer (AquaSAVE, Mitsubishi Rayon) was spin-coated on the top (2500 rpm) and soft-baked at 100 °C for 120 s. Patterns corresponding to randomly distributed nanorod arrays with an overall size of 2 × 1 mm^2 were exposed via an electron beam (Raith eLINE Plus, 20 kV), after which the AquaSAVE layer was washed off by purified water. Samples were developed for 30 s in a 3:1 mixture of isopropyl alcohol (IPA) and methyl isobutyl ketone (MIBK) followed by immersing in a stopper (IPA) for 30 s. Metal layers (1.5 nm of Cr and 30 nm of Au) were then deposited using an ultra-high-vacuum thermal evaporator (UHV 350, Balzers), followed by washing out the sacrificial layer in acetone (45 °C) in an ultrasonic bath (Elmasonic P30H). The sensing substrates for conventional SPR measurements were produced by evaporation of metal layers (1.5 nm of Cr and 50 nm of Au, 2 × 1 mm^2 overall size) on glass slides.

Surface Biofunctionalization and Assay. Both the nanostructured substrates and the continuous gold layer were functionalized via the attachement of thiol-derivatized DNA probes (SdT_{20}, SH-5′-$(dT)_{20}$-3′; Integrated DNA Technologies, USA) using chemisorption. Prior to functionalization, the substrates were rinsed with ethanol and Milli-Q water, dried with a stream of nitrogen, and imersed in cleaning solution (NH3:H_2O_2:milli Q water in the ratio 4:3:28) for 30 min at 40

DOI: 10.1021/acsphotonics.7b01319
ACS Photonics 2018, 5, 1019−1025

°C. They were then rinsed with water, dried, and cleaned with UV-ozone cleaner for 5 min. The substrates were then immersed in a 2 μM solution of thiolated DNA probes in $Tris_{Mg}$ buffer (10 mM Tris-HCl, 30 mM $MgCl_2$, pH 7.4 at 25 °C) and incubated in a refrigerator overnight in a humid atmosphere. Preceding measurements, substrates were rinsed with water, dried with a stream of nitrogen, and mounted to the ATR setup. A 1 M solution of blocking alkanethiol solution (mercaptohexanol; Sigma-Aldrich, Czech Republic) in phosphate-buffered saline (PBS) was injected into the flow cell at a flow rate of 20 μL min^{-1} for 20 min, which was followed by a 5 min injection of PBS buffer, a 5 min injection of 2 mM NaOH, and finally a 5 min injection of PBS buffer. Preceding the detection step, a running buffer ($Tris_{Mg}$) was introduced to generate a baseline. Finally, a solution of target DNA (5′-$(dA)_{20}$-3′, M_W = 6281.21 Da, variable c) in the running buffer was injected for 10 min (20 μL min^{-1}), after which the sensor surface was flushed with buffer for 5 min.

Optical Setup for Real-Time Monitoring of Surface Processes. In this work we used a four-channel laboratory SPR sensor platform that was developed at the Institute of Photonics and Electronics (Prague). The sensor is based on the Kretschmann geometry of the attenuated total reflection method and spectral modulation. In this sensor, light from a halogen lamp (Ocean Optics, HL-2000-HP-B) passes through a collimator, dichroic polarizer, and a BK7 glass prism interfaced with a sensing chip using index matching fluid. A flow cell with four separate flow chambers was interfaced with the chip. A multichannel peristaltic pump was used to deliver liquid samples to the flow cell. All experiments were performed at a temperature of 25 °C. The reflected light was collected by a custom-built spectrograph composed of a gold-coated diffraction grating, imaging optics, and a CMOS camera (Basler, acA1920-155um). The reflectivity spectra of the plasmonic structures were obtained by normalizing the light reflected from the sensing structures by the light reflected from the plain glass slide (after subtraction of the dark signal). The sensor output (position of the reflectance dip, λ_r) was determined using the centroid method: λ_r corresponds to the geometrical center of the portion of the spectral dip with intensities lower than half of its depth. The sensor response to different concentrations of the target molecule was referenced to the sensor response obtained from a reference channel containing running buffer. The binding curves were corrected for a constant drift, which was determined as a mean value of the slope of the binding curve 5 min before and 5 min after detection.

■ ASSOCIATED CONTENT

Supporting Information

The Supporting Information is available free of charge on the ACS Publications website at DOI: 10.1021/acsphotonics.7b01319.

Details of the calculation methods as well as the optimization of the NP shape and the angle of incidence (PDF)

■ AUTHOR INFORMATION

Corresponding Author

*E-mail: homola@ufe.cz. Phone: +420 266 773 404. Fax: +420 284 681 534.

ORCID

Barbora Špačková: 0000-0002-8442-5641
N. Scott Lynn Jr.: 0000-0002-8649-9214
Hana Šípová: 0000-0002-5383-9120

Present Address

†B.S.: Department Physics, Chalmers University of Technology, 412 96 Göteborg, Sweden

Notes

The authors declare no competing financial interest.

■ ACKNOWLEDGMENTS

This work was supported by the Praemium Academiae of the Czech Academy of Sciences, the Czech Science Foundation (contract #15-06785S), and European Union's Horizon 2020 research and innovation program (project ULTRAPLACAD, contract #633937).

■ REFERENCES

(1) Gordon, J.; Ernst, S. Surface Plasmons as a Probe of the Electrochemical Interface. *Surf. Sci.* **1980**, *101*, 499−506.
(2) Liedberg, B.; Nylander, C.; Lunström, I. Surface Plasmon Resonance for Gas Detection and Biosensing. *Sens. Actuators* **1983**, *4*, 299−304.
(3) Homola, J. Surface Plasmon Resonance Sensors for Detection of Chemical and Biological Species. *Chem. Rev.* **2008**, *108*, 462−493.
(4) Kaminski, T. P.; Gunnarsson, A.; Geschwindner, S. Harnessing the Versatility of Optical Biosensors for Target-Based Small-Molecule Drug Discovery. *ACS Sensors* **2017**, *2*, 10−15.
(5) Masson, J.-F. Surface Plasmon Resonance Clinical Biosensors for Medical Diagnostics. *ACS Sensors* **2017**, *2*, 16−30.
(6) Johnson, S.; Krauss, T. F. Label-Free Affinity Biosensor Arrays: Novel Technology for Molecular Diagnostics. *Expert Rev. Med. Devices* **2017**, *14*, 177−179.
(7) Chocarro-Ruiz, B.; Fernández-Gavela, A.; Herranz, S.; Lechuga, L. M. Nanophotonic Label-Free Biosensors for Environmental Monitoring. *Curr. Opin. Biotechnol.* **2017**, *45*, 175−183.
(8) Gaudin, V. Advances in Biosensor Development for the Screening of Antibiotic Residues in Food Products of Animal Origin−A Comprehensive Review. *Biosens. Bioelectron.* **2016**, *90*, 363−377.
(9) Biswas, A.; Bayer, I. S.; Biris, A. S.; Wang, T.; Dervishi, E.; Faupel, F. Advances in Top-Down and Bottom-Up Surface Nanofabrication: Techniques, Applications & Future Prospects. *Adv. Colloid Interface Sci.* **2012**, *170*, 2−27.
(10) Jones, M. R.; Osberg, K. D.; Macfarlane, R. J.; Langille, M. R.; Mirkin, C. A. Templated Techniques for the Synthesis and Assembly of Plasmonic Nanostructures. *Chem. Rev.* **2011**, *111*, 3736−3827.
(11) Stockman, M. I. Nanoplasmonics: Past, Present, and Glimpse into Future. *Opt. Express* **2011**, *19*, 22029−22106.
(12) Lopez, G. A.; Estevez, M.; Soler, M.; Lechuga, L. M. Recent Advances in Nanoplasmonic Biosensors: Applications and Lab-on-a-Chip Integration. *Nanophotonics* **2017**, *6*, 123−136.
(13) Jackman, J. A.; Ferhan, A. R.; Cho, N.-J. Nanoplasmonic Sensors for Biointerfacial Science. *Chem. Soc. Rev.* **2017**,.46361510.1039/C6CS00494F
(14) Špačková, B.; Wrobel, P.; Bocková, M.; Homola, J. Optical Biosensors Based on Plasmonic Nanostructures: A Review. *Proc. IEEE* **2016**, *104*, 2380−2408.
(15) Estevez, M.-C.; Otte, M. A.; Sepulveda, B.; Lechuga, L. M. Trends and Challenges of Refractometric Nanoplasmonic Biosensors: A Review. *Anal. Chim. Acta* **2014**, *806*, 55−73.
(16) Dahlin, A. B.; Wittenberg, N. J.; Höök, F.; Oh, S.-H. Promises and Challenges of Nanoplasmonic Devices for Refractometric Biosensing. *Nanophotonics* **2013**, *2*, 83−101.
(17) Dahlin, A. B. Sensing Applications Based on Plasmonic Nanopores: The Hole Story. *Analyst* **2015**, *140*, 4748−4759.

(18) Offermans, P.; Schaafsma, M. C.; Rodriguez, S. R. K.; Zhang, Y.; Crego-Calama, M.; Brongersma, S. H.; Gmez Rivas, J. Universal Scaling of the Figure of Merit of Plasmonic Sensors. *ACS Nano* **2011**, *5*, 5151−5157.
(19) Yanik, A. A.; Cetin, A. E.; Huang, M.; Artar, A.; Mousavi, S. H.; Khanikaev, A.; Connor, J. H.; Shvets, G.; Altug, H. Seeing Protein Monolayers with Naked Eye through Plasmonic Fano Resonances. *Proc. Natl. Acad. Sci. U. S. A.* **2011**, *108*, 11784−11789.
(20) Špačková, B.; Homola, J. Sensing Properties of Lattice Resonances of 2D Metal Nanoparticle Arrays: An Analytical Model. *Opt. Express* **2013**, *21*, 27490−27502.
(21) Cetin, A. E.; Yanik, A. A.; Yilmaz, C.; Somu, S.; Busnaina, A.; Altug, H. Monopole Antenna Arrays for Optical Trapping, Spectroscopy, and Sensing. *Appl. Phys. Lett.* **2011**, *98*, 111110.
(22) Luk'yanchuk, B.; Zheludev, N. I.; Maier, S. A.; Halas, N. J.; Nordlander, P.; Giessen, H.; Chong, C. T. The Fano Resonance in Plasmonic Nanostructures and Metamaterials. *Nat. Mater.* **2010**, *9*, 707−715.
(23) Gallinet, B.; Martin, O. J. F. Refractive Index Sensing with Subradiant Modes: A Framework To Reduce Losses in Plasmonic Nanostructures. *ACS Nano* **2013**, *7*, 6978−6987.
(24) Zhan, Y.; Lei, D. Y.; Li, X.; Maier, S. A. Plasmonic Fano Resonances in Nanohole Quadrumers for Ultra-Sensitive Refractive Index Sensing. *Nanoscale* **2014**, *6*, 4705−4715.
(25) Kubo, W.; Fujikawa, S. Au Double Nanopillars with Nanogap for Plasmonic Sensor. *Nano Lett.* **2011**, *11*, 8−15.
(26) Lassiter, J. B.; Sobhani, H.; Fan, J. A.; Kundu, J.; Capasso, F.; Nordlander, P.; Halas, N. J. Fano Resonances in Plasmonic Nanoclusters: Geometrical and Chemical Tunability. *Nano Lett.* **2010**, *10*, 3184−3189.
(27) Zhang, S.; Bao, K.; Halas, N. J.; Xu, H.; Nordlander, P. Substrate-Induced Fano Resonances of a Plasmonic Nanocube: A Route to Increased-Sensitivity Localized Surface Plasmon Resonance Sensors Revealed. *Nano Lett.* **2011**, *11*, 1657−1663.
(28) Kabashin, A. V.; Evans, P.; Pastkovsky, S.; Hendren, W.; Wurtz, G. A.; Atkinson, R.; Pollard, R.; Podolskiy, V. A.; Zayats, A. V. Plasmonic Nanorod Metamaterials for Biosensing. *Nat. Mater.* **2009**, *8*, 867−871.
(29) Li, J.; Ye, J.; Chen, C.; Li, Y.; Verellen, N.; Moshchalkov, V. V.; Lagae, L.; Van Dorpe, P. Revisiting the Surface Sensitivity of Nanoplasmonic. *ACS Photonics* **2015**, *2*, 425−431.
(30) Otte, M. A.; Seplveda, B.; Ni, W.; Juste, J. P.; Liz-Marzn, L. M.; Lechuga, L. M. Identification of the Optimal Spectral Region for Plasmonic and Nanoplasmonic Sensing. *ACS Nano* **2010**, *4*, 349−357.
(31) Svedendahl, M.; Chen, S.; Dmitriev, A.; Käll, M. Refractometric Sensing Using Propagating versus Localized Surface Plasmons: A Direct Comparison. *Nano Lett.* **2009**, *9*, 4428−4433.
(32) Kvasnička, P.; Homola, J. Optical Sensors Based on Spectroscopy of Localized Surface Plasmons on Metallic Nanoparticles: Sensitivity Considerations. *Biointerphases* **2008**, *3*, FD4−FD11.
(33) Squires, T. M.; Messinger, R. J.; Manalis, S. R. Making It Stick: Convection, Reaction and Diffusion in Surface-Based Biosensors. *Nat. Biotechnol.* **2008**, *26*, 417−426.
(34) Feuz, L.; Jonsson, P.; Jonsson, M. P.; Höök, F. Improving the Limit Of Detection Of Nanoscale Sensors by Directed Binding to High-Sensitivity Areas. *ACS Nano* **2010**, *4*, 2167−2177.
(35) Feuz, L.; Jonsson, M. P.; Höök, F. Material-Selective Surface Chemistry for Nanoplasmonic Sensors: Optimizing Sensitivity and Controlling binding to Local Hot Spots. *Nano Lett.* **2012**, *12*, 873−879.
(36) Shah, P. N.; Shaqfeh, E. S. Heat/mass Transport in Shear Flow Over a Heterogeneous Surface With First-Order Surface-Reactive Domains. *J. Fluid Mech.* **2015**, *782*, 260−299.
(37) Lynn, N. S., Jr; Homola, J. (Bio)Sensing Using Nanoparticle Arrays: On the Effect of Analyte Transport on Sensitivity. *Anal. Chem.* **2016**, *88*, 12145−12151.
(38) Myszka, D. G.; He, X.; Dembo, M.; Morton, T. A.; Goldstein, B. Extending the Range of Rate Constants Available from BIACORE: Interpreting Mass Transport-Influenced Binding Data. *Biophys. J.* **1998**, *75*, 583−594.
(39) Tumolo, T.; Angnes, L.; Baptista, M. S. Determination of the Refractive Index Increment (dn/dc) of Molecule and Macromolecule Solutions by Surface Plasmon Resonance. *Anal. Biochem.* **2004**, *333*, 273−279.
(40) Piliarik, M.; Homola, J. Surface Plasmon Resonance (SPR) Sensors: Approaching Their Limits? *Opt. Express* **2009**, *17*, 16505−16517.
(41) Han, S. P.; Yoda, S.; Kwak, K. J.; Suga, K.; Fujihira, M. Interpretation of DNA Adsorption on Silanized Surfaces by Measuring Interaction Forces at Various pHs Using Atomic Force Microscopy. *Ultramicroscopy* **2005**, *105*, 148−154.
(42) Otte, M. A.; Estvez, M.-C.; Regatos, D.; Lechuga, L. M.; Seplveda, B. Guiding Light in Monolayers of Sparse and Random Plasmonic Meta-Atoms. *ACS Nano* **2011**, *5*, 9179−9186.

DOI: 10.1021/acsphotonics.7b01319
ACS Photonics 2018, 5, 1019−1025

Appendix IV

Plasmonic Biosensor Based On A Gold Nanostripe Array For Detection Of MicroRNA Related To Myelodysplastic Syndromes

Slabý, J., Bocková, M., and Homola, J.

Sensors and Actuators B: Chemical, 2021. **347**,130629.

Sensors & Actuators: B. Chemical 347 (2021) 130629

Contents lists available at ScienceDirect

Sensors and Actuators: B. Chemical

journal homepage: www.elsevier.com/locate/snb

Plasmonic biosensor based on a gold nanostripe array for detection of microRNA related to myelodysplastic syndromes

Jiří Slabý, Markéta Bocková, Jiří Homola *

Institute of Photonics and Electronics of the CAS, Chaberská 1014/57, 182 51 Prague, Czech Republic

ARTICLE INFO

Keywords:
Plasmonic biosensor
Metal nanostripe array
Surface plasmon resonance
MiRNA detection

ABSTRACT

We present a new optical biosensor based on surface plasmons excited on an array of gold nanostripes via attenuated total reflection. We investigate performance of the biosensor using a theoretical model that considers both optical and mass transport aspects. The analysis of optical aspects employs two different approaches: a complex model incorporating optical characteristics of the nanostructure as well as the noise characteristics of the optical readout system and a simple model based solely on the figure of merit of the nanostructure. The theoretical analysis suggests that the optimized biosensor is able to detect molecular analytes at concentrations lower by a factor of ~ 10 than conventional surface plasmon resonance biosensors. In order to validate the theoretical model, we characterize the gold nanostripe arrays of different designs in model refractometric and biosensing experiments. We show that the nanoplasmonic sensor exhibits refractive index sensitivity of 1989 nm/RIU and refractive index resolution down to 3.6×10^{-7}RIU. In addition, we use the nanoplasmonic biosensor for the detection of a microRNA biomarker of myelodysplastic syndromes (miRNA-125b) and demonstrate that the biosensor can detect miRNA-125b at concentrations down to ~ 17 pM.

1. Introduction

In the last three decades, optical biosensors based on surface plasmons (SPs), commonly referred to as surface plasmon resonance (SPR) biosensors, have matured into a powerful technology with a broad variety of biophysical applications. SPR biosensors have become a leading technology for the real-time label-free investigation of biomolecular interactions [1]. Moreover, they have been increasingly researched for the development of analytical devices for medical diagnostics, environmental monitoring, food safety, and security [2–4]. Over the last decade, advances in nanoscience and nanotechnology have stimulated the research of plasmonic nanostructures and their use in biosensing devices [5–8]. First nanoplasmonic biosensors were based on localized SPs excited on metal nanoparticles on a dielectric substrate [9]. Various nanoparticle shapes have been investigated, such as nanorods, nanorings, nanoprisms, nanostars, or bipyramids [10–13]. In addition, nanostructures based on ordered arrays of metal nanoparticles have been investigated and shown to allow for the excitation of special plasmonic modes (e.g. Fano resonances [14], lattice resonances [15]), that can offer improved figures of merit (and thus potentially improved analytical performance) [16,17]. Metal stripes and their arrays have also been investigated and shown to support a variety of SPs propagating along the stripes or in the direction perpendicular to the stripes. Sarkar et al. conducted a theoretical study of gold stripes with a low height/width ratio and evaluated the potential of SP modes supported by such stripes for sensing [18]. Berini's group investigated long-range SPs propagating on a low height/width ratio stripe [19], demonstrating that these SP modes can be used to detect red blood cells [20], bacteria in urine [21], or human cardiac troponin [22]. Chowdhury et al. investigated an array of low height/width stripes of nanoscopic dimensions and showed that they can support Fano resonances originating from the coupling between localized SPs and the Rayleigh anomaly [23]. A similar plasmonic nanostructure was realized and investigated experimentally by Ronur Praful et al. [24]. While nanostructures provide multitude of plasmonic modes of different characteristics (e.g. electromagnetic field distribution), they also provide specific (and potentially diverse) conditions for the transport of target molecules to receptors immobilized in the sensing areas of plasmonic nanostructures [25–28]. Therefore, in order to develop nanoplasmonic biosensors with the best analytical performance, both optical and mass transport aspects need to be considered [29].

In this paper, we propose a novel type of biosensor based on

* Corresponding author.
E-mail address: homola@ufe.cz (J. Homola).

https://doi.org/10.1016/j.snb.2021.130629
Received 3 May 2021; Received in revised form 23 July 2021; Accepted 17 August 2021
Available online 20 August 2021

propagating plasmonic modes excited on an array of tall gold nanostripes via attenuated total reflection. We investigate both the optical and analyte transport contributions to the performance of the new biosensor and demonstrate the ability of the biosensor to detect low levels of miRNA-125b.

2. Materials and methods

2.1. Fabrication of nanostripe arrays

Arrays of gold nanostripes were fabricated on BK7 glass substrates using the electron-beam lithography and lift-off process. Initially, a glass substrate (microscope slide) was cleaned with acetone and dried with a stream of nitrogen. Then the substrate was exposed to ozone for 10 min (UVO, Jelight), rinsed with ethanol, and Q-water (Milli-Q, Millipore); the ozone cleaning procedure was repeated twice. A resist layer of poly (methyl methacrylate) in anisole (PMMA A4 950 kDa, Microchem) was spin-coated (60 s at 1000 rpm, Laurell WS650) on the substrate and soft-baked at 120 °C for 120 s. Then, a conductive polymer layer of Aqua-SAVE (Mitsubishi Rayon) was spin-coated (30 s at 2500 rpm) and soft-baked at 100 °C for 120 s. The nanostripe array pattern (overall size 1.6 ×2.6 mm^2, 4 arrays per substrate) was produced using electron-beam lithography (eLINE Plus, Raith) at 10 kV. The conductive polymer layer was removed by rinsing with Q-water. The pattern was developed in a mixture of methyl-isobutyl-ketone and isopropanol (1:3) for 120 s at 22 °C followed with a stopper (isopropanol) for 30 s at 22 °C. After drying the surface with a flow of nitrogen, a short oxygen plasma treatment (30% generator power for 20 s, Nano, Diener) was applied to remove the PMMA residues. Metal layers (5 nm thick adhesion layer of titanium followed with a 200 nm thick layer of gold) were deposited using an e-beam deposition in a vacuum (PLS 570, Pfeiffer Vacuum). The lift-off of the sacrificial layers was carried out in an acetone bath in an ultrasonic cleaner at 50 °C. Then, the resulting sensor chip was cleaned with ethanol and Q-water. The SPR chips used in reference experiments were prepared by coating the glass substrate with a 1.5 nm thick adhesion layer of titanium and a 48 nm thick layer of gold.

2.2. Optical platform

Spectroscopy of SPs on nanostripe arrays was performed using an optical platform based on the attenuated total reflection and prism coupling [29]. In this optical platform, light from a halogen lamp (HL-2000-HP-N, OceanOptics) was collimated and polarized parallel to the plane of incidence (TM polarization) and made incident onto a substrate with a nanostripe array (sensor chip) through a prism made of BK7 glass. The chip was attached to the prism in such a way that the nanostripes were parallel with the plane of incidence. The reflected light was projected onto a grating that dispersed the light over a camera (acA1920–155 μm, Basler). The sensor chip was interfaced with a 4-channel acrylic microfluidic flow cell that provided flow in the direction perpendicular to that of nanostripes. Dispersionless microfluidics [30] and a multichannel peristaltic pump (IPC 8 ISM 931 8, Ismatec) were employed to deliver liquid samples to the flow cell. The images collected by the camera were processed as follows. Firstly, approximately 1000 images (equal to the total acquisition time of 3 s) were collected and averaged. Secondly, 12 lines of pixels corresponding to a microfluidic channel were binned to create a raw spectrum from which a dark spectrum (obtained under no illumination) was subtracted and the resulting spectrum was divided by a spectrum taken when the microfluidic flow cell was filled with air. This normalized spectrum was fitted with a polynomial curve to obtain the spectral position of the plasmonic dip (resonance wavelength). The same optical platform and data processing were employed in comparative experiments using SPR chips with a continuous gold layer.

2.3. Chip functionalization

The nanostripe array chips were functionalized with thiolated DNA probes using the procedure described below. Prior to the functionalization, the chips were cleaned with ozone for 10 min, rinsed with ethanol, Q-water, and dried with nitrogen. The chips were then immersed in a 2 μM solution of thiolated HS-probes (HS - 5′-CCC CCT CAC AAG TTA GG-3′) in $Tris_{Mg30}$ buffer (10 mM Tris + 30 mM $MgCl_2$, pH 7.4) and stored refrigerated overnight to ensure the attachment of thiolated probes to the gold nanostripes. Subsequently, the chips were rinsed with Q-water, dried with nitrogen, mounted on the optical platform, and interfaced with a microfluidic flow cell (Section 2.2). The surface of the chips was washed by consecutive injections of $Tris_{Mg30}$ (5 min), 2 mM NaOH (2 min), $Tris_{Mg30}$ (5 min), PBS (5 min), and 100 μM mercaptohexanol (20 min). Finally, the chips were washed with a sequence of PBS (5 min), 2 mM NaOH (5 min), and PBS (5 min). SPR sensor chips with continuous gold films were functionalized using the same procedure.

2.4. Biosensing experiment

In the performed biosensing experiments, miR125b was detected. MiR125b was purchased in HPLC grade from Integrated DNA Technologies. All other reagents were purchased in molecular biology grade or higher (Sigma Aldrich). Buffer solutions were prepared using Q-water (Milli-Q, Millipore). The biosensing experiments were performed at a temperature of 25 °C and a flow rate of 20 μl/min. In the experiments, the biosensor was exposed to different concentrations of analyte (miR125b) in buffer and the sensor response was recorded. The experiments followed the protocol outlined below. First, $Tris_{Mg50}$ (10 mM Tris + 50 mM $MgCl_2$, pH 7.4) flowed through the flow cell until the sensor response baseline was established. Then, a solution of miR125b (5′-r (UCC CUG AGA CCC UAA CUU GUG A)-3′) at variable concentrations (0.1–100 nM) was injected for 10 min. Finally, $Tris_{Mg50}$ was flowed through the flow cell for at least 10 min. After each association/dissociation cycle, the biosensor surface was treated with Tris (10 min, 10 mM Tris, pH 7.4) to remove the bound miR125b from the biosensor surface enabling the repeated use of the chip. The experiments revealed that as many as eight regeneration cycles were possible on both types of plasmonic chips without observing any substantial reduction in the binding efficiency. The chip-to-chip reproducibility of the sensor response to the binding of miR125b was higher than 78% for all the used miR125b concentrations.

3. Theory

3.1. Theoretical analysis of plasmonic sensor based on nanostripe array

The investigated plasmonic nanostructure consists of an array of gold nanostripes on a planar substrate (Fig. 1A). The substrate is assumed to be made of glass ($n_{substrate}$ = 1.51) and the sensing structure is in contact with an aqueous environment (n_{medium} = 1.33). In our simulations, we considered the width of nanostripes in the range from 100 to 500 nm and the array period in the range from 1 to 12 μm. The height of the nanostripes was kept constant at 200 nm, as our initial simulations confirmed that strong coupling of light to SP can be achieved on the nanostripes of such height. We assumed that light was incident on the nanostripe array from the substrate; the angle of incidence was larger than the critical angle for the substrate-sample system to allow for the excitation of SPs propagating along the nanostripes via attenuated total reflection. The reflectivity of the nanostructure and the distribution of the electromagnetic field of the SPs were calculated using the rigorous coupled-wave analysis (RCWA) [31]. The simulations show that a single gold nanostripe supports an SP mode that propagates along the nanostripe and exhibits a strong electromagnetic field (hot spot) at the top of the nanostripe. The components of the electric field of the SP mode are

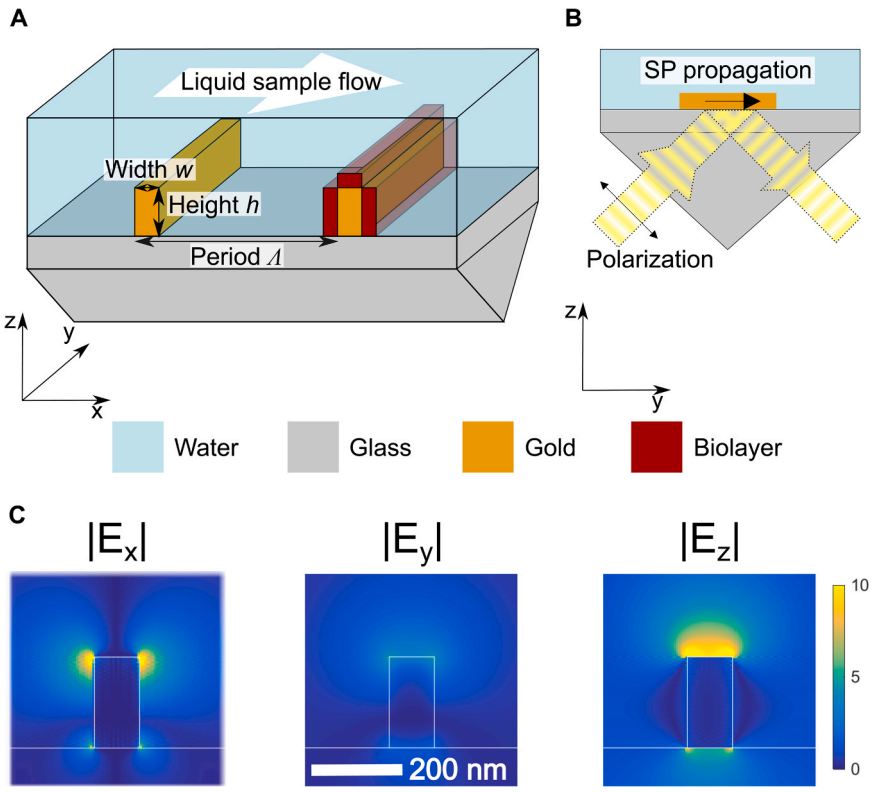

Fig. 1. A – Scheme of the plasmonic nanostripe array, B – Excitation geometry, C – Modulus of electric field for one period of a nanostripe array (height – 200 nm, width – 100 nm, period – 2 μm, wavelength – 850 nm) calculated by RCWA.

shown in Fig. 1B. The normal component of the electric field of the SP mode decays exponentially with a distance from the top surface and its penetration depth is ~ 125 nm.

When the light is made incident on the substrate with a gold nanostripe array, a portion of the light is coupled to SPs causing a drop in the intensity of the reflected light (and a dip in the spectrum of reflected light). The wavelength at which the coupling of light to SP is strongest (the reflected light intensity reaches a minimum) is referred to as the resonance wavelength. The resonance wavelength and resonance depth (contrast) vary with the angle of incidence. We calculated the resonance contrast for all considered design parameters and determined the optimum angle of incidence yielding the highest spectral contrast for each design. The reflectivity of the nanostripe array with height – 200 nm, width – 100 nm, and period – 2 μm is shown in Fig. 2A. The simulations suggest that the resonance wavelength decreases with increasing angle of incidence. The strongest excitation of SP occurs at the angle of incidence of ~ 75 deg and the wavelength of 850 nm (for comparison: the coupling to an SP on a continuous gold film occurs at the same wavelength when the angle of incidence is ~ 66.5 deg). Fig. 2B shows the dependence of reflectivity on the wavelength of incident light and reveals the characteristic spectral dips corresponding to the excitation of SPs. The depth of the dips decreases with the increasing period of the nanostripe array. Conversely, the resonance wavelength does not depend on the distance between the gold nanostripes, which suggests

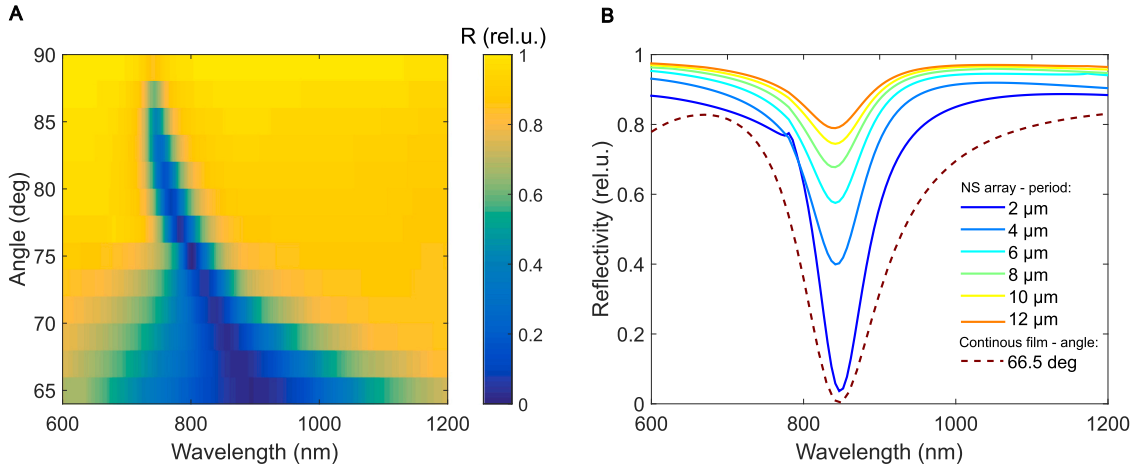

Fig. 2. Reflectivity of nanostripe arrays: A – Reflectivity of a nanostripe array (height – 200 nm, width – 100 nm, period array – 2 μm) as a function of angle of incidence and wavelength, B – Spectral reflectivity calculated for six different periods of the nanostripe array (height – 200 nm, width – 100 nm angle of incidence – 75 deg); reflectivity calculated for a continuous gold film is provided for comparison.

that there is no coupling between the SPs propagating on individual nanostripes.

3.2. Performance of sensor based on nanostripe array

The performance of a nanoplasmonic sensor can be described by several performance characteristics. The bulk refractive-index sensitivity S_B (i.e. sensitivity of resonance wavelength to changes in the refractive index of the dielectric medium adjacent to the nanostructure) may be expressed as:

$$S_B = \frac{d\lambda_{res}}{dn} \tag{1}$$

where λ_{res} and n are the resonance wavelength and refractive index of the dielectric, respectively. The surface sensitivity S_S may be expressed similarly by confining the refractive change to a distance from the sensor surface smaller than the penetration depth of the SP mode (sensing volume in Fig. 1).

Another parameter that is commonly used to compare the potential of various nanoplasmonic sensors is the figure of merit (FOM). Surface and bulk *FOM*s can be defined as:

$$FOM_{S,B} = \frac{S_{S,B}}{\Omega} \tag{2}$$

where Ω is the width of the plasmonic spectral dip [32]. In this paper, the width of the dip is defined as the full width in the half of the depth of the spectral dip. When the nanostructures under consideration produce dips of a variable contrast (depth), this effect may be taken into consideration by using the modified figure of merit *FOM** which can be expressed as:

$$FOM^*_{S,B} = \frac{S_{S,B}}{\Omega}\Delta \tag{3}$$

where Δ is the depth of the plasmonic spectral dip [33]. In this paper, the depth of the dip is defined as a difference between the maximum value of the normalized light intensity (outside the resonance) and the minimum value of the normalized light intensity (in the resonance).

We investigated the dependence of $FOM_{S,B}$ and $FOM^*_{S,B}$ on the main design parameters. To reduce the number of design parameters used for the optimization of the nanostripe array, we started the optimization by investigating the effect of the stripe width on $FOM^*_{S,B}$ while keeping the h/w ratio not too high ($h \leq 200$ nm, $w \geq 100$ nm) for technological reasons. The simulations revealed that higher FOM^*_S can be achieved when using nanostripes with a lower width (see Fig. S1 in Supplementary Material). Therefore, we used nanostripes with $w = 100$ nm, h = 200 nm in all further simulations. We also computed the dependence of $FOM_{S,B}$ and $FOM^*_{S,B}$ on the array period (see Fig. S2 in Supplementary Material) and found that $FOM^*_{S,B}$ increases with decreasing the array period (as the depth of the resonance feature increases), whereas $FOM_{S,B}$ remain constant.

In order to investigate the potential of the plasmonic nanostructure for affinity biosensing, we used the theory described in Ref. [29], which predicts the minimum detectable concentration of analyte $c_{\min}$ as follows:

$$c_{\min} = \frac{3\sigma}{S_\Gamma \kappa} \tag{4}$$

where $\sigma$is the standard deviation of sensor response, S_Γ is the sensitivity of sensor response to the changes of the surface density of the captured analyte, and κ is the efficiency of analyte transport from a bulk solution to the sensor surface and analyte capture by receptors.

We calculated the minimum detectable concentration of analyte $c_{\min}$ for nanostripe arrays of different periods (Fig. 3) by using the RCWA method to determine the optical performance characteristics and an analytical model to calculate the efficiency of the mass transport. The full description of the calculation and all parameters used in the calculation are provided in Supplementary Material. As follows from Fig. 3, the minimum detectable concentration decreases with increasing array period until it reaches a minimum (for an array period of 4 μm) when it starts to increase again. This behavior confirms that the performance of the biosensor is determined by two contributions that exhibit an opposite trend with respect to the array period: an optical performance that decreases with increasing array period (mainly due to the decrease in the resonance contrast) and mass-transport efficiency that increases with increasing array period. This is exemplified in Fig. S3 (Supplementary Material), which shows (i) the mass transport expressed in terms of $1/\kappa$ and (ii) the resolution in surface analyte coverage expressed in terms of σ/S_Γ, as a function of the period of array. Fig. 3 also reveals that $FOM_{S,B}$ does not describe this aspect properly and that $FOM^*_{S,B}$ is better able to capture this trend. Notably, the calculations suggest that the nanostripe array biosensor of an optimal design could detect analyte concentrations lower by a factor of ~ 10 than the SPR biosensor using a continuous gold film.

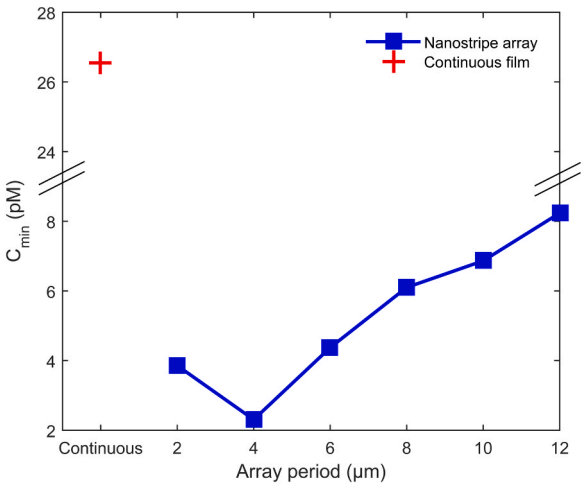

Fig. 3. The minimum detectable concentration of analyte as a function of the nanostripe array period for the nanoplasmonic biosensor (height – 200 nm, width – 100 nm). The minimum detectable concentration calculated for a conventional SPR biosensor based on a continuous gold film is provided for comparison.

4. Experimental

4.1. Characterization of nanostripe arrays

Laboratory samples of nanostripe arrays were fabricated using the procedure described in Section 2.1. An atomic force microcopy (AFM) image and scanning electron microscopy (SEM) images illustrating parameters and morphology of the realized nanostripe arrays are shown in Fig. 4. As follows from the AFM image (Fig. 4A), the parameters of fabricated nanostripes were close to the design parameters (height ~200 nm and the width ~ 100 nm). Fig. 4B suggests that the nanostripes exhibit the desired rectangular cross-section. The periods of nanostripe arrays were measured using SEM and were found to be in good agreement with the design values (8 μm and 2 μm, Figs. 4C and 4D).

To characterize the coupling of light into SPs on nanostripe arrays, the nanostripe array chips were interfaced with the optical platform described in Section 2.2 and spectral reflectivity of the nanostripe arrays was measured. Fig. 5 shows the normalized spectra obtained from 6 different nanostripe arrays with a period ranging from 2 μm to 10 μm. The experimental spectra are in good agreement with those predicted by simulations (Fig. 2B). The blue shift of the experimental dips with

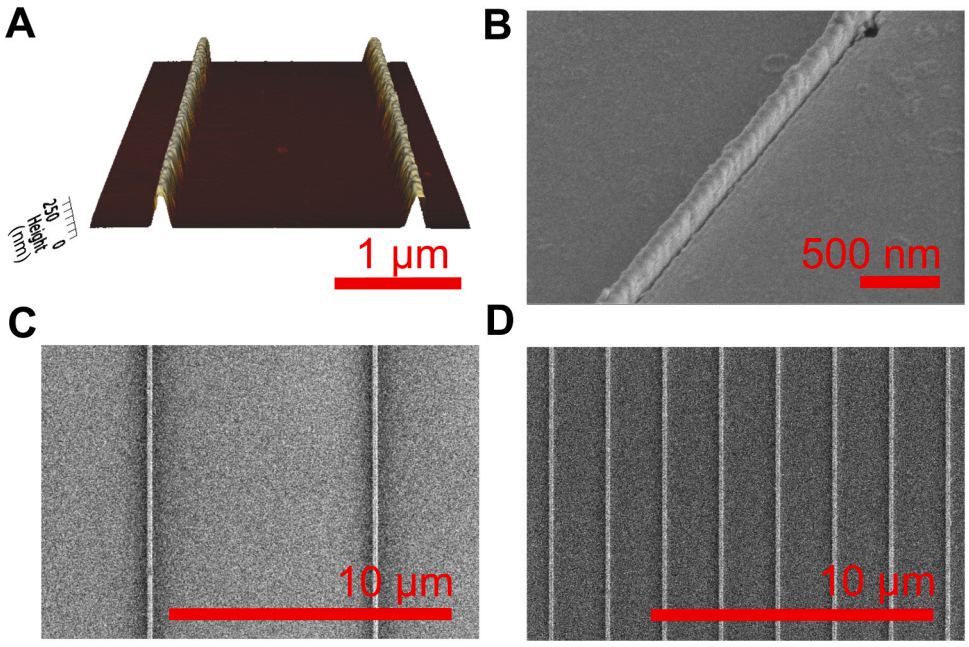

Fig. 4. Laboratory samples of nanostripe arrays: A – An AFM image of the array with a period of 2 µm, B – An SEM image of an individual nanostripe C and D – SEM images of nanostripe array with periods of 8 and 2 µm, respectively.

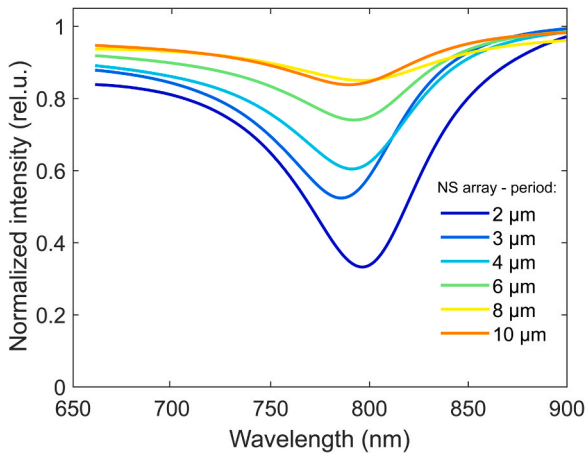

Fig. 5. Normalized spectra measured for nanostripe arrays with 6 different periods (internal angle of incidence – 75 deg, sample: Q-water).

respect to simulations can be attributed to the discrepancies between the actual dimensions and optical constants of the nanostripes and the values used in the simulations. The observed reduction in the contrast of plasmonic dips may be caused by the damping of surface plasmons due to surface roughness and by a rather oblique incidence (while the angle of incidence in the prism was 75 deg, the external angle of incidence was as high as 82 deg).

4.2. Nanostripe array sensor for refractometry

To characterize the performance of the nanostripe array sensor as a refractive index sensor, we performed a refractometric experiment in which 4 solutions of Q-water and different concentrations of sodium chloride (1–4%) were injected into the flow cell and the sensor response was recorded. The sensorgram obtained using the sensor chip with the nanostripe array with a period of 2 µm is shown in Fig. 6A (data for all the used nanostripe array periods are shown in Fig. S5 in Supplementary Material). The refractive index of the solutions was independently measured using the temperature-stabilized refractometer (DSR-Λ, Schmidt and Haensch). The magnitude and noise of the sensor response were determined for each solution to allow for the determination of refractive index sensitivity and resolution. The values of refractive index sensitivity obtained at different array periods and different channels exhibited only small differences and the average sensitivity (including data obtained for all array periods) was (1989 ± 74) nm/RIU. This value corresponds well with the sensitivity value predicted by the theory (1906 nm/RIU). Fig. 6B shows the refractive index resolution calculated as a change in the refractive index corresponding to a standard deviation of the baseline noise for different periods of the nanostripe array. As expected, the best refractive resolutions (3.6×10^{-7}RIU) were obtained with densest nanostripe arrays (lowest array periods), as such arrays exhibit plasmonic dips with the highest depth.

4.3. Nanostripe array sensor for the detection of miRNA

We performed a model experiment in which we applied the nanostripe array sensor functionalized with DNA probes (see Section 2.3) for the detection of miRNA-125b. To enable comparison with conventional SPR biosensor technology, we performed the same experiment using an SPR sensor based on spectroscopy of surface plasmons on a continuous gold film. Prior to detection experiments, we investigated stability of the used plasmonic sensing structures in buffer. Rather low drifts were observed when using continuous gold films (drift: ~ 16 pm/min) and nanostripe arrays (drift: 25–40 pm/min) which confirmed good stability of the functionalized nanostructures based on nanostripe arrays. Then, we measured the response of two types of plasmonic biosensors to six different concentrations of miRNA-125b and a blank sample ($Tris_{Mg50}$ buffer without miR125b). A typical example of sensor response to miR125b is provided in Fig. S5 in Supplementary Material. The experiments revealed that both the magnitude and rate of the sensor response increase with increasing array period. It should be noted that the same trend holds for the noise of the sensor response which is consistent with the trend observed in the refractometric experiments. In order to investigate selectivity of the sensor, experiments were carried out in which the functionalized surface was exposed to non-complementary miRNA. In these experiments, only negligible sensor response was observed suggesting that the interaction between the target miRNA and

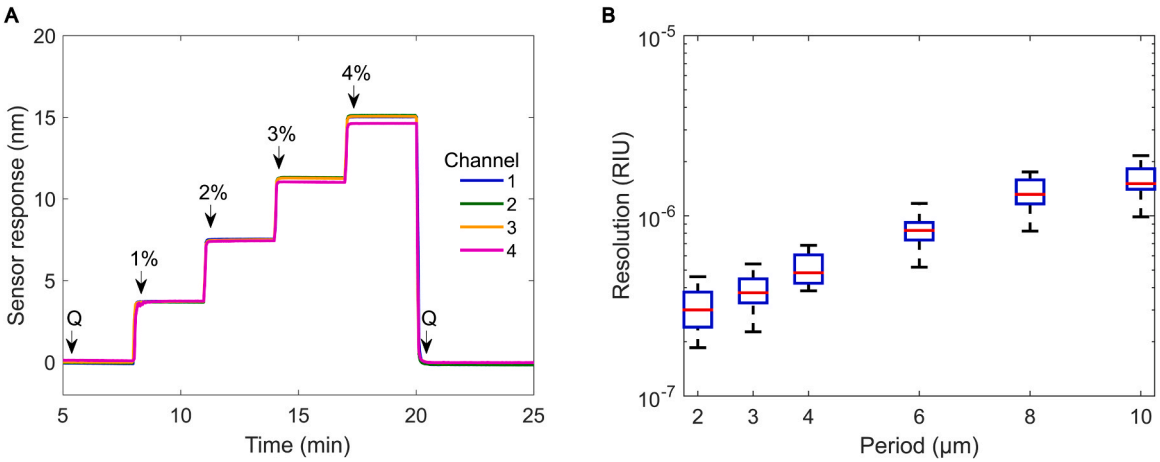

Fig. 6. Refractive-index sensing with nanostripe arrays: A – Sensor response for 4 different concentrations of NaCl and 4 nanostripe arrays with the period of 2 μm, and B – Bulk RI resolution for 6 different periods of nanostripe arrays.

DNA probes was indeed specific and there was no interaction between the DNA probes and the non-complementary miRNA (Fig. S6). The sensor response expressed in terms of the binding rate $d\lambda_{res}/dt$ was determined for a range of miR125b concentrations for both a nanostripe array biosensor and a conventional SPR biosensor. The resulting calibration curves are shown in Fig. 7A. Each data point was obtained from at least 6 measurements. The minimal detectable concentration c_{min} was determined from Eq. 4 using the standard deviation of a binding rate to blank sample and slope of a calibration curve.

As follows from Fig. 7B, the dependence of the minimum detectable concentration on the array agrees well with that provided by our theoretical model. Importantly, the minimal detectable concentration for the optimal nanostripe biosensor is lower than that for the conventional SPR biosensor based on a continuous gold film, leading to the improvement in the detection limit by a factor of 2. The difference between the improvement predicted by the theoretical model and that obtained by the experiments may be attributed to: (a) the differences in the dimensions/shapes of the real and simulated nanostripes, (b) the higher noise at the selected period as compared to the theoretical model (dominantly due to the real resonance features being shallower than predicted by the theoretical model; see Figs. 2B and 5) and (c) the analyte binding occurring also on the vertical walls of the nanostripes that (due to the limited overlap with the EM field of SPs, see Fig. 1B) contributes very little to the sensor response. The reduction of the binding of an analyte to these areas provides an avenue for improving the performance of the sensor. In the biosensors based on an array of metal nanostripes on a dielectric substrate, this can be achieved by forming a low-fouling coating on the dielectric substrate using orthogonal functionalization chemistry [34].

5. Conclusions

We report on a novel biosensor based on surface plasmons supported by a gold nanostripe array. We show that the widely used approach to the optimization of performance of nanoplasmonic biosensors based on the figure of merit fails to describe the complex behavior of nanoplasmonic biosensors and that the proper assessment of performance of nanoplasmonic biosensors requires consideration of both optical and mass transport characteristics of plasmonic nanostructures. We show that the theoretical model considering both optical and mass transport aspects can provide a nanostripe array with an optimal biosensing performance that is able to detect molecular analytes at concentrations lower by a factor of ~ 10 than conventional SPR biosensors. Finally, we demonstrate the potential of the nanostripe array-based biosensor in an experiment in which we detected miRNA related to myelodysplastic syndromes at concentrations as low as 17 pM. The demonstrated performance can be further improved by optimizing the fabrication of nanostripe arrays and by employing site-specific functionalization methods.

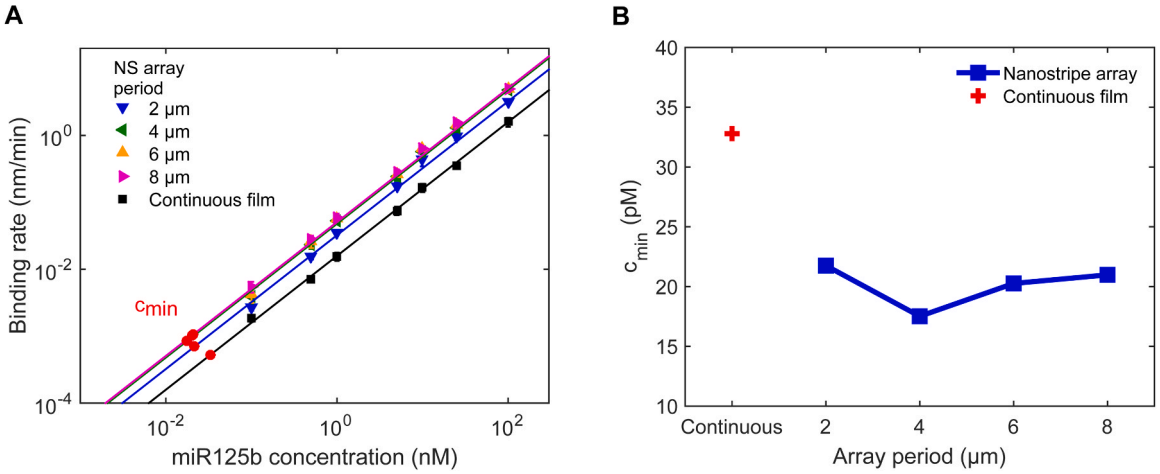

Fig. 7. Detection of miR125b by the nanostripe-based plasmonic biosensor: A – Calibration curve and B – The minimum detectable concentration for 4 different periods of nanostripe array biosensor and SPR biosensor based on a continuous gold film.

CRediT authorship contribution statement

Jiří Slabý: conceptualization, Methodology, Investigation, Writing – original draft. **Markéta Bocková:** Methodology, Writing – review & editing, **Jiří Homola:** Conceptualization, Methodology, Funding acquisition, Writing – review & editing.

Declaration of Competing Interest

The authors declare that they have no known competing financial interests or personal relationships that could have appeared to influence the work reported in this paper.

Acknowledgments

The authors would like to acknowledge the contribution of Ludmila Jurgová (SPR biosensor experiments), Petra Lebrušková, and Petr Dvořák (preparation of plasmonic nanostructures). This research was supported by the Czech Science Foundation contract 20-23787X.

Appendix A. Supporting information

Supplementary data associated with this article can be found in the online version at doi:10.1016/j.snb.2021.130629.

References

[1] R. Karlsson, SPR for molecular interaction analysis: a review of emerging application areas, J. Mol. Recognit. 17 (3) (2004) 151–161.
[2] J. Zhou, Q. Qi, C. Wang, Y. Qian, G. Liu, Y. Wang, L. Fu, Surface plasmon resonance (SPR) biosensors for food allergen detection in food matrices, Biosens. Bioelectron. 142 (2019), 111449.
[3] H.R. Jang, A.W. Wark, S.H. Baek, B.H. Chung, H.J. Lee, Ultrasensitive and ultrawide range detection of a cardiac biomarker on a surface plasmon resonance platform, Anal. Chem. 86 (1) (2014) 814–819.
[4] T. Onodera, K. Toko, Towards an electronic dog nose: surface plasmon resonance immunosensor for security and safety, Sensors 14 (9) (2014) 16586–16616.
[5] B. Špačková, P. Wrobel, M. Bocková, J. Homola, Optical biosensors based on plasmonic nanostructures: a review, Proc. IEEE 104 (12) (2016) 2380–2408.
[6] M.C. Estevez, M.A. Otte, B. Sepulveda, L.M. Lechuga, Trends and challenges of refractometric nanoplasmonic biosensors: a review, Anal. Chim. Acta 806 (2014) 55–73.
[7] R.T. Hill, Plasmonic biosensors, Wiley Interdiscip. Rev. Nanomed. Nanobiotechnol. 7 (2) (2015) 152–168.
[8] J.A. Jackman, A.R. Ferhan, N.-J. Cho, Nanoplasmonic sensors for biointerfacial science, Chem. Soc. Rev. 46 (12) (2017) 3615–3660.
[9] A.J. Haes, R.P. Van Duyne, A nanoscale optical biosensor: sensitivity and selectivity of an approach based on the localized surface plasmon resonance spectroscopy of triangular silver nanoparticles, J. Am. Chem. Soc. 124 (35) (2002) 10596–10604.
[10] H.-Y. Lin, C.H. Huang, S.H. Lu, I.T. Kuo, L.K. Chau, Direct detection of orchid viruses using nanorod-based fiber optic particle plasmon resonance immunosensor, Biosens. Bioelectron. 51 (2014) 371–378.
[11] M. Toma, K. Cho, J.B. Wood, R.M. Corn, Gold nanoring arrays for near infrared plasmonic biosensing, Plasmonics 9 (4) (2014) 765–772.
[12] S.K. Dondapati, T.K. Sau, C. Hrelescu, T.A. Klar, F.D. Stefani, J. Feldmann, Label-free biosensing based on single gold nanostars as plasmonic transducers, ACS Nano 4 (11) (2010) 6318–6322.
[13] S. Lee, K.M. Mayer, J.H. Hafner, Improved localized surface plasmon resonance immunoassay with gold bipyramid substrates, Anal. Chem. 81 (11) (2009) 4450–4455.
[14] B. Luk'yanchuk, N.I. Zheludev, S.A. Maier, N.J. Halas, P. Nordlander, H. Giessen, C.T. Chong, The Fano resonance in plasmonic nanostructures and metamaterials, Nat. Mater. 9 (9) (2010) 707–715.
[15] V.G. Kravets, A.V. Kabashin, W.L. Barnes, A.N. Grigorenko, Plasmonic surface lattice resonances: a review of properties and applications, Chem. Rev. 118 (12) (2018) 5912–5951.
[16] A. Danilov, G. Tselikov, F. Wu, V.G. Kravets, I. Ozerov, F. Bedu, A.N. Grigorenko, A.V. Kabashin, Ultra-narrow surface lattice resonances in plasmonic metamaterial arrays for biosensing applications, Biosens. Bioelectron. 104 (2018) 102–112.
[17] J. Li, J. Ye, C. Chen, Y. Li, N. Verellen, V.V. Moshchalkov, L. Lagae, P. Van Dorpe, Revisiting the surface sensitivity of nanoplasmonic biosensors, ACS Photon. 2 (3) (2015) 425–431.
[18] M. Sarkar, M. Chamtouri, J. Moreau, M. Besbes, M. Canva, Introducing 2D confined propagating plasmons for surface plasmon resonance sensing using arrays of metallic ribbons, Sens. Actuators B 191 (2014) 115–121.
[19] O. Krupin, H. Asiri, C. Wang, R.N. Tait, P. Berini, Biosensing using straight long-range surface plasmon waveguides, Opt. Express 21 (1) (2013) 698–709.
[20] O. Krupin, C. Wang, P. Berini, Selective capture of human red blood cells based on blood group using long-range surface plasmon waveguides, Biosens. Bioelectron. 53 (2014) 117–122.
[21] P. Béland, O. Krupin, P. Berini, Selective detection of bacteria in urine with a long-range surface plasmon waveguide biosensor, Biomed. Opt. Express 6 (8) (2015) 2908–2922.
[22] O. Krupin, P. Berini, Long-range surface plasmon-polariton waveguide biosensors for human cardiac troponin I detection, Sensors 19 (3) (2019) 631.
[23] D. Chowdhury, M.C. Giordano, G. Manzato, R. Chittofrati, C. Mennucci, F. Buatier de Mongeot, Large-area microfluidic sensors based on flat-optics Au nanostripe metasurfaces, J. Phys. Chem. C 124 (31) (2020) 17183–17190.
[24] T. Ronur Praful, N. Jerop, N. Noginova, Ultra-sensitive plasmonic sensing based on gold nanostrip arrays, Opt. Lett. 44 (17) (2019) 4199–4202.
[25] T.M. Squires, R.J. Messinger, S.R. Manalis, Making it stick: convection, reaction and diffusion in surface-based biosensors, Nat. Biotechnol. 26 (4) (2008) 417–426.
[26] A.B. Dahlin, Size matters: problems and advantages associated with highly miniaturized sensors, Sensors 12 (3) (2012) 3018–3036.
[27] Jr Lynn NS, T. Špringer, J. Slabý, B. Špačková, M. Gráfová, M.L. Ermini, J. Homola, Analyte transport to micro-and nano-plasmonic structures, Lab Chip 19 (24) (2019) 4117–4127.
[28] N.S. Lynn Jr., J. Homola, Microfluidic analyte transport to nanorods for photonic and electrochemical sensing applications, Chem. Eur. J. 24 (46) (2018) 12031–12036.
[29] B. Špačková, N.S. Lynn, J. Slabý, H. Šípová, J. Homola, A route to superior performance of a nanoplasmonic biosensor: consideration of both photonic and mass transport aspects, ACS Photon. 5 (3) (2018) 1019–1025.
[30] T. Špringer, M. Piliarik, J. Homola, Surface plasmon resonance sensor with dispersionless microfluidics for direct detection of nucleic acids at the low femtomole level, Sens. Actuators B 145 (1) (2010) 588–591.
[31] Kwiecien, P. and I. Richter. *Efficient three dimensional aperiodic rigorous coupled wave analysis technique*. in 2011 13th International Conference on Transparent Optical *Networks*. 2011. IEEE.
[32] J. van Gent, P.V. Lambeck, H.J. Kreuwel, G.J. Gerritsma, E.J. Sudhölter, D. N. Reinhoudt, T.J. Popma, Optimization of a chemooptical surface plasmon resonance based sensor, Appl. Opt. 29 (19) (1990) 2843–2849.
[33] L.Y.M. Tobing, G.Y. Goh, A.D. Mueller, L. Ke, Y. Luo, D.H. Zhang, Polarization invariant plasmonic nanostructures for sensing applications, Sci. Rep. 7 (1) (2017) 7539.
[34] L. Feuz, P. Jönsson, M.P. Jonsson, F. Höök, Improving the limit of detection of nanoscale sensors by directed binding to high-sensitivity areas, ACS Nano 4 (4) (2010) 2167–2177.

Jiří Slabý received the MSc. degree in physical engineering from the Czech Technical University in Prague, Czech Republic in 2014. He is currently the Ph.D. candidate in the Optical Biosensors research team at the Institute of Photonics and Electronics of the Czech Academy of Sciences, Prague. His research interests include surface plasmons and their application in optical sensors and biosensors.

Markéta Bocková received the MSc. degree in biochemistry and the PhD. degree in biophysics, chemical and macromolecular physics from Charles University in Prague, Czech Republic in 2009 and 2019, respectively. She is currently the postdoctoral fellow in the Optical Biosensors research team at the Institute of Photonics and Electronics of the Czech Academy of Sciences, Prague, where she was appointed a Deputy head of the team in 2020. Her research interests include plasmonic biosensors, functional coatings and assay development for detection of biomolecules and investigation of biomolecular interactions as well as affinity biosensors for medical diagnostics.

Jiří Homola graduated in physical engineering at the Faculty of Nuclear and Physical Engineering of the Czech Technical University (CTU) in 1988. He obtained the PhD degree in electronics and vacuum technology and the DSc degree in electrical engineering, electronics, optoelectronics and photonics from the Czech Academy of Sciences (CAS) in 1993 and 2009, respectively. Since 1993, he has worked at the Institute of Photonics and Electronics of the CAS as a researcher and since 2003 he has led a research team. From 2012 to 2021, he served as the Director of the Institute. Between 1997 and 2002, he was with the University of Washington, Seattle (USA), since 2001 as a Research Associate Professor. He also lectured at the University of Oulu (Finland). He was appointed Associate Professor and Professor of quantum optics and optoelectronics at Charles University in 2009 and 2014, respectively. Prof. Homola is a Senior Member of IEEE, a Fellow of SPIE and a member of the Learned Society of the Czech Republic. His research interests are in (bio)photonics, plasmonics, optical sensors, and biosensors.

Appendix V

Actuated plasmonic nanohole arrays for sensing and optical spectroscopy applications

Kotlarek, D., Fossati, S., Venugopalan, P., Quilis, N. G., Slabý, J., Homola, J., Lequeux, M., Amiard, F., de la Chapelle, M.L., Jonas, U., and Dostálek, J.

Nanoscale, 2020. **12**, 9756-9768

Nanoscale

ROYAL SOCIETY OF CHEMISTRY

PAPER

View Article Online
View Journal | View Issue

Cite this: *Nanoscale*, 2020, **12**, 9756

Actuated plasmonic nanohole arrays for sensing and optical spectroscopy applications†

Daria Kotlarek,‡[a] Stefan Fossati,[a] Priyamvada Venugopalan,§[a,b] Nestor Gisbert Quilis,[a] Jiří Slabý,[c] Jiří Homola,[c] Médéric Lequeux,[d] Frédéric Amiard,[e] Marc Lamy de la Chapelle,[e] Ulrich Jonas[f] and Jakub Dostálek *[a]

Received 28th January 2020,
Accepted 30th March 2020

DOI: 10.1039/d0nr00761g

rsc.li/nanoscale

Herein, we report a new approach to rapidly actuate the plasmonic characteristics of thin gold films perforated with nanohole arrays that are coupled with arrays of gold nanoparticles. The near-field interaction between the localized and propagating surface plasmon modes supported by the structure was actively modulated by changing the distance between the nanoholes and nanoparticles and varying the refractive index symmetry of the structure. This approach was applied by using a thin responsive hydrogel cushion, which swelled and collapsed by a temperature stimulus. The detailed experimental study of the changes and interplay of localized and propagating surface plasmons was complemented by numerical simulations. We demonstrate that the interrogation and excitation of the optical resonance to these modes allow the label-free SPR observation of the binding of biomolecules, and is applicable for *in situ* SERS studies of low molecular weight molecules attached in the gap between the nanoholes and nanoparticles.

Metallic nanohole arrays (NHAs) have attracted increasing attention after Ebbesen's observation of the extraordinary optical transmission[1] assigned to surface plasmon-mediated light tunneling through periodically arranged subwavelength pores. Subsequently, NHA structures have been employed in diverse application areas including optical filters,[2,3] amplification of weak spectroscopy signals such as fluorescence[4,5] and Raman scattering,[6–9] second-harmonic generation,[10] and particularly sensing. To date, NHA-based sensors have been utilized for the direct optical probing of proteins,[11,12–14] exosomes,[15] viruses,[16,17] bacteria,[18] and even cancer cells[19,20] and organelles.[21] Moreover, NHA have enabled studies on lipid membranes that span over the holes[22] and allowed the facile incorporation of membrane proteins for interaction studies with drug candidates.[16,23]

NHA structures enable the electromagnetic field to be strongly confined inside subwavelength nanoholes[24] due to the excitation of two types of surface plasmon modes, propagating surface plasmons (PSPs, also referred to as surface plasmon polaritons) traveling along the metal surface and localized surface plasmons (LSPs), which occur at the sharp edges of the holes. The coupling to these modes can be tailored for specific purposes by controlling the structure geometry, including hole shape, diameter, and lateral periodic or quasi-periodic spacing.[25] In addition, a more complex spectrum of supported plasmonic modes can be utilized by combining complementary geometries that support LSP modes at similar wavelengths based on Babinet's principle.[26] When the NHA geometry approaches that of complementary metallic nanoparticle (NP) arrays, additional LSP resonance is introduced, which can near-field couple with the NHA.[27] Moreover, NHA structures that comprise stacks of periodically perforated metallic films[28] and NHA + NP structure with a defined lateral offset of NPs with respect to the nanohole center[29] have been investigated. Herein, we report a new approach to rapidly actuate the plasmonic characteristics of thin gold films perforated with nanohole arrays by thermo-responsive hydrogel and demonstrate its utilization to sensing with flow-through format SPR and SERS readout.[30] It is worth noting that arran-

[a]*Biosensor Technologies, AIT-Austrian Institute of Technology GmbH, Konrad-Lorenz-Straße 24, 3430 Tulln an der Donau, Austria. E-mail: jakub.dostalek@ait.ac.at*
[b]*CEST Kompetenzzentrum für elektrochemische Oberflächentechnologie GmbH, TFZ, Wiener Neustadt, Viktor-Kaplan-Strasse 2, 2700 Wiener Neustadt, Austria*
[c]*Institute of Photonics and Electronics of the Czech Academy of Sciences, Chaberská 57, 18251 Praha 8, Czech Republic*
[d]*Université Paris 13, Sorbonne Paris Cité, Laboratoire CSPBAT, CNRS, (UMR 7244), 74 rue Marcel Cachin, 93017 Bobigny, France*
[e]*Institut des Molécules et Matériaux du Mans (IMMM – UMR CNRS 6283), Avenue Olivier Messiaen, 72085 Le Mans cedex 9, France*
[f]*Macromolecular Chemistry, Department Chemistry-Biology, University of Siegen, Adolf Reichwein-Strasse 2, Siegen 57076, Germany*

†Electronic supplementary information (ESI) available. See DOI: 10.1039/d0nr00761g

‡Current address: Captor Therapeutics Inc., ul. Duńska 11, 54-427 Wroclaw, Poland.
§Current address: NYU Abu Dhabi, Saadiyat Campus, P.O. Box 129188, Abu Dhabi, United Arab Emirates.

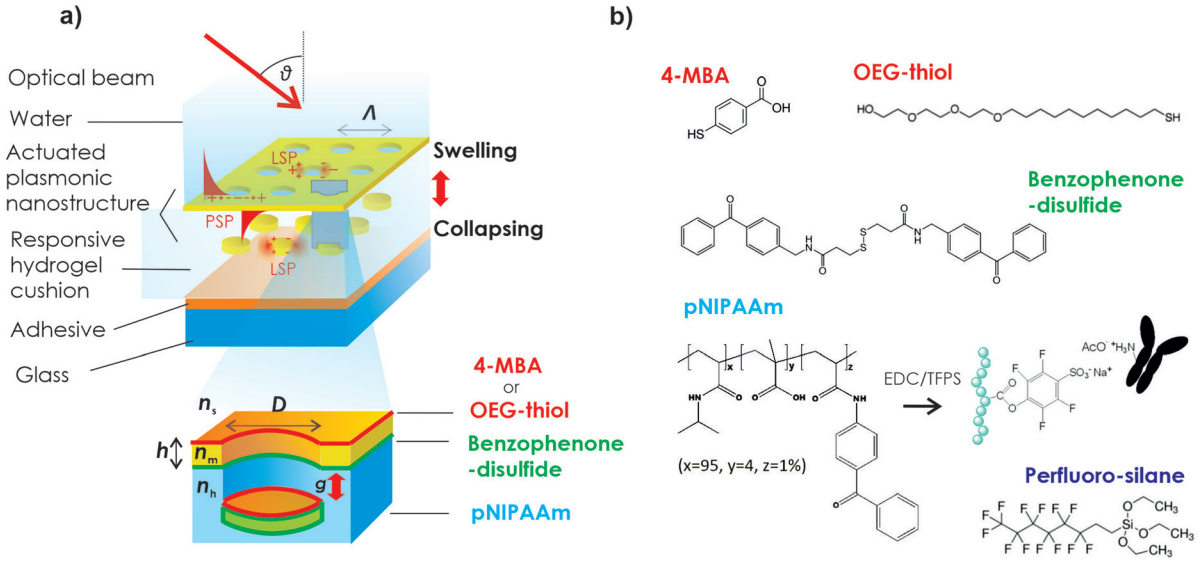

Fig. 1 (a) Schematics of plasmonic nanostructure composed of periodic nanohole arrays (NHA) coupled with arrays of nanoparticles (NP) by the use of responsive hydrogel cushion implemented by materials with the chemical structure shown in (b).

ging the metallic nanoholes and nanoparticles in periodic arrays also decreases the damping of plasmonic modes by their diffraction coupling through the formation of the so-called surface lattice resonances.[31]

Perforated metal layer structures with NHA have been recently prepared using a range of lithography processes. In top-down approaches, a variety of geometries become accessible using focused ion beam milling (FIB) and electron beam lithography (EBL).[32,33] Nanoimprint lithography and template stripping[34] are used to partially alleviate the limited throughput of EBL and FIB by the replication of the NHA structure from pre-fabricated templates. Alternatively, NHAs were also prepared using bottom-up approaches, mostly relying on the self-organization of colloid particles.[35] Using sub-monolayer surface coverage of colloids, the colloid particles are used as a mask for the preparation of sparse and disordered nanoholes, while dense monolayers of colloids are employed to create well-ordered nanohole geometries.[28,29,36] This approach allows the pattern period, Λ, to be controlled by the size of the colloid particles and the hole diameter, D, can be independently adjusted *via* isotropic etching of the assembled particles before metal deposition. This technique was further extended for the preparation of nanoholes on cavities,[37] and a lift-off approach of the NHA membrane was also adopted for its subsequent transfer to more complex structures with multiple stacked patterned metallic layers.[28]

Typically, NHAs used for sensing applications are prepared *via* stripping-based techniques or lithographic methods directly on a non-permeable solid support, which is loaded to a microfluidic device.[38,39] However, the liquid sample to be analyzed is flowed over the perforated NHA surface with closed-ended pores, where the liquid flow velocity is equal to zero, and consequently, the transport of molecules to and inside the pores is dominantly driven by slow diffusion.[40,41] Thus, to overcome this limitation, there a flow-through assay format has been developed, in which the analyte solution is transported internally across the nanoporous film.[8,16,41,42] However, these experiments typically rely on the structure of the NHA prepared on thin nitride membranes, which requires multiple lithography steps and complicates their application in sensing experiments.

The present study demonstrates a new type of NHA + NP structure, which is supported by a thermo-responsive hydrogel cushion. It is made from an *N*-isopropylacrylamide hydrogel material that can expand and contract in an aqueous environment, thereby actuating the plasmonic properties of metallic nanostructures.[43–45] In this architecture, the hydrogel cushion accommodates arrays of gold NPs, which are located below the NHA and their mutual distance, g, can be on demand actuated (Fig. 1). Herein, we investigate the spectra of supported PSP and LSP modes and their spectral detuning by temperature-induced reversible swelling and collapsing of a hydrogel cushion. In addition, the hydrogel can serve as a three-dimensional binding matrix for the immobilization of bio-functional molecules and the applicability of the structure for SPR (surface plasmon resonance) and SERS (surface-enhanced Raman scattering) detection is demonstrated with the use of plasmonic modes that probe the open pores, through which aqueous samples can be actively flowed.

Results and discussion

We developed a method to prepare a nanostructure geometry that combines thin gold films perforated with NHA and arrays of gold NP, which are suspended in a thin layer of a poly(*N*-isopropyl acrylamide) (pNIPAAm)-based hydrogel. It serves as a responsive cushion, which responds to temperature changes

since pNIPAAm exhibits a lower critical solution temperature (LCST) of 32 °C. Below its LCST, it is hydrophilic, and it contains large amounts of water in its polymer network structure. When the temperature increases above its LCST, it abruptly collapses by expelling water. In the nanostructure geometry (Fig. 1a), the pNIPAAm-based hydrogel cushion was allowed to swell and collapse *via* the diffusion of water through the NHA pores and its volume changes were utilized for active control of the distance, g, between NHA and NP. In addition, the hydrogel was made from a terpolymer that carries pendant groups attached to its backbone, enabling its post-modification with bio-functional molecules (Fig. 1b) for application in optical spectroscopy and biosensors.[46] It is worth noting that this thermo-responsive hydrogel cushion allowed the controlled opening and closing of the nanohole arrays of pores, and switching to the open state was accompanied by the rapid diffusion of water, which drags contained biomolecules through the pores, where a plasmonic hotspot occurs. The spectrum of plasmonic modes probing the pores of the structure and their near field coupling was investigated in detail, as follows.

Preparation of NHA + NP structure with hydrogel cushion

The NHA + NP structure featuring actively tunable plasmonic properties was prepared by a combination of UV nanoimprint lithography (UV-NIL) and template-stripping (Fig. 2a). Arrays of nanopillars cast to the transparent OrmoStamp material were used as a template. AFM observation of the structure topography showed that the arrays of nanopillars exhibited a diameter of D = 100 nm, height of 100 nm, and they were arranged in rectangular arrays with a set period of Λ = 460 nm (Fig. 2b). The arrays of OrmoStamp nanopillars were then activated by UV-ozone treatment and modified with perfluoro-silane using vapor deposition to reduce their surface energy. Subsequently, the nanopillars with a perfluoro-silane anti-adhesive layer were coated by a gold layer with a thickness of h = 50 nm. SEM observation (Fig. 2c) revealed that the gold deposition led to the formation of a continuous layer, which is protruded by the nanopillars and their top is capped by gold that is not connected to the bottom continuous gold layer. Afterward, the outer gold surface was modified by a self-assembled monolayer of photo-active benzophenone-disulfide, and subsequently coated with a pNIPAAm-based terpolymer layer. This terpolymer contains the same photo-reactive benzophenone groups in its backbone (see Fig. 1b) and upon irradiation with UV light these chains were simultaneously covalently crosslinked and attached to the gold *via* the benzophenone-disulfide linker. Then, the outer surface of the crosslinked pNIPAAm-based polymer was pressed against a glass substrate with a soft adhesive layer (Ostemer resin pre-cured with UV light), which was subsequently thermally cured overnight at a temperature of 50 °C. Finally, the assembly was stripped at the OrmoStamp–gold interface (treated with anti-adhesive layer) to yield a structure with a thin gold film perforated by NHA, which were attached to the pNIPAAm-based crosslinked polymer networks and underneath comprised of embedded gold NPs spatially separated from the perforated continuous gold film. The AFM topography image in Fig. 2d shows that the pores exhibit the same diameter, D, as the nanopillars and the SEM image of an edge of the structure in Fig. 2e confirms that under the NHA, arrays of gold NPs are present (which were stripped from the top of the OrmoStamp pillars). It is worth noting that the distortions of the surface that are visible in Fig. 2e are a result of breaking the sample to obtain the cross-section image.

Optical observation of plasmonic modes

The spectra of the LSP and PSP modes supported by the prepared nanostructure were investigated *via* optical transmission measurements. To distinguish between the diffraction coupling to the dispersive PSP modes (traveling along the gold film) and non-dispersive LSP resonances (supported by the pores in the NHA + NP nanostructure), transmission spectra were measured *via* collimated beam impinging on the NHA + NP structure at angles in the range of θ = 0° to 25°. The transmitted beam emitted from a halogen light bulb was then analyzed with a spectrometer in the wavelength range of λ = 500–850 nm. Firstly, the wavelength-angular dependence of the transmission was measured for a structure that was dry and in contact with air (with a refractive index of n_s = 1). As presented in Fig. 3a, the acquired spectrum shows that the excitation of non-dispersive resonance is manifested as a dip centered at a wavelength of λ_A = 600 nm. Moreover, an additional dispersive mode occurs, and its excitation is associated with the dip in the transmission spectrum at λ_C^d = 750 nm, which splits when the angle of incidence, θ, deviates from zero. Secondly, the structure was clamped to a flow-cell and water (with a refractive index of n_s = 1.33) was flowed over its surface, which was kept at a temperature of T = 40 °C. This temperature is above the LCST of pNIPAAm, and thus this material exhibits hydrophobic properties, preventing the diffusion of water into the polymer networks through the NHA pores. Since the refractive index of the dielectric above the structure n_s increased, a new dispersive dip resonance centered at a wavelength of λ_B^d = 650 nm appeared, while the resonance features λ_A and λ_C^d changed negligibly (Fig. 3b). Thirdly, the structure in contact with water was cooled to T = 22 °C, which is below the LCST of pNIPAAm. Then, a strong blueshift in the λ_A and λ_C^d resonances occurred in the transmission spectrum, and also much weaker spectral shift of λ_B^d accompanied by a decrease in coupling efficiency at this wavelength (Fig. 3c). These observations indicate that the resonances at λ_A and λ_C^d are associated with the coupling to the surface plasmon modes that confine the electromagnetic field in the inner side of the structure in contact with the pNIPAAm-based hydrogel (with a refractive index of n_h = 1.47 at T = 22 °C and n_h = 1.37 at T = 40 °C, see ESI, Fig. S1†). The resonance λ_B^d probes the upper part of the structure in contact with water (n_s = 1.33), which changes its refractive index with temperature much less than pNIPAAm. Since the resonances at λ_B^d and λ_C^d are dispersive, they can be attributed to the PSP modes travelling at the upper or bottom interface of the gold film, respect-

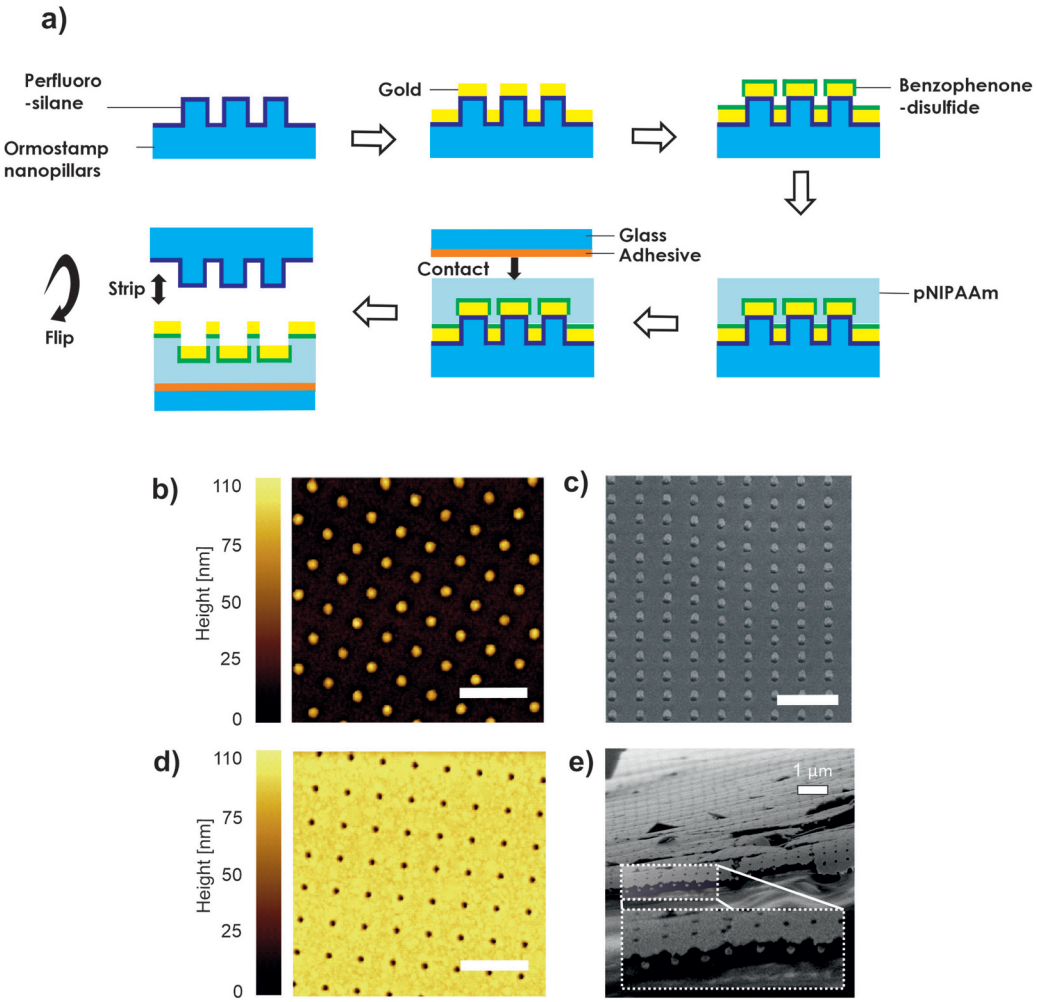

Fig. 2 (a) Schematic of the preparation steps of the investigated NHA + NP nanostructure, (b) AFM image of the template with arrays of nanopillars cast to OrmoStamp, (c) SEM image after coating of the template with a 50 nm thick gold layer, (d) AFM image of the topography of the stripped surface with gold NHA, and (e) SEM image of a broken edge of the NHA + NP structure tethered to a solid surface *via* the responsive pNIPAAm-based polymer. All scale bars are 1 µm in length.

ively. The non-dispersive nature of the λ_A resonance indicates it can be ascribed to the LSP mode.

A more detailed dependence of the transmission spectra on temperature T was investigated for the normal angle of incidence θ = 0 (Fig. 3d). The spectra were measured using a different light source (supercontinuum laser) in order to extend the wavelength range to 900 nm, which allowed us to observe an additional feature manifested as a transmission peak at λ_C^p = 810 nm. Moreover, this showed more clearly that close to λ_B^d, a peak appeared at a wavelength λ_B^p. It is worth noting that the measured transmission spectra were normalized with that obtained for a flat 50 nm thick gold film, which exhibited a rapidly decreasing transmission with wavelength in the red and near infrared region of the spectrum. Therefore, the measurement of absolute transmission values was not possible, and thus only relative values are presented. In addition, the spectral positions of the resonances in Fig. 3a, b and d slightly differ since they were measured with different (although fabricated under identical conditions) NHA + NP nanostructures.

Identification of plasmonic modes aided by simulations

The five observed resonant features in the measured transmission spectra were identified using numerical finite difference time domain (FDTD) simulations. This model was employed to calculate the absorption wavelength spectra and near-field distribution of the electromagnetic field occurring in the structure upon a plane wave normally impinging at its surface. The simulations of the absorption spectra allowed us to distinguish the resonant excitation of the LSP and PSP modes (which is accompanied with damping) from other features occurring in the transmission spectrum, which are related to the interference between multiple specular and non-specular diffracted beams and their falling after the horizon in the superstrate or substrate. As shown in Fig. 4a (blue curve), we initially analyzed a structure composed of only arrays of

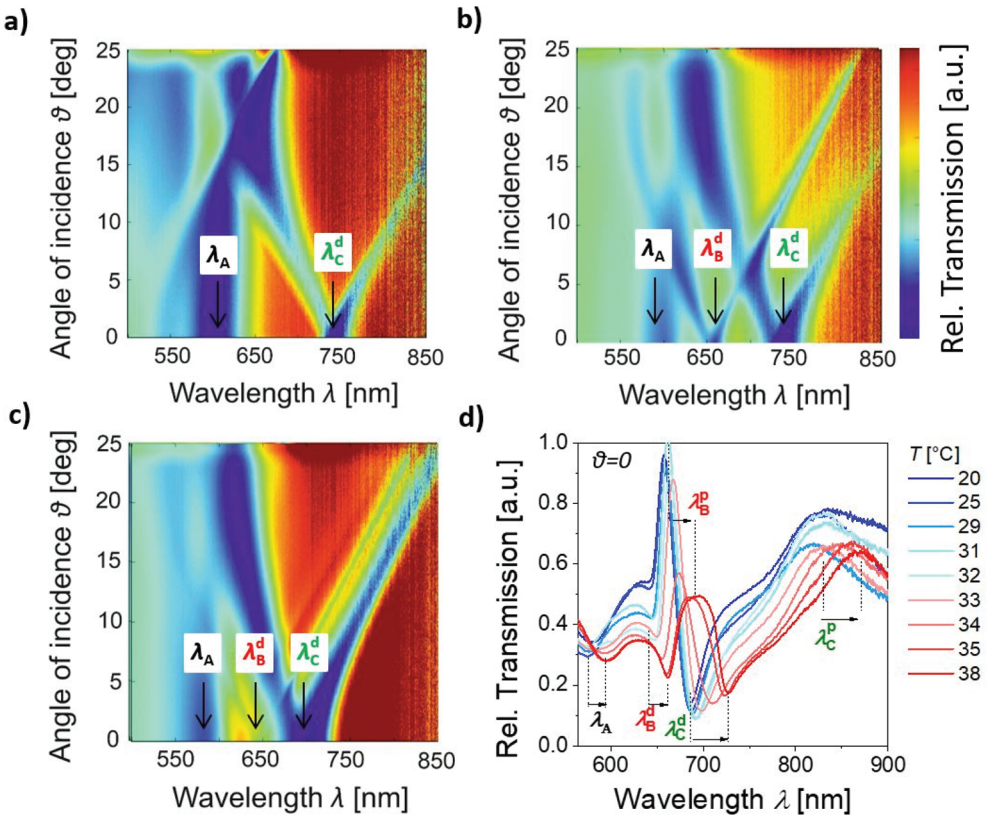

Fig. 3 Measured dependence of wavelength transmission spectra on angle of incidence, θ, for the NHA + NP structure in contact with (a) air (n_s = 1 and n_h = 1.48), (b) for the collapsed state of the pNIPAAm-based cushion that is in contact with water at T = 40 °C (n_s = 1.33 and n_h = 1.48), and (c) for the swollen state of pNIPAAm cushion in water at T = 22 °C (n_s = 1.33 and n_h = 1.37). (d) Comparison of the wavelength transmission spectra for θ and NHA + NP structure in contact with water at varying temperature, T. The transmission spectra were normalized with that measured for the flat structure without the perforated Au film.

cylindrically shaped nanoparticles (NPs with a height of h = 50 nm, average diameter of D = 100–120 nm, and period of Λ = 460 nm) embedded between dielectrics with the refractive indices of n_h = 1.47 and n_s = 1.33. The simulated spectrum reveals that the resonance associated with the coupling to LSP on the arrays of NPs is manifested as a strong absorption peak at a wavelength of about 707 nm. The complementary NHA structure was composed of a 50 nm thick gold film that was perforated with arrays of cylindrical nanoholes exhibiting the same diameter D and sandwiched between the same dielectrics with refractive indices of n_h = 1.47 and n_s = 1.33. The absorption spectrum in Fig. 4a (red curve) shows three resonances located at the wavelengths of λ_A = 630 nm, λ_B = 676 nm, and λ_C = 774 nm. At these wavelengths, the near-field distribution of the electric field amplitude $|E|$ (normalized with that of the incidence plane wave $|E_0|$) was simulated, as can be observed in the right part of Fig. 4a. These plots reveal that the resonance at wavelength λ_A exhibits the characteristics of the dipolar LSP mode, which confines the field inside the nanohole. The resonance at the longer wavelength λ_B shows a more delocalized field profile on the top interface of the gold film with the superstrate n_s = 1.33, which confirms it is due to first-order diffraction coupling to the traveling PSP mode at this surface. The resonance at the NIR wavelength λ_C is accompanied with the confinement of the electric field at the bottom gold layer interface with the dielectric n_h = 1.47, which peaks at the mouth of the pore and its distribution suggests the main origin corresponds to the first-order diffraction coupling to the PSPs traveling along the bottom gold film surface. It should be noted that these simulations were carried out for the mouth of the nanopores filled by a dielectric with a refractive index n_s since the fabrication procedure involving stripping from arrays of nanopillars suggests this geometry (see Fig. 2a).

The simulations in Fig. 4b (brown curve) reveal that the short wavelength resonance was blue-shifted to λ_A = 621 nm, the middle resonance blue-shifted to λ_A = 672 nm, and the long-wavelength resonance red-shifted to λ_C = 813 nm after the coupling of the nanohole arrays with the cylindrical nanoparticle arrays (NHA + NP). In these simulations, the gap distance between the bottom edge of the nanopore and the upper surface of the cylindrically shaped nanoparticle was set to g = 50 nm, which corresponds to the difference between the nanopillar height of 100 nm and the thickness of the gold layer of h = 50 nm (see Fig. 1 and 2). When the refractive index of the superstrate decreased from n_s = 1.33 (representing

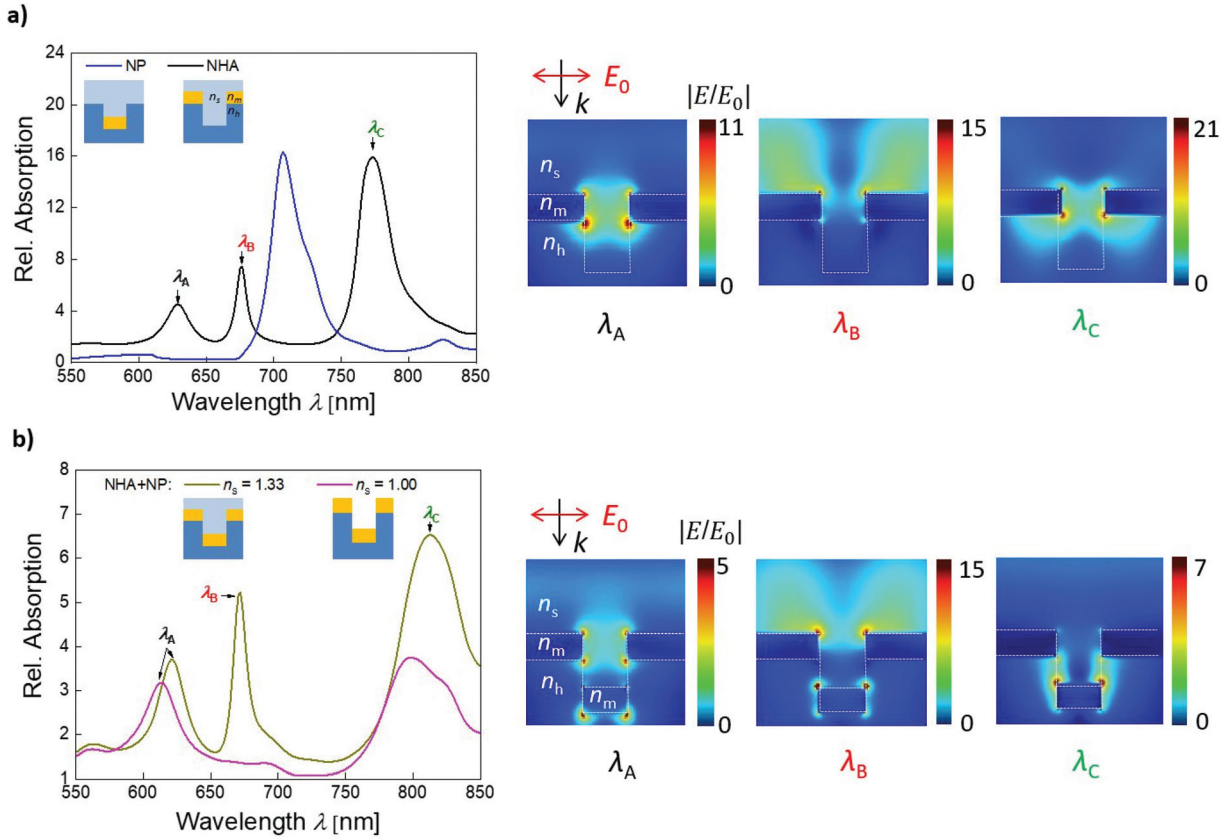

Fig. 4 Simulation-based investigation of the spectrum of supported plasmonic modes: absorption spectra obtained for normally incident beam at (a) structure with a thin gold film perforated with arrays of nanoholes (NHA), with arrays of cylindrical nanoparticles (NP), and for the combined geometry (NHA + NP) with superstrate refractive indices n_s = 1 and 1.33 and substrate refractive index n_h = 1.47. (b) Absorption spectrum simulated for the NHA + NP geometry for superstrate refractive indices n_s = 1 and 1.33. The substrate refractive index was of n_h = 1.47, gap distance between NP and NHA was of g = 50 nm, period of Λ = 460 nm, diameter averaged between D = 100–120 nm, and height of h = 50 nm. The cross-section of spatial distribution of the electric field amplitude was simulated for the plasmonic modes as indicated in the inset.

water) to n_s = 1 (representing air), the middle-wavelength resonance disappeared, as shown in Fig. 4b (green curve). This observation agrees with the measurements presented in Fig. 3 and confirms that the middle resonance occurs due to the first-order diffractive coupling to the PSP mode at the outer gold layer surface, which is the most sensitive to variations in refractive index on the upper interface (superstrate n_s). In addition, this refractive index decrease led to a slight blue shift in λ_A and λ_C since the field distribution corresponding to these resonances also partially probe the dielectric n_s. The spatial profile of the near field-enhanced electric field amplitude in the right part of Fig. 4b shows that the presence of gold disk nanoparticles slightly perturbed the nanohole LSP resonance at λ_A as the field is dragged to the bottom part of the disk nanoparticle. The resonance at λ_B due to the PSPs traveling on the top interface only weakly couples with the disk nanoparticles, contrary to the bottom PSP mode λ_C, which exhibits a field distribution with a more pronounced confinement in the gap.

Interestingly, the simulations predicted that only three plasmonic modes are supported in the investigated wavelength range (Fig. 4b, brown curve) when the geometry of NHA (with three plasmonic modes, black curve Fig. 4a) and NP arrays (with one mode, blue curve in Fig. 4a) are combined to yield the experimentally investigated structure NHA + NP. However, five features were identified in the experimental transmission data presented Fig. 3, which is greater than the number of predicted plasmonic modes. The discrepancy between the simulated absorption spectra and experimentally measured specular transmission can be explained by the Fano shape of the two measured transmission resonances. The middle wavelength peak at λ_B^p and dip at λ_B^d can be attributed to the excitation of a single PSP mode at the interface of the structure with superstrate n_s and its asymmetric shape can be ascribed to the interference with additional waves generated by the structure in a broader wavelength range (previously observed for related plasmonic nanostructure by simulations[3]). Similarly, the long wavelength peak at λ_C^p and dip at λ_C^d can be attributed to the excitation of the PSP mode at the opposite interface of the structure with superstrate n_h.

In the next step, we performed more detailed simulations to reveal the spectral detuning of the resonances by the refrac-

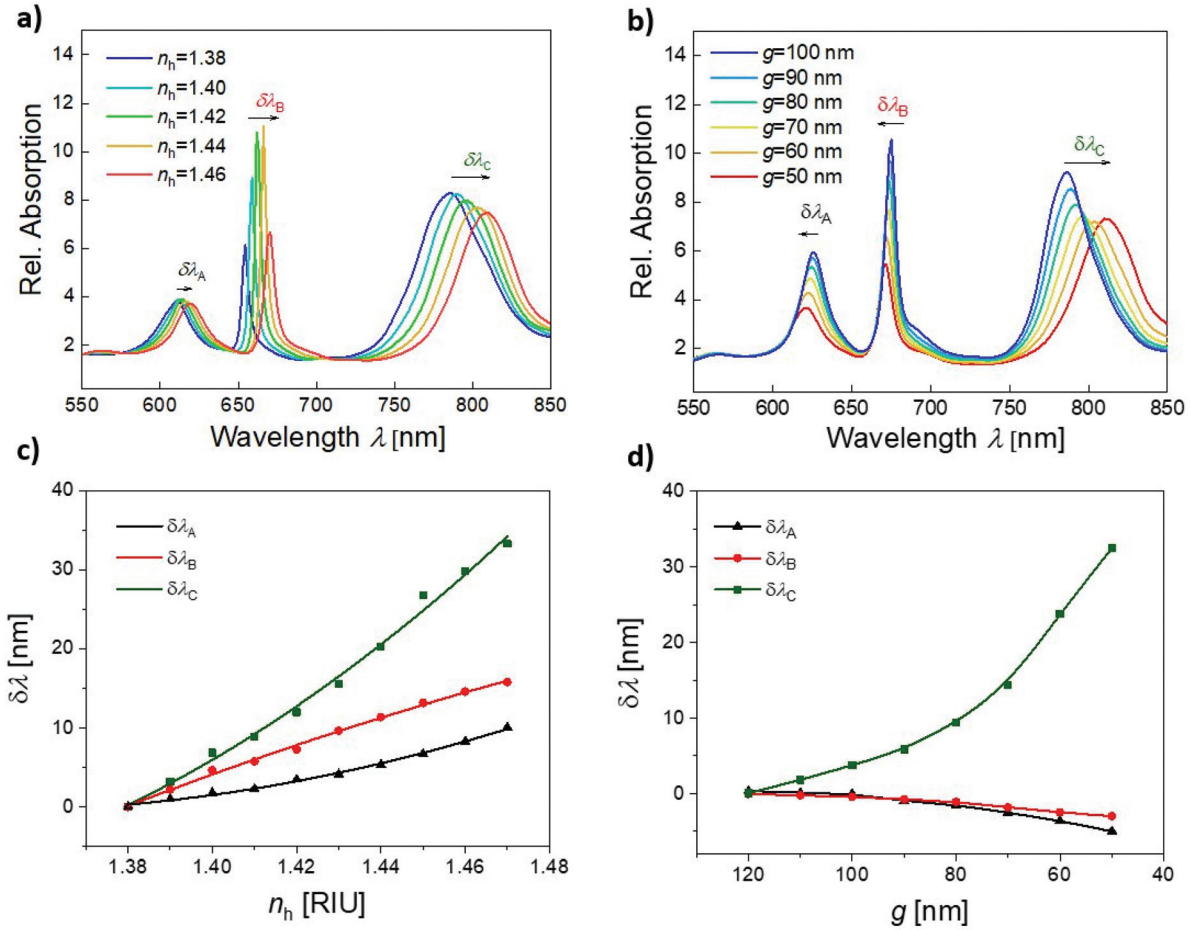

Fig. 5 Simulated absorption spectra for the structure NHA + NP for varying: (a) refractive index of substrate n_h and (b) distance g between NHA and NP. From these spectra, the spectral shift of three resonant features were determined for changes in (c) n_h and (d) g. The superstrate refractive index was set to n_s = 1.33, the substrate refractive index for (b) and (d) was n_h = 1.47, gap distance between NP and NHA for (a) and (c) was set as g = 50 nm, period was Λ = 460 nm, average diameter between D = 100–120 nm, and height h = 50 nm.

tive index changes of the bottom dielectric n_h and distance g between the gold NPs and NHA. These simulations represent the expected effect of the swelling and collapsing of the pNIPAAm-based hydrogel cushion. In general, an increase in swelling is assumed to be accompanied with a prolongation of distance g, a decrease in polymer volume content, and consequently a decrease in the refractive index n_h. Fig. 5a and b show that the refractive index n_h gradually increased from 1.38 to 1.46 and distance g varied between 50 and 100 nm, respectively. The increase in the substrate refractive index n_h led to a redshift for all three resonances (Fig. 5a), which is consistent with the experimental data presented in Fig. 3d. For small changes in the refractive index, the variations in the resonant wavelengths can be assumed to be linear, and accordingly, the determined refractive index sensitivity of $\delta\lambda_B/\delta n_h$ = 190 nm RIU^{-1} and $\delta\lambda_C/\delta n_h$ = 390 nm RIU^{-1} were obtained from the simulated data. These values are in the range reported for another SPR sensor configuration, which utilizes grating coupling to PSP modes.[47] The lower sensitivity of $\delta\lambda_A/\delta n_h$ = 90 nm RIU^{-1} for the LSP mode is also in accordance with the previous observations on LSPR.[44] Similarly, the refractive index sensitivity of the three plasmon modes to a change in the refractive index of the superstrate n_s was determined to be $\delta\lambda_A/\delta n_s$ = 137 nm RIU^{-1}, $\delta\lambda_B/\delta n_s$ = 260 nm RIU^{-1} and $\delta\lambda_C/\delta n_s$ = 83 nm RIU^{-1} according to the data presented in Fig. S2.† Apparently, the highest sensitivity is observed for the mode at λ_B, which is ascribed to the PSP at the outer interface, where the field is dominantly confined.

The simulated spectra for varying gap distances g are presented in Fig. 5b. They show more complex behavior and the resonances λ_A and λ_B are weakly blue-shifted with a decrease in distance g, while λ_C is strongly red-shifted. These changes exhibit non-linear behavior, and for the shorter distances of g, they are more pronounced than for the longer distances of g. Therefore, this observation can be attributed to the near-field coupling between the gold NPs and NHA, which is particularly pronounced for the resonance λ_C with its field tightly confined in the gap (see right part of Fig. 4b). Interestingly, for the long distance g, an increase in the absorption close to the wavelength of 700 nm occurred, which may be due to the re-occur-

rence of the LSP resonance supported by gold NP arrays not coupled with NHA, as presented in Fig. 4a.

Actuating of plasmonic modes

The swelling and collapsing of the pNIPAAm-based hydrogel cushion by varying the temperature around its LCST were further exploited for actuating the plasmonic modes supported by the prepared structure NHA + NP. In this experiment, we varied temperature in the range of T = 20–38 °C and tracked the resonant positions of all the identified spectral features, including the transmission dip at λ_A = 577 nm due to the LSP in the nanoholes, spectral dip at λ_B^d = 641 nm and peak at λ_B^p = 658 nm, which are ascribed to the Fano resonance of the PSPs on the top NHA surface, and spectral dip at λ_C^d = 684 nm and peak at a wavelength of λ_C^p = 825 nm attributed to the Fano resonance of PSP at the bottom NHA surface coupled with arrays of NPs (measured at temperature T = 20 °C). The obtained response was measured with time upon a step-wise increase and decrease in temperature T according to the analysis of the spectra presented in Fig. 3d. The obtained time kinetics in Fig. 6 show that the changes are reversible. The features presented in Fig. 6a show a gradual increase in spectral position with an increase in temperature T. The Fano resonance features λ_B^d and λ_B^p exhibit similar shifts and the maximum change of about 20 nm occurred when the temperature increased from T = 22 °C to 38 °C. The highest slope in the shift occurred close to the LCST of pNIPAAm of 32 °C. At a higher temperature, it was not possible to track the spectral shift in the peak due to the fact that it became weakly pronounced. The spectral dip λ_C^d showed the same trend and exhibited a stronger maximum shift of 40 nm for the temperature increase from T = 22 °C to 38 °C.

Interestingly, the dependence of λ_A and λ_C^p shows different behavior. When the temperature increased above T = 22 °C, an initial decrease in the resonance λ_A occurred followed by an increase with a local maximum at T = 29 °C, then it decreased again, and above the LCST of pNIPAAm, it rapidly increased and shifted by about 20 nm. The peak position λ_C^p showed a complementary trend and it strongly decreased by 15 nm when the temperature increased from 22 °C to 27 °C, and then it increased with the local maximum at 30 °C, and when passing the LCST it rapidly red-shifted by 38 nm. These anomalous dependencies can be explained by the competing effect of the near-field coupling (which is dominantly controlled by distance g and exhibit non-linear dependence, as shown in Fig. 5d) and refractive index change, which shifts the resonance linearly (see Fig. 5c). The anomalous changes occurred below the LCST of pNIPAAm, which indicates that distance g is not directly proportional to the swelling degree of the hydrogel cushion layer, and other effects such as filling the pores with the swelling polymer networks can occur.

Local probing of molecular binding events

To explore the potential of the developed hybrid nanostructure for applications in sensing, we employed the plasmonic resonances for local probing of molecular binding events at specific parts. In the first experiment, we directly monitored the binding of biomolecules in the pNIPAAm-based hydrogel cushion from the associated refractive index changes. These changes detuned the SPR wavelengths, where the excitation of the modes probing different the sub-parts of the structure occurred. After the stripping of the structure, the outer gold surface and the mouth of the pores were passivated by the thiol SAM with oligoethylene glycol (OEG) groups. Then, the pNIPAAm-based hydrogel cushion was post-modified *in situ* by covalent coupling of mouse immunoglobulin G, mIgG. The

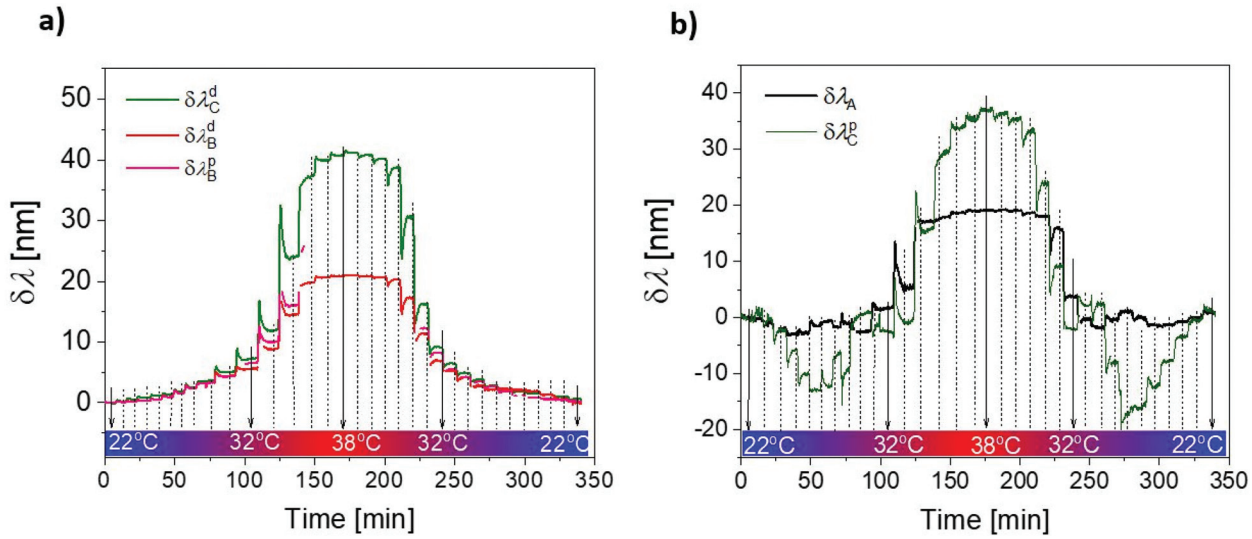

Fig. 6 Dependence of spectral position of plasmonic features plotted as function of time for different temperatures in the range of T = 22 °C to T = 38 °C: (a) gradual variation in the spectral positions of dips λ_B^d and λ_C^d and peak at λ_B^p and (b) anomalous variations in the spectral positions of dip λ_A and peak λ_C^p.

spectral positions of the resonances at λ_A and λ_C^d were monitored by tracking their spectral detuning upon the surface reactions, as can be seen in Fig. 7a. These two resonances were selected since they probe different parts of the structure and are well pronounced in the transmission spectrum. To activate the carboxylic groups within the hydrogel cushion, they were reacted with EDC/TFPS and then a solution with mIgG was flowed over the surface in the time range of 45 to 120 min. After rinsing with a buffer at time 120 min, resonance λ_C^d shifted by 6 nm due to the covalent coupling of mIgG, while resonance λ_A showed a much weaker shift of about 0.5 nm. This observation proves that the mIgG molecules could diffuse through the pores and bind to the bottom swollen hydrogel (probed at λ_C^d), while they do not attach to the pores (probed at λ_A). Then, a series of PBS solutions with sucrose dissolved at a concentration of 2%, 4% and 8% was flowed over the surface to change the bulk refractive index by 2.8, 5.6 and 11.2 × 10^{-3} RIU, respectively. These low molecular weight molecules did not interact with the structure but freely diffused into the pNIPAAm-based hydrogel, and thus changed the refractive index on both sides of superstrate n_s and substrate hydrogel cushion n_h. From the measured shifts in λ_A and λ_C^d, the sensitivity of these resonances was determined to be $d\lambda_A/d_n$ = 218 nm RIU^{-1} and $d\lambda_C^d/d_n$ 454 nm RIU^{-1}, respectively. These values are close to the predicted sum of the sensitivities $d\lambda/dn_s$ and $d\lambda/dn_h$ and support the fact that the refractive index changes at both interfaces of the permeable thin gold film.

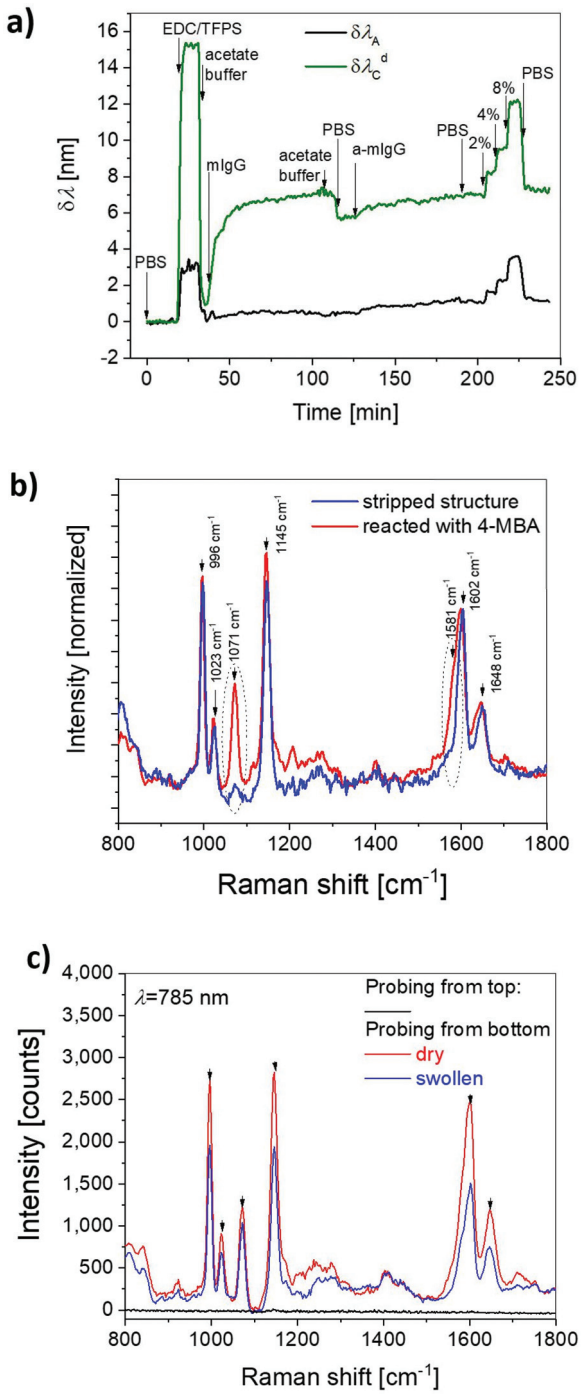

Fig. 7 (a) Probing of covalent coupling of immunoglobulin G molecules (IgG) to pNIPAAm hydrogel polymer networks with the plasmonic modes centred at λ_A and λ_C^d. (b) SERS spectra measured before and after post-modification of the stripped area of gold with 4-MBA, as measured with a laser wavelength of 785 nm. The structure NHA + NP was swollen in water. (c) Comparison of the acquired Raman spectra from the top (dry NHA + NP structure) and bottom (swollen and dry NHA + NP structure).

In the second experiment, we tested the structure as a substrate for SERS detection. Accordingly, we probed the upper and bottom interfaces by a laser beam focused from the superstrate or substrate side by a lens with a numerical aperture of 0.5. The laser beam had a wavelength of λ = 785 nm, which is close to the resonance observed at λ_C^p associated with the confinement of the incident field in the gap between the NHA and NP (see Fig. 4b). In this experiment, we directly used a structure that was stripped and compared the acquired Raman (Stokes shifted) spectra with that acquired for the same structure in which the upper gold surface and the pore mouth were modified with a Raman-active 4-MBA monolayer (see schematic in Fig. 1b). The results presented in Fig. 7b show a series of Raman peaks in the spectral range of 800–1800 cm^{-1} for the pristine stripped structure that was probed from the bottom substrate through the pNIPAAm-based cushion. These peaks can be ascribed to the benzophenone molecules at the inner gold interface since their spectral positions are close to that reported in previous works.[48] After modifying the pore mouth and the upper gold interface with 4-MBA, two additional peaks appeared at 1071 cm^{-1} (aromatic ring breathing, symmetric C–H in-plane bending, and C–S stretching) and 1581 cm^{-1} (aromatic ring C–C stretching, asymmetric C–H in-plane bending). These spectral positions are close to that observed previously for this molecule.[48,49]

Finally, a comparison of the Raman peak intensity was carried out for probing from the top (through the superstrate) and from the bottom (through the pNIPAAm cushion substrate). As can be seen in Fig. 7c, the Raman peaks were observed only for the probing from the bottom, where the mode at λ_C^p could be efficiently excited with the laser beam at the wavelength of 785 nm. In addition, the spectral tuning of

this mode by collapsing and swelling the structure led to variations in the Raman peak intensity. An increase in the Raman peak intensity by about 45% occurred by collapsing the structure (by drying) with respect to the geometry when the hydrogel cushion was swollen in water. This can be attributed to the potentially stronger field intensity enhancement in the gap between the nanopores in the NHA and the bottom metallic nanoparticles as well as the shift in the resonance at λ_C^p to its optimized spectral position with respect to the excitation wavelength and Raman scattered peaks, which was observed to provide most efficient SERS.[50–55]

Conclusions

We developed a new approach for the preparation of a hybrid plasmonic nanostructure that can be actuated and consists of arrays of nanoholes in a thin gold film, which is connected to arrays of gold nanoparticles by a responsive hydrogel cushion attached to a solid substrate. We explored the spectrum of the plasmonic modes supported by the structure and identified their origin due to the resonant excitation of three localized surface plasmons (confined in the nanopores and at the surface of the nanoparticles) and diffractive coupling to propagating surface plasmons (traveling along the top and bottom interfaces of the thin gold film). By swelling and collapsing the hydrogel cushion, the characteristics of these modes could be changed on-demand and the field confinement as well as resonant wavelength (up to 50 nm shifts) could be actively actuated. Among the modes, the near-field coupling between the nanoparticles and nanoholes was observed, and the simulations predicted that it leads to strong confinement of the electromagnetic field in the respective gap in the near-infrared part of the spectrum. This is particularly attractive for biosensing applications, as demonstrated by SPR observation of the attachment of 160 kDa IgG molecules inside the structure and SERS measurement of low molecular weight Raman active 4-MBA molecules immobilized in the pore mouth. In addition, this structure offers a unique opportunity to open and close the pores by swelling and collapsing the hydrogel cushion. Accordingly, the pores can be switched between the dead-end geometry and open state when water molecules are actively driven through the pores, dragging dissolved biomolecules across the plasmonic hotspot by diffusion.

Experimental

Materials

OrmoStamp® resin was purchased from Micro Resist Technology GmbH (Germany). Ostemer 322 Crystal Clear was purchased from Mercene Labs AB (Sweden). Polydimethylsiloxane Sylgard 184 (PDMS) was obtained from Dow Corning (USA). Trichloro (1*H*,1*H*,2*H*,2*H*-perfluorooctyl)silane (perfluoro-silane), dimethyl sulfoxide (DMSO) and 1-ethyl-3-(3-dimethylaminopropyl)carbodiimide (EDC) were obtained from Sigma Aldrich (Germany). (11-Mercaptoundecyl)triethylene glycol (PEG-thiol, SPT-0011) was purchased from SensoPath Technologies Inc. (USA). The pNIPAAm-based terpolymer composed of *N*-isopropylacrylamide, methacrylic acid, and 4-methacryloyloxybenzophenone (in a ratio of 94 : 5 : 1), benzophenone-disulfide and 4-sulfotetrafluorophenol (TFPS) were synthesized in our laboratory, as previously reported.[56,57] IgG from mouse serum (mIgG, I 5381) and Tween 20 (P9416) were purchased from Sigma Aldrich (Austria), and phosphate-buffered saline (PBS) and sodium acetate were obtained from VWR Chemicals (Austria). Goat anti-mouse IgG (a-mIgG, A11375) was acquired from Life Technologies, (Eugene OR, US).

UV-nanoimprint lithography

A template structure bearing arrays of nanopillars was fabricated from a silicon master that carried 1 cm^2 rectangular arrays of nanoholes with a diameter of D = 90 nm, depth 260 nm, and period Λ = 460 nm, fabricated by Temicon GmbH (Germany). 200 μL of OrmoPrime was spun on a clean BK7 glass substrate at 4000 rpm for 60 s and hard-baked at 150 °C for 5 min. The BK7 substrate coated with OrmoPrime was contacted with the silicon master using a drop of OrmoStamp and kept still for 10 min to spread over the structure and fill the pores. The OrmoStamp was cured using UV light at λ = 365 nm with the irradiation dose of 1 J cm^{-2} (UV lamp Bio-Link 365, Vilber Lourmat). Then, the silicon master was carefully detached, leaving the BK7 substrate with an imprinted pattern of nanopillars in the OrmoStamp resin. The fabricated arrays of nanopillars were treated with UV-ozone for 5 min to remove the excess OrmoStamp and activate the surface for silanization. An anti-adhesive layer was deposited on the OrmoStamp structure under an argon atmosphere using 13 μL of trichloro(1*H*,1*H*,2*H*,2*H*-perfluorooctyl)silane in a desiccator (volume 5.8 L) heated to T = 250 °C for 20 min. A 50 nm thin layer of gold was deposited on the arrays of nanopillars, serving as a template, by vacuum thermal evaporation (HHV AUTO 306 from HHV Ltd) at a deposition rate of 2 Å s^{-1} in a vacuum greater than 10^{-6} mbar. Each sample consisted of a nanostructured region and a flat region for reference in the optical measurements.

Deposition of the responsive polymer

The OrmoStamp arrays of nanopillars coated with 50 nm of gold were incubated overnight in a 1 mM solution of benzophenone-disulfide in DMSO to form a self-assembled monolayer serving as a linker. Then, this structure was coated with a uniform layer of pNIPAAm-based terpolymer by spin-coating 3 wt% ethanolic solution of the polymer at a spin rate of 2000 rpm for 1 min. The layer of the pNIPAAm-based terpolymer was dried overnight under vacuum at 50 °C yielding, a thickness of 230 nm. The resulting polymer film was crosslinked *via* the benzophenone moieties by UV light at λ = 365 nm with an irradiation dose of 10 J cm^{-2}.

Template stripping

A drop of Ostemer epoxy was spread on clean BK7 glass by contacting it with a flat piece of PDMS and irradiating it with UV-

light at λ = 365 nm (2 J cm^{-2}). The PDMS block was peeled-off leaving a glass substrate with a flat layer of pre-cured Ostemer epoxy on its top. Then, the Ostemer surface was pressed against the template coated with the crosslinked pNIPAAm-based film and incubated overnight at 50 °C to allow its attachment to the pNIPAAm-based surface *via* its epoxy groups. Due to the pre-curing step, the Ostemer did not penetrate the pNIPAAm polymer network layer. Finally, the BK7 substrate with a layer of Ostemer was used to strip off the pNIPAAm-based film with the layer of gold from the template modified with the thin anti-adhesive layer.

Morphological characterization

Atomic force microscopy (AFM) measurements of the patterned structures in air were performed in tapping mode using PPP-NCHR-50 tips (Nanosensors, Switzerland) and a PicoPlus instrument (Molecular Imaging, Agilent Technologies, USA). In addition, a scanning electron microscope (Zeiss Supra 40 VP (Carl Zeiss Microscopy GmbH, Germany) was used for imaging of the longitudinal and cross-section interfaces of the nanostructures at an electron high tension of EHT = 5 kV. The height, diameter and lateral spacing of the nanoscale features were determined using the Gwyddion free software (version 2.47 from gwyddion.net).

Optical configuration for angular-wavelength transmission measurement

Transmission optical spectra were acquired using a polychromatic light beam emitted from a halogen lamp (LSH102 LOT-Oriel, Germany), which was coupled to a multimode optical fiber and collimated with a lens. It was made incident at the structure and the transmitted beam was collected by a lens to another multimode optical fiber and delivered to a spectrometer (HR4000, Ocean Optics, USA). The obtained transmission spectra were normalized with that obtained on a reference flat 50 nm thick gold film. A flow-cell with a Peltier element[58] connected to a controller from Wavelength Electronics Inc. (USA) was clamped against the investigated structure to control the temperature of the liquid flowed over its surface. Deionized water was flowed by employing a peristaltic pump from Ismatec (Switzerland). The investigated structure with a flow cell was mounted on a rotation stage driven by a stepper motor from Huber GmbH (Germany) to control the angle of incident light, θ. Transmission spectra were recorded using the in-house developed Labview software and processed using a dedicated Python script.

Tracking of resonant wavelengths

Polychromatic light emitted from a supercontinuum laser source (WhiteLaser Micro, Fianium, UK) was collimated and the beam was expanded and spectrally filtered by a long-pass filter. The beam was made incident at a normal angle on the structure mounted in the temperature-stabilized flow cell. The transmitted beam was collected by a GRIN lens to a multimode fiber and delivered to the input of a spectrometer (S2000, Ocean Optics, USA). The acquired transmission spectra were normalized to that measured for a reference flat gold film (thickness of 50 nm) and analyzed using the SPR UP software developed at the Institute of Photonics and Electronics, Czech Academy of Sciences.

Finite-difference time-domain simulations

FDTD simulations were performed using the Lumerical FDTD Solutions software. The geometry of the nanoparticle arrays was described using Cartesian coordinates with the *x*- and *y*-axis in the plane and the *z*-axis perpendicular to the plane of the arrays. Infinite arrays were considered in the simulations by choosing periodic boundary conditions (symmetric or anti-symmetric) along the *x*- and *y*-axis and using perfectly matched layers (PML) above and below the structure. For the field profile simulations, the simulation mesh was set to 2 nm over the volume of the unit cell. A transmission monitor was placed 0.4 μm below the nanoparticle arrays and a 2D monitor in the *xz*-plane was employed for simulating the near field distribution of the electric field intensity. The structure was illuminated by a normally incident plane wave with its polarization set along the *x*-direction. The optical constants for Au were taken from the CRC Optical Data Tables (450–950 nm). To consider the deviations in the experimental geometry from the (idealized) simulated geometry, the diameter *D* was varied in the range of 100–120 nm and the respective optical response was averaged.

Immunoassay experiment

The substrate carrying the NHA + NP structure was clamped against a transparent flow-cell and loaded in an optical system for tracking of the SPR dips or peaks in the transmission spectrum. A polychromatic optical beam was made incident at a normal angle of incidence of θ = 0° at the structure, and by analysis of the transmitted light spectrum, the variations in the resonant wavelengths were monitored with time. These variations were determined by fitting the acquired spectrum with a polynomial function, as reported previously,[47] and which allowed the spectral shifts of the dip or peak features to be measured with the accuracy of 0.1–0.01 nm, depending on the coupling strength and noise in the transmission spectrum. Firstly, the baseline in the resonant wavelength kinetics was established upon a flow of PBS for 20 min. Then, a mixture of EDC/TFPS dissolved in water at concentrations 75 and 21 mg mL^{-1}, respectively, was flowed over the structure for 10 min to activate the carboxylic moieties of the pNIPAAm hydrogel. The surface was quickly rinsed with pH 5 acetate buffer and reacted with a solution of 50 μg mL^{-1} mouse IgG in the same buffer for 60 min to covalently attach the mIgG molecules to the polymer chains. Finally, the structure was rinsed with PBS, followed by the flow of PBS spiked with 2%, 4% and 8% sucrose (Δn = 2.8 × 10^{-3}, 5.6 × 10^{-3} and 11.2 × 10^{-3} RIU, respectively).

SERS experiments

The NHA + NP structure was incubated overnight in 1 mM ethanolic solution of 4-mercaptobenzoic acid to form a self-

assembled monolayer of SERS-active molecules. Prior to the experiment, the structure was rinsed with ethanol and dried. The SERS experiments were performed using an Xplora Raman microspectrometer (Horiba Scientific, France) with a ×50 long working distance objective (numerical aperture of 0.5). The laser beam at λ = 785 nm was focused at the investigated NHA + NP structure. The spectrum was accumulated for 20 s.

Conflicts of interest

There are no conflicts to declare.

Acknowledgements

DK acknowledges funding from the European Union's Horizon 2020 research and innovation programme under grant agreement no. 642787, Marie Sklodowska-Curie Innovative Training Network BIOGEL. SF, JS, JD, JH and UJ were supported by European Union's Horizon 2020 research and innovation programme under grant agreement no. 633937, project ULTRAPLACAD. PV, ML, and MDLC are grateful for the financing from the project jointly funded by Agence Nationale de la Recherche (ANR) and Austrian Science Fund (FWF) under the grant agreements ANR-15-CE29-0026 and I 2647, respectively. SF and JD received support by the Austrian Research Promotion Agency (FFG) with grant agreement no. 861578 (ERANET project PLABAN). JS and JH acknowledge financial support from the Czech Science Foundation, grant agreement #19-02739S. The Raman analysis was performed at the Vibrational Spectroscopy platform of the IMMM, Université du le Mans.

Notes and references

1 T. W. Ebbesen, H. J. Lezec, H. F. Ghaemi, T. Thio and P. A. Wolff, *Nature*, 1998, **391**, 667–669.
2 M. Najiminaini, F. Vasefi, B. Kaminska and J. J. L. Carson, *Sci. Rep.*, 2013, **3**, 1–7.
3 M. S. Ahn, T. Chung and K. H. Jeong, *Nanoscale*, 2018, **10**, 6313–6317.
4 A. G. Brolo, S. C. Kwok, M. G. Moffitt, R. Gordon, J. Riordon and K. L. Kavanagh, *J. Am. Chem. Soc.*, 2005, **127**, 14936–14941.
5 Q. Zhang, L. Wu, T. I. Wong, J. Zhang, X. Liu, X. Zhou, P. Bai, B. Liedberg and Y. Wang, *Int. J. Nanomed.*, 2017, **12**, 2307–2314.
6 A. G. Brolo, E. Arctander, R. Gordon, B. Leathem and K. L. Kavanagh, *Nano Lett.*, 2004, **4**, 2015–2018.
7 P. Zheng, S. K. Cushing, S. Suri and N. Wu, *Phys. Chem. Chem. Phys.*, 2015, **17**, 21211–21219.
8 S. Kumar, S. Cherukulappurath, T. W. Johnson and S. Oh, *Chem. Mater.*, 2014, **26**, 6523–6530.
9 T. Wu and Y. W. Lin, *Appl. Surf. Sci.*, 2018, **435**, 1143–1149.
10 S. P. Sahu, A. Mahigir, B. Chidester, G. Veronis and M. R. Gartia, *Nano Lett.*, 2019, **19**, 6192–6202.
11 M. E. Stewart, N. H. Mack, V. Malyarchuk, J. A. N. T. Soares, T.-W. Lee, S. K. Gray, R. G. Nuzzo and J. A. Rogers, *Proc. Natl. Acad. Sci. U. S. A.*, 2006, **103**, 17143–17148.
12 A. A. Yanik, A. E. Cetin, M. Huang, A. Artar, S. H. Mousavi and A. Khanikaev, *Proc. Natl. Acad. Sci. U. S. A.*, 2011, **108**, 11784–11789.
13 K. Nakamoto, R. Kurita, O. Niwa, T. Fujii and M. Nishida, *Nanoscale*, 2011, **3**, 5067–5075.
14 X. Li, M. Soler, C. I. Özdemir, A. Belushkin, F. Yesilköy and H. Altug, *Lab Chip*, 2017, **17**, 2208–2217.
15 H. Im, H. Shao, Y. I. Park, V. M. Peterson, C. M. Castro, R. Weissleder and H. Lee, *Nat. Biotechnol.*, 2014, **32**, 490–495.
16 A. A. Yanik, M. Huang, O. Kamohara, A. Artar, T. W. Geisbert, J. H. Connor and H. Altug, *Nano Lett.*, 2010, **10**, 4962–4969.
17 J. A. Jackman, E. Linardy, D. Yoo, J. Seo, W. B. Ng, D. J. Klemme, N. J. Wittenberg, S. H. Oh and N. J. Cho, *Small*, 2016, **12**, 1159–1166.
18 J. Gomez-Cruz, S. Nair, A. Manjarrez-Hernandez, S. Gavilanes-Parra, G. Ascanio and C. Escobedo, *Biosens. Bioelectron.*, 2018, **106**, 105–110.
19 L. Tu, X. Li, S. Bian, Y. Yu, J. Li, L. Huang, P. Liu, Q. Wu and W. Wang, *Sci. Rep.*, 2017, **7**, 11020.
20 J. T. Lim, Y. S. Yoon, W. Y. Lee, J. T. Jeong, G. S. Kim, T. G. Kim and S. K. Lee, *Nanoscale*, 2017, **9**, 17224–17232.
21 S. Kumar, G. G. Wolken, N. J. Wittenberg, E. A. Arriaga and S. H. Oh, *Anal. Chem.*, 2015, **87**, 1973–11977.
22 M. P. Jonsson, P. Jönsson, A. B. Dahlin and F. Höök, *Nano Lett.*, 2007, **7**, 3462–3468.
23 L. Plucinski, M. Ranjan, W. R. Arnold, A. Ameen, T. Chang, A. Hsiao, G. Logan and A. Das, *Biosens. Bioelectron.*, 2016, **75**, 337–346.
24 W.-C. Liu and T. D. Ping, *Phys. Rev. B: Condens. Matter Mater. Phys.*, 2002, **65**, 155423.
25 F. J. Garcia-Vidal, L. Martin-Moreno, T. W. Ebbesen and L. Kuipers, *Rev. Mod. Phys.*, 2010, **82**, 729–787.
26 M. Horak, V. Krapek, M. Hrton, A. Konecna, F. Ligmajer, M. Stoeger-Pollach, T. Samoril, A. Patak, Z. Edes, O. Metelka, J. Babocky and T. Sikola, *Sci. Rep.*, 2019, **9**, 4004.
27 L. Wang, B. Xu, W. Bai, J. Zhang, L. Cai, H. Hu and G. Song, *Plasmonics*, 2012, **7**, 659–663.
28 C. Stelling and M. Retsch, *Adv. Mater. Interfaces*, 2018, **5**, 1–7.
29 R. Mohammadi, M. Ochs, A. Andrieu-Brunsen and N. Vogel, *J. Phys. Chem. C*, 2020, **124**, 2609–2618.
30 M. Hentschel, T. Weiss, S. Bagheri and H. Giessen, *Nano Lett.*, 2013, **13**, 4428–4433.
31 V. G. Kravets, A. V. Kabashin, W. L. Barnes and A. N. Grigorenko, *Chem. Rev.*, 2018, **118**, 5912–5951.
32 J. F. Masson, M. P. Murray-Méthot and L. S. Live, *Analyst*, 2010, **135**, 1483–1489.

33 C. Escobedo, *Lab Chip*, 2013, **13**, 2445–2463.
34 H. Im, S. H. Lee, N. J. Wittenberg, T. W. Johnson, N. C. Lindquist, P. Nagpal, D. J. Norris and S. H. Oh, *ACS Nano*, 2011, **5**, 6244–6253.
35 S. H. Lee, K. C. Bantz, N. C. Lindquist, S.-H. Oh and C. L. Haynes, *Langmuir*, 2009, **25**, 13685–13693.
36 B. Ai, Y. Yu, H. Möhwald, G. Zhang and B. Yang, *Adv. Colloid Interface Sci.*, 2014, **206**, 5–16.
37 J. Junesch, T. Sannomiya and A. B. Dahlin, *ACS Nano*, 2012, **6**, 10405–10415.
38 H. Im, J. N. Sutherland, J. A. Maynard and S.-H. Oh, *Anal. Chem.*, 2012, **84**, 1941–1947.
39 A. Barik, L. M. Otto, D. Yoo, J. Jose, T. W. Johnson and S. H. Oh, *Nano Lett.*, 2014, **14**, 2006–2012.
40 J. Dostálek and W. Knoll, *Plasmonics*, 2012, vol. 2.
41 Y. Zhao, G. Gaur, S. T. Retterer, P. E. Laibinis and S. M. Weiss, *Anal. Chem.*, 2016, **88**, 10940–10948.
42 C. Escobedo, A. G. Brolo, R. Gordon and D. Sinton, *Anal. Chem.*, 2010, **82**, 10015–10020.
43 N. Sharma, C. Petri, U. Jonas and J. Dostalek, *Opt. Express*, 2016, **24**, 2457.
44 N. Gisbert Quilis, M. van Dongen, P. Venugopalan, D. Kotlarek, C. Petri, A. Moreno Cencerrado, S. Stanescu, J. L. Toca Herrera, U. Jonas, M. Möller, A. Mourran and J. Dostalek, *Adv. Opt. Mater.*, 2019, **7**, 1–11.
45 N. Sharma, H. Keshmiri, X. Zhou, T. I. Wong, C. Petri, U. Jonas, B. Liedberg and J. Dostalek, *J. Phys. Chem. C*, 2016, **120**, 561–568.
46 A. Aulasevich, R. F. Roskamp, U. Jonas, B. Menges, J. Dostálek and W. Knoll, *Macromol. Rapid Commun.*, 2009, **30**, 872–877.
47 A. T. Reiner, N. G. Ferrer, P. Venugopalan, R. C. Lai, S. K. Lim and J. Dostálek, *Analyst*, 2017, **142**, 3913–3921.
48 Y. Fleger, Y. Mastai, M. Rosenbluh and D. H. Dressler, *Surf. Sci.*, 2009, **603**, 788–793.
49 N. G. Quilis, M. Lequeux, P. Venugopalan, I. Khan, W. Knoll, S. Boujday, M. L. de la Chapelle and J. Dostalek, *Nanoscale*, 2018, **10**, 10268–10276.
50 S. J. Lee, Z. Guan, H. Xu and M. Moskovits, *J. Phys. Chem. C*, 2007, **111**, 17985–17988.
51 M. Chirumamilla, A. Gopalakrishnan, A. Toma, R. P Zaccaria and R. Krahne, *Nanotechnology*, 2014, **25**, 235303.
52 N. Guillot and M. L. de la Chapelle, *J. Quant. Spectrosc. Radiat. Transfer*, 2012, **113**, 2321–2333.
53 N. Guillot, B. Fremaux, H. Shen, O. Péron, E. Rinnert, T. Toury and M. Lamy De La Chapelle, *Appl. Phys. Lett.*, 2010, **97**, 023113.
54 S. Kessentini, D. Barchiesi, C. D'Andrea, A. Toma, N. Guillot, E. Di Fabrizio, B. Fazio, O. M. Maragó, P. G. Gucciardi and M. Lamy De La Chapelle, *J. Phys. Chem. C*, 2014, **118**, 3209–3219.
55 F. J. Colas, M. Cottat, R. Gillibert, N. Guillot, N. Djaker, N. Lidgi-Guigui, T. Toury, D. Barchiesi, A. Toma, E. Di Fabrizio, P. G. Gucciardi and M. L. De La Chapelle, *J. Phys. Chem. C*, 2016, **120**, 13675–13683.
56 P. W. Beines, I. Klosterkamp, B. Menges, U. Jonas and W. Knoll, *Langmuir*, 2007, **23**, 2231–2238.
57 K. Sergelen, C. Petri, U. Jonas and J. Dostalek, *Biointerphases*, 2017, **12**, 051002.
58 M. Toma, U. Jonas, A. Mateescu, W. Knoll and J. Dostalek, *J. Phys. Chem. C*, 2013, **117**, 11705–11712.

Appendix VI

Surface-Enhanced Raman Scattering (SERS) on Gold Nanohole Arrays in Symmetrical Dielectric Environments Exhibiting Electric Field Extension

Galvan, D., Špačková, B., Slabý, J., Sun, F., Ho, Y-H. Homola, J. and Yu, Q.

Journal of Physical Chemistry C, 2016. **120**, 25519–25529.

THE JOURNAL OF PHYSICAL CHEMISTRY C

Article

pubs.acs.org/JPCC

Surface-Enhanced Raman Scattering on Gold Nanohole Arrays in Symmetrical Dielectric Environments Exhibiting Electric Field Extension

Daniel David Galvan,[†] Barbora Špačková,[‡] Jiří Slabý,[‡] Fang Sun,[†] Yu-Han Ho,[†] Jiří Homola,*[,‡] and Qiuming Yu*[,†]

[†]Department of Chemical Engineering, University of Washington, Seattle, Washington 98195, United States

[‡]Institute of Photonics and Electronics, The Czech Academy of Sciences, 182 51 Prague, Czech Republic

Supporting Information

ABSTRACT: The electromagnetic enhancement in surface-enhanced Raman scattering (SERS) caused by localized surface plasmon resonance is a near-field effect, often limiting the practicality of SERS in many applications. However, no attempts have been made to investigate field extension through symmetrical refractive index modulation in a SERS-based system. Here, we report the development and characterization of refractive index-matched SERS substrates supporting electric field extension to realize what is termed "long-range SERS" (LR-SERS). Finite-difference time-domain simulations were employed to tune the plasmonic responses and investigate electric field distributions of gold nanohole arrays (NHAs) as a function of the dielectric environment and geometric parameters. SERS substrates supporting long-range behavior were compared against "conventional" substrates without long-range behavior. SERS intensities from rhodamine 6G (R6G) aqueous solutions of 2.0×10^3 and 1.5×10^2 counts s^{-1} mW^{-1} were produced by the LR-SERS and conventional substrates, respectively, on the gold surface. Moreover, a signal response of 9.0×10^1 counts s^{-1} mW^{-1} was produced by LR-SERS substrates with a 10 nm separation between the R6G solution and NHA, while no signal was observed from the conventional substrate. As a proof of principle study, the results demonstrate the potential to use LR-SERS substrates in applications where the target analyte is located further from the SERS-active surface.

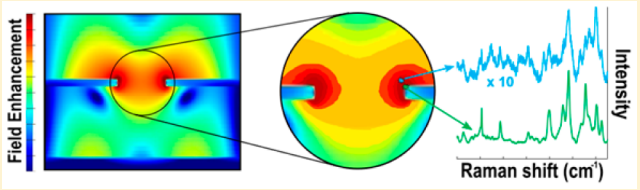

INTRODUCTION

Surface-enhanced Raman scattering (SERS) is a sensitive spectroscopic technique that has been used in a variety of fields of study, including biomedicine,[1] environmental science,[2] and homeland security,[3] and with proper experimental considerations has realized single-molecule detection.[4,5] The bifurcated SERS mechanism consists of electromagnetic (EM) and chemical (CM) contributions that enhance the Raman scattering efficiency.[6] Chemical enhancement is attributed to charge transfer between adsorbed molecules and the metal surface, whereas EM enhancement is due to amplified electric fields generated by localized surface plasmon resonance (LSPR) on nanostructured, noble metal surfaces. While the CM mechanism contributes to the enhancement by a factor of $\sim 10^1 - 10^2$,[7] the EM enhancement is generally accepted as dominant with enhancement factors up to $10^7 - 10^9$.[8] However, the amplified electric fields responsible for EM enhancement decay rapidly from nanostructured surfaces. Multiple studies have been conducted to investigate the distance at which the SERS intensity decays from nanostructured surfaces, including ultrathin cladding layers[9] and alkanethiols[10] on electrochemically roughened Ag films, atomic layer deposition of Al_2O_3 on Ag nanodots fabricated via nanosphere lithography,[11] SiO_2-coated Ag nanosphere dimers,[12] and DNA conjugated with Raman probes on Au nanoparticles.[13] Results vary from substrate to substrate and because of differences in the experimental setup, but there is agreement that within ~5 nm from the sensing surface the SERS signal is effectively diminished. Thus, SERS is considered a near-field effect, and although a molecule does not need to be adsorbed to the surface to undergo excitation, it must be within the immediate vicinity of the light-coupling nanostructure. The shortcomings created by the near-field effect necessitate the development of SERS substrates with "long-range" capability through electric field extension, enabling molecular detection at distances beyond the current SERS-active substrates.

One route to achieve field extension in SERS-active substrates is to create metal/dielectric interfaces that support long-range surface plasmon resonance (LR-SPR). LR-SPR is a unique SPR mode. Generally, SPR is the cumulative oscillation of conduction band electrons induced through coupling to the electric field component of incident light at the interface of metal and dielectric materials.[14] Evanescent waves produced on SPR-supporting 50 nm gold films on glass substrates ($n \sim 1.52$)

Received: August 16, 2016
Revised: October 10, 2016
Published: October 13, 2016

DOI: 10.1021/acs.jpcc.6b08294
J. Phys. Chem. C 2016, 120, 25519−25529

extend into the metal film and aqueous dielectric environment (n = 1.33), with penetration depths of 25 and 400 nm, respectively, for near-infrared excitation.[15] LR-SPR is excited when the metal film is made ultrathin (i.e., ∼ 20 nm) and placed in a symmetrical dielectric environment (i.e., the refractive indices on either side of the film are equal).[16] The two stipulations allow the evanescent waves at opposite interfaces to couple, thus producing LR-SPR. The main features offered by LR-SPR include strong electric fields at the metal surface, narrow reflectance bands, and extended electric field penetration depths. Typical penetration depths in LR-SPR are 1.2 μm, compared to 400 nm for conventional SPR.[15,16] LR-SPR was first theoretically predicted by solving the SPR dispersion relation as a function of metal film thickness[17] and later experimentally verified by determining the propagation and attenuation constants of thin metal films.[18] Since then, LR-SPR has been implemented in a variety of SPR biosensing studies including antibody−antigen binding events,[19] SPR-coupled fluorescence emission,[20] and sensitive biosensing for bacterial[21] and eukaryotic cells.[22]

LR-SPR generated with ultrathin Ag films has demonstrated the long-range SERS (LR-SERS) effect. Liu et al. utilized the Kretschmann configuration to generate LR-SPR by separating an ultrathin Ag film (16 nm) with a 1750 nm thick MgF_2 layer (n = 1.38) from the underlying glass substrate.[23] Because the refractive index of MgF_2 is close to that of water (n = 1.33), the Ag film satisfied the symmetrical dielectric condition and thus supported LR-SPR generation. The extended electric fields produced by the LR-SPR enabled detection of 4-mercaptopyridine monolayers SERS signals at a distance of ∼500 nm from the Ag film. Later work by the researchers used the same device architecture with the addition of Ag nanoparticles (NPs) into the aqueous solution to increase the sensitivity through Ag film−NP coupling.[24] Here, however, it is important to note that the Ag NPs themselves are not responsible for the long-range effect, but rather it is the LR-SPR-supporting, planar Ag films.

In this work, we designed SERS-active plasmonic nanostructures on a dielectrically symmetrical, layered substrate to capitalize on the beneficial electric field characteristics made available by LR-SPR. We systematically investigated the resonant modes and electric field distributions of two-dimensional (2-D), square-lattice nanohole arrays (NHAs) of ultrathin gold films on three classes of layered substrates (Figure 1a) immersed in water using the finite-difference time-domain (FDTD) method. Conventional and pseudo long-range (PLR) substrates were used to study the SERS response of the asymmetrical and symmetrical dielectric conditions, respectively. A "resonant mirror" was inserted between the glass/Cytop interface in PLR substrates to induce strong constructive interference on the surface of gold NHAs due to the formation of Fabry−Pérot optical cavity between the resonant mirror and NHA. The trilayered, Fabry−Pérot containing structure is referred as the "long-range" SERS (LR-SERS) class of substrates. Optical and geometrical parameters were varied, and electric field extension was observed in the LR-SERS substrates. Following the theoretical investigation, the three classes of substrates were fabricated, and the SERS response was measured as a function distance from the Au/H_2O interface. Long-range behavior was experimentally demonstrated with successful detection of Raman reporters separated 10 nm from the gold NHA surface. The extended probing depth afforded by LR-SERS substrates make them an interesting platform to further explore fundamental and applied SERS studies.

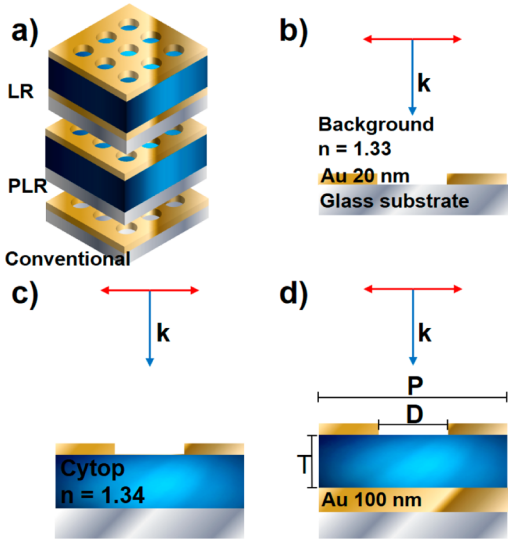

Figure 1. (a) Three-dimensional schematics for the three types of SERS substrates investigated: long-range (LR), pseudo long-range (PLR), and conventional. Illustrations of the unit cells used in the FDTD simulations for (b) the conventional SERS substrate, (c) the PLR SERS substrate, and (d) LR-SERS substrate. The 2-D lattice pitch (P) and the gold film thicknesses of NHAs were fixed to 604 and 20 nm, respectively, for all three classes of substrates. For the LR-SERS structures, the underlying gold mirror was fixed at 100 nm.

MATERIALS AND METHODS

Chemicals and Reagents. Rhodamine 6G (R6G), (3-mercaptopropyl)trimethoxysilane (3-MPTMS), 4-mercaptobenzoic acid (4-MBA), and trichloro(1H,1H,2H,2H-perfluorooctyl)silane were purchased from Sigma-Aldrich (St. Louis, MO). Vinylmethlysiloxane (VDT-731), 1,3,5,7-tetravinyl-1,3,5,7-tetramethylcyclotetrasiloxane (SIT7900.0), platinum catalyst (SIP6831.2), and methylhydrosiloxane (HMS-301) were purchased from Gelest (Morrisville, PA). The Sylgard 184 PDMS and curing agent elastomer kit was purchased from Dow Corning (Midland, MI). Poly(methyl methacrylate) (PMMA, 950PMMA A6) was purchased from MircoChem (Westborough, MA). Cytop CTL-809 M and additional solvent (CT-SOLV180) were purchased from Asahi Glass (Tokyo, Japan). All materials were used as received.

Finite-Difference Time-Domain Simulations. Commercially available software (Lumerical, FDTD Solutions) was used to investigate the plasmonic properties of three types of SERS structures. The three classes of structures investigated contained a 20 nm thick gold nanohole array (NHA) on (1) a glass substrate, (2) a Cytop-coated glass substrate, and (3) a Cytop-coated glass substrate with a 100 nm thick gold film inserted between the Cytop layer and glass substrate, which are termed the conventional, pseudo long-range (PLR), and long-range (LR) substrates, respectively. The three-dimensional (3-D) unit cell used in the simulations was defined in the xy plane by the pitch of the substrate (P = 604 nm) and in the vertical dimension by extending 500 nm above the Au/H_2O interface and 500 nm below the Au/glass (or Cytop/glass) interface. A plane wave in the spectral window of 700−950 nm was impinged from a distance of 400 nm above and normal to the surface, with the electric component polarized along the x-axis.

DOI: 10.1021/acs.jpcc.6b08294
J. Phys. Chem. C 2016, 120, 25519−25529

A frequency monitor was placed 450 nm above the Au/H_2O interface to collect reflectance spectra. Power monitors were placed at the Au/H_2O interface, distances of 5, 10, 25, and 50 nm above the Au/H_2O interface, and through the center of the nanohole in the *xz*-plane to collect electric field intensities and distributions. Periodic boundary conditions were used in the *x* and *y* directions, while the perfectly matched layer (PML) boundary condition was used in both *z* directions. Stringent meshing was added around the nanohole by refining the mesh size to 2 nm in all spatial dimensions. The fine mesh around the nanohole encompassed the entire *xy* plane and was extended 60 nm from the two nanohole array interfaces. Convergence was ensured by continually reducing the mesh refinement in the vicinity of the nanostructures until the relative location or peak intensities remained stable. Additionally, the number of PML layers was maximized to prohibit reflections from reentering the simulation cell. The relative dielectric functions for the Cytop films, glass substrates, and aqueous backgrounds were taken as constants with relative refractive indices of 1.34, 1.52, and 1.33, respectively, while the dielectric function of gold was taken from the literature and fit with a multicoefficient model.[25]

Substrate Fabrications and Characterizations. Gold NHAs were fabricated using solvent-assisted molding (Figure S1).[26] A silicon master mold with 100 μm × 100 μm nanopillar arrays was fabricated using electron beam lithography and reactive ion etching. The nanopillar arrays are defined by a pitch of 604 nm, height of 150 nm, and diameter of 300 nm. h-PDMS/PDMS composite stamps containing nanoholes were cast from the silicon master. All substrates were fabricated using the same composite stamp to form the nanostructures.

For the conventional structures, glass substrates (1 cm^2) were sequentially cleaned by ultrasonication in soapy deionized (DI) H_2O, DI H_2O, acetone, and IPA for 20 min each at 40 °C and were placed in an ultraviolet−O_3 cleaner for 20 min. An adhesion promoter (3-MPTMS) was formed by placing the cleaned substrates in a vacuum desiccator with a 50 μL drop of 3-MPTMS for 2 h. A 3% by weight solution of PMMA in anisole was immediately spun cast at 4000 rpm for 40 s, and the sample was baked on a hot plate at 180 °C for 90 s to form a uniform film of ∼100 nm. A 14 μL drop of acetone was placed on the stamp. The PMMA-coated substrate was then brought into contact with the composite stamp on a hot plate at 60 °C for 5 min to form PMMA nanopillars. To remove residual PMMA between nanopillars, the substrate was then placed in an oxygen plasma cleaner (Diener, 50 W) with air as the flowgas for 90 s. It is important to note that both solvent-assisted molding and plasma etching shrink the diameter of the PMMA nanopillars from 300 to 150 nm. Finally, 20 nm gold films were thermally evaporated (Edwards Auto306) onto the substrates at a rate of 0.02 nm/s with a base pressure of 2 × 10^{-6} mbar. The fabrication of the conventional substrates was completed by removal of PMMA nanopillars capped with gold nanodisks through a lift-off process consisting of tape striping and rinsing with copious amounts of acetone.

PLR substrates were fabricated by spin coating Cytop films directly onto the cleaned glass substrates and annealing on a hot plate at 100, 150, and 200 °C for 60, 30, and 30 min, respectively. Cytop films were exposed to oxygen plasma for 30 s prior to spinning 3% PMMA to increase the surface energy of Cytop to make smooth, strongly adhered PMMA films. The gold NHAs were fabricated following the same steps as described for the conventional substrates.

LR substrates were fabricated by first forming a 3-MPTMS adhesion promoter on clean glass substrates following the same procedures as with the conventional substrates. An optically opaque gold film (100 nm) was then thermally evaporated. The adhesion robustness of the Au films on the glass substrates was qualitatively assessed by "Scotch tape" and ultrasonication tests. Control substrates that lacked the 3-MPTMS promoter were found to completely delaminate after both tests, whereas the substrates that contained the 3-MPTMS promoter were found to create stable films that remained adhered to the glass substrates. Cytop was immediately spun cast onto the gold film and annealed with the same recipe as the PLR substrates. Then, the gold NHAs were fabricated following the same steps as described for the conventional substrates. Fabricated NHAs on conventional, PLR, and LR substrates were characterized using scanning electron microscopy (Sirion XL30, FEI). SEM images of the conventional and LR substrates show that the NHAs were resolved with good quality (Figure S2).

SERS Measurements on Conventional and PLR Substrates. Monolayers of 4-MBA were formed on conventional and PLR substrates. First, substrates were cleaned via UV−O_3 exposure for 20 min. 4-MBA was dissolved in a 10% ethanol:DI H_2O (by volume) solution to a concentration of 1 mM. The conventional and PLR substrates were immersed in the 4-MBA solution for 6 h, rinsed thoroughly with ethanol and DI H_2O, and dried in air. SERS measurements were immediately conducted. The substrates were immersed in DI H_2O in a home-built Teflon container and covered with a microscope slide to prevent water evaporation while collecting the SERS spectra. The distance from the NHA surface to the coverslip was ∼500 μm. All SERS measurements were carried out using a Renishaw inVia Raman spectroscope connected to a Leica upright DMLM microscope. A 785 nm near-infrared laser was focused with a 50× objective (N.A. 0.8, W.D. 0.5 mm) to form a laser spot size of ∼2 μm × 20 μm, which allowed for multiple measurements to be taken from different locations on the nanohole array. The laser power was measured with a hand-held laser power meter (Edmund Optics) in the focal plane of the substrates to be 2.4 mW. The acquisition time was set to 10 s with a single accumulation. The raw data were acquired by the Wire 2.0 software (Renishaw). All spectra were analyzed and baseline corrected using MATLAB.

Distance Dependence of LR and Conventional Substrates. LR and conventional substrates were cleaned by UV−O_3 exposure for 20 min. Aqueous solutions of R6G (1 mM) were then dropped on the substrates in 200 μL aliquots and remained for 30 min to allow R6G adsorption. The R6G solution was then removed from the substrates. The substrates were dried and placed in the Teflon holder. The Teflon holder was then filled with DI H_2O (200 μL) and covered with a microscope slide. SERS spectra of R6G were acquired immediately with a single 10 s accumulation time, using the same setup described in the previous section. Cytop capping layers of ∼10 nm were spun cast on freshly fabricated LR and conventional substrates by diluting the stock Cytop solution with CT-180 SOLV in a 20:1 ratio (v:v) at 3000 rpm for 40 s. All film thicknesses were measured by ellipsometry (α-SE, J.A. Woollam) and profilometry (Alpha-Step 500, KLA Tencor). R6G (1 mM) was again allowed to adsorb to the surface for 30 min before removal and subsequent immersion in DI H_2O. SERS spectra were immediately acquired and processed as previously described.

DOI: 10.1021/acs.jpcc.6b08294
J. Phys. Chem. C 2016, 120, 25519−25529

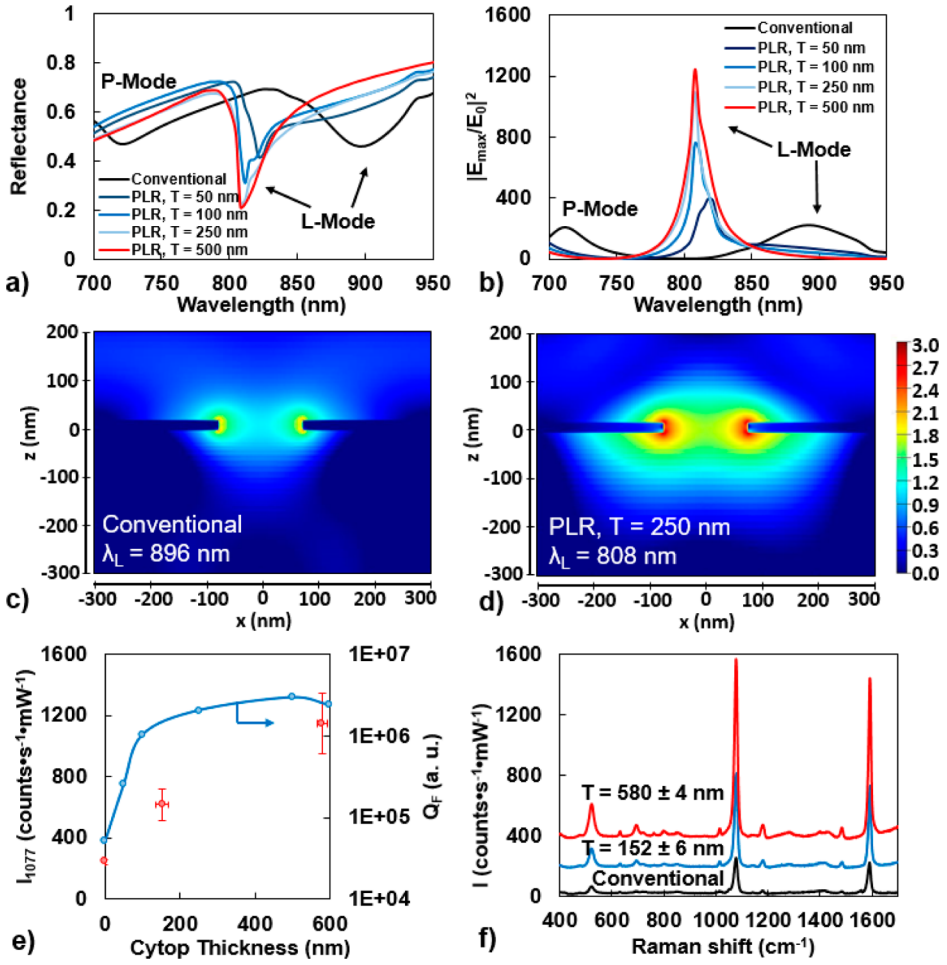

Figure 2. (a) Reflectance spectra and (b) maximum electric field intensity ($|E_{max}/E_0|^2$) at the Au/H_2O interface as a function of wavelength for conventional and PLR substrates with increasing Cytop thickness; cross-sectional view of the electric field distributions of (c) the conventional substrate and (d) PLR substrate with T = 250 nm in the x−z plane. The intensity was normalized to the incident light (E_0 = 1 V m^{-1}). The localized (L) and propagating (P) modes have been labeled. The scale bar represents $|E_{max}/E_0|^2$ on a log scale. (e) Quality factor (Q_F) and intensity of the 1077 cm^{-1} band as a function of Cytop thickness. Quality factors were calculated from the electric field intensities obtained from FDTD simulations. Error bars represent three standard deviations from SERS and profilometry measurements collected from different locations on the individual 100 μm × 100 μm arrays. (f) SERS spectra of 4-MBA monolayers collected on conventional and PLR SERS substrates. Spectra have been offset by 200 counts·s^{-1}·mW^{-1} for clarity. All spectra were collected in a single 10 s accumulation, with a 2.4 mW laser, measured through a 50× (N.A. 0.8) objective.

RESULTS AND DISCUSSION

Single nanohole and arrays of nanoholes can act as point sources for the excitation of SPR.[27] The theoretical pitch necessary to generate SPR with light at normal incidence to a 2-D grating coupler can be predicted by[28]

$$\frac{\lambda}{P}\sqrt{m_x^{\,2} + m_y^{\,2}} = \mathrm{Re}\left\{\sqrt{\frac{\varepsilon_d \varepsilon_m}{\varepsilon_d + \varepsilon_m}}\right\} + \Delta n_{ef} \quad (1)$$

where P is the pitch of neighboring nanostructures; m_x and m_y are integers corresponding to grating orders of the diffracted light; λ is the resonant wavelength of a surface plasmon; ε_d and ε_m are the relative permittivities of the surrounding dielectric media and metal, respectively; Δn_{ef} accounts for the difference in the propagation of the surface plasmon on a planar film relative to the grating. Additionally, Δn_{ef} accounts for the differences of single-interface (asymmetric) and long-range (symmetric) surface plasmons. It is commonly accepted that the optimal wavelength of LSPR (λ_{LSPR}) for SERS substrates exhibiting a Lorentzian-shaped LSPR peak can be described by[29]

$$\lambda_{LSPR} = \frac{1}{2}(\lambda_{Ex} + \lambda_{RS}) \quad (2)$$

where λ_{Ex} and λ_{RS} correspond to the wavelengths of the excitation source and the inelastically scattered Raman photons, respectively. The validity of this equation holds for LSPR that overlap with the wavelength of the Raman scattered photons and the wavelength of excitation. Generally, this holds true so long as the three wavelengths of interest fall within a ∼120 nm window of one another.[29] In this work, a 785 nm near-infrared laser was used as an excitation source, and Raman shifted photons were collected in the range of 300−1800 cm^{-1}. Therefore, as dictated by eq 2, λ_{LSPR} should be tuned within the spectral window of 794−849 nm for optimal SERS response. For this work, λ_{LSPR} = 800 nm was selected in order to determine the NHA pitch. Using eq 1, a pitch of 604 nm was predicted for a 20 nm gold film perforated with a 2-D NHA immersed in an aqueous medium (n_d = 1.33). Values for the

DOI: 10.1021/acs.jpcc.6b08294
J. Phys. Chem. C 2016, 120, 25519−25529

relative permittivity of gold[25] and Δn_{ef}[28] were taken from the literature.

FDTD simulations were carried out to investigate the resonant modes and electric field distributions of the three classes of plasmonic nanostructures (Figure 1a). Initially, FDTD simulations were performed to compare the plasmonic resonances and the electric field distributions as the dielectric environment surrounding the NHA was converted from the asymmetric (i.e., the conventional substrate) to the symmetrical (i.e., PLR substrate) condition. Panels b and c of Figure 1 show the unit cells used in FDTD simulations for the conventional and PLR substrates, respectively. For reference, the LR simulation cell is presented in Figure 1d. Relative dielectric functions for the gold film were obtained from the literature[25] and fit with a multicoefficient model as a function of wavelength, while the relative dielectric functions for the Cytop films, glass substrates, and aqueous background were taken as constants with corresponding refractive indices of 1.34, 1.52, and 1.33, respectively. For the entirety of the simulations, both classes of substrates had 2-D square lattice periods, diameters, and gold film thicknesses of 604, 150, and 20 nm, respectively. To monitor the dielectric transition, the gold NHA was incrementally separated from the glass substrate by incorporation of Cytop cladding layers.

Two resonant modes are observed at 712 and 892 nm for the conventional substrate as shown in the reflectance spectrum in Figure 2a, which correspond to the propagating mode (P-mode) and localized mode (L-mode), respectively. Mode assignment was determined by the properties of the z-component of the electric field distribution (E_z) shown in Figure S3 of the Supporting Information. The E_z polarity oscillation propagated along the two interfaces throughout the entire unit cell for the P-mode (Figure S3a), while the oscillation was completely confined to the nanohole edges for the L-mode (Figure S3b). The cross-sectional total electric field ($E_x^2 + E_y^2 + E_z^2$) distribution of the L-mode also showed confined electric fields at the nanohole edges (Figure 2c). The two modes exhibited similar maximum electric field intensities of $|E_{max}/E_0|^2 = \sim 2.1 \times 10^2$ at the Au/H_2O interface (Figure 2b). When a refractive index-matched Cytop layer was inserted between the gold NHA film and glass substrate, the dielectric environment surrounding the gold NHA transitioned from asymmetric to symmetric, that is, from the configuration of conventional to PLR substrates.

It is expected that the resonances are dependent on the Cytop thickness. Therefore, we varied the Cytop thickness of the interstitial layer from 50 to 100, 250, and 500 nm. The reflectance spectra in Figure 2a shows the L-mode blueshifted from 822 to 808 nm for Cytop thicknesses of 50 and 500 nm, respectively, while the P-mode blueshifted outside of the 700 nm spectral window minimum. Additionally, the L-mode generated by the PLR substrates exhibited a narrower reflectance dip compared to the L-mode of the conventional substrate. The L-mode comprises two peaks, a strong peak and slightly red-shifted shoulder mode. The shoulder mode is much more pronounced for thinner Cytop films, and the two modes coalesced as the Cytop thickness was increased. The E_z distributions of the PLR substrates with these four Cytop thicknesses displayed the same confinement at the nanohole edges (Figure S4), confirming the characteristics of the L-mode.

The maximum electric field intensity at the Au/H_2O interface of L-modes increased from $|E_{max}/E_0|^2 = 4.0 \times 10^2$, 7.6×10^2, 1.1×10^3 to 1.3×10^3 for Cytop thicknesses of 50, 100, 250, and 500 nm, respectively. The small increase of the maximum electric field intensity with the increase of the Cytop layer from 250 to 500 nm indicates that the Cytop layer was thick enough to attenuate the glass interference. Figure 2d shows the corresponding cross-sectional total electric field distribution of the L-mode for the PLR substrate with a Cytop thickness of 250 nm, indicating a much stronger electric field enhancement through effective plasmon coupling afforded by the symmetrical dielectric environment. For all Cytop thicknesses investigated the electric field distributions were confined to the nanohole edge (data not shown for the thicknesses of 50, 100, and 500 nm).

The intensity of the SERS signal (I_{SERS}) is directly related to the electromagnetic enhancement factor (EF_{EM}) through contributions of the amplified electric fields at the laser excitation frequency and the frequency of the Raman shifted photons[6]

$$I_{SERS} \propto EF_{EM} = \left|\frac{E(\omega_{Ex})}{E_0(\omega_{Ex})}\right|^2 \left|\frac{E(\omega_{RS})}{E_0(\omega_{RS})}\right|^2 \quad (3)$$

where $E(\omega_{Ex})$ and $E(\omega_{RS})$ are the electric field intensities at the Au/H_2O interface at the laser excitation frequency, ω_{Ex}, and the Raman scattering frequency, ω_{RS}, respectively; $E_0(\omega_{Ex})$ and $E_0(\omega_{RS})$ are the incident light electric fields at ω_{Ex} and ω_{RS}, respectively.

To quantify the additional contributions of all inelastically scattered photons interacting with the plasmonic nanostructure, a quality factor (Q_F) was adapted from Blaber et. al.[30] The Q_F used in this work is defined as

$$Q_F = \frac{1}{\beta}\int_{\omega_{RS}^{min}}^{\omega_{RS}^{max}} \left|\frac{E(\omega_{Ex})}{E_0(\omega_{Ex})}\right|^2 \left|\frac{E(\omega_{RS})}{E_0(\omega_{RS})}\right|^2 d\omega_{RS} \quad (4)$$

where ω_{RS}^{min} and ω_{RS}^{max} correspond to the range of Raman shifted frequencies under investigation (300−1,800 cm^{-1}) and β is a normalization constant defined as $\beta \equiv \omega_{RS}^{max} - \omega_{RS}^{min}$. The Q_F was calculated using the FDTD-simulated electric field intensities for the conventional and four PLR substrates and plotted as a function of Cytop thickness in Figure 2e. The Q_F experienced a sharp increase with respect to Cytop thickness, rising from 4.7×10^4 for the conventional substrate to 2.5×10^5 and 1.0×10^6 for the PLR substrates with 50 and 100 nm Cytop interstitial layers, respectively, and then a slow increase to 3.0×10^6 for Cytop thicknesses ≥250 nm, consistent with the observation of the surface maximum electric fields in Figure 2b. The plateauing behavior held true for Cytop thicknesses up to 1 μm (data not shown). This, once again, suggests that for Cytop films >250 nm the NHA can no longer "feel" the underlying glass substrate and can be considered embedded in a truly symmetric dielectric environment.

The correlation between SERS performance and the electric field intensity of plasmonic nanostructures has been demonstrated in our previous studies.[31−34] Here, we conducted a series of SERS experiments on conventional and PLR substrates with the gold NHAs fabricated via solvent-assisted molding.[26,35] The NHAs had P = 604 nm, D = 148 ± 8 nm, and gold film thickness of 19 ± 2 nm. Conventional substrates were fabricated with gold NHAs directly on glass, while the PLR structures contained interstitial Cytop layers between the gold NHAs and glass substrate with thicknesses of 152 ± 6 and 580 ± 4 nm. Scanning electron microscopy (SEM) images of a

DOI: 10.1021/acs.jpcc.6b08294
J. Phys. Chem. C 2016, 120, 25519−25529

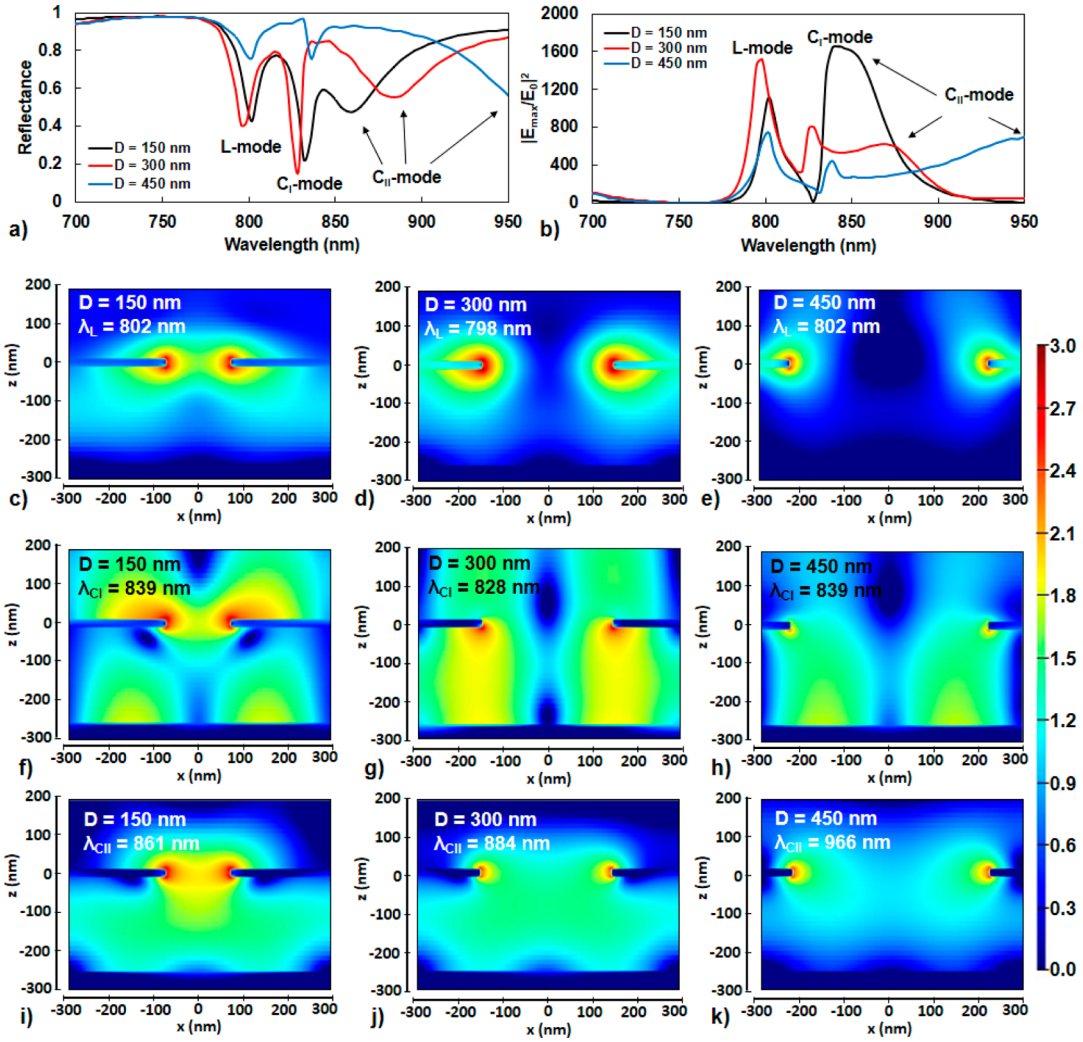

Figure 3. (a) Reflectance spectra and (b) maximum electric field surface intensities as a function of wavelength for LR substrates with a fixed Cytop thickness (T = 250 nm) and increasing nanohole diameters (D = 150, 300, and 450 nm). Electric field distributions for (c–e) the localized (L) modes, (f–h) the first-order coupled (C_I) modes, and (i–k) the second-order coupled (C_{II}) modes, respectively, in the x–z plane. The scale bar represents $|E_{max}/E_0|^2$ on a log scale.

representative conventional substrate in Figure S2a,b show that the uniform, large-area NHAs were resolved into the gold films. Monolayers of 4-mercaptobenzoic acid were immobilized on the NHAs. The substrates were then loaded in a homemade Teflon holder, filled with deionized water, and covered with a glass coverslip. Immersion of the substrates in water was necessary to fulfill dielectric symmetry. As discussed in the preceding section, the NHAs no longer "feel" the underlying glass substrate when separated by Cytop cladding layers ≥250 nm. Because the depth of the water separating the substrates and glass coverslips is ∼500 μm, it can be assumed that the NHAs do not sense the presence of the coverslips and thus should not deteriorate the desired dielectric symmetry.

Figure 2f shows the SERS spectra of 4-MBA monolayers collected from the conventional and PLR substrates. Several prominent vibrational modes are observed, with the most notable being the bands at 525, 1077, and 1590 cm^{-1} which correspond to the C–S stretching mode, the in-plane benzene ring breathing mode, and totally symmetric benzene ring breathing mode, respectively.[36,37] The SERS intensity increased from the conventional to the PLR substrate with Cytop thickness of 152 ± 6 nm, and further for the PLR substrate with a Cytop thickness of 580 ± 4 nm. Because the chemical enhancements of adsorbed 4-MBA can be assumed to be the same on all substrates, the increase in the SERS intensity is attributed only to the coupling of LSPRs at opposite interfaces of the NHAs from the PLR substrates and consequent electromagnetic enhancement. The experimentally measured peak intensity of the 1077 cm^{-1} band increased from 243 counts s^{-1} mW^{-1} for the conventional substrate, to 619 and 1147 counts s^{-1} mW^{-1} for the PLR substrates with Cytop thicknesses of 152 ± 6 and 580 ± 4 nm, respectively. These values are also plotted in Figure 2e. The experimentally measured SERS intensities follow the same trend as a function of Cytop thickness as predicted by the FDTD-calculated Q_F.

Previous studies conducted on LR-SPR substrates demonstrated that leakage of light through the substrate could reduce both the efficiency of plasmon generation at the Au/H_2O interface, and the penetration depth of the evanescent field above the Au/H_2O interface.[38] To combat the light leakage, an optically opaque "resonant mirror" was placed between the glass substrate and Cytop film to effectively prohibit light from passing through the substrate. Therefore, we also inserted a "resonant mirror" between the glass/Cytop interface in PLR

DOI: 10.1021/acs.jpcc.6b08294
J. Phys. Chem. C 2016, 120, 25519–25529

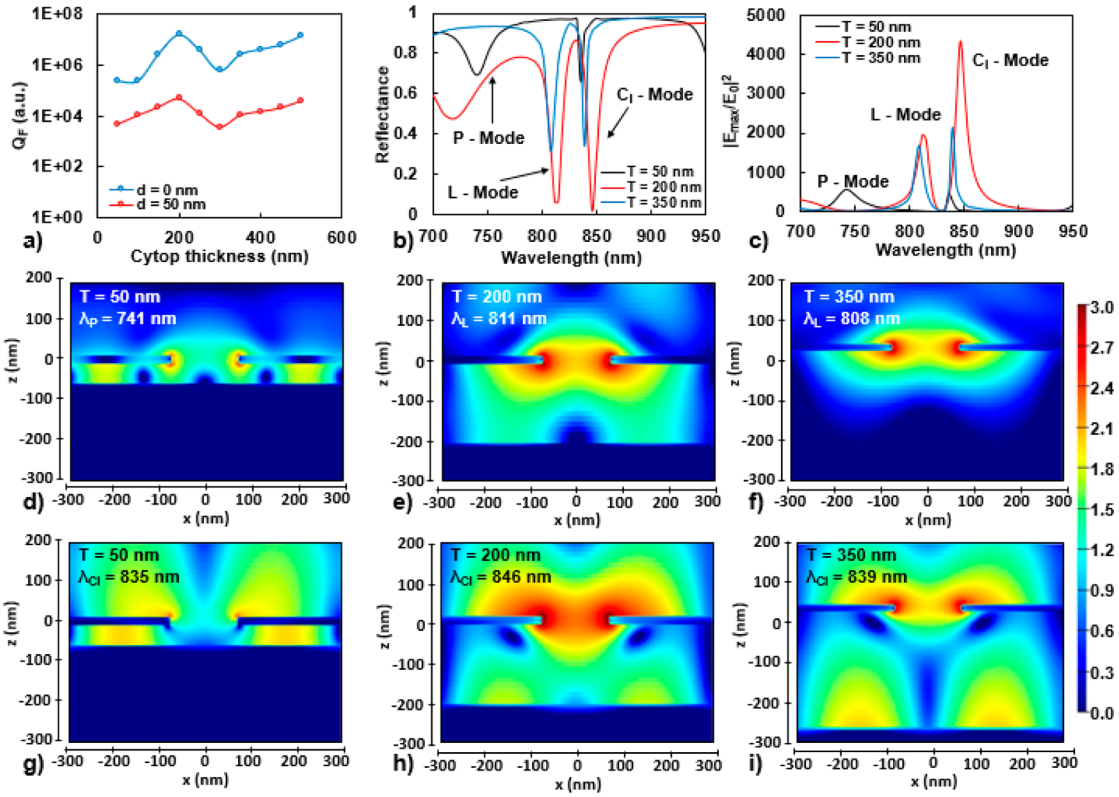

Figure 4. (a) Quality factor (Q_F) at the Au/H_2O interface (d = 0 nm) and a distance of 50 nm (d = 50 nm) above the Au/H_2O interface plotted as a function of Cytop thickness. (b) Reflectance spectra and (c) maximum electric field surface intensity as a function of wavelength for LR substrates with a fixed nanohole diameter (D = 150 nm) and increasing Cytop thicknesses (T = 50, 200, and 350 nm). The propagating (P), localized (L), and first-order coupled (C_I) modes are indicated. Electric field distributions for (d) the P-mode (T = 50 nm) and (e, f) the L-mode (T = 200 and 350 nm), and (g–i) the C_I-mode (T = 50, 200, 350 nm), respectively, in the x–z plane. The scale bar represents $|E_{max}/E_0|^2$ on a log scale.

substrates. The mirror induced strong constructive interference on the surface of gold NHAs through formation of a Fabry–Pérot optical cavity between the resonant mirror and NHA. The unit cell of this class of LR-SERS substrates for the FDTD simulations is shown in Figure 1d.

The plasmon resonances and the electric field distributions of LR-SERS substrates were first investigated as a function of nanohole diameter, with the Cytop thickness held constant. The thickness for the initial simulations was fixed at 250 nm because it was observed with PLR substrates that this thickness was sufficiently large for the gold NHA to completely decouple from the glass substrate. Figure 3a shows the reflectance spectra for three representative diameters (D = 150, 300, and 450 nm) of LR-SERS substrates. Three resonance modes are observed. The mode around 800 nm is attributed to the localized mode, which is similar to that present in the PLR substrate (T = 250 nm) at λ_L = 808 nm. Figure S5a–c shows that the E_z polarity oscillation of the L-mode exhibited strong confinement at the nanohole edges, as observed for the conventional (Figure S3b) and PLR substrates (Figure S4). This L-mode was unaffected by the underlying gold film and was independent of diameter. Additionally, two new modes are generated and attributed to the first- and second-order coupling between the gold NHAs and underlying gold film, which are termed C_I and C_{II}, respectively. The first-order coupling can be seen in the E_z distributions (Figure S 5d–f). Polarity oscillation occurs not only laterally but also vertically between the NHA and resonant mirror. For D = 300 nm, an in-phase oscillation is observed (Figure S5e), whereas for D = 150 and 450 nm an out-of-phase oscillation is observed (Figure S5d,f). Similar to the L-mode, the resonance wavelength of the first-order coupled mode remained largely invariant with respect to diameter. The second-order coupling displayed a coupling pattern similar to that of the first-order mode (Figures S5g–i). However, the resonance wavelength red-shifted as the diameter was increased (Figure 3a).

Figure 3b shows $|E_{max}/E_0|^2$ at the Au/H_2O interface as a function of wavelength for the three substrates. With respect to the localized mode, $|E_{max}/E_0|^2$ at the Au/H_2O interface increased as the diameter was increased from 150 to 300 nm and then decreased as the diameter was further increased to 450 nm. A maximum intensity of $|E_{max}/E_0|^2 = 1.51 \times 10^3$ for D = 300 nm was observed, while values of $|E_{max}/E_0|^2 = 1.11 \times 10^3$ and 7.43×10^2 were observed for diameters of 150 and 450 nm, respectively. Both coupled modes exhibited a decrease in $|E_{max}/E_0|^2$ as the diameter was increased. For a fixed diameter, however, the coupled modes exhibited similar intensities.

Inspection of the cross-sectional total electric field profiles for the three modes can provide insight into the plasmonic nature of LR-SERS substrates and how they can be tuned for optimal SERS-based detection. Figure 3c–e shows that the excitation of the L-mode produced two distinct hot-spots at the edges of the nanoholes, and negligible electric field density was located in the optical cavity between the NHA and resonant mirror. Intuitively, as the diameter was made larger, the two hot-spots became decoupled in the L-mode because of increased separation distance. Figure 3f–h show that the C_I-mode exhibited greater electric field density located in the

DOI: 10.1021/acs.jpcc.6b08294
J. Phys. Chem. C 2016, 120, 25519–25529

optical cavity due to increased coupling between the NHA and underlying gold film. A smaller diameter (D = 150 nm) resulted in strong electric field localization above the Au/H_2O interface (Figure 3f). With increased diameter (D = 300 and 450 nm), the electric field localization shifted below the Au/Cytop interface (Figure 3g,h). The C_{II}-mode exhibited the inverse behavior compared to the C_I-mode, with electric field density localizing to the interstitial cavity as the diameter decreased (Figures 3i-k). The highest $|E_{max}/E_0|^2$ value at the Au/H_2O interface was obtained for the case of D = 150 nm. Therefore, to further investigate the plasmonic response of LR-SERS substrates, the diameter was fixed at D = 150 nm, and the thickness of the Fabry–Pérot optical cavity on the plasmonic response was explored.

It is well-known that the separation distance between two metal films in a Fabry–Pérot optical cavity can have profound effects on the resonant modes and the electric field distributions of plasmonic nanostructures.[31,33,39,40] Cytop thicknesses were varied from 50 to 500 nm by 50 nm increments, and the Q_F was calculated from FDTD-simulated electric field intensities at the Au/H_2O interface (d = 0 nm) and at d = 50 nm above the Au/H_2O interface. The plasmonic sensitivity to the cavity depth becomes apparent when comparing the Q_F as a function of Cytop thickness (Figure 4a). The Q_F sharply increased as the Cytop film was increased from 50 to 200 nm, where the Q_F exhibits its maximum value. A local minimum was reached at T = 350 nm with a gradual increase in the Q_F as the Cytop film was further increased to 500 nm. The same oscillatory trend of the Q_F was observed at d = 50 nm, with a corresponding drop of approximately 2 orders of magnitude in the Q_F. A detailed analysis was carried out on three representative thicknesses (T = 50, 200, and 350 nm) which encompassed the global maximum and minima in the Q_F at d = 0 and 50 nm.

Figure 4b shows the reflectance spectra of LR-SERS substrates with Cytop thicknesses of T = 50, 200, and 350 nm. Two resonant modes are generated at 741 and 835 nm for T = 50 nm. The E_z distribution of the mode at 741 nm shown in Figure S6a clearly displays the characteristics of the P-mode that was observed for the conventional and PLR substrates at shorter wavelengths. Although no L-mode was observed because of the shallow optical cavity, the first-order coupled mode (C_I) appeared at λ_{CI} = 835 nm, which can be confirmed by the characteristics shown in the E_z distribution in Figure S6d. As the Cytop thickness was increased to 200 nm, the L and C_I modes red-shifted to λ_L = 811 nm and λ_{CI} = 846 nm, respectively, while the P-mode blueshifted to λ_P = 720 nm. The E_z distributions of the modes at 811 and 846 nm shown in Figures S6b and e exhibited the characteristics of the L and C_I modes, respectively. The E_z distribution of the P-mode is not shown. As the Cytop thickness was further increased to 350 nm, both the L and C_I modes exhibited blueshifted resonances to λ_L = 808 nm and λ_{CI} = 839 nm, respectively (Figures S6c and f). The P-mode further blueshifted out of the spectral range governed by eq 2.

The complementary $|E_{max}/E_0|^2$ values at the Au/H_2O interface for the three thicknesses are shown in Figure 4c. With T = 50 nm, both the P and C_I modes produced very weak intensities. Because the P-mode is out of the lower integral limit of eq 4, this mode does not contribute to the Q_F or the SERS signal. The substrates with thicker Cytop layers showed comparable values of $|E_{max}/E_0|^2 = 1.97 \times 10^3$ and 1.67×10^3 generated by the localized mode for T = 200 and 350 nm, respectively. The C_I-mode showed a drastic increase in $|E_{max}/E_0|^2$ for T = 200 nm with a value of $|E_{max}/E_0|^2 = 4.37 \times 10^3$ compared to $|E_{max}/E_0|^2 = 2.13 \times 10^3$ for T = 350 nm. Because both localized and C_I modes are within the integral limits of eq 4, the strong electric field makes Q_F a maximum at T = 200 nm (Figure 4a).

Again, the cross-sectional electric field distributions are inspected to help elucidate the nature of the field enhancements. In contrast to the conventional and PLR substrates that exhibited the propagating mode bound to the Au/H_2O interface (Figures S3a and 4a–d), the propagating mode displayed by the LR-SERS substrate with T = 50 nm showed stronger polarity oscillation bound to the cavity between the NHA and resonant mirror (Figure S6a). Although polarity oscillation was observed at the Au/H_2O interface for the LR-SERS substrate (T = 50 nm), the intensity was weaker than that of the interstitial cavity. Proximity of the NHA to the resonant mirror allowed for increased coupling efficiency and enhancement of the electric field in the cavity (Figure 4d). When the Cytop thickness increased from T = 200 to 350 nm, the coupling between the NHA and resonant mirror was weakened, and the electric field distribution of the localized mode became more confined to the nanohole edges as shown in panels e and f of Figure 4, respectively. When the electric field distributions of the C_I-mode for the three thicknesses in Figure 4g–i are compared, for T = 200 nm, the electric field was not only strongly enhanced at the Au/H_2O interface as exhibited by $|E_{max}/E_0|^2$ in Figure 4c, but most importantly, the strong electric field was extended to greater distances above the Au/H_2O interface. Therefore, it is expected that the LR-SERS substrate with D = 150 nm and T = 200 nm will yield the long-range behavior.

LR-SERS substrates were fabricated with the optimized geometrical configurations obtained by the FDTD simulations to verify the extended field profile. We first verified the influence of the symmetry of dielectric media on the surface electric field intensity, that is, the SERS signals of molecules on the NHA surfaces. We formed monolayers of 4-MBA on freshly prepared LR-SERS substrates. To create dielectric symmetry on both sides of the NHA of the LR-SERS substrate, a 500 nm Cytop film was spun cast on top of the NHA with a 4-MBA monolayer. The SERS spectrum was collected and is shown in Figure 5a. To break dielectric symmetry, the SERS spectrum of 4-MBA on the freshly made LR-SERS substrate was collected directly in air (n = 1). The refractive index difference between air and Cytop creates an asymmetric dielectric environment, which leads to a reduction in the SERS signal, as shown in Figure 5a. Comparison of the 1077 cm^{-1} benzene ring breathing bands show an intensity of $I_{1077} = 6.69 \times 10^3$ and 1.12×10^4 counts s^{-1} mW^{-1} for the SERS spectra collected on bare and Cytop-coated LR-SERS substrates, respectively. The electric field intensity of $|E_{max}/E_0|^2$ for the asymmetrical case (Figure S7) also shows a lower value compared to the symmetrical case (Figure 4c).

The distance dependence of SERS signals on LR-SERS substrates was then investigated and compared to the conventional substrates. Ultrathin Cytop cladding layers were used to control the distance of the Raman reporter molecule, rhodamine 6G (R6G), from the gold NHA surfaces while maintaining the dielectric symmetry. A 10 nm Cytop cladding layer was spun cast on the gold NHA surfaces of LR-SERS and conventional substrates. Even though the spin-casting method cannot control the thickness precisely, nor offer many different

DOI: 10.1021/acs.jpcc.6b08294
J. Phys. Chem. C 2016, 120, 25519–25529

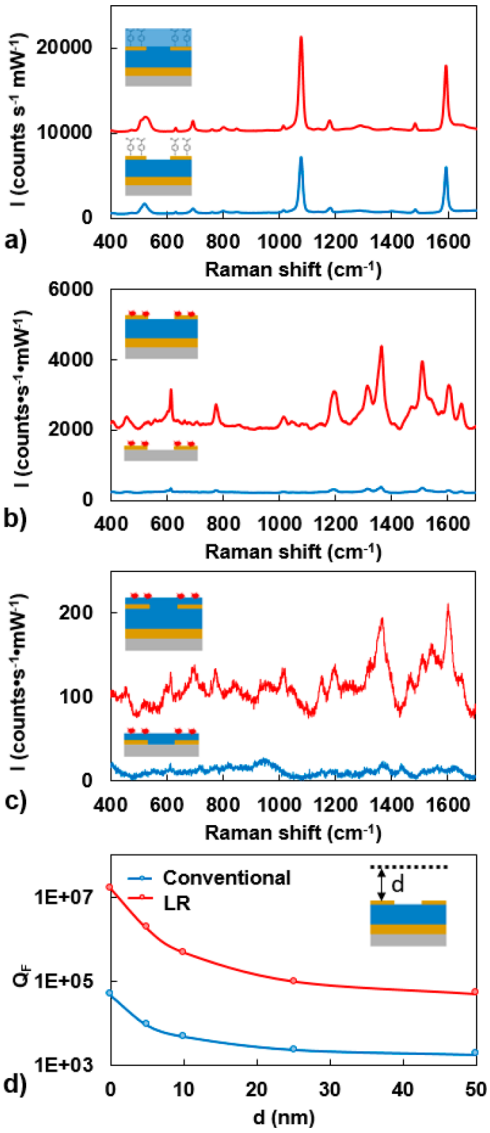

Figure 5. (a) SERS spectra of 4-MBA collected in air on bare gold and Cytop-coated LR-SERS substrates. SERS spectra of 1 mM rhodamine 6G collected on LR-SERS substrates (red traces) and conventional substrates (blue traces) at (b) the surface of the Au/H_2O interface and (c) Cytop/H_2O interface with a Cytop capping layer thickness of 10 ± 1 nm. The spectra have been background-corrected and offset for clarity. Spectra were collected in a single 10 s accumulation, and the laser power was measured to be 2.4 mW through a 50× (N.A. 0.8) objective. (d) FDTD-calculated quality factor (Q_F) for conventional and LR-SERS substrates as a function of distance from the Au/H_2O interface.

thicknesses with a high resolution as the atomic layer deposition (ALD) technique provides,[41] it offers a quick, easy way to maintain the dielectric symmetry with Cytop. SERS spectra were collected with R6G on LR-SERS and conventional substrates with bare gold NHA surfaces and 10 nm Cytop-coated surfaces. To do so, the substrates were exposed to a 1 mM R6G aqueous solution for 30 min, air-dried, and then backfilled with DI H_2O in the Teflon holder. Figure 5b shows the SERS spectra of R6G at the gold NHA surfaces of the LR-SERS and conventional substrates. The LR-SERS substrate generated much stronger signals of the characteristic bands at 614, 77, 1197, 1314, 1365, and 1511 cm^{-1}, corresponding to the in-plane bending, C−H out-of-plane bending, and xanthene and phenyl ring breathing, respectively.[42,43] Using the 1365 cm^{-1} band as an indicator, the peak intensities are 2.0×10^3 and 1.5×10^2 counts cm^{-1} mW^{-1} for the LR-SERS and conventional substrates, respectively. The SERS spectra of R6G collected from the 10 nm Cytop-coated surfaces of the LR-SERS and conventional substrates are shown in Figure 5c.

The LR-SERS substrate still displayed prominent R6G characteristic bands while none were observed in the conventional substrate, confirming the presence of the extended electric fields predicted by the FDTD simulations. The peak height of the 1365 cm^{-1} band for the 10 nm Cytop-coated LR-SERS substrates was found to be 9.0×10^1 counts·cm^{-1}·mW^{-1} compared to 2.0×10^3 counts·cm^{-1}·mW^{-1} for the bare gold, LR-SERS substrate. Addition of the 10 nm Cytop cladding layer resulted in a signal intensity conservation of 4% compared to the bare gold LR-SERS substrate. The decrease of the SERS signal could be due to three factors: the decay of the electric field (the electromagnetic enhancement mechanism), the absence of possible charge transfer between R6G and gold (the chemical enhancement mechanism), and the difference of R6G adsorption on Cytop and gold surfaces. The electromagnetic enhancement effect can be estimated from the Q_F. Figure 5d shows the Q_F as a function of distance from the Au/H_2O interface for the LR-SERS substrates. The Q_F drops from 1.6×10^7 at the Au/H_2O interface (d = 0 nm) to 4.9×10^5 at the distance of 10 nm above the Au/H_2O interface (d = 10 nm), which is about 3%.

The Q_F was also compared as a function of distance from the Au/H_2O interface for both the LR-SERS and conventional substrates (Figure 5d). At the surface of the NHAs (d = 0 nm), the LR-SERS substrate showed a Q_F of 1.6×10^7, compared to 4.7×10^4 for that of the conventional substrate. The amplified Q_F is attributed to the order of magnitude increase in the localized mode of the LR-SERS substrate over the conventional substrate, and the presence of the first-order coupled mode in the LR-SERS substrate that is not generated by the conventional substrate. As the distance from the NHAs was increased to d = 10 nm, the Q_F of the conventional substrate decayed to 10% of the surface intensity. The LR-SERS substrate decayed to 4.9×10^5, corresponding to 3% of the surface intensity. The faster decay rate of the Q_F observed in the LR-SERS substrate suggests strong confinement of the hot-spot. This observation is in contrast to typical LR-SPR, which produces a longer penetration depth. However, the Q_F in the immediate vicinity of the LR-SERS substrate remains larger than that of the conventional substrate, which enables successful detection of R6G.

CONCLUSIONS

We have observed long-range behavior in plasmonically engineered SERS substrates. This was accomplished by capitalizing on the benefits afforded by long-range surface plasmon resonance through incorporation of nanohole arrays into a symmetrical dielectric environment. FDTD modeling was performed to investigate the effects of the substrate and geometric parameters of the nanohole arrays on the electric field extension. Symmetrical dielectric environments were shown to increase the SERS intensity of the Raman label, 4-mercaptobenzoic acid. An increase of 70% was observed for the symmetrical LR-SERS substrate relative to the asymmetrical substrate. Importantly, distance dependence measurements showed that the LR-SERS substrates were capable of R6G detection with a separation distance of 10 nm between the

DOI: 10.1021/acs.jpcc.6b08294
J. Phys. Chem. C 2016, 120, 25519−25529

SERS-active surface and Raman reporter. The LR-SERS substrates described here represent an interesting class of SERS substrates that can be fundamentally expanded to include other plasmonic nanostructures or applied to SERS applications requiring an extended probing depth.

■ ASSOCIATED CONTENT

Supporting Information

The Supporting Information is available free of charge on the ACS Publications website at DOI: 10.1021/acs.jpcc.6b08294.

FDTD-simulated electric field z-component of conventional, PLR, and LR-SERS substrates; FDTD-simulated reflectance, surface intensity, electric field z-component, and cross-sectional total electric field intensity of the optimized LR-SERS substrate with dielectric background of $n = 1$; and schematic of the fabrication process (PDF)

■ AUTHOR INFORMATION

Corresponding Authors

*Phone: +420-266-773-404. E-mail: homola@ufe.cz.
*Phone: +1-206-543-4807. E-mail: qyu@u.washington.edu.

Notes

The authors declare no competing financial interest.

■ ACKNOWLEDGMENTS

The authors gratefully acknowledge the financial support provided by the National Science Foundation (NSF, CBET 1159609), the University of Washington (UW) Royalty Research Fund, the Czech Science Foundation (P205/12/G118), and the Academy of Sciences of the Czech Republic (Praemium Academiae). Raman and SEM experiments were performed at the Molecular Analysis Facility (MAF). We also thank Dr. Richard Bojko at the Washington Nanofabrication Facility (WNF) for fabrication of the silicon master mold. The MAF and WNF are part of the National Nanotechnology Coordinated Infrastructure (NNCI) at UW supported by the NSF (ECCS-1542101).

■ REFERENCES

(1) Schlucker, S. Surface-Enhanced Raman Spectroscopy: Concepts and Chemical Applications. *Angew. Chem., Int. Ed.* **2014**, *53*, 4756−4795.

(2) Halvorson, R. A.; Vikesland, P. J. Surface-Enhanced Raman Spectroscopy (SERS) for Environmental Analyses. *Environ. Sci. Technol.* **2010**, *44*, 7749−7755.

(3) Golightly, R. S.; Doering, W. E.; Natan, M. J. Surface-Enhanced Raman Spectroscopy and Homeland Security: A Perfect Match? *ACS Nano* **2009**, *3*, 2859−2869.

(4) Kneipp, K.; Wang, Y.; Kneipp, H.; Perelman, L. T.; Itzkan, I.; Dasari, R.; Feld, M. S. Single Molecule Detection Using Surface-Enhanced Raman Scattering (SERS). *Phys. Rev. Lett.* **1997**, *78*, 1667−1670.

(5) Nie, S. M.; Emery, S. R. Probing Single Molecules and Single Nanoparticles by Surface-Enhanced Raman Scattering. *Science* **1997**, *275*, 1102−1106.

(6) Stiles, P. L.; Dieringer, J. A.; Shah, N. C.; Van Duyne, R. P. Surface-Enhanced Raman Spectroscopy. *Annu. Rev. Anal. Chem.* **2008**, *1*, 601−626.

(7) Valley, N.; Greeneltch, N.; Van Duyne, R. P.; Schatz, G. C. A Look at the Origin and Magnitude of the Chemical Contribution to the Enhancement Mechanism of Surface-Enhanced Raman Spectroscopy (SERS): Theory and Experiment. *J. Phys. Chem. Lett.* **2013**, *4*, 2599−2604.

(8) Schatz, G. C.; Van Duyne, R. P. Electromagnetic Mechanism of Surface-Enhanced Spectroscopy. In *Handbook of Vibrational Spectroscopy*; Chalmers, J. M., Griffiths, P. R., Eds.; Wiley: New York, 2002; pp 759−774.

(9) Murray, C. A.; Allara, D. L.; Rhinewine, M. Silver-Molecule Seperation Dependence of Surface-Enhanced Raman-Scattering. *Phys. Rev. Lett.* **1981**, *46*, 57−60.

(10) Kennedy, B. J.; Spaeth, S.; Dickey, M.; Carron, K. T. Determination of the Distance Dependence and Experimental Effects for Modified SERS Substrates Based on Self-Assembled Monolayers Formed Using Alkanethiols. *J. Phys. Chem. B* **1999**, *103*, 3640−3646.

(11) Whitney, A. V.; Elam, J. W.; Zou, S. L.; Zinovev, A. V.; Stair, P. C.; Schatz, G. C.; Van Duyne, R. P. Localized Surface Plasmon Resonance Nanosensor: A High-Resolution Distance-Dependence Study Using Atomic Layer Deposition. *J. Phys. Chem. B* **2005**, *109*, 20522−20528.

(12) Kumari, G.; Kandula, J.; Narayana, C. How Far Can We Probe by SERS? *J. Phys. Chem. C* **2015**, *119*, 20057−20064.

(13) Singh, A. K.; Khan, S. A.; Fan, Z.; Demeritte, T.; Senapati, D.; Kanchanapally, R.; Ray, P. C. Development of a Long-Range Surface-Enhanced Raman Spectroscopy Ruler. *J. Am. Chem. Soc.* **2012**, *134*, 8662−8669.

(14) Homola, J. Surface Plasmon Resonance Sensors for Detection of Chemical and Biological Species. *Chem. Rev.* **2008**, *108*, 462−493.

(15) Homola, J.; Yee, S. S.; Gauglitz, G. Surface Plasmon Resonance Sensors: Review. *Sens. Actuators, B* **1999**, *54*, 3−15.

(16) Berini, P. Long-Range Surface Plasmon Polaritons. *Adv. Opt. Photonics* **2009**, *1*, 484−588.

(17) Sarid, D. Long-Range Surface-Plasma Waves on Very Thin Metal-Films. *Phys. Rev. Lett.* **1981**, *47*, 1927−1930.

(18) Craig, A. E.; Olson, G. A.; Sarid, D. Experimental-Observation of the Long-Range Surface-Plasmon Polariton. *Opt. Lett.* **1983**, *8*, 380−382.

(19) Dostalek, J.; Kasry, A.; Knoll, W. Long Range Surface Plasmons for Observation of Biomolecular Binding Events at Metallic Surfaces. *Plasmonics* **2007**, *2*, 97−106.

(20) Toma, K.; Dostalek, J.; Knoll, W. Long Range Surface Plasmon-Coupled Fluorescence Emission for Biosensor Applications. *Opt. Express* **2011**, *19*, 11090−11099.

(21) Vala, M.; Etheridge, S.; Roach, J. A.; Homola, J. Long-Range Surface Plasmons for Sensitive Detection of Bacterial Analytes. *Sens. Actuators, B* **2009**, *139*, 59−63.

(22) Chabot, V.; Miron, Y.; Grandbois, M.; Charette, P. G. Long Range Surface Plasmon Resonance for Increased Sensitivity in Living Cell Biosensing Through Greater Probing Depth. *Sens. Actuators, B* **2012**, *174*, 94−101.

(23) Liu, Y.; Xu, S. P.; Xuan, X. Y.; Zhao, B.; Xu, W. Q. Long-Range Surface Plasmon Field-Enhanced Raman Scattering Spectroscopy Based on Evanescent Field Excitation. *J. Phys. Chem. Lett.* **2011**, *2*, 2218−2222.

(24) Xuan, X. Y.; Xu, S. P.; Liu, Y.; Li, H. B.; Xu, W. Q.; Lombardi, J. R. A Long-Range Surface Plasmon Resonance/Probe/Silver Nanoparticle (LRSPR-P-NP) Nanoantenna Configuration for Surface-Enhanced Raman Scattering. *J. Phys. Chem. Lett.* **2012**, *3*, 2773−2778.

(25) Palik, E. D.; Ghosh, G.*Handbook of Optical Constants of Solids*; Academic Press: San Diego, CA, 1998.

(26) Qin, D.; Xia, Y.; Whitesides, G. M. Soft Lithography for Micro and Nanoscale Patterning. *Nat. Protoc.* **2010**, *5*, 491−502.

(27) Chang, S. H.; Gray, S. K.; Schatz, G. C. Surface Plasmon Generation and Light Transmission by Isolated Nanoholes and Arrays of Nanoholes in Thin Metal Films. *Opt. Express* **2005**, *13*, 3150−3165.

(28) Homola, J. *Surface Plasmon Resonance Based Biosensors*; Springer: Berlin, 2006.

(29) Haynes, C. L.; Van Duyne, R. P. Plasmon-Sampled Surface-Enhanced Raman Excitation Spectroscopy. *J. Phys. Chem. B* **2003**, *107*, 7426−7433.

(30) Blaber, M. G.; Schatz, G. C. Extending SERS into the Infrared with Gold Nanosphere Dimers. *Chem. Commun.* **2011**, *47*, 3769−3771.

(31) Xu, J. J.; Guan, P.; Kvasnicka, P.; Gong, H.; Homola, J.; Yu, Q. M. Light Transmission and Surface-Enhanced Raman Scattering of Quasi-3D Plasmonic Nanostructure Arrays with Deep and Shallow Fabry-Perot Nanocavities. *J. Phys. Chem. C* **2011**, *115*, 10996−11002.
(32) Xu, J.; Zhang, L.; Gong, H.; Homola, J.; Yu, Q. Tailoring Plasmonic Nanostructures for Optimal SERS Sensing of Small Molecules and Large Microorganisms. *Small* **2011**, *7*, 371−376.
(33) Xu, J.; Kvasnicka, P.; Idso, M.; Jordan, R. W.; Gong, H.; Homola, J.; Yu, Q. Understanding the Effects of Dielectric Medium, Substrate, and Depth on Electric Fields and SERS of Quasi-3D Plasmonic Nanostructures. *Opt. Express* **2011**, *19*, 20493−20505.
(34) Xu, J.; Turner, J. W.; Idso, M.; Biryukov, S. V.; Rognstad, L.; Gong, H.; Trainer, V. L.; Wells, M. L.; Strom, M. S.; Yu, Q. In Situ Strain-Level Detection and Identification of Vibrio Parahaemolyticus Using Surface-Enhanced Raman Spectroscopy. *Anal. Chem.* **2013**, *85*, 2630−2637.
(35) King, E.; Xia, Y. N.; Zhao, X. M.; Whitesides, G. M. Solvent-Assisted Microcontact Molding: A Convenient Method for Fabricating Three-Dimensional Structures on Surfaces of Polymers. *Adv. Mater.* **1997**, *9*, 651−654.
(36) Szafranski, C. A.; Tanner, W.; Laibinis, P. E.; Garrell, R. L. Surface-Enhanced Raman Spectroscopy of Aromatic Thiols and Disulfides on Gold Electrodes. *Langmuir* **1998**, *14* (13), 3570−3579.
(37) Han, S. W.; Lee, S. J.; Kim, K. Self-Assembled Monolayers of Aromatic Thiol and Selenol on Silver: Comparative Study of Adsorptivity and Stability. *Langmuir* **2001**, *17*, 6981−6987.
(38) Wang, Y.; Knoll, W.; Dostalek, J. Bacterial Pathogen Surface Plasmon Resonance Biosensor Advanced by Long Range Surface Plasmons and Magnetic Nanoparticle Assays. *Anal. Chem.* **2012**, *84*, 8345−8350.
(39) Stewart, M. E.; Mack, N. H.; Malyarchuk, V.; Soares, J.; Lee, T. W.; Gray, S. K.; Nuzzo, R. G.; Rogers, J. A. Quantitative multispectral biosensing and 1D imaging using quasi-3D plasmonic crystals. *Proc. Natl. Acad. Sci. U. S. A.* **2006**, *103*, 17143−17148.
(40) Artar, A.; Yanik, A. A.; Altug, H. Fabry-Perot Nanocavities in Multilayered Plasmonic Crystals for Enhanced Biosensing. *Appl. Phys. Lett.* **2009**, *95*, 051105.
(41) Masango, S. S.; Hackler, R. A.; Large, N.; Henry, A.-I.; McAnally, M. O.; Schatz, G. C.; Stair, P. C.; Van Duyne, R. P. High-Resolution Distance Dependence Study of Surface-Enhanced Raman Scattering Enabled by Atomic Layer Deposition. *Nano Lett.* **2016**, *16*, 4251−4259.
(42) Hildebrandt, P.; Stockburger, M. Surface-Enhanced Resonance Raman-Spectroscopy of Rhodamine-6G Adsorbed on Colloidal Silver. *J. Phys. Chem.* **1984**, *88*, 5935−5944.
(43) Watanabe, H.; Hayazawa, N.; Inouye, Y.; Kawata, S. DFT Vibrational Calculations of Rhodamine 6G Adsorbed on Silver: Analysis of Tip-Enhanced Raman Spectroscopy. *J. Phys. Chem. B* **2005**, *109*, 5012−5020.

DOI: 10.1021/acs.jpcc.6b08294
J. Phys. Chem. C 2016, 120, 25519−25529